Chasing H- in Rare-earth Metal Oxyhydride Thin Films

Chaykina, D.

DOI
10.4233/uuid:a88fbe40-ff1e-47a7-bc8e-030f92213066

Publication date
2022

Document Version
Final published version

Citation (APA)
Chaykina, D. (2022). *Chasing H- in Rare-earth Metal Oxyhydride Thin Films*. [Dissertation (TU Delft), Delft University of Technology]. https://doi.org/10.4233/uuid:a88fbe40-ff1e-47a7-bc8e-030f92213066

Chasing H$^-$ in Rare-earth Metal Oxyhydrides

Diana Chaykina

Chasing H^- in Rare-earth Metal Oxyhydride Thin Films

Chasing H^- in Rare-earth Metal Oxyhydride Thin Films

Dissertation

for the purpose of obtaining the degree of doctor
at Delft University of Technology,
by the authority of the Rector Magnificus prof. dr. ir. T. H. J. J. van der Hagen,
chair of the Board for Doctorates
to be defended publicly on
Wednesday 23 November 2022 at 17.30 o'clock

by

Diana CHAYKINA

Master of Science in Nanoscience, Nanotechnology, & Nanoengineering,
Catholic University of Leuven, Belgium,
Born in Gomel, Belarus

This dissertation has been approved by the promotors

promotor: Prof. dr. B. Dam
copromotor: Dr. S. W. H. Eijt

Composition of the doctoral committee:

Rector Magnificus,	chairperson
Prof. dr. Bernard Dam,	Delft University of Technology (NL), promotor
Dr. Stephan W. H. Eijt,	Delft University of Technology (NL), copromotor
Independent members:	
Dr. Thomas Prokscha,	Paul Scherrer Institute (CH)
Prof. dr. ing. Bjørn C. Hauback,	University of Oslo (NO)
Prof. dr. habil. phys. Juris Purāns,	University of Latvia (LV)
Prof. dr. Bernard A. Boukamp,	University of Twente (NL)
Prof. dr. ir. Sybrand van der Zwaag	Delft University of Technology (NL)
Prof. dr. Hans Geerlings,	Delft University of Technology (NL), reserved member

Front cover artwork by: Diana Chaykina
Printed by: printerpro.nl

ISBN 978-94-6384-391-1
An electronic version of this dissertation is available at
`http://repository.tudelft.nl/`.

This doctoral research has been carried out in the Materials for Energy Conversion and Storage (MECS) group, Department of Chemical Engineering, Faculty of Applied Sciences, Delft University of Technology, The Netherlands. This work is part of the Materials for Sustainability (Mat4Sus) research programme (project number 680.M4SF.034), which is financed by the Netherlands Organisation for Scientific Research (NWO).

Contents

1

Introduction

The aim of this thesis is to understand more about the fundamentals of photochromism and H^- mobility in rare-earth metal oxyhydride thin films, two phenomena which, at the beginning of this work, were thought to be related. In order to understand the extent of this relationship, we used hydrogen-sensitive techniques to study local dynamics, changed the chemistry of the material, and analysed the electrochemical signals of the material. This chapter is an overview of the properties and applications of these materials, as well as an explanation of photochromism and H^- mobility, setting the context for the work of this thesis.

1.1 Sustainability

1.1.1 Potential role of rare-earth metal oxyhydrides

Rare-earth metal oxyhydrides are in a class of materials known as “multi-anion” compounds [1]. Oxyhydrides are particularly notable because they contain hydride (H^-) ions in their structure, which is rather uncommon [2], and leads to many interesting phenomena. Below is a non-exhaustive list of possible applications of rare-earth metal oxyhydrides. Of particular interest to this thesis are the first two.

Photochromic smart windows

In 2011, it was shown that “oxygen-containing yttrium hydride” thin films are transparent yellow materials which become dark when exposed to solar radiation [3] (Fig. 1.1a). Coupled to this colour change is a reduction of the electrical resistance. Both of these effects are reversible; the material goes back to its original transparent insulating state when the light is removed.

Materials that reversibly change colour due to light exposure are called “photochromic” and can be used for a variety of applications. The most basic application is as a coating for eyeglasses that change colour in the sun. More interesting, however, is to use photochromic rare-earth oxyhydride thin films as coatings for smart windows. In this case, a smart window is one that prevents sunlight, and importantly, heat from entering a building. A growing expense (both financial and in terms of our collective carbon footprint) is cooling [4]. A photochromic smart window would be able to absorb excess heat, stopping it from entering the building and automatically adjust its opacity/heat absorption based on the sunlight conditions outside without any intervention from the person inside the building, thereby decreasing the need for cooling and temperature regulation.

At present, there are still fundamental aspects of this effect in rare-earth metal oxyhydrides that are not completely clear, although some key findings are discussed in section 1.3 and throughout this thesis. From a practical point-of-view, the colour switching speed and the maximum opacity that can be reached are tunable in a variety of ways, also discussed in section 1.3 and in several chapters. What remains to be solved is the so-called “memory effect”, where the performance of the films changes with repeated illumination [3]. As well, stability over time should be addressed. One solution to this is to add a protective coating without changing the oxyhydride material [5].

Solid-state H^- conductors

Solid-state ion conductors are of growing interest because they are important for electrochemical devices such as batteries, where ion conductors act as the electrolyte between two electrodes. Hydride-ion conduction could be useful in H_2-based devices such as fuels cells, or in metal hydride batteries (Fig. 1.1b).

It has been known since 2006 that H^- is mobile in some oxyhydrides [10], but progress in this direction began to accelerate with a publication in 2016 that showed a proof-of-concept device using $TiH_2|La_2LiHO_3|Ti$ and showing the pure H^- conduction through the middle oxyhydride [6] (Fig. 1.1b).

Soon after, pure H^- conduction was reported in La- and Nd-oxyhydrides with stoichiometric compositions [11], and with varying O:H compositions [12]. So far, La-oxyhydride pellets have the highest H^- conductivity of any oxyhydride material, although all reported

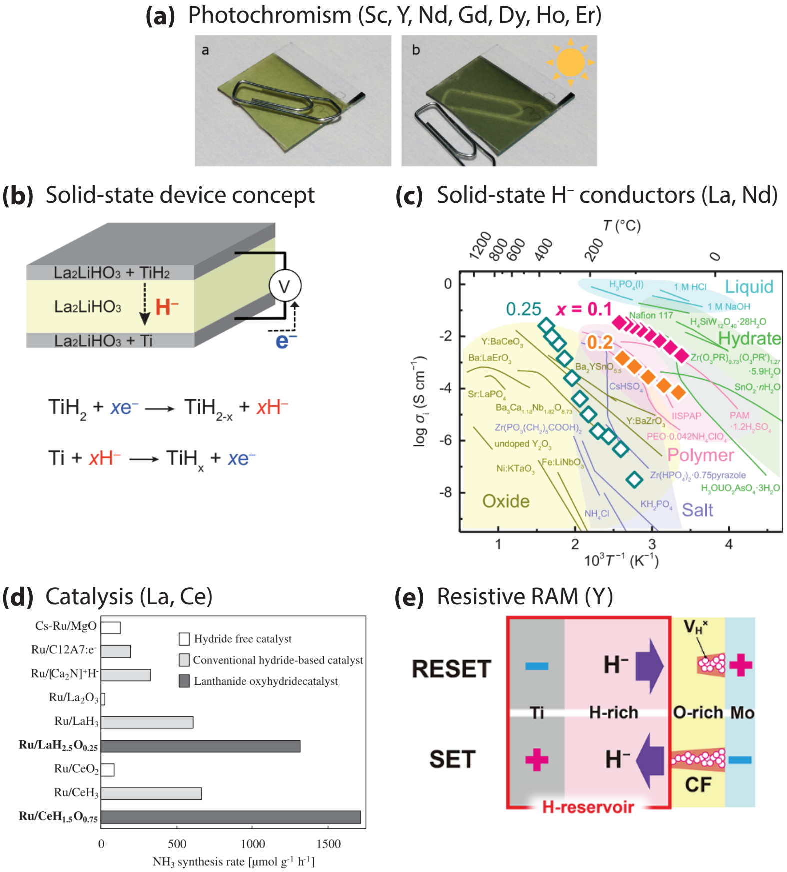

Figure 1.1: Visual overview of some applications of rare-earth metal oxyhydrides. (a) Photochromic Y-oxyhydride thin films are yellow and transparent (left), but become opaque when exposed to UV light (right). Adapted from [3]. (b) A concept for a device using a complex oxyhydride as the solid-state electrolyte, shuttling H^- ions between the two electrodes. Adapted from [6]. (c) Ionic conductivity as a function of temperature (Arrhenius plot) for $LaH_{3-2x}O_x$ with different O:H content. This is compared primarily to H^+ conductors. Adapted from [7]. (d) Ammonia synthesis rate for different modified Ru catalysts, highlighting the improved performance when using rare-earth oxyhydrides as a Ru support. Adapted from [8]. (e) Schematic of how a conductive filament may form in Y-oxyhydride when it is used in an ReRAM device with specific contacts. Adapted from [9].

materials operate optimally at moderate temperatures (>250-350°C). Recently, however, Fukui, et al. [7] reported that they could achieve an ionic conductivity of 1 mS/cm at room temperature for H-rich La-oxyhydrides (x<0.25) (Fig. 1.1c). Approaching the ionic conductivity of the best solid-state lithium-ion conductors (~10 mS/cm) [13, 14], this result is promising for such a young field. Some questions remain, however, about the stability of materials like La-oxyhydride in air [15] and the performance in a real electrochemical device with many cycles of charge and discharge.

Catalysis

Inspired by the H^- conductivity shown in La-oxyhydrides [12], and the suggestion that this may be an inherent property of light rare-earth metals (La→Nd) [11], Gd-, Sm-, La-, and Ce-oxyhydrides were used for catalytic ammonia production, with La- and Ce-oxyhydrides exhibiting the best performance [8, 16]. Ammonia is an important part of the energy transition because (1) it is considered to be a good carrier for H_2, (2) it is used in fertilizer, (3) it can be used as a fuel, and others [17]. However, the synthesis of ammonia, at present, is done primarily by the Haber-Bosch process, which requires a high energy input in the form of high temperature and pressure even when using a catalyst.

Ruthenium is one of the most reactive catalysts for ammonia production [18] because of its optimal N_2 adsorption energy, although it can adsorb H_2 too strongly [8]. Based on this, and previous work showing hydride materials improving the catalytic performance of Ru, the authors decided to try La- or Ce-oxyhydride supports loaded with a Ru catalyst, as described in Ref. [8]. These systems eventually showed a higher ammonia production rate than other Ru-catalyst supports (Fig. 1.1d), owing to the apparent high H^- surface mobility on the oxyhydride.

For this technology, the necessity of the Ru catalyst should be investigated since Ru is a very rare (and expensive) metal. On the industrial scale, Fe-based catalysts are used for the Haber-Bosch process, but many other metals are also possible, although with different efficiency [18]. Perhaps the combination with a rare-earth oxyhydride will also improve the ammonia production rate of other metals.

Resistive RAM (ReRAM)

Random-access memory (RAM) is used in many devices in order to store information. Each "memory component" should be able to switch between two states. A simple example is phase-change memory where the material switches between an amorphous (high resistance) and a crystalline (low resistance) state.

For resistive RAM (ReRAM), the material also changes between two regimes of conductivity, but the underlying mechanism is more complicated. In general, metal oxides (high-κ materials) are used for ReRAM, with the most famous being HfO_2. In this case, a "conductive filament" (CF) is created through HfO_2 that extends between the top and bottom electrodes, forming a bridge made up of oxygen-vacancies [19]. Another way to form this conductive filament is to segregate metal atoms for the same purpose.

Recently, Yamasaki et al. [9] tested La- and Y-oxyhydride thin films and their ability to be used as ReRAM materials. For La-oxyhydrides, it was already shown that the ionic and electronic conductivities of the material were dependent on the O:H ratio of the composition and the amount of hydride-vacancies. Here, the authors deposited a Y-oxyhydride with specifically chosen top and bottom contacts in order to create H-rich (Ti) and O-rich (Mo) regions near the interfaces of the contacts (Fig. 1.1e). During voltage sweeping H^- diffused from one side to the other, either occupying anion vacancies in the O-rich region (high resistance), or moving back to form a H-rich region near the Ti electrode (low resistance).

In my opinion, using RE-oxyhydrides as ReRAM is a unique idea for applications and creative thinking is required to rationalise all the results. Putting this in the context of ReRAM devices in general, to compete with other materials, Y-oxyhydride would have to achieve very fast switching (both "on" and "off"), have a large difference in conductivity between the on and off states, use a low voltage input, have reliable cycling long term, and be easy to incorporate into the semiconductor fabrication scheme [19]. Perhaps the most difficult are the last two points, since the preparation of rare-earth metal oxyhydrides is different from normal semiconductor manufacturing, requires a few extra steps, and may not be reproducible enough. However, this can probably be improved if needed.

1.1.2 Rare-earth metals: less mining, more recycling

The name “rare-earth (RE) metals” is given to the lanthanide series of the periodic table (La-Lu), as well as scandium (Sc) and yttrium (Y) (Fig. 1.2a). The name, however, is misleading because these elements are rather abundant in the Earth’s crust (Fig. 1.2b), especially when compared to other common metals such as copper [20]. On the other hand, these elements are seldom found in large ore deposits which becomes a problem for sourcing and mining these metals [20, 21]. Between the 1950’s and mid-80’s, the main source of RE metals was the Mountain Pass ore in the Mojave Desert of California. Since 1985, production has also sprung from the Bayan Obo source in Inner Mongolia, China, which now dominates around 90% of the RE metal market [20–23].

The mining of RE metals is not without issues. Although RE metals can be found in economically relevant quantities in the Mountain Pass and Bayan Obe sources, the ore grade (measure of the concentration of desired material) is still normally below 10% [20]. The remaining >90% of the ore can contain traces of radioactive elements such as thorium, which can lead to health complications for miners who experience chronic exposure on the job [23, 26, 27]. Additionally, the mining itself is done with strong acids and the wastewater can leech into nearby water sources if not handled adequately [26, 27]. Last, the usage of large swaths of land for RE mining leads to deforestation and displacement of people from rural areas [26, 27].

At the same time, RE metals are finding increased usability in “green” technology in the form of, for example, high-speed electric trains (Nd, Sm), wind turbines (Nd), and nickel-metal hydride batteries (La). They are also used in lighting (Y, Eu, Tb), cameras (La), catalysts for petroleum refining and converters in cars (La, Ce), steel alloys (Ce, La, Nd, Pr, Er), aluminium alloys (Sc), MRI contrast agents (Gd), other medical devices (Tm, Lu), and

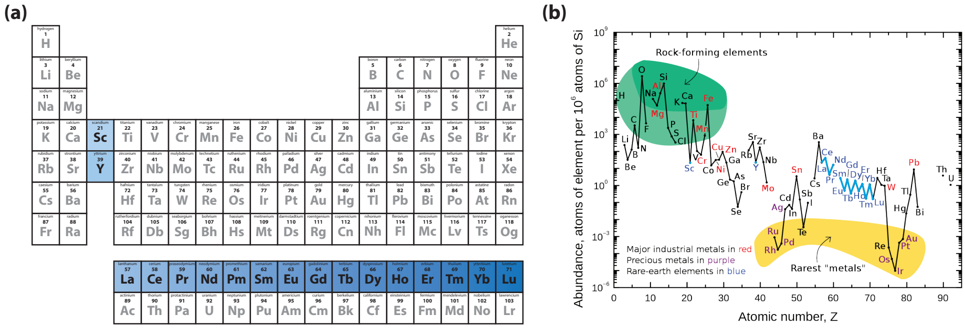

Figure 1.2: (a) Periodic table of elements with the rare-earth metals highlighted in blue (adapted from Brian D’Alessandro [24]). (b) Elemental abundance (per 1 million Si atoms) in the Earth’s crust (adapted from U.S. Geological Survey [20] and Wikipedia [25]).

others [23, 28]. Mentioned in section 1.1.1 and throughout this thesis are other applications such as photochromic smart windows (Sc, Y, Nd, Gd) and hydride batteries (Nd, Gd). It is, therefore, important to look at the recycling of these elements so that we can depend less on mining. Jowitt, et al. [28] and Haque, et al. [23] cite a few major roadblocks for effective recycling such as lack of infrastructure and lack of cost-effective purification/separation methods. The latter is a fundamental issue related to the similar chemistries of many RE elements. Fortunately, research in this direction is underway [28–30]. Another approach is to devote research into alternatives for RE metals in specific applications.

It is worth mentioning that when a material becomes important for technology or energy applications and its supply is uncertain, geopolitical issues may arise. China, having the majority of production and the largest stockpile of RE metals in the world, can unilaterally control the price and supply of these materials, leading, for example, to the "2010 supply scare" [21, 31]. More recently, during the unnecessary trade war initiated by ex-U.S. President Trump, some journalists considered the role of rare-earth metals in this new geopolitical context [31, 32]. Articles with a more optimistic tone [31] reaffirmed the importance of using alternative materials to REs and the need for recycling these elements in order to avoid conflicts.

With this information, I want to illustrate the point that there is an angle to research that is not often addressed or discussed, which is the sourcing and disposing of materials. While it is important to study RE-based materials and find new use cases for them, it is also important to consider where they come from, how to take care of these devices when they are no longer usable, and whether using RE metals is really the best option. These are also key components of a green society.

1.2 Rare-earth metal oxyhydrides

Although the term "oxyhydride" can be traced in the literature as early as 1952 [33], oxyhydride compounds and their applications have been studied primarily in the last two decades, with the first report of a stable oxyhydride in 2002 [34, 35], the first instance of photochromism in rare-earth metal oxyhydrides in 2011 [3], and the first proof-of-concept H^- conductor in 2016 [6]. During this time, there has also been a great deal of research aimed at synthesising new oxyhydride materials, developing new synthesis methods, realising new applications for these materials, and explaining their behaviour [1]. Focusing specifically on rare-earth metal oxyhydride thin films, below is a description of how these materials are prepared, and the current state-of-the-art in the understanding of them.

1.2.1 Deposition

The deposition of our rare-earth (RE) metal oxyhydrides follows a different procedure compared to other (multi-)cation oxyhydrides for two reasons: (1) a large fraction of the oxyhydride literature is about bulk powders while we work with thin films, and (2) the starting material for the bulk powders is usually an oxide while we use the RE-dihydride. As a result, much of the literature depends on topochemical and high-pressure synthesis to prepare oxyhydrides. Here, we instead use reactive magnetron sputtering to deposit thin films of the RE-dihydride, and post-oxidise them to the oxyhydride phase.

Sputtering deposition

RE-oxyhydride thin films are prepared by sputtering the RE-dihydride in a reactive atmosphere of Ar/H_2 with controlled gas flows. With reactive magnetron sputtering, there are a number of parameters that can be changed in order to achieve different thin film properties (e.g., target tilt, target-substrate distance, substrate heating, total gas flow, ratio of Ar/H_2 gas, DC/pulsed DC/RF power supply, input power during sputtering, deposition pressure, etc.). Keeping the other parameters constant, we generally alter the deposition pressure (p_{dep}) to change the properties of our thin films. The deposition pressure is the combined pressure of Ar and H_2 in the vacuum chamber controlled by the adaptive pressure controller.

It was found that an increasing p_{dep} results in more porous as-deposited RE-dihydride films. More porous films later oxidise to a greater extent when exposed to air, and have an oxyhydride composition with a larger O:H ratio [36, 37]. However, there is also a critical deposition pressure (p^*_{dep}), which is the minimum deposition pressure needed to achieve an oxyhydride phase upon post-oxidation [38]. This indicates that a minimum porosity is required for the as-deposited RE-dihydride film to oxidise in air. Below the p^*_{dep}, the film remains in the RE-dihydride, while close to the p^*_{dep}, partially oxidised films are obtained which have a gradient in composition [37]. At this point, several RE-oxyhydrides have been made by post-oxidation of the as-deposited RE-dihydride, and the tunability of the composition and properties have been shown for Sc, Y, Gd, and Nd-oxyhydrides [5, 37], and alluded to for Dy and Er-oxyhydrides [38].

Post-oxidation

In almost all reports to date, air has been used as the oxidising agent for the transformation of the RE-dihydride to the oxyhydride phase. Even though air contains many other compounds than just O_2 and H_2O, and changes in pressure/humidity daily, air-oxidation of as-deposited RE-dihydrides has worked for the last 11 years.

However, to have more control over the process and the resultant material, another option is “dry-oxidation”, which involves oxidising the RE-dihydride film with a flow of O_2 gas in an otherwise neutral environment. Recently, it was shown that only a few minutes are required for the films to gain at least 50% of their transparency when oxidised with a flow of O_2 in the sputtering vacuum chamber [39]. Similarly, we have found that as-deposited RE-dihydrides visually become transparent within seconds of exposure to O_2 gas, although the minimum O_2 pressure required to initiate oxidation depends on: (1) the RE-metal used (Sc-based films require a higher p_{O_2}), (2) the sputtering deposition pressure (more porous films require a lower p_{O_2}), and (3) the thickness of the sample. Such samples have been used for experiments involving electrochemical impedance spectroscopy (Ch 5) and nuclear magnetic resonance (NMR) [54, 55, 77]. Dry oxidation has also been used by other groups for the preparation of RE-oxyhydride thin films [9, 40].

Isotopes (D, ^{17}O)

In addition to post-oxidation by air or dry O_2 gas, we can use isotopic ^{17}O to label all the oxide ions in the resultant film. To date, there is no record of such labelling in the literature. Here, we use labelled ^{17}O Y-oxyhydrides for NMR analysis since ^{16}O has no nuclear magnetic moment [54, 55, 77]. Isotopes of H^- are also possible, made by sputtering the RE-metal in deuterium gas instead of H_2 [41]. These samples are also important for NMR analysis, as well as other H-sensitive techniques such as neutron reflectometry.

1.2.2 Composition

The composition of RE-oxyhydrides has been measured experimentally by ion-beam analysis several times, resulting in two different formulas: $REH_{2-\delta}O_\delta$ [42, 43] and $REH_{3-2x}O_x$ [44], with the latter being more widely accepted to describe RE-oxyhydrides [7, 8, 12, 40]. Importantly, as shown by Cornelius, et al. [44], these materials follow a distinctly different composition line than RE-hydroxides (H^+), providing evidence for the presence of hydrogen in its negatively charged state (H^-). As mentioned above, the O:H ratio of RE-oxyhydrides can be tuned in a wide range depending on the preparation conditions [37, 44]. This, in turn, influences the opto-electronic properties of the films, discussed throughout the thesis and in section 1.3.

1.2.3 Structure

RE-cation lattice

The crystal structures of RE-oxyhydrides have been characterised by methods such as X-ray diffraction (XRD), a technique sensitive to the periodicity of heavy atoms (RE-cations). The majority of RE-oxyhydrides made by our group exhibit a face-centred cubic ($Fm\bar{3}m$) crystal structure (Sc, Y, Gd, Dy, Er) [37, 38, 44]. The lattice constant, a, generally follows the size of the cation, observed also for stoichiometric REHO bulk powders [11, 16].

For some RE-cations, however, a tetragonally distorted lattice ($P4/nmm$) is observed as in the case of La, Ce, Pr, and Nd [5, 7, 11, 12, 16, 45]. Both di- and tri-hydride phases of these RE metals exhibit a cubic crystal structure [46], meaning that the presence of a tetragonal distortion is not necessarily expected. Some authors explain that this difference in crystal strcuture is a consequence of the ordered anion-sublattice for oxyhydrides based on La-Nd [11, 16].

Other crystal structures outside the cubic $Fm\bar{3}m$ and tetragonal $P4/nmm$ have been reported for some RE-oxyhydrides including monoclinic (La - $P2_1/m$)[47], orthorhombic (Y, Lu - $Pnma$)[48, 49], cubic (Dy, Er, Lu - $F\bar{4}3m$)[49]. This may depend, in part, on the synthesis conditions. For example, the crystal structure of Nd-oxyhydrides can be modified from tetragonal to cubic by either using epitaxy [50] or the sputtering p_{dep} [5].

Anion sub-lattice

For RE-dihydrides and -trihydrides, the positions of H^- in the RE-lattice have been characterised extensively. In general, it is understood that H^- occupies the tetrahedral interstitial sites of the RE-lattice first, and then the octahedral sites for compositions where $x > 2$ (REH_x) [46]. Some exceptions exist and this description is not strict, but it acts as a general picture of the filling of interstitial sites in the RE-lattice as more H^- is added.

The situation with RE-oxyhydrides is more complicated due to the presence of two different anions (O^{2-} and H^-). For bulk powders of RE-oxyhydrides, a combined analysis of the XRD and neutron diffraction patterns of the material gives a complete description of the cation and anion lattices. In the case of stoichiometric powders of REHO (RE = La-Er), it was found that anion ordering is present in the tetragonal oxyhydrides (La-Nd), while the rest are anion disordered and cubic (Sm-Er) [11]. Not only does this report suggest that anion ordering and cation crystal structure are inherently related, but it also predicted that only tetragonal and anion-ordered RE-oxyhydrides have measurable H^- mobility. This was later challenged by the works of Fukui, et al. [12, 47] where the best H^- conductor so far (La-oxyhydride) exhibited a tetragonal crystal structure, but likely with anion disorder. Notably, this La-oxyhydride was far from the stoichiometric LaHO composition (more H-rich), which may partly explain the different conclusions [51].

Unfortunately, neutron diffraction is a somewhat inaccessible technique for thin films due to the low interaction cross-section of neutrons with matter. Samples for this method should be on the order of several millimetres thick, while our films are on the order of nanometres in thickness. Therefore, other methods must be used to deduce information about the anion positions in RE-oxyhydride thin films. One such method is X-ray absorption spectroscopy (specifically EXAFS), where an atom absorbs an X-ray and creates a photoelectron which can backscatter from a neighbouring atom back to the absorbing atom. Based on the interference effect caused by the backscattering of the electron, one can obtain information about the local structure of the material. For Gd-oxyhydride, it was found that the oxide ions preferentially occupy the tetrahedral interstitial sites, leaving H^- to take the remaining sites [52, 53]. In this way, the as-deposited RE-dihydride likely has most H^- ions in tetrahedral interstitial sites. However, upon exposure to air, O^{2-} ions take those sites and push the H^- ions into the octahedral sites.

In general, we assume that our RE-oxyhydrides made by post-oxidation of an as-deposited RE-dihydride are anion disordered due to the rapid oxidation (far from thermodynamic minimum) [44]. This is confirmed by computational methods (DFT), where simulations of anion disordered Y-oxyhydrides better matched experimental observations than the ordered compounds [51]. Lastly, NMR analysis can contribute further information about the local structure and compositions of our RE-oxyhydrides [54, 55].

1.3 Photochromic Effect

1.3.1 What is photochromism?

The photochromic effect is one where an input of light (*ϕωτοσ* - *photos*) results in a colour change of the material (*χρωμα* - *chroma*) [56]. A popular example of this in the literature are Cu-doped Ag-halide glasses [57], where exposure to light creates photo-generated charge carriers which become trapped; the holes (h^+) oxidise copper ($Cu^+ \rightarrow Cu^{2+}$), while the electrons (e^-) reduce silver ($Ag^+ \rightarrow Ag^0$). These atoms of Ag^0 are mobile and create metallic clusters which change the optical transmission of the glass, and the trapping of the photo-generated carriers in this way prolongs the presence of this “dark” state of the glass. The reverse process involves the recombination of these carriers, depending on the diffusion of the Ag^0 atoms.

Other materials show a photochromic effect, though by other mechanisms. For photochromic organic molecules, light induces a reaction in the molecule such as photoisomerization, H^+ transfer, and others, altering the absorption of the molecule [56]. For some inorganic systems, colour centres form when photo-generated electrons are trapped in vacant anion sites in the crystal structure, changing the optical absorption of the material (e.g., CaF_2) [58].

The photochromic effect in RE-metal oxyhydrides, on the other hand, is not easily explained and several lines of reasoning are present in the literature. One explanation is in analogy to the Ag-halide glasses, where metallic centres are formed in the RE-oxyhydride matrix [59–61]. Other models focus on reactions with the H^- ion to form different optically absorbing species (e.g., “dihydrogen”, $(OH)^-$) [40, 62] or the release of gas during the experiment [63]. Starting from a different premise, some suggest H^- exchange between pre-existing phases in the material [64]. At present, there is no consensus on which ideas and experimental evidence are the most relevant. As well, there is no single technique which will answer these questions directly. Therefore, below is an overview of some experiments performed on RE-metal oxyhydride thin films and the influence (or lack thereof) on our understanding of photochromism.

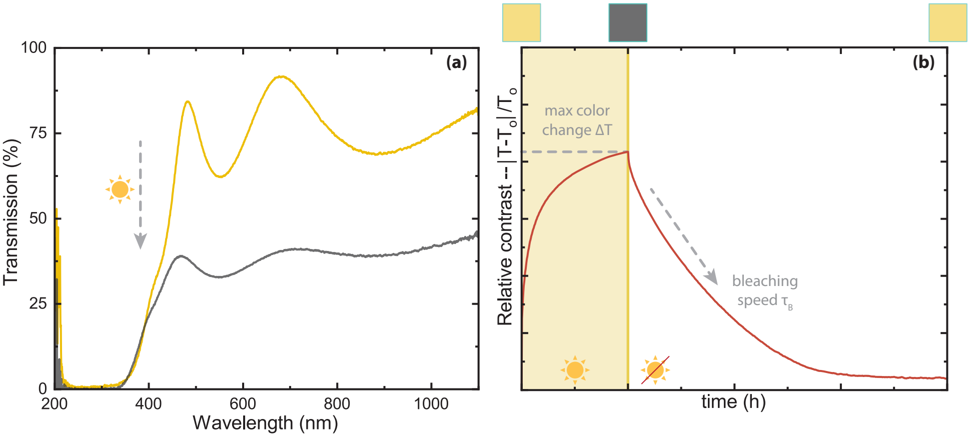

Figure 1.3: (a) Transmission spectra for the transparent state (yellow) and the darkened state (grey) used to calculate the average transmission $<T>$. (b) An example of a measurement of photochromism, where the y-axis is the relative contrast and the x-axis is time. The relative contrast ($|T - T_0|/T_0$) is obtained considering the original transparency of the film (T_0). All values of T are actually the average transmission $<T>$ for a wavelength range of 450-1000 nm. The shaded yellow rectangle indicates the illumination period, during which, the relative contrast increases from 0. The reported value in the literature is the maximum colour change after the illumination period (ΔT). The amount of time required to return to the original transparency is measured by the bleaching speed (τ_B). The visual appearance of the film is pictured above the graph, being yellow transparent at the beginning and end of the measurement, but opaque during illumination.

1.3.2 Terminology

Throughout this thesis, the photochromic effect in RE-oxyhydrides will be described by two figures of merit: (1) the photochromic contrast (ΔT), and (2) the bleaching speed (τ_B) (Fig. 1.3). The first is a measurement of the extent of colour change the material showed after a given illumination time. In general, it can be expressed as an absolute (T/T_0) or relative contrast ($|T - T_0|/T_0$), with the latter being used most often in this thesis. In these expressions, T_0 is the original average transmission of the material before illumination. The bleaching speed is a measure of the speed with which the original transparency of the film returns after illumination is stopped. This is modelled by a first-order kinetic rate constant [38].

1.3.3 What influences photochromism & what doesn't?

Experimental effects

Some basic details about photochromism come from the tuning of experimental parameters. The **illumination conditions**, for example, can be changed in a variety of ways. Most significant is the energy (wavelength) of the incident light which should be large (short) enough to induce the photochromic effect [65, 66]. In general, this suggests that the photochromic effect is initiated by carrier promotion across the band gap. In cases where light with very low energy (e.g., ~510-570 nm as in Ref. [67]) triggers a photochromic response, it is likely that the measured films have a multi-phase nature.

The **temperature** at the sample stage has been shown a number of times to influence the photodarkening and bleaching speeds of the sample, with darkening observed at temperatures as low as 5 K [5, 68, 69]. In short, higher temperatures lead to faster bleaching, meaning that bleaching is a thermally activated process. This also affects the contrast, which is lower at high temperatures where bleaching is faster. This leads to the suspicion that the two figures of merit (contrast and bleaching speed) are directly related, though this idea is later challenged in this thesis (Chapters 3 & 4).

RE-oxyhydride composition

The composition of RE-oxyhydrides is an important factor for photochromism and can be broken down into different aspects. The choice of **RE-cation** appears to change both the photochromic contrast and bleaching speed, especially when comparing Sc, Y, and Gd which are cations from different periods of the periodic table [37]. As the cation size increases, the photochromic contrast increases and the bleaching speed becomes faster. On the other hand, when comparing Nd- and Gd-oxyhydrides which are in the same period, the difference in photochromic contrast is negligible as described in Chapter 3 and Ref. [5]. This can be interpreted to mean that the size of the cation is important because of the lattice size or the stability of the "dark phase" produced with different cations.

A somewhat more significant effect stems from the **anion ratio (O:H)**, where more H-rich oxyhydrides have a higher photochromic contrast, yet slower bleaching speed [5, 37, 70, 71]. It has also been suggested that not all oxyhydrides may have photochromic properties, with very H-rich phases being potentially unstable [51]. As well, in Chapter 4 and Ref. [72], it is proposed that if all the octahedral sites are vacated, the photochromic contrast will reduce to 0%. These observations point to the idea that the amount of H^- in the material and its position in the lattice is a key component to photochromism.

Annealing & crystallinity

Most protocols for the deposition of RE-oxyhydride thin films involve a series of steps at room temperature. This generally results in a polycrystalline as-deposited RE-dihydride thin film, which is then rapidly oxidised in air. Several authors have noticed that the resultant oxyhydride films have a number of imperfections including texture or preferential orientation of certain planes [5, 37, 52, 61, 71], differences in grain size due to the deposition pressure [71] or film thickness [73], and residual stress [5, 64]. On a smaller scale, there is always a certain number of cation point defects present in the films [61], perhaps related to an intrinsic defect concentration. Other defects may be present, such as compositional inhomogeneity, especially for thick films which must oxidise starting from the surface.

Heating RE-oxyhydrides at **moderate temperatures** (87°C), as shown in Chapter 3 and Ref. [5], already changes the photochromic properties of Gd- and Nd-oxyhydride thin films, primarily by increasing the bleaching speed, leaving the contrast nearly the same. The same has been shown for Y-oxyhydride thin films heated below 100°C, although above this temperature, the contrast decreases due to oxidation [42]. Heating RE-oxyhydride thin films below 100°C does not seem to change: (1) the anion composition [42], (2) the XRD pattern regardless of heating duration (crystal lattice, residual stress, and texture the same) [5], nor (3) the cation point defect structure [5]. Thus, something else is affected by this moderate annealing, resulting in a slower bleaching speed for the same contrast. One possibility is the irreversible formation of neutral divacancies which has been observed in Y-oxyhydride after illumination [37] and heating [74], and in Nd-oxyhydrides after heating (Chapter 3), potentially due to H_2 liberation from the sample at these temperatures.

Recently, **epitaxial** Y-oxyhydride films were reported which transition from a transparent insulating to a dark conducting state [40]. However, the reverse process (bleaching) is not spontaneous as it is for the polycrystalline films. Instead, bleaching is forced in the epitaxial films by heating them under an Ar atmosphere. This also points to a peculiarity of the photochromic effect, the reversibility of which is apparently only spontaneous when the film has certain imperfections.

Surrounding gas & protective coatings

Some authors have investigated the role of the **surrounding environment** for photochromism, concluding that either air is required for bleaching because O-atoms leave the film during darkening [63], or that the environment around the sample has no influence on the observed bleaching kinetics [66]. To address this debate with a different approach, some have used **protective coatings** on the thin films in an effort to prevent, for example, H_2 or O_2 from exchanging with the film. However, it was found that neither Al_2O_3 nor Si_3N alone affected the photochromic properties [5, 75]. Therefore, material exchange with the environment can be ruled out as a necessity for photochromism, meaning that the photochromic effect can be considered an internal restructuring of the compound.

Isotopes & oxidation conditions

Anion isotopes (D, ^{17}O, ^{18}O) have been used either to study long-range diffusion throughout the film [41, 76] or for an enhanced NMR signal to determine structural information along with anion dynamics [54, 55, 77]. However, none of these isotopes seem to influence the photochromic effect (Fig. 1.4a). Based on this, one can assume that long range mobility of the anions is not an essential ingredient for photochromism. This is because the isotopes are slightly heavier and larger than the "normal" anions, which should result in a slower diffusion of the atoms, and perhaps a slower bleaching time. As well, as mentioned above, the most H-rich oxyhydrides have the slowest bleaching rate [37], while also being the best H^- conductors [7].

What is more notable, is the fast bleaching (τ_B <10 min) that occurs for dry oxidised samples. It was found, though, that this is not due to any preparation or oxidation methods, but rather due to the **age** of the film (Fig. 1.4b). When measured right after removal from the vacuum chamber (or right after oxidation in the glovebox, considered "day 0"), the samples show very fast bleaching. However, after a few days of storage in air or in the glovebox, the bleaching speed becomes slower. Interestingly, the sample stored and measured in the glovebox had a slower bleaching speed with age, while the contrast was constant, different from the samples stored and measured in air. It may be that there are several processes contributing to “ageing” such as oxidation in air/humidity, or internal reactions within the film (e.g., H_2 liberation) as it stabilises after rapid oxidation.

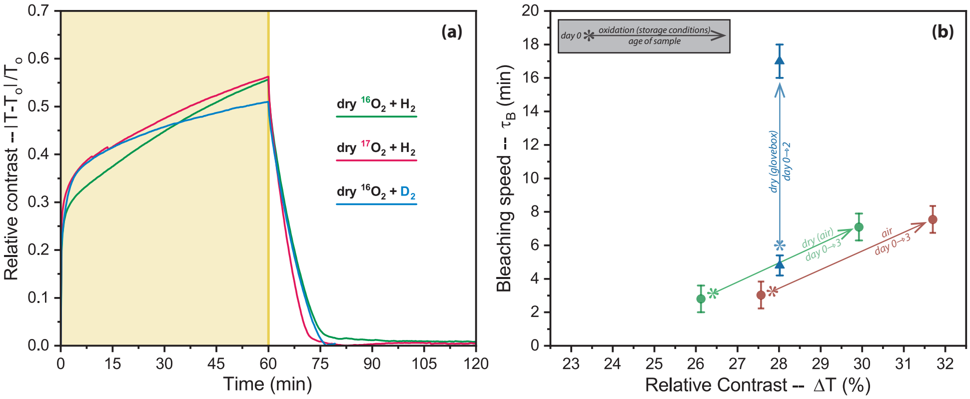

Figure 1.4: (a) Relative photochromic contrast for Y-oxyhydride (0.5 Pa) films (~1000 nm) made by oxidation with dry oxygen gas (green), oxidation with isotopic oxygen gas (pink), and oxidation with dry oxygen gas but deposition of the dihydride with deuterium (blue). The illumination time is 1 h. (b) Comparison of the τ_B (y-axis) and photochromic contrast (x-axis) for samples prepared in three different ways: (1) oxidised, stored, and measured in air (red), (2) oxidised with dry O_2, stored and measured in air (green), and (3) oxidised with dry O_2, stored and measured in the glovebox (blue). Each sample was measured on the day of deposition right after removal from the vacuum chamber or just in the glovebox on day 0. A twin of each sample was measured on day 2-3 to check the difference in ageing.

1.4 H^- Mobility

1.4.1 Techniques

There has long been the idea that the photochromic effect involves the mobility of hydrogen throughout the material in some form, be it H^-, H^0, or something else (see Section 1.3). However, mobility is a very general word, and it is important to consider length- and time-scales.

Length-scale refers to the length of the diffusion pathway of the ion. This can be anything from local displacement from one site to another, to long range diffusion across the entire length of the material. The latter, for example, is a necessary property for a solid-state electrolyte. In terms of photochromism, it may not be necessary for atoms to rearrange on a large length-scale for the reversible colour change to occur.

In addition, time-scale of diffusion is an essential aspect to consider because the visibility of diffusion is usually dependent on the time-scale sensitivity of the technique used to study the mobility [78]. Some studies, for example, use quasi-elastic neutron scattering (QENS) to study hydrogen motion in oxyhydrides [10, 79], but this technique is sensitive to local mobility (~1-100 Å) on a time-scale of 10^{-9}-10^{-12} s. Despite that, Bridges, et al. [10] studied $LaSrCoO_3H_{0.7}$ by QENS, deriving a jump distance and time between jumps.

They then used this information to estimate an ionic conductivity for their measurement temperature range (685-750 K or ~412-477°C).

Next, muon spin rotation (μ^+SR), discussed in Chapter 2 and Refs. [69, 80], is also sensitive to local mobility because the signal is dominated by the magnetic fields closest to the muon, but the time-scale is somewhat different (10^{-4}-10^{-12} s) depending on the sample environment. It has been used in Li-based materials [81] and metal hydrides [82] to observe the onset of diffusion, and in oxyhydrides to investigate possible diffusion pathways [80].

Solid-state nuclear magnetic resonance (NMR) can also be used to probe dynamics of particular atoms and has been used to study oxyhydrides [54, 55, 83, 84] and photochromism [77, 85]. NMR is capable of probing dynamics on a longer time-scale than the aforementioned techniques, extending into the regime of seconds. For example, NMR can be used to differentiate between deuterium exchange with the atmosphere (intensity changes) as a result of aging, and more localised ion motion (hopping between sites based on linewidth narrowing) [77].

Electrochemical impedance spectroscopy (EIS) is a method by which ion mobility is measured across the entire length of the material and the technique is, in principle, sensitive to phenomena occurring between the 10^{-6}-10^{6} s. Importantly, although this time-scale overlaps with NMR to some extent, the length-scale probed by EIS is across the entire length of the material, which is not necessarily the case for NMR that is sensitive to more localised phenomena. EIS has been used to probe H^- conductivity in a variety of oxyhydrides (e.g., [6, 7]) and will be described in Chapter 5.

Last, density functional theory (DFT) can be used in a variety of ways to simulate diffusion pathways and energetics in oxyhydrides [86–90]. Recently, some authors used molecular dynamics (MD) and machine learning (ML) to create a model that matches the observed high ionic conductivity, yet large activation energy barrier, found experimentally for La-oxyhydrides [7, 91].

1.4.2 Strontium cobalt oxyhydride

The majority of this introduction focussed on rare-earth metal oxyhydrides, which generally contain one cation (or two in the case of doping). However, this is only a small subset of the oxyhydride world which includes a variety of perovskite oxyhydrides (two cations) and complex Ruddelsden-popper oxyhydrides (three cations). One of the most well-studied perovskite oxyhydrides is $BaTiO_{3-x}H_x$ [2], likely because it was a good case study for a number of techniques and helped the field learn about oxyhydride properties. What was interesting to us at the beginning of this PhD was the transport properties of $BaTiO_{3-x}H_x$. There were several reports of high electronic conductivity [92–94], as well as labile H^- [79, 89, 95–98] in $BaTiO_{3-x}H_x$ powders and thin films. Eventually, $BaTiO_{3-x}H_x$ was used as a reversible electrode in a device [99]. Despite all this, the ionic conductivity of this material was never fully characterised because the high electronic conductivity of the compound obscured the measurement of the ionic contribution.

We wanted to produce our own perovskite oxyhydrides in the form of thin films to test if we could find efficient H^- conductors made by methods other than topochemical and high-pressure synthesis. I chose strontium cobalt oxyhydride as the goal based on the following selection criteria (considering the perovskite $ABO_{3-x}H_x$ composition):

1. the A cation should be Ba, Sr, or Ca

2. the B cation cannot be expensive or rare (many transition metals eliminated)
3. the oxyhydride should be already reported in the literature, but not by high-pressure synthesis (Ni, Zn, Cu, Mn, Sc, V, Cr eliminated as B-cation options)
4. the reported oxyhydride cannot have metallic properties (Ti and Fe eliminated as B-cation options)
5. a small, dense pulsed laser deposition (PLD) target should be available commercially

Part of this selection criteria was practical; it would be difficult for us to synthesis our own dense oxide pellets and even more difficult to develop a completely new perovskite oxyhydride compound given the time and resources available. Part of the criteria was also based on fundamental considerations, meaning that we wanted the material to be an insulator so that the ionic conductivity could be dominant, a key property in view of applications as electrolytes.

Strontium cobalt oxyhydride was reported to be an insulator (band gap 2.1 eV) made by topochemical synthesis [100]. This synthesis took advantage of the fact that strontium cobalt oxide is stable for a range of O-concentrations ($SrCoO_x$, x = 2.5-3) [101–103]. The presence of anion vacancies allows for possibility of H-insertion and formation of the oxyhydride phase. As well, the two compositions of the oxide can be easily discriminated by XRD since $SrCoO_{2.5}$ exhibits a brownmillerite crystal structure, while $SrCoO_3$ is a cubic perovskite [101–103]. In this way, after buying a target from the supplier, and during different stages of deposition, the O-content of the oxide can be quickly validated.

The insertion of H^- can occur *in situ* by ablating the target in a combination of O_2/H_2 gasses [50, 104], co-ablation with $SrCoO_x$ and a hydride-containing compound such as SrH_2 [105], ablation of the oxide in H_2 [105], or by topochemical synthesis under strongly reducing conditions (i.e., post-reduction of an as-deposited oxide thin film) [100]. Some literature is available about the deposition of O-deficient $SrCoO_{2.5}$ thin films by PLD, giving some indications about how to approach this synthesis [106]. For example, Jeen et al. [101] showed that it is impossible to deposit $SrCoO_3$ by PLD and only the O-deficient composition was attainable. Post-oxidation was required to achieve the $SrCoO_3$ composition.

Eventually, this line of pursuit was ended due to the failure of the high voltage power supply of the pulsed laser, a part which could no longer be replaced due to the age of the laser.

1.5 This Thesis

The aim of this thesis is to better understand the photochromic effect in rare-earth metal oxyhydride thin films, specifically with regards to the role of H^-. This is done by (1) using hydrogen-sensitive techniques, (2) developing rare-earth metal oxyhydride thin films with different crystal structure, and (3) altering the chemistry and defect structure of the film by aliovalent doping or annealing. As well, H^- is investigated in these films for its mobility throughout the material by using techniques that operate in different time and length scale regimes from muon spin rotation to electrochemical impedance spectroscopy.

The work of this thesis is within the context presented above:

Chapter 2 explains the use of a H^--sensitive local probing technique (muon spin rotation) to understand Y-oxyhydride thin films. Although mobility was not observed on the time-scale (microseconds) of the experiment, we found a fraction of muonium which recovered to a diamagnetic state in a way that was dependent on the local environment of the sample. This led to the suggestion that a reversible local structural or compositional rearrangement occurs during photochromism.

Chapter 3 is the first overview of Nd-oxyhydride thin films, investigating their structural and photochromic properties as a function of the O:H ratio. Nd-based oxyhydrides are believed to have significantly better long-range H^- mobility than, for example, Gd-oxyhydrides, partly due to the crystal structures (tetragonal vs. cubic, respectively). However, this difference did not matter for photochromism which appeared very similar in Nd- and Gd-oxyhydrides, suggesting that long-range mobility is not a requirement for photochromism. More important was the moderate annealing inadvertently performed while applying a protective ALD-coating, hinting towards the importance of defects for the reverse process of photochromism (bleaching).

Chapter 4 is another attempt at changing the chemistry of a rare-earth metal oxyhydride to observe a change in the photochromic properties. Here, Y-oxyhydride thin films were aliovalently doped with Ca to create anion vacancies. The photochromic contrast decreased linearly with the amount of Ca in the sample, predicting 0% contrast for ~54% Ca. We propose this to be due to a complete emptying of the octahedral sites. The bleaching speed was faster with the addition of Ca, as the result of a larger pre-exponential factor, and indicating that local H^- hopping may be important for bleaching.

Chapter 5 describes the use of electrochemical impedance spectroscopy for thin film materials where the majority carrier is unknown. In our case, it is not clear *a priori* if rare-earth metal oxyhydrides are electron, hole, ion, or mixed conductors. This chapter gives a full description of how to address such a scenario with experimental evidence. Eventually, we conclude that electronic conductivity is dominant in Gd-oxyhydride thin films, although, at high temperatures, there may be a signature of either a measurement artefact, or H-mobility as a result of material decomposition (e.g., H_2 release). Several suggestions are given for improving measurements, and measuring other rare-earth oxyhydride materials.

Chapter 6 summarises results from experiments which cannot be directly explained, specifically, observations of factors that reduce the photochromic effect and factors that lead to very slow bleaching (>60 h).

References

[1] H. Kageyama, K. Hayashi, K. Maeda, J. P. Attfield, Z. Hiroi, J. M. Rondinelli, and K. R. Poeppelmeier, *Expanding frontiers in materials chemistry and physics with multiple anions,* Nature Communications **9**, 772 (2018).

[2] Y. Kobayashi, O. Hernandez, C. Tassel, and H. Kageyama, *New chemistry of transition metal oxyhydrides,* Sci Technol Adv Mater **18**, 905 (2017).

[3] T. Mongstad, C. Platzer-Björkman, J. P. Maehlen, L. P. A. Mooij, Y. Pivak, B. Dam, E. S. Marstein, B. C. Hauback, and S. Z. Karazhanov, *A new thin film photochromic material: Oxygen-containing yttrium hydride,* Solar Energy Materials and Solar Cells **95**, 3596 (2011).

[4] IEA, *The Future of Cooling: Opportunities for energy-efficient air conditioning*, e-Article (International Energy Agency, 2018) https://www.iea.org/reports/the-future-of-cooling .

[5] D. Chaykina, F. Nafezarefi, G. Colombi, S. Cornelius, L. J. Bannenberg, H. Schreuders, and B. Dam, *Influence of crystal structure, encapsulation, and annealing on photochromism in Nd oxyhydride thin films,* The Journal of Physical Chemistry C **126**, 2276 (2022).

[6] G. Kobayashi, Y. Hinuma, S. Matsuoka, A. Watanabe, M. Iqbal, M. Hirayama, M. Yonemura, T. Kamiyama, I. Tanaka, and R. Kanno, *Pure H^- conduction in oxyhydrides,* Science **351**, 1314 (2016).

[7] K. Fukui, S. Iimura, A. Iskandarov, T. Tada, and H. Hosono, *Room-temperature fast H^- conduction in oxygen-substituted lanthanum hydride,* Journal of American Chemical Society **144**, 1523 (2022).

[8] K. Ooya, J. Li, K. Fukui, S. Iimura, T. Nakao, K. Ogasawara, M. Sasase, H. Abe, Y. Niwa, M. Kitano, and H. Hosono, *Ruthenium catalysts promoted by lanthanide oxyhydrides with high hydride-ion mobility for low-temperature ammonia synthesis,* Advanced Energy Materials **11**, 2003723 (2020).

[9] T. Yamasaki, R. Takaoka, S. Iimura, J. Kim, H. Hiramatsu, and H. Hosono, *Characteristic resistive switching of rare-earth oxyhydrides by hydride ion insertion and extraction,* ACS Applied Materials & Interfaces **14**, 19766 (2022).

[10] C. A. Bridges, F. Fernandez-Alonso, J. P. Goff, and M. J. Rosseinsky, *Observation of hydride mobility in the transition-metal oxide hydride $LaSrCoO_3H_{0.7}$,* Advanced Materials **18**, 3304 (2006).

[11] H. Ubukata, T. Broux, F. Takeiri, K. Shitara, H. Yamashita, A. Kuwabara, G. Kobayashi, and H. Kageyama, *Hydride conductivity in an anion-ordered fluorite structure LnHO with an enlarged bottleneck,* Chemistry of Materials **31**, 7360 (2019).

[12] K. Fukui, S. Iimura, T. Tada, S. Fujitsu, M. Sasase, H. Tamatsukuri, T. Honda, K. Ikeda, T. Otomo, and H. Hosono, *Characteristic fast H^- ion conduction in oxygen-substituted lanthanum hydride,* Nature Communications **10**, 2578 (2019).

[13] Y. Meesala, A. Jena, H. Chang, and R.-S. Liu, *Recent advancements in Li-ion conductors for all-solid-state Li-ion batteries,* ACS Energy Letters **2**, 2734 (2017).

[14] X. Chen and P. M. Vereecken, *Solid and solid-like composite electrolyte for lithium ion batteries: Engineering the ion conductivity at interfaces,* Advanced Materials Interfaces **6**, 1800899 (2018).

[15] B. Malaman and J. F. Brice, *Etude structurale de l-hydruro-oxyde LaHO par diffraction des rayons X et par diffraction des neutrons,* Journal of Solid State Chemistry **53**, 44 (1984).

[16] H. Yamashita, T. Broux, Y. Kobayashi, F. Takeiri, H. Ubukata, T. Zhu, M. A. Hayward, K. Fujii, M. Yashima, K. Shitara, *et al.*, *Chemical pressure-induced anion order-disorder transition in LnHO enabled by hydride size flexibility,* Journal of the American Chemical Society **140**, 11170 (2018).

[17] S. Giddey, S. P. S. Badwal, and A. Kulkarni, *Review of electrochemical ammonia production technologies and materials,* International Journal of Hydrogen Energy **38**, 14576 (2013).

[18] E. Dražević and E. Skúlason, *Are there any overlooked catalysts for electrochemical* NH_3 *synthesis - new insights from analysis of thermochemical data,* iScience **23**, 101803 (2020).

[19] D. Kumar, R. Aluguri, U. Chand, and T. Y. Tseng, *Metal oxide resistive switching memory: Materials, properties and switching mechanisms,* Ceramics International **43**, S547 (2017).

[20] M. Diggles, *Rare Earth Elements - Critical Resources for High Technology*, e-Article (U.S. Geological Survey: Fact Sheet 087-02, 2005) https://pubs.usgs.gov/fs/2002/fs087-02/ .

[21] A. Drobniak and M. Mastalerz, *Rare earth elements: A brief overview,* Indiana Journal of Earth Sciences **4**, 1 (2022).

[22] C. Ayora, F. Macias, E. Torres, A. Lozano, S. Carrero, J. M. Nieto, R. Perez-Lopez, A. Fernandez-Martinez, and H. Castillo-Michel, *Recovery of rare earth elements and yttrium from passive-remediation systems of acid mine drainage,* Environmental Science & Technology **50**, 8255 (2016).

[23] M. Haque, A. Hughes, S. Lim, and C. Vernon, *Rare earth elements: Overview of mining, mineralogy, uses, sustainability and environmental impact,* Resources **3**, 614 (2014).

[24] B. D'Alessandro, *The Periodic Table of the Elements in Adobe Illustrator Format*, e-Article (Blog, 2010) https://www.briandalessandro.com/blog/the-periodic-table-of-the-elements-in-adobe-illustrator-format/ .

[25] Wikipedia, *Rare-earth element*, e-Article (Wikipedia, 2022).

[26] J. Nayar, *Not So "Green" Technology: The Complicated Legacy of Rare Earth Mining*, e-Article (Harvard International Review, 2021) https://hir.harvard.edu/not-so-green-technology-the-complicated-legacy-of-rare-earth-mining/ .

[27] J. Kaiman, *Rare earth mining in China: the bleak social and environmental costs*, e-Article (The Guardian, 2014) https://www.theguardian.com/sustainable-business/rare-earth-mining-china-social-environmental-costs .

[28] S. M. Jowitt, T. T. Werner, Z. Weng, and G. M. Mudd, *Recycling of the rare earth elements,* Current Opinion in Green and Sustainable Chemistry **13**, 1 (2018).

[29] J. A. Bogart, C. A. Lippincott, P. J. Carroll, and E. J. Schelter, *An operationally simple method for separating the rare-earth elements neodymium and dysprosium,* Angewandte Chemie International Edition **54**, 8222 (2015).

[30] J. A. Bogart, B. E. Cole, M. A. Boreen, C. A. Lippincott, B. C. Manor, P. J. Carroll, and E. J. Schelter, *Accomplishing simple, solubility-based separations of rare earth elements with complexes bearing size-sensitive molecular apertures,* Proceedings of the National Academy of Sciences **113**, 14887 (2016).

[31] J. Hsu, *Scientific American*, e-Article (Scientific American, 2019) https://www.scientificamerican.com/article/dont-panic-about-rare-earth-elements/ .

[32] *Rare earths give China leverage in the trade war, at a cost*, e-Article (The Economist, 2019) https://www.economist.com/china/2019/06/15/rare-earths-give-china-leverage-in-the-trade-war-at-a-cost .

[33] G. H. Wagner and A. N. Pines, *Silicon oxyhydride,* Industrial and Engineering Chemistry **44**, 321 (1952).

[34] M. A. Hayward, E. J. Cussen, J. B. Claridge, M. Bieringer, M. J. Rosseinsky, C. J. Kiely, S. J. Blundell, I. M. Marshall, and F. L. Pratt, *The hydride anion in an extended transition metal oxide array: $LaSrCoO_3H_{0.7}$,* Science **295**, 1882 (2002).

[35] K. Poeppelmeier, *Solid state chemistry. a mixed oxide-hydride perovskite,* Science **295**, 1849 (2002).

[36] C. C. You, T. Mongstad, J. P. Maehlen, and S. Karazhanov, *Engineering of the band gap and optical properties of thin films of yttrium hydride,* Applied Physics Letters **105**, 031910 (2014).

[37] G. Colombi, T. De Krom, D. Chaykina, S. Cornelius, S. W. H. Eijt, and B. Dam, *Influence of cation (RE = Sc, Y, Gd) and O/H anion ratio on the photochromic properties of REO_xH_{3-2x} thin films,* ACS Photonics **8**, 709 (2021).

[38] F. Nafezarefi, H. Schreuders, B. Dam, and S. Cornelius, *Photochromism of rare-earth metal-oxy-hydrides,* Applied Physics Letters **111**, 103903 (2017).

[39] M. Zubkins, I. Aulika, E. Strods, V. Vibornijs, L. Bikse, A. Sarakovskis, G. Chikvaidze, J. Gabrusenoks, H. Arslan, and J. Purans, *Optical properties of oxygen-containing yttrium hydride thin films during and after the deposition,* Vacuum **203**, 111218 (2022).

[40] Y. Komatsu, R. Shimizu, R. Sato, M. Wilde, K. Nishio, T. Katase, D. Matsumura, H. Saitoh, M. Miyauchi, J. R. Adelman, R. M. L. McFadden, D. Fujimoto, J. O. Ticknor, M. Stachura, I. McKenzie, G. D. Morris, W. A. MacFarlane, J. Sugiyama, K. Fukutani, S. Tsuneyuki, and T. Hitosugi, *Repeatable photoinduced insulator-to-metal transition in yttrium oxyhydride epitaxial thin films,* Chemistry of Materials **34**, 3616 (2022).

[41] M. V. Moro, S. M. Aðalsteinsson, D. Moldarev, M. Wolff, and D. Primetzhofer, *Photochromism in isotopically labeled oxygen-containing yttrium-hydride and deuteride thin-film systems,* physica status solidi (RRL) - Rapid Research Letters **16**, 2100508 (2021).

[42] D. Moldarev, M. V. Moro, C. C. You, E. M. Baba, S. Z. Karazhanov, M. Wolff, and D. Primetzhofer, *Yttrium oxyhydrides for photochromic applications: Correlating composition and optical response,* Physical Review Materials **2**, 115203 (2018).

[43] S. M. Aðalsteinsson, M. V. Moro, D. Moldarev, S. Droulias, M. Wolff, and D. Primetzhofer, *Correlating chemical composition and optical properties of photochromic rare-earth oxyhydrides using ion beam analysis,* Nuclear Instruments and Methods in Physics Research Section B: Beam Interactions with Materials and Atoms **485**, 36 (2020).

[44] S. Cornelius, G. Colombi, F. Nafezarefi, H. Schreuders, R. Heller, F. Munnik, and B. Dam, *Oxyhydride nature of rare-earth-based photochromic thin films,* The Journal of Physical Chemistry Letters **10**, 1342 (2019).

[45] M. Widerøe, H. Fjellvåg, T. Norby, F. Willy Poulsen, and R. Willestofte Berg, *NdHO, a novel oxyhydride,* Journal of Solid State Chemistry **184**, 1890 (2011).

[46] G. G. Libowitz and A. J. Maeland, *Hydrides,* in *Handbook on the Physics and Chemistry of Rare Earths*, edited by K. A. Gschneidner, Yr. and L. Eyring (North-Holland Publishing Company, 1979) Book section 26, pp. 299–336.

[47] K. Fukui, S. Iimura, J. Wang, T. Tada, T. Honda, K. Ikeda, T. Otomo, and H. Hosono, *Stabilization factor of anion-excess fluorite phase for fast anion conduction,* Chemistry of Materials **33**, 1867 (2021).

[48] N. Zapp, H. Auer, and H. Kohlmann, *YHO, an air-stable ionic hydride,* Inorganic Chemistry **58**, 14635 (2019).

[49] N. Zapp, D. Sheptyakov, and H. Kohlmann, *Computational chemistry-guided syntheses and crystal structures of the heavier lanthanide hydride oxides DyHO, ErHO, and LuHO,* Crystals **11**, 750 (2021).

[50] D. Kutsuzawa, Y. Hirose, Y. Sugisawa, J. Kikuda, D. Sekiba, and T. Hasegawa, *Enhanced ferromagnetic transition temperature in NdO_xD_y epitaxial thin films,* Physical Review Materials **3**, 044408 (2019).

[51] G. Colombi, R. Stigter, D. Chaykina, S. Banerjee, A. P. M. Kentgens, S. W. H. Eijt, B. Dam, and G. de Wijs, *Energy, metastability, and optical properties of anion-disordered* REO_xH_{3-2x} *RE = (Y, La) oxyhydrides: a computational study,* Physical Review B **105**, 054208 (2022).

[52] G. Colombi, S. Cornelius, A. Longo, and B. Dam, *Structure model for anion-disordered photochromic Gd oxyhydride thin films,* The Journal of Physical Chemistry C **124**, 13541 (2020).

[53] H. Kumazoe, Y. Igarashi, F. Iesari, R. Shimizu, Y. Komatsu, T. Hitosugi, D. Matsumura, H. Saitoh, K. Iwamitsu, T. Okajima, Y. Seno, M. Okada, and I. Akai, *Bayesian sparse modeling of extended X-ray absorption fine structure to determine interstitial oxygen positions in yttrium oxyhydride epitaxial thin film,* AIP Advances **11**, 125013 (2021).

[54] S. Banerjee, D. Chaykina, R. Stigter, G. Colombi, B. Dam, G. de Wijs, and A. Kentgens, *Solid state nmr studies on yttrium oxyhydrides: exploring multi-anion chemistry,* in preparation (2022).

[55] S. Banerjee, D. Chaykina, B. Dam, G. de Wijs, and A. Kentgens, *Understanding the ScHO structure by solid-state NMR,* in preparation .

[56] K. Nakatani, J. Piard, P. Yu, and R. Métivier, *Photochromic Materials: Preparation, Properties and Applications* (Wiley-VCH Verlag GmbH & Co. KGaA, 2016) pp. 1–45.

[57] R. J. Araujo, *Photochromism in glasses containing silver halides,* Contemporary Physics **21**, 77 (1980).

[58] R. Araujo, *Inorganic photochromic systems,* Molecular Crystals and Liquid Crystals Science and Technology. Section A. Molecular Crystals and Liquid Crystals **297**, 1 (2006).

[59] J. Montero, F. A. Martinsen, M. García-Tecedor, S. Z. Karazhanov, D. Maestre, B. Hauback, and E. S. Marstein, *Photochromic mechanism in oxygen-containing yttrium hydride thin films: An optical perspective,* Physical Review B **95**, 201301(R) (2017).

[60] J. Montero and S. Z. Karazhanov, *Spectroscopic ellipsometry and microstructure characterization of photochromic oxygen-containing yttrium hydride thin films,* physica status solidi (a) **215**, 1701039 (2018).

[61] Z. Wu, T. de Krom, G. Colombi, D. Chaykina, G. van Hattem, H. Schut, M. Dickmann, W. Egger, C. Hugenschmidt, E. Brück, B. Dam, and S. W. H. Eijt, *Formation of vacancies and metallic-like domains in photochromic rare-earth oxyhydride thin films studied by in-situ illumination positron annihilation spectroscopy,* Physical Review Materials **6**, 065201 (2022).

[62] J. Chai, Z. Shao, H. Wang, C. Ming, W. Oh, T. Ye, Y. Zhang, X. Cao, P. Jin, S. Zhang, and Y.-Y. Sun, *Ultrafast processes in photochromic material* YH_xO_y *studied by excited-state density functional theory simulation,* Science China Materials **63**, 1579 (2020).

[63] E. M. Baba, J. Montero, E. Strugovshchikov, E. Ö. Zayim, and S. Karazhanov, *Light-induced breathing in photochromic yttrium oxyhydrides,* Physical Review Materials **4**, 025201 (2020).

[64] M. Hans, T. T. Tran, S. M. Aðalsteinsson, D. Moldarev, M. V. Moro, M. Wolff, and D. Primetzhofer, *Photochromic mechanism and dual-phase formation in oxygen-containing rare-earth hydride thin films,* Advanced Optical Materials **8**, 2000822 (2020).

[65] F. Nafezarefi, *Photochromic Properties of Rare-Earth Oxyhydrides*, Ph.D. thesis, Delft University of Technology (2020).

[66] D. Moldarev, L. Stolz, M. V. Moro, S. M. Aðalsteinsson, I.-A. Chioar, S. Z. Karazhanov, D. Primetzhofer, and M. Wolff, *Environmental dependence of the photochromic effect of oxygen-containing rare-earth metal hydrides,* Journal of Applied Physics **129**, 153101 (2021).

[67] C. C. You and S. Z. Karazhanov, *Effect of temperature and illumination conditions on the photochromic performance of yttrium oxyhydride thin films,* Journal of Applied Physics **128**, 013106 (2020).

[68] E. M. Baba, P. M. Weiser, E. O. Zayim, and S. Karazhanov, *Temperature-dependent photochromic performance of yttrium oxyhydride thin films,* physica status solidi (RRL) - Rapid Research Letters **15**, 2000459 (2020).

[69] D. Chaykina, T. W. H. de Krom, G. Colombi, H. Schreuders, a. Suter, T. Prokscha, B. Dam, and S. W. H. Eijt, *Structural properties and anion dynamics of yttrium dihydride and photochromic oxyhydride thin-films examined by in situ* μ^+SR*,* Physical Review B **103**, 224106 (2021).

[70] C. C. You, D. Moldarev, T. Mongstad, D. Primetzhofer, M. Wolff, E. S. Marstein, and S. Z. Karazhanov, *Enhanced photochromic response in oxygen-containing yttrium hydride thin films transformed by an oxidation process,* Solar Energy Materials and Solar Cells **166**, 185 (2017).

[71] E. M. Baba, J. Montero, D. Moldarev, M. V. Moro, M. Wolff, D. Primetzhofer, S. Sartori, E. Zayim, and S. Karazhanov, *Preferential orientation of photochromic gadolinium oxyhydride films,* Molecules **25**, 3181 (2020).

[72] D. Chaykina, I. Usman, G. Colombi, H. Schreuders, B. Tyburska-Pueschel, Z. Wu, S. Eijt, L. J. Bannenberg, G. A. de Wijs, and B. Dam, *Aliovalent calcium doping of yttrium oxyhydride thin films and implications for photochromism,* The Journal of Physical Chemistry C **126**, 14742–14749 (2022).

[73] D. Moldarev, M. Wolff, E. M. Baba, M. V. Moro, C. C. You, D. Primetzhofer, and S. Z. Karazhanov, *Photochromic properties of yttrium oxyhydride thin films: Surface versus bulk effect,* Materialia **11**, 100706 (2020).

[74] M. P. Plokker, S. W. H. Eijt, F. Naziris, H. Schut, F. Nafezarefi, H. Schreuders, S. Cornelius, and B. Dam, *Electronic structure and vacancy formation in photochromic yttrium oxy-hydride thin films studied by positron annihilation,* Solar Energy Materials and Solar Cells **177**, 97 (2018).

[75] M. V. Moro, S. M. Aðalsteinsson, T. T. Tran, D. Moldarev, A. Samanta, M. Wolff, and D. Primetzhofer, *Photochromic response of encapsulated oxygen-containing yttrium hydride thin films,* physica status solidi (RRL) - Rapid Research Letters **15**, 2000608 (2021).

[76] D. Moldarev, C. Aracheloff, M. V. Moro, E. Pitthan, M. Wolff, and D. Primetzhofer, *Oxygen mobility in yttrium hydride films studied by isotopic labelling,* EPJ Web of Conferences **261**, 01001 (2022).

[77] S. Banerjee, D. Chaykina, B. Dam, G. de Wijs, and A. Kentgens, *Investigating photochromism in rare-earth metal oxyhydrides (Y, Sc) by solid-state NMR,* in preparation (2023).

[78] J. Sugiyama, *Spin polarized beam for battery materials research: $\mu^{\pm}SR$ and β-NMR,* Hyperfine Interactions **240**, 17 (2019).

[79] C. Eklöf-Österberg, R. Nedumkandathil, U. Häussermann, A. Jaworski, A. J. Pell, M. Tyagi, N. H. Jalarvo, B. Frick, A. Faraone, and M. Karlsson, *Dynamics of hydride ions in metal hydride-reduced batio3 samples investigated with quasielastic neutron scattering,* The Journal of Physical Chemistry C **123**, 2019 (2018).

[80] T. U. Ito, A. Koda, K. Shimomura, W. Higemoto, T. Matsuzaki, Y. Kobayashi, and H. Kageyama, *Excited configurations of hydrogen in the $BaTiO_{3-x}H_x$ perovskite lattice associated with hydrogen exchange and transport,* Physical Review B **95**, 020301(R) (2017).

[81] J. Sugiyama, K. Mukai, Y. Ikedo, H. Nozaki, M. Mansson, and I. Watanabe, *Li diffusion in Li_xCoO_2 probed by muon-spin spectroscopy,* Physical Review Letters **103**, 147601 (2009).

[82] J. Sugiyama, I. Umegaki, M. Matsumoto, K. Miwa, H. Nozaki, Y. Higuchi, T. Noritake, O. K. Forslund, M. Månsson, S. P. Cottrell, A. Koda, E. J. Ansaldo, and J. H. Brewer, *Desorption reaction in MgH_2 studied with* in-situ *μ^+SR,* Sustainable Energy & Fuels **3**, 956 (2019).

[83] R. Nedumkandathil, A. Jaworski, J. Grins, D. Bernin, M. Karlsson, C. Eklöf-Österberg, A. Neagu, C.-W. Tai, A. J. Pell, and U. Häussermann, *Hydride reduction of $BaTiO_3$ - oxyhydride versus O vacancy formation,* ACS Omega **3**, 11426 (2018).

[84] T. Misaki, I. Oikawa, and H. Takamura, *Negative knight shift in ba-ti oxyhydride: An indication of the multiple hydrogen occupation,* Chemistry of Materials **31**, 7178 (2019).

[85] C. V. Chandran, H. Schreuders, B. Dam, J. W. G. Janssen, J. Bart, A. P. M. Kentgens, and P. J. M. van Bentum, *Solid-state NMR studies of the photochromic effects of thin films of oxygen-containing yttrium hydride,* The Journal of Physical Chemistry C **118**, 22935 (2014).

[86] Q. Bai, X. He, Y. Zhu, and Y. Mo, *First-principles study of oxyhydride* H^- *ion conductors: Toward facile anion conduction in oxide-based materials,* ACS Applied Energy Materials **1**, 1626 (2018).

[87] O. S. Fjellvåg, J. Armstrong, P. Vajeeston, and A. O. Sjåstad, *New insights into hydride bonding, dynamics, and migration in* La_2LiHO_3 *oxyhydride,* The Journal of Physical Chemistry Letters **9**, 353 (2018).

[88] O. S. Fjellvåg, K. H. Nygard, P. Vajeeston, and A. O. Sjåstad, *Advances in the LiCl salt flux method and the preparation of phase pure* $La2-xNd_xLiHO_3$ $(0 \leq x \leq 2)$ *oxyhydrides,* Chem Commun (Camb) **55**, 3817 (2019).

[89] X. Liu, T. S. Bjørheim, and R. Haugsrud, *Formation and migration of hydride ions in* $BaTiO_{3-x}H_x$ *oxyhydride,* Journal of Materials Chemistry A **5**, 1050 (2017).

[90] X. Liu, T. S. Bjørheim, and R. Haugsrud, *Formation of defects and their effects on hydride ion transport properties in a series of* K_2NiF_4*-type oxyhydrides,* Journal of Materials Chemistry A **6**, 1454 (2018).

[91] A. Iskandarov, T. Tada, S. Iimura, and H. Hosono, *Characteristic mechanism for fast* H^- *conduction in* $LaH_{2.5}O_{0.25}$*,* Acta Materialia **230**, 117825 (2022).

[92] Y. Kobayashi, O. J. Hernandez, T. Sakaguchi, T. Yajima, T. Roisnel, Y. Tsujimoto, M. Morita, Y. Noda, Y. Mogami, A. Kitada, M. Ohkura, S. Hosokawa, Z. Li, K. Hayashi, Y. Kusano, J. Kim, N. Tsuji, A. Fujiwara, Y. Matsushita, K. Yoshimura, K. Takegoshi, M. Inoue, M. Takano, and H. Kageyama, *An oxyhydride of* $BaTiO_3$ *exhibiting hydride exchange and electronic conductivity,* Nature Materials **11**, 507 (2012).

[93] T. Yajima, A. Kitada, Y. Kobayashi, T. Sakaguchi, G. Bouilly, S. Kasahara, T. Terashima, M. Takano, and H. Kageyama, *Epitaxial thin films of* $ATiO_{3-x}H_x$ *(A = Ba, Sr, Ca) with metallic conductivity,* Journal of American Chemical Society **134**, 8782 (2012).

[94] G. Bouilly, T. Yajima, T. Terashima, W. Yoshimune, K. Nakano, C. Tassel, Y. Kususe, K. Fujita, K. Tanaka, T. Yamamoto, Y. Kobayashi, and H. Kageyama, *Electrical properties of epitaxial thin films of oxyhydrides* $ATiO_{3-x}H_x$ *(A = Ba and Sr),* Chemistry of Materials **27**, 6354 (2015).

[95] J. J. Zhang, G. Y. Gou, and B. C. Pan, *Study of phase stability and hydride diffusion mechanism of* $BaTiO_3$ *oxyhydride from first-principles,* The Journal of Physical Chemistry C **118**, 17254 (2014).

[96] N. Masuda, Y. Kobayashi, O. Hernandez, T. Bataille, S. Paofai, H. Suzuki, C. Ritter, N. Ichijo, Y. Noda, K. Takegoshi, C. Tassel, T. Yamamoto, and H. Kageyama, *Hydride in* $BaTiO_{2.5}H_{0.5}$*: A labile ligand in solid state chemistry,* Journal of the American Chemical Society **137**, 15315 (2015).

[97] T. Yajima, F. Takeiri, K. Aidzu, H. Akamatsu, K. Fujita, W. Yoshimune, M. Ohkura, S. Lei, V. Gopalan, K. Tanaka, C. M. Brown, M. A. Green, T. Yamamoto, Y. Kobayashi, and H. Kageyama, *A labile hydride strategy for the synthesis of heavily nitridized $BaTiO_3$,* Nature Chemistry **7**, 1017 (2015).

[98] Y. Tang, Y. Kobayashi, K. Shitara, A. Konishi, A. Kuwabara, T. Nakashima, C. Tassel, T. Yamamoto, and H. Kageyama, *On hydride diffusion in transition metal perovskite oxyhydrides investigated via deuterium exchange,* Chemistry of Materials **29**, 8187 (2017).

[99] T. Uchimura, F. Takeiri, K. Okamoto, T. Saito, T. Kamiyama, and G. Kobayashi, *Direct synthesis of barium titanium oxyhydride for use as a hydrogen permeable electrode,* Journal of Materials Chemistry A **9**, 20371 (2021).

[100] T. Katayama, A. Chikamatsu, H. Kamisaka, Y. Yokoyama, Y. Hirata, H. Wadati, T. Fukumura, and T. Hasegawa, *Topotactic synthesis of strontium cobalt oxyhydride thin film with perovskite structure,* AIP Advances **5**, 107147 (2015).

[101] H. Jeen, W. S. Choi, J. W. Freeland, H. Ohta, C. U. Jung, and H. N. Lee, *Topotactic phase transformation of the brownmillerite $SrCoO_{2.5}$ to the perovskite $srcoo_{3-\delta}$,* Advanced Matter **25**, 3651 (2013).

[102] S. Hu and J. Seidel, *Oxygen content modulation by nanoscale chemical and electrical patterning in epitaxial $SrCoO_{3-\delta}$ $(0 < \delta \leq 0.5)$ thin films,* Nanotechnology **27**, 325301 (2016).

[103] L. Liang, S. Qiao, S. Du, S. Zhang, J. Wu, and Z. Liu, *Role of interstitial hydrogen in $SrCoO_{2.5}$ antiferromagnetic insulator,* Physical Review Materials **2**, 114409 (2018).

[104] Y. Hirose, M. Tsuchii, K. Shigematsu, Y. Kakefuda, T. Mori, and T. Hasegawa, *Thermoelectric properties of amorphous ZnO_xN_y thin films at room temperature,* Applied Physics Letters **114**, 193903 (2019).

[105] Y. Zhu, T. Yamazaki, Z. Chen, Y. Hirose, S. Nakao, I. Harayama, D. Sekiba, and T. Hasegawa, *High-mobility and air-stable amorphous semiconductor composed of earth-abundant elements: Amorphous zinc oxysulfide,* Advanced Electronic Materials **6**, 1900602 (2019).

[106] N. Ichikawa, M. Iwanowska, M. Kawai, C. Calers, W. Paulus, and Y. Shimakawa, *Reduction and oxidation of $SrCoO_{2.5}$ thin films at low temperatures,* Dalton Transactions **41**, 10507 (2012).

2

Structural properties & anion dynamics of Y dihydride and photochromic oxyhydride thin-films examined by *in situ* μ^{+}SR

Isidor Isaac Rabi (1944 Physics Nobel Laureate) on the discovery of the muon:
"Who ordered that??"

Thin-films of rare-earth metal oxyhydrides, such as yttrium oxyhydrides ($YH_{3-2x}O_x$), show a photochromic effect where the transparency of the films decreases reversibly upon exposure to UV light. However, the exact mechanism behind this effect is unknown. In this paper, we describe the behaviour of $YH_{3-2x}O_x$ thin-films, with different O^{2-}:H^{-} ratios, under dark and illuminated conditions using *in situ* muon spin relaxation (μ^{+}SR), and compare that to an oxygen-free reference compound, yttrium dihydride ($YH_{2-\delta}$). The muon acts as a local magnetic probe in our compounds, giving information related to electronic, structural, and photochromic properties. Although $YH_{2-\delta}$ is the parent compound to $YH_{3-2x}O_x$, the muon behaviour in these two materials is different—the muon electrostatically interacts primarily with H^{-} (dihydride) or O^{2-} (oxyhydride)—leading to the use of different theoretical models. For $YH_{2-\delta}$, we observed the formation of an entangled H-μ complex and the onset of Mu^{+} diffusion and H^{-} rearrangement above 150 K ($E_{A,\Gamma}$ = 67 ± 13 meV). For the oxyhydrides, we adopted a transition state model, where Mu^{0} formation and gradual Mu^{+} recovery take place, accompanied by the formation of a Mu^{+}-O^{2-} complex and a polaron at the Y-cation. The activation energy ($E_{A,dia}$) associated with Mu^{+} recovery is dependent on lattice relaxation and is lower for thin-films of higher H-content ($E_{A,dia}$ = 29-45 meV). *In situ* illumination further reduces this energy barrier for all measured oxyhydrides, suggesting that the photochromic effect involves a reversible structural rearrangement during photo-darkening.

This chapter is partly based on *D. Chaykina, et al., Structural properties and anion dynamics of yttrium dihydride and photochromic oxyhydride thin films examined by in situ μ^{+}SR, Phys. Rev. B., 103, 224106, 2021.* [1].

2.1 Introduction

Multi-anion compounds are a relatively new and emerging class of materials, containing two or more different anions [2]. While cation substitutions are more common, here, the variation of properties is achieved by anion substitution. Specifically, this study focuses on oxyhydrides, consisting of oxide (O^{2-}) and hydride (H^-) anions.

Rare-earth metal (RE) oxyhydrides undergo a photochromic effect, and exhibit ionic conductivity as well. In particular, thin-films of $REH_{3-2x}O_x$, where RE = Sc, Y, Gd, Dy, Er [3–6], show the photochromic effect, while powdered $REH_{3-2x}O_x$ (RE = La, Nd) [7, 8] are reported as H^- conductors. Because of this overlap, we suspect that photochromism and ionic mobility are related.

The photochromic effect is a phenomenon where the optical transmittance of a material changes when it is exposed to light with photon energy greater than its band gap. Thin-films of $REH_{3-2x}O_x$, for example, are transparent materials which become opaque under UV light [9]. The mechanism behind this colour change in $REH_{3-2x}O_x$ is not well-understood, but may follow a similar mechanism to Cu-doped Ag halide glasses. When these glasses are exposed to light, electron-hole pairs are generated and atoms rearrange, creating metallic Ag^0 clusters that account for the dark appearance [10, 11].

Similarly, $YH_{3-2x}O_x$ shows increased conductivity [9] and disappearance of the most mobile H^- fraction [12] under UV light, suggesting an analogous mechanism. However, there is an alternative explanation for photochromism which involves the presence of optically active defects (known as colour centres) spanning the wide absorption range of these materials [10, 13]. Further, although these materials may also be ion conductors, according to Ubukata et al. [8], certain $REH_{3-2x}O_x$ compounds are predicted to form anion-disordered compounds which would impede ionic mobility. Thus, any ion diffusion may be very local and not long-range.

To understand the photochromic effect, we investigated thin-films of $YH_{3-2x}O_x$ by low-energy muon spin rotation (LE-μ^+SR). These films are deposited by reactive magnetron sputtering YH_x at various deposition pressures (p_{dep}), and are then oxidised in ambient air [3]. If $p_{dep} < 0.4$ Pa, the resultant film is metallic $YH_{2-\delta}$. Transparent $YH_{3-2x}O_x$ films are achieved when $p_{dep} > 0.4$ Pa, resulting in increasing O^{2-}:H^- ratio on exposure to air as p_{dep} increases. While $YH_{2-\delta}$ films are non-photochromic and metallic, the addition of oxygen changes the films to transparent, photochromic, and semiconducting $YH_{3-2x}O_x$. The semiconducting gap is similar to that in the non-photochromic YH_3 phase. We showed previously that several properties evolve with the change in O^{2-}:H^- ratio, including the photochromic efficiency [6].

Here, we apply the muon spin rotation technique to study the electronic and structural properties of $YH_{2-\delta}$ and $YH_{3-2x}O_x$ thin-films. The muon (μ^+) is very sensitive to local magnetic fields which, in these compounds, are primarily due to the presence of H^- ions which carry large nuclear magnetic dipole moments. This technique has been used to study ionic mobility in battery materials [14] and metal hydrides [15], as well as the excited configurations of H^- in an oxyhydride ($BaTiO_{3-x}H_x$) [16]. To investigate the photochromic effect, we use *in situ* μ^+SR where the sample is illuminated to induce the photochromic effect during data collection.

In this chapter, we show that $YH_{2-\delta}$ and $YH_{3-2x}O_x$ are distinctly different compounds. Local H^- mobility and formation of a H-μ spin-entangled complex was observed in sub-stoichiometric $YH_{\sim 1.9}$. In the oxyhydrides, we used a transition state model [17] to explain the muon behaviour. This model involves a temperature-driven change in the muon configuration from interstitial Mu^0 (octahedral site) to bound Mu^+-O^{2-}. The transition is characterised by a lattice deformation and relaxation around Mu^0, and the formation of a polaron on the Y^{3+} cation. The associated lattice deformation had a lower activation energy for H-rich oxyhydrides, and was further lowered by illumination. This suggests that a reversible change in the lattice occurs during photochromism, providing an element for the understanding of the photochromic mechanism in rare-earth metal oxyhydrides.

2.2 Experimental Methods

Thin-films of yttrium dihydride ($YH_{2-\delta}$) and yttrium oxyhydrides ($YH_{3-2x}O_x$) were deposited on 25x25 mm quartz plates (Ted Pella Inc.) by reactive magnetron sputtering as described in a previous publication [3]. The deposition pressure was kept constant by a flow of Ar and H_2 gases at a ratio of 7:1 Ar/H_2. $YH_{2-\delta}$ was deposited at a total pressure of 0.3 Pa, while the oxyhydrides were deposited at 0.5, 0.6, and 0.7 Pa. From this point on, they will be referred to as YHO-05, YHO-06, and YHO-07, respectively. Briefly, the deposition pressure influences the O^{2-}:H^- ratio in the resultant films after exposure to air, where a higher pressure leads to more oxidation and a higher O^{2-}:H^- ratio [6]. Deposition times were chosen so that all the films were ~150 nm thick. The $YH_{2-\delta}$ was capped with a thin layer of Pd (~12 nm) directly after deposition to prevent oxidation [18].

The band gap energies and photochromic properties of the films were measured optically (Fig. 2.A.1) using a custom-built optical fibre spectrometer where the light sources were a deuterium and a quartz tungsten halogen lamp (DH2000-BAL, Ocean Optics B.V.) with a Si array wavelength-dispersive spectrometer (HR4000, Ocean Optics B.V.). The optical transmission of the $YH_{3-2x}O_x$ films was measured the day of deposition, 5 days after, and 10 days after to ensure that the air-oxidation process was complete (Fig. 2.A.2. Tauc plots were used to determine the indirect band gap energies of the $YH_{3-2x}O_x$ films (Table 2.1 and Table 2.A.1).

The photochromic properties were probed by illuminating the $YH_{3-2x}O_x$ films with a narrow wavelength LED (λ = 385 nm, I ~ 75 mW/cm^2) for 2 h and measuring the average transmittance (λ = 450-1000 nm) with respect to time. After 2 h, the LED was turned off and the bleaching process was measured for several hours. The resultant contrast and bleaching rate constants are shown in Table 2.1. The contrast is the amount of colour change which occurs during illumination, or the change in transmittance after 2 h compared to the initial value [3, 6]. The return of original transparency after the LED is turned off is characterised by a bleaching rate constant, τ_B, based on first-order kinetics [4, 6]. All optical measurements were taken at room temperature (~295 K).

Muon spin relaxation (μ^+SR) experiments were done with the low-energy μ^+SR spectrometer (LE-μ^+SR) at the μE4 beamline [19] of the Swiss Muon Source (Paul Scherrer Institut, Switzerland). Transverse field (TF) and zero field (ZF) configurations were used, where the applied magnetic field in the TF had a magnitude of 10 mT. The temperature was varied between 10-300 K for the TF and 10-260 K ($YH_{3-2x}O_x$) or 10-300 K ($YH_{2-\delta}$) for the ZF experiments. The implantation profile of the muon beam was simulated for various implantation energies using TrimSP [20, 21], and the implantation energy of 13.5 keV was chosen specifically to probe the centre of the film. For *in situ* experiments, a bluepoint

Table 2.1: Summary of oxyhydride properties measured by optical methods. The indirect band gap (E_g) values for samples 10 days after deposition are shown along with two parameters describing the photochromic performance (contrast and bleaching rate constant, τ_B, at 295 K).

Compound Name	E_g (eV)	Contrast (%)	τ_B (min)
YHO-05	2.50 ± 0.05	21	41 ± 8
YHO-06	2.55 ± 0.04	16	23 ± 3
YHO-07	2.58 ± 0.03	10	12 ± 2

LED (HoenleGroup, λ = 365 nm) was mounted along the muon beam direction. $YH_{3-2x}O_x$ films were illuminated during the μ^+SR measurements for ~2 h at T = 50 K and allowed to bleach back to their original state for several hours.

2.3 Results

2.3.1 Yttrium dihydride, $YH_{2-\delta}$

Transverse Field

Transverse field (TF) measurements were performed for the entire set of samples to characterise their electronic properties and distribution widths of their local magnetic fields (ΔB_{local}). In particular, we use this information to characterise the structure of metallic $YH_{2-\delta}$ and the mobility of H^-/Mu^+ in its lattice. The $YH_{2-\delta}$ data was fit by a Gaussian cosine [22]:

$$A(t) = A_{dia,TF} \cos(2\pi\nu t + \phi)\, e^{-\frac{1}{2}\sigma_{TF}^2 t^2} , \tag{2.1}$$

where $A_{dia,TF}$ is the diamagnetic asymmetry (decay asymmetry of the muons precessing at the Larmor frequency), ν is the Larmor frequency (related to external applied field, B_{ext}), and σ_{TF} is the Gaussian relaxation rate (related to ΔB_{local}). More specifically, the

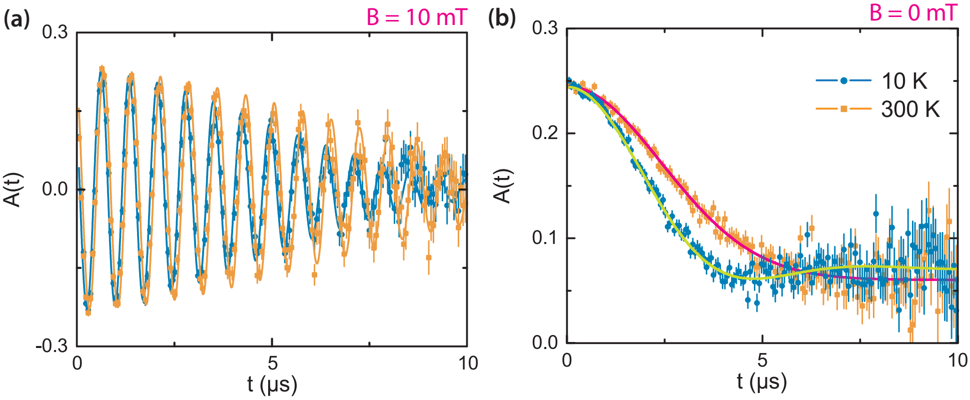

Figure 2.1: μ^+SR spectra for $YH_{2-\delta}$ under (a) TF of 10 mT and (b) ZF conditions. Measurements taken at 10 K and 300 K appear as blue and orange points, respectively. Solid curves correspond to best-fit analysis (see text).

relationship between ν and B_{ext} is given by

$$\nu = \frac{\gamma_\mu B_{ext}}{2\pi}, \tag{2.2}$$

where γ_μ is the muon gyromagnetic ratio ($\gamma_\mu/2\pi$ = 135.53 MHz/T) [23]. Figure 2.1a shows fitted spectra of the time evolution of the muon spin polarisation at the two extremes of temperature (10 and 300 K). The frequency of the oscillations is related to the precession of the muon spin in the B_{ext}, described by the aforementioned Larmor frequency. The $A_{dia,TF}$ is obtained from the amplitude of the oscillations, while the σ_{TF} comes from the rate of decay of the cosine.

The electronic properties of our films are deduced from the asymmetry ($A_{dia,TF}$) (Fig. 2.2a). The asymmetry is close to the maximum values of the LE-μ^+SR spectrometer and independent of temperature, consistent with the fact that $YH_{2-\delta}$ is metallic. In general, implanted muons (Mu^+) can interact with electrons during thermalisation to form paramagnetic muonium (Mu^0) [24–26]. This Mu^0 is normally considered a “missing fraction" of the asymmetry because its fast precession and depolarisation make it difficult to observe in most μ^+SR experiments [27]; thus, formation of Mu^0 results in a reduced diamagnetic asymmetry. However, in metals, Mu^0 formation is prevented due to electron shielding of the positive muon [23]. In $YH_{2-\delta}$, we determine the maximum asymmetry attainable in our experiments, $A_{dia,max} = 0.2361 \pm 0.0012$. This is similar to other studies carried out at the same instrument [20] and acts as a reference point to characterise the oxyhydrides, discussed later.

The magnitude of σ_{TF} (~0.22 μs^{-1}) at low temperatures (T < 150 K), shown in Figure 2.2b, is a clear indication that the local field distribution experienced by the Mu^+ is related to the nuclear dipolar fields of the surrounding nuclei, and similar values were found in other metal hydrides [15, 28]. The nuclear dipolar fields are primarily the result of neighbouring H^- anions with a minor contribution from Y^{2+} cations. This is due to the large magnetic moment of hydrogen and negligible magnetic moment of yttrium in their

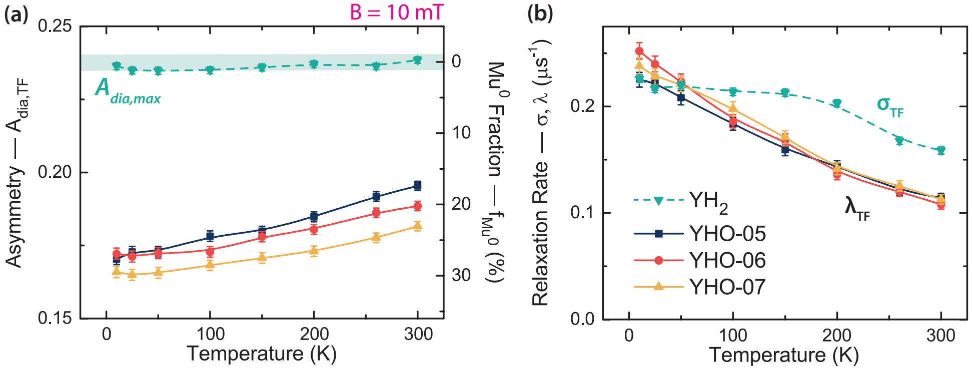

Figure 2.2: Temperature dependence of the fitted (a) asymmetry and (b) relaxation rate from TF (B = 10 mT) data of $YH_{2-\delta}$ (green, dashed), YHO-05 (navy), YHO-06 (red), and YHO-07 (yellow). These were obtained from Eq (2.1) for the $YH_{2-\delta}$ and Eq (2.8) for all the oxyhydrides. In (a), the asymmetry is converted to the Mu^0 fraction based on $A_{dia,max}$ (0.2361 ± 0.0012) by $f_{Mu^0} = (A_{dia,max} - A_{dia,TF}(T))/A_{dia,max}$. Dashed and solid curves are guides-to-the-eye.

most abundant isotopes (^{1}H = 2.79 μ_N, ^{89}Y = 0.14 μ_N). The hydrogen nuclei surrounding the muon have random spin directions, generating a distribution of local magnetic fields with a Gaussian shape. Each muon sees a slightly different set of randomly oriented nuclear spins, resulting in the total muon depolarisation observed in the experiment. Thus, σ_{TF} can be used to study the behaviour of H$^-$ in $YH_{2-\delta}$.

At low temperatures (T = 10-150 K), σ_{TF} is constant (Fig. 2.2b), suggesting that the distribution of local magnetic fields, ΔB_{local}, is static ($d\Delta B_{local}/dt = 0$) with respect to the muon lifetime (2.2 μs). Above 150 K, σ_{TF} decreases with increasing temperature, a clear sign of the onset of dynamic behaviour known as “motional narrowing". If the Mu$^+$ or the nuclear magnetic moments around it start to move, the B_{local} distribution will appear effectively narrower and the relaxation rate will decrease as a result. Potentially, both the Mu$^+$ and the surrounding H$^-$ ions begin diffusing above 150 K. Because it is not possible to differentiate between Mu$^+$ and H$^-$ diffusion by μ^+SR [29], we assume at this point that both are mobile.

The Abragam function can help to further characterise the “motional narrowing" effect in $YH_{2-\delta}$ [22, 30]:

$$A(t) = A_{TF,dia}\, exp[-\frac{{\sigma^2}_{abg}}{\Gamma^2}\, exp(-\Gamma t)\; -1+t] \\ \cos(2\pi \nu t+\phi)\,. \tag{2.3}$$

This is a general function describing dynamics which considers a Gaussian relaxation (σ_{abg}) with the addition of a hopping rate (Γ). When fitting the data, σ_{abg} was fixed to the low temperature value of σ_{TF} from Figure 2.2b [31, 32]. As seen in Figure 2.3, Γ is nearly zero between 10-150 K, confirming that no dynamic behaviour occurs in this temperature range. Above 150 K, Γ is non-zero and constantly increasing, indicating the onset of diffusion since the hopping rates, particularly above 200 K, are larger than $\sigma_{abg} \sim 0.2$ MHz [22, 30].

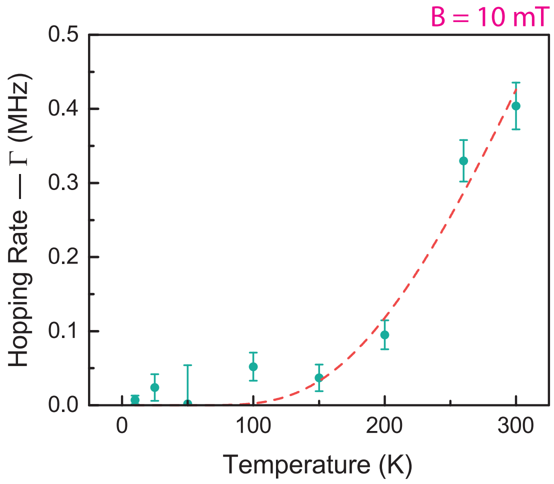

Figure 2.3: The points indicate the hopping rate, Γ, obtained from fitting $YH_{2-\delta}$ TF data by the Abragam function, Eq (2.3). These were further fitted by an Arrhenius equation (dashed line). The activation energy derived from this plot reflects the energy barrier for Mu$^+$/H$^-$ hopping in $YH_{2-\delta}$ thin-films.

The temperature dependency of the hopping rate is fitted by an Arrhenius equation (dashed line,Fig. 2.3):

$$\Gamma \ = \Gamma_o \ exp(-\frac{E_{A,\Gamma}}{k_B T}), \tag{2.4}$$

where Γ_o is the pre-exponential factor or attempt frequency, $E_{A,\Gamma}$ is the activation energy, and k_B is the Boltzmann constant. The $E_{A,\Gamma}$ for Mu^+/H^- diffusion here is 770 ± 150 K (67 ± 13 meV) with a Γ_o of 5.6 ± 3.0 MHz. The interpretation of this is discussed in Sec III.A.3.

Zero field

The interaction between the muon spin and the sample environment under zero-field (ZF) conditions is different from what was observed under TF. In the latter case, the applied B_{ext} is often larger than the strength of the interactions with the surroundings, so the muon spin simply precesses as Mu^+ with a depolarisation rate determined by the field distribution of the surrounding nuclear magnetic dipoles. In the absence of B_{ext}, the Mu^+ can, for example, form a spin-entangled complex with neighbouring nuclei. This is particularly relevant for systems containing atoms with large nuclear magnetic moments (such as H^- and F^-), and has been used to describe muons in metal hydrides [15] and oxyhydrides [16]. We use the ZF depolarisation signal of the complex to further analyse the structure of $YH_{2-\delta}$ and the mobility of H^-/Mu^+.

The static and dynamic Gaussian Kubo-Toyabe (KT) functions were also considered for analysing the ZF data, detailed in the appendix (Table 2.B.1-2.B.4). The static-KT analysis was disregarded due to a lower fit quality. The dynamic-KT analysis leads to comparable fit quality as the H-μ complex, but with significantly higher relaxation rates compared to the transverse field results, suggesting that this model is not compatible with the data.

The ZF spin depolarisation of the H-μ complex considered here is described by the following general expression:

$$A(t) = \ F_{H\mu} \ (A_{H\mu}, \sigma_{ZF}, f_{H\mu}) + A_{NR}, \tag{2.5}$$

where A_{NR} represents the fraction of non-relaxing muons which do not form the H-μ state, and $F_{H\mu}$ is an equation describing a spin-entangled H-μ complex [16, 33]:

$$\begin{aligned} F_{H\mu} = \ & A_{H\mu} \ (\frac{1}{6} + \frac{1}{6}\cos(2\pi f_{H\mu} t) + \frac{1}{3}\cos(\pi f_{H\mu} t) \\ & + \frac{1}{3}\cos(3\pi f_{H\mu} t)) \ \mathrm{e}^{-\frac{1}{2}\sigma_{ZF}^2 t^2} \ . \end{aligned} \tag{2.6}$$

In this equation, $A_{H\mu}$ is the asymmetry related to the H-μ complex, σ_{ZF} is the Gaussian relaxation rate due to surrounding nuclei, and $f_{H\mu}$ is a frequency which depends on the distance between H^- and Mu^+ by [16, 34]:

$$f_{H\mu} = \frac{\mu_0 \hbar \gamma_\mu \gamma_H}{8\pi^2 d^3}. \tag{2.7}$$

Here, γ_μ and γ_H are the gyromagnetic ratios of a muon and a hydrogen atom, and d is the H-μ distance. An H-μ-H complex is also possible and has been used in highly concentrated systems [33–35]. However, we dismiss it here because it did not match the oscillations in

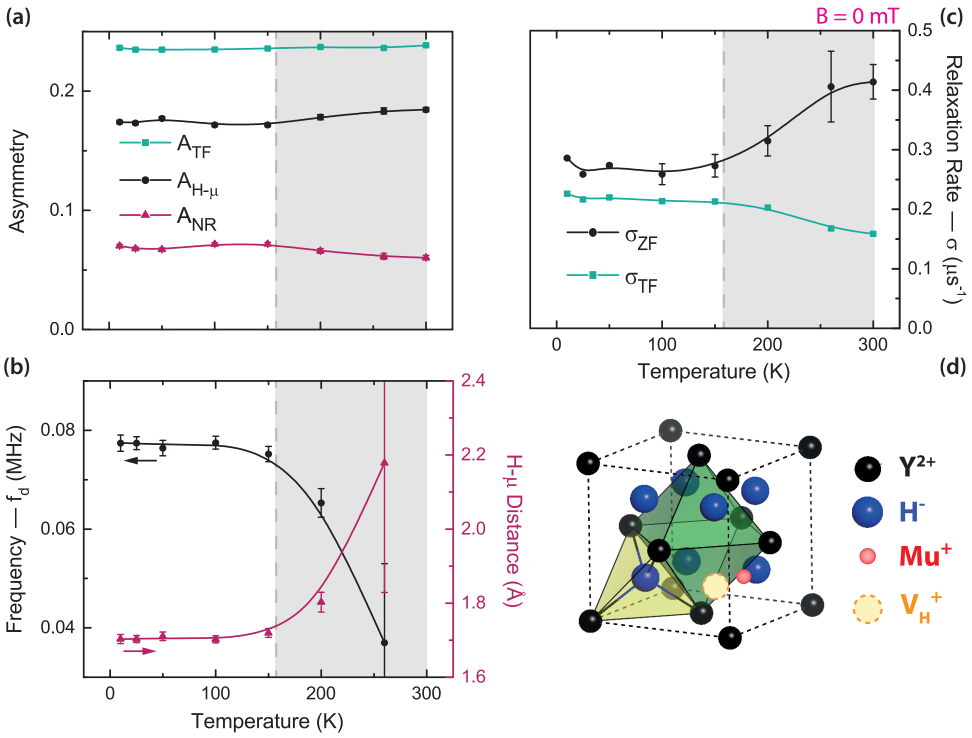

Figure 2.4: Summary of parameters fitted from the H-μ equation. The grey separation denotes the static-to-dynamic transition found from TF, with mobility beginning above 150 K. (a) The ZF asymmetry contributions are compared to the asymmetry found from TF. The sum of the two ZF contributions ($A_{H\mu} + A_{NR}$) is equivalent to $A_{TF,dia}$. (b) The fitted frequency (black) and calculated H-μ distance (purple). (c) Comparison of the Gaussian relaxation rates from TF (green) and ZF (black). (d) Image of the proposed muon stopping site in $YH_{2-\delta}$ based on the H-μ equation fitting (see text).

our data (Fig. 2.1b), likely due to the structural properties of $YH_{2-\delta}$ involving the presence of anion vacancies, as discussed below.

The asymmetry contributions are plotted in Figure 2.4a. $A_{H\mu}$ accounts for the majority of the total asymmetry and is independent of temperature. Since we observe this even above the static-to-dynamic transition temperature of ~150 K, we infer that the majority of Mu^+ are in the H-μ complex for the entire temperature range (10-300 K). It is important to note that the total asymmetry ($A_{H\mu} + A_{NR}$) is equivalent to the asymmetry found in the TF experiments (A_{TF}), validating the use of Eq (2.5).

The frequency, $f_{H\mu}$, and the corresponding H-μ distance are plotted in Figure 2.4b. Up to 150 K, the H-μ distance is constant with a value of 1.71 ± 0.01 Å. From this value, we propose a muon stopping site (Fig. 2.4d) where Mu^+ (the option Mu^- is unlikely for the H-μ complex in $YH_{1.9}$, as explained in footnote: [1]) is placed next to a H^- ion, and

---

[1] The diamagnetic character of the depolarisation signal shows that the muon is either in the Mu^+ or Mu^- state. However, the short H-μ distance points to a strong binding of the muon to a neighbouring H^-, indicating that the muon is positively charged. Moreover, for the muon to accommodate two electrons in a Mu^- state, the

adjacent to an anion vacancy. We choose this site for several reasons. First, the distance between two anion sites is much larger than the H-μ distance, so the Mu^+ cannot be in a nearest neighbour anion position (tetrahedral to: tetrahedral ~2.75 Å, octahedral ~2.38 Å). Second, the equation for an entangled H-μ-H (see e.g. Ref. [33]) complex did not fit the data, suggesting that the Mu^+ is not surrounded by multiple equidistant H^- ions. Lastly, an anion vacancy in this compound should be positively charged, slightly repelling the Mu^+ and pushing it towards the neighbouring H^- ion electrostatically.

Elongation of this H-μ "bond" is observed for $T > 150$ K; however, the error bars are very large as the frequency becomes poorly defined at high temperatures, visible also in the spectrum in Figure 2.1b. This elongation can be the result of thermal vibrations [33] or Mu^+/H^- hopping [15]. For T ~ 200 K, thermal vibrations are likely dominant since the hopping rate from TF was also low. However, for temperatures above 260 K, the frequency becomes ill-defined due to the gradual "breaking" of the H-μ bond as the two species move away from each other in favour of mobility.

The Gaussian relaxation rate, σ_{ZF}, is compared to σ_{TF} in Figure 2.4c, with σ_{ZF} coming from Eq (2.6) and σ_{TF} from Eq (2.1). Both relaxation rates are temperature-independent in the range of 10-150 K, indicating static behaviour. The value of σ_{ZF} is larger than σ_{TF} because in the TF, only the magnetic field distribution along the direction of B_{ext} is measured, while in the ZF case, the muon is sensitive to the field distribution in all directions [22]. This results in $\sigma_{ZF} > \sigma_{TF}$.

Above 150 K, σ_{TF} decreases while σ_{ZF} increases, both of which are indicators of Mu^+/H^- diffusion. The different temperature trends are a result of the different muon-sample spin interactions. Under TF conditions, the spin-entanglement between Mu^+ and H^- is quenched, and the muon is sensitive to the field distribution of the nuclear magnetic dipoles only. When the Mu^+ or H^- begin to move, this field distribution is "motionally narrowed", as mentioned before, and the relaxation rate decreases. In the ZF, however, the situation is different because the muon is spin-entangled to a neighbouring H^-. Mobility of the Mu^+ and H^- leads to faster relaxation of the muon spin in this complex, thus a higher relaxation rate [33]. This finding confirms that Mu^+ and possibly H^-, as discussed below, are mobile above 150-200 K in our $YH_{2-\delta}$ films.

Implications on the structure & H^- dynamics of $YH_{2-\delta}$

A $YH_{2-\delta}$ thin-film is used here as a reference to study the behaviour of $YH_{3-2x}O_x$ thin-films, which are made by air-oxidation of $YH_{2-\delta}$. Based on the temperature independent asymmetries in both TF and ZF, we conclude that no Mu^0 formation occurred in the $YH_{2-\delta}$ film, in accordance with its metallic behaviour. Although Y-metal hydrides (YH_x) span a wide range of hydrogen concentration ($0 \leq x \leq 3$), only compositions where x approaches 3 are insulating, while the rest are metallic [18, 36]. To obtain the x ~ 3 semiconducting state would require H_2 (g) partial deposition pressures much higher ($p_{H_2} \geq 10$ Pa) than what is used in our deposition procedure [3, 37]. The formation of the dihydride phase requires only $p_{H_2} > 10^{-29}$ Pa [37].

---

muon would need to reside in an interstitial site like the H^-, which is excluded in view of the observed short H-μ distance. Lastly, it is unlikely for a Mu^- to replace a H^- due to its light mass. Thus, although Mu^- may be present in this material, the vast majority (~75%) of the muons behave as Mu^+ and are described well by the H-μ spin-entangled complex.

Previous work has shown that the solubility of hydrogen in the dihydride phase ranges between sub-stoichiometric $YH_{1.9}$ and super-stoichiometric $YH_{2.1}$ [38]. These extremes can be distinguished based on their optical properties, where $YH_{1.9}$ shows an optical transmission window, while $YH_{2.1}$ is opaque. Optical measurements show a transmission window (Fig. 2.A.1), suggesting that our film has a composition of $YH_{\sim 1.9}$. In such a compound there will be many anion vacancies due to the partial occupation of tetrahedral interstitial sites by H^-. These structural characteristics lead to the assignment of the muon site in Figure 2.4d, explained in Sec III.A.2.. DFT calculations could be helpful in order to examine in detail the muon site and energetics of muon binding in the H-μ complex in the sub-stoichiometric $YH_{1.9}$ phase, but are also challenging in view of disorder that may be present in the H^- anion sub-lattice.

We observe dynamic behaviour in $YH_{\sim 1.9}$ above 150 K, which we attribute to Mu^+ and H^- mobility. The activation energy $E_{A,\Gamma}$ we derived for this mobility (67 ± 13 meV) is much lower than the values obtained in other metal hydrides (e.g. $TiH_{2\pm\delta}$ and $YH_{2\pm\delta}$) for long-range H^- motion (~400-500 meV) [28, 39–42]. It can instead be related to local anion reorganisation. Particularly, Kossler et al. [28] found two "motional narrowing" steps in $YH_{2.00}$, with the first relating to anion reorganisation (H^- moving from tetrahedral to octahedral sites) and the second relating to long-range H^- diffusion. Additionally, a similar onset temperature was reported in $YH_{2.1}$ where, at 155 K, the resistivity changed due to the reorganisation of H^- anions in the octahedral sites, many of which are vacant [43]. Therefore, it is likely that in this $YH_{\sim 1.9}$ thin-film there is also a local rearrangement of H^- and vacancies above ~150 K.

The activation energy $E_{A,\Gamma}$ obtained here is likely influenced by the simultaneous diffusion of Mu^+ throughout the material. Mu^+ diffusion was reported in several other *fcc* metals with comparable activation energies [31]. Not only is it impossible to distinguish between Mu^+ and H^- by μ^+SR [15, 29], but the Mu^+ is lighter in mass than H^-, so it expectedly will move faster than the H^- which may result in a lower $E_{A,\Gamma}$. Initial μ^-SR measurements have been performed for MgH_2 to decouple Mu^+/H^- motion and to understand how they contribute to the overall mobility observed in $\mu^\pm$SR experiments [29, 44]. Therefore, we conclude that above 150 K, Mu^+ diffusion and H^- anion reorganisation contribute to the overall mobility in $YH_{\sim 1.9}$ thin-films.

2.3.2 Yttrium oxyhydride, $YH_{3-2x}O_x$

Transverse Field

Yttrium oxyhydrides require a different analysis of the μ^+SR data. This is due to the presence of both H^- and O^{2-} in the compound, where both ions can influence the muon behaviour. In addition to various μ^+-H^- interactions, the muon can bond to O^{2-} as μ^+-O^{2-}, seen in many oxides [17, 45, 46]. Further, we must consider that the addition of oxygen leads to the appearance of semiconducting properties. Thus, we follow a different type of analysis for $YH_{3-2x}O_x$ (compared to $YH_{2-\delta}$), acknowledging these aspects.

Unlike $YH_{2-\delta}$ (Eq (2.1)), the TF data for the $YH_{3-2x}O_x$ thin-films (Fig. 2.C.1) was fit by an exponentially damped cosine:

$$A(t) = A_{dia,TF}\cos(2\pi\nu t + \phi)\, e^{-\lambda_{TF}t} \ , \tag{2.8}$$

where $A_{dia,TF}$ is the diamagnetic asymmetry, ν is the Larmor frequency, and λ_{TF} is the exponential relaxation rate. In general, a Lorentzian B_{local} distribution is used to describe a dilute distribution of magnetic moments [22, 47] or rapidly fluctuating magnetic fields, either due to fast muon diffusion or due to fast fluctuating magnetic moments [32, 48]. In our case, the Lorentzian B_{local} distribution is likely due to the presence of quickly fluctuating magnetic moments near the muon because the H^- content in $YH_{3-2x}O_x$ is too high (O^{2-}:H^- ~ 0.5) to be considered a dilute magnetic system [5].

The $A_{dia,TF}$ values of the $YH_{3-2x}O_x$ films follow a very different trend compared to $YH_{2-\delta}$ (Fig. 2.2a). While the asymmetry in $YH_{2-\delta}$ is high and temperature-independent, the asymmetries of the $YH_{3-2x}O_x$ films are reduced and constantly increasing with temperature. In general, we find values smaller than $A_{dia,max}$ due to Mu^0 formation, which is very common in semiconductors and insulators [23–26]. As stated previously, Mu^0 is difficult to measure under our experimental conditions and appears rather as a “missing fraction" of the diamagnetic asymmetry. We observe that for more insulating thin-films (higher p_{dep}), the amount of Mu^0 increases, indicating a relationship between the O^{2-}:H^- ratio and the electronic properties of the material. For example, YHO-07 (which has the largest band gap of 2.58 ± 0.04 eV and highest O^{2-} content [5, 6]) showed the largest Mu^0 fraction (Table 2.2).

Interestingly, the $YH_{3-2x}O_x$ asymmetries show a temperature dependence, increasing over a broad temperature range. We conclude that this is due to a gradual recovery of the diamagnetic muon state (Mu^+ or Mu^-). Such recovery may occur due to Mu^0 ionization or charge carrier capture. First, thermally-driven Mu^0 ionization typically occurs in a narrow temperature range [24, 49–51], which is not the case here. Next, Mu^0 formation and capture of thermally excited charge carriers has also been observed in lowly doped semiconductors where Mu^0 forms a defect level close to the valence or conduction band [51, 52]. However, although our samples likely have low carrier densities (based on their high resistivity [7–9, 53]), this process should again occur in a narrow temperature range (related to the defect level) and not gradually between 10-300 K. Instead, we propose that Mu^0 is not the lowest energy configuration of the muon, and that it undergoes a site change through a transition state, eventually forming Mu^+ [17, 54].

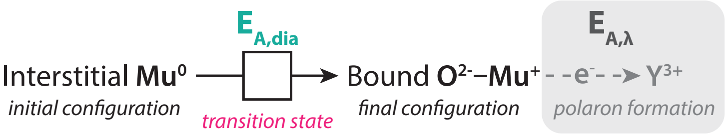

Figure 2.5: Schematic image showing the transition state model and the associated activation energies where the muon makes a site change and forms a polaron on the nearest cation. Inspired by Ref. [17].

Such a transition state model has been proposed for several different oxides (TiO_2 [55], ZrO_2 [56], Nb:SnO_2 [57] and Lu_2O_3 [54]), and a schematic representation of this model is shown in Figure 2.5. A detailed explanation can be found in Ref. [17]. During thermalisation, implanted muons may form Mu^0 and come to rest at an interstitial site. However, the presence of this Mu^0 may cause a lattice distortion. As the lattice relaxes, Mu^0 may move to a bound state with a nearby O^{2-} anion, via a “transition state". The relaxation of the lattice and coupled movement of Mu^0 are related to an activation energy, referred to here as $E_{A,dia}$.

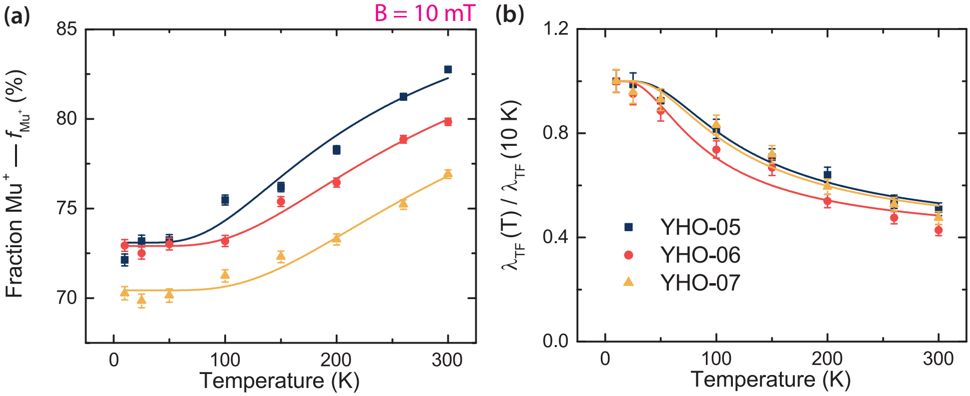

Figure 2.6: Boltzmann fitting results of (a) the Mu^+ fraction and (b) the λ_{TF} for three $YH_{3-2x}O_x$ thin-films (YHO-05 (navy), YHO-06 (red), YHO-07 (yellow)). The Mu^+ fraction is calculated from the TF asymmetry in Figure 2.2 by $f_{Mu^+} = 100 - f_{Mu^0}$. The relaxation rate, λ_{TF}, is normalised to the value at 10 K. Eq (2.9) and Eq (2.10) are used to obtain the energy barriers (a) $E_{A,dia}$ and (b) $E_{A,\lambda}$, respectively.

In the bound state, the electron density of the Mu^0 shifts to a neighbouring cation to form a polaron at the metal cation. The formation of this polaron is associated with an additional activation energy ($E_{A,\lambda}$), sometimes called the muon-electron binding energy [17, 56]. In general, $E_{A,\lambda}$ is lower than $E_{A,dia}$ [17, 56]. In this way, although the muon initially forms interstitial Mu^0, as the temperature increases, more muons can surmount these energy barriers in favour of the final Mu^+-O^{2-} state.

Table 2.2: Summary of the E_g energies (from optical measurements), Mu^0 fractions (f_{Mu^0}), and activation energies (E_A) (from μ^+SR) for $YH_{2-\delta}$ and $YH_{3-2x}O_x$. Mu^0 fractions are from TF measurements and based on $A_{dia,max}$. The $E_{A,\Gamma}$ is related to Mu^+/H^- diffusion, found only in metallic $YH_{2-\delta}$. The other activation energies are related to the muon transition state model used to describe the muon behaviour in the semiconducting oxyhydrides (see text).

Name	f_{Mu^0} (10 K) (%)	f_{Mu^0} (300 K) (%)	$E_{A,\Gamma}$ (meV)	$E_{A,dia}$ (meV)	$E_{A,\lambda}$ (meV)
$YH_{2-\delta}$	0	0	67±13	-	-
YHO-05	28	17	-	29±2	17±1
YHO-06	27	20	-	39±1	12±1
YHO-07	30	23	-	45±2	16±1

The activation energy $E_{A,dia}$ can be determined based on the fitting of the increasing Mu^+ fraction (Fig. 2.6a) by a Boltzmann-like equation [58]:

$$f_{Mu^+}(T) = f_0 + \frac{(100 - f_0)Ne^{-E_{A,dia}/k_BT}}{1 + Ne^{-E_{A,dia}/k_BT}}, \tag{2.9}$$

where f_0 is the initial Mu^+ fraction at 10 K, N is a density of states parameter (fixed at 1.7), k_B is the Boltzmann constant, and $E_{A,dia}$ is the activation energy for converting interstitial Mu^0 to the bound state (Table 2.2).

In general, the values for $E_{A,dia}$ are lower than what has been reported previously in oxides (~120-260 meV) [17, 56]. However, our samples are different from previous work because they are not pure oxides, but contain a significant amount of H^- and anion vacancies [5, 6]. Values outside this range have also been reported, for example, for CIGS and CZTS thin-films which had $E_{A,dia}$ barriers of 50-70 meV and 100-160 meV, respectively [58]. This could be the result of the nature of the anions (Se or S, respectively), the amount of defects, or other aspects. Differences may also be attributed to structural properties; the $E_{A,dia}$ values obtained for some monoclinic oxides were consistently larger than those for cubic oxides [56]. Hence, we conclude that $E_{A,dia}$ depends on the local lattice structure of the material.

Indeed, our values for $E_{A,dia}$ depend on the O^{2-}:H^- ratio, being higher as the films become more O-rich (higher p_{dep}), which is likely due to structural differences between the oxyhydrides. For example, the O^{2-}:H^- ratio determines the quantity and distribution of vacancies in the interstitial sublattice (Fig. 2.7). Cornelius et al. [5] proposed an anion-disordered model to describe the anion occupancy in $REH_{3-2x}O_x$ thin-films, where tetrahedral sites (T) are occupied preferentially by O^{2-} [59]. Since addition of O^{2-} leads to removal of two H^-, one from an octahedral (Oc) and one from a T site, more O-rich thin-films have more Oc (and eventually T) vacancies. Interstitial Mu^0 likely stops in an Oc vacancy, since this may be the only available site in the films measured here [6]. Thus, the availability of vacancies and their quantity may affect the stability of the interstitial Mu^0 state.

In some RE-oxides (Y_2O_3 [60] and Lu_2O_3 [54, 61]), the Mu^0 state was described as the lowest energy configuration, opposite from our finding. These oxides are typically characterised by anion vacancies. This suggests that, not only the quantity, but the type of available vacancy is important for the muon behaviour. Vacant T and Oc sites differ, with Oc sites being larger and 6-fold coordinated [59]. Thus, the Mu^0 state may be stabilised in compounds with many Oc vacancies such as YHO-07, and further stabilised in the presence of additional T vacancies, as in Y_2O_3.

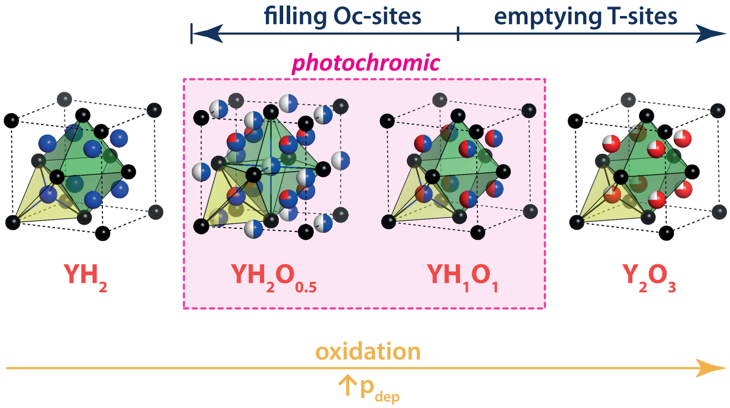

Figure 2.7: Schematic representation of yttrium dihydride (YH_2), two oxyhydrides ($YH_{3-2x}O_x$), and yttrium oxide (Y_2O_3), highlighting their structural differences. In this anion-disordered model, partial occupancy of interstitial sites is denoted by multi-coloured circles: $Y^{+2/+3}$ (black), H^- (blue), O^{2-} (red), and vacancies (white). As the p_{dep} increases, more oxidised compounds are formed, where YHO-05, YHO-06, and YHO-07 likely fall in the photochromic range between $YH_2O_{0.5}$ and YHO. More detailed explanations can be found in Ref. [5, 6, 59].

Another reason for the instability of the Mu^0 state in oxyhydrides may be the “flexibility" or deformability of their lattices. While our compounds have a face-centred cubic crystal structure, Y_2O_3 has a bixbyite structure, which is a distorted *fcc* lattice [5]. This distorted lattice may be resistant to relaxation around a foreign species like Mu^0. Note also that, H^- is a very polarisable ion [2] which can be mobile in hydrides (see above) and oxyhydrides [7]. Thus, more H-rich oxyhydrides may need less energy for lattice relaxation since this process is related to local atom displacements [17], and O^{2-} can be considered a hard-shell ion while H^- is polarisable.

From the temperature dependence of λ_{TF} (Fig. 2.2b), an activation energy can be determined based on another Boltzmann-like equation (Fig. 2.6b):

$$\lambda_{TF}(T) = \frac{1}{1+N\mathrm{e}^{-E_{A,\lambda}/k_B T}}, \tag{2.10}$$

where where the empirical parameter N relates to the shape of the binding potential (fixed to 1.7), k_B is the Boltzmann constant, and $E_{A,\lambda}$ is the muon-electron binding energy (Table 2.2). The magnitude of $E_{A,\lambda}$ is similar to what has been found for other compounds (5-15 meV) [56] and appears to be independent of the O^{2-}:H^- ratio.

$E_{A,\lambda}$ describes the shift of the Mu^0 electron density towards the nearest metal cation, reducing its oxidation state ($Y^{3+} \rightarrow Y^{2+}$) and forming a polaron [17, 56]. At low temperatures, the electron is close to the Mu^+ in the bound state, resulting in a larger relaxation rate. But as the temperature increases, the electron gradually moves closer to the cation, reducing the hyperfine interactions between Mu^+ and the polaronic electron, and leading to a lower relaxation rate. The Mu^0 electron density in Y_2O_3, for example, was described as being centred on the cation by DFT [60]. As well, yttrium can be stable in a divalent oxidation state (able to form compounds such as $YH_{2-\delta}$) and has a relatively small reduction potential (E^0 (Y^{3+}/Y^{2+}) = -2.81 V) [62]. Such cation reduction has also been seen in ZrO_2 [56] and TiO_2 [55] where the oxidation state of Ti, for example, was reduced from 4+ to 3+ upon formation of a polaron and transition to the bound Mu^+-O^{2-} configuration. In this way, the transition state model explains the temperature-dependent trends of both the Mu^+ fraction ($A_{dia,TF}$) and λ_{TF}.

Zero Field

As we showed in previous sections on $YH_{2-\delta}$, ZF measurements can be used to both probe different muon-sample interactions compared to the TF, and to give further evidence for ideas derived from TF results. Similarly, for the oxyhydrides, we use the ZF results to comment on the behaviour of H^- (to which the TF was insensitive), and to support the transition state model we proposed based on the TF temperature trends.

In the $YH_{2-\delta}$ sample, the ZF data was considered in terms of H-μ complex formation and local mobility of H^- ions. A similar H-μ complex was found in a metallic oxyhydride ($BaTiO_{3-x}H_x$) [16], showing that such a complex can form despite the presence of O^{2-} and regardless of the (large) O^{2-}:H^- ratio. However, in our $YH_{3-2x}O_x$ films, this is not the case. The muon behaviour more closely resembles the transition state model and the H-μ equation did not fit the data well (Fig. 2.C.1), possibly due to the amount of defects and anion disorder present in our samples, as well as Mu^0 formation. Though a small fraction of muons may have formed this complex, other interactions between the muon and sample environment are more relevant. Thus, a different treatment of the data follows for the $YH_{3-2x}O_x$ films.

The ZF data for the $YH_{3-2x}O_x$ films was fitted by a phenomenological description of the static Gaussian Kubo-Toyabe (KT) equation:

$$A(t) = A_{KT}(\frac{1}{3} + \frac{2}{3}\,[1-(\Delta_{ZF}t)^2]\,\mathrm{e}^{-\frac{1}{2}(\Delta_{\mathrm{ZF}}\mathrm{t})^2})\,\mathrm{e}^{-\lambda_{\mathrm{ZF}}\mathrm{t}} + A_{NR}, \tag{2.11}$$

where A_{KT} is the asymmetry related to the Kubo-Toyabe function, Δ_{ZF} is the Gaussian relaxation rate, λ_{ZF} is the exponential relaxation rate, and A_{NR} is related to the fraction of non-relaxing muons. Without the exp(-λ_{ZF}t) term, the static Gaussian KT function describes a muon surrounded by static nuclear spins which generate an isotropic B_{local} distribution with a Gaussian shape [22]. However, if there are also rapidly fluctuating interactions of the muon with surrounding electrons, adding the exponential term significantly improves the fits by including the different contributions to the muon spin depolarisation [14, 44, 47]. This is especially important when dealing with the combined contributions of nuclei and electrons which normally result in relaxation rates of very different magnitudes [14, 32, 44]. We note that longitudinal field (LF) measurements are also useful for discriminating between different phenomena, and are open for future study.

Figure 2.8a shows the asymmetry contributions from Eq (2.11) compared to the TF asymmetry from Eq (2.8). The sum of the ZF asymmetry components (A_{KT} + A_{NR}) is equivalent to A_{TF}. Further, the phenomenological KT equation represents the majority of the data, with a small contribution from the non-relaxing muon fraction. Overall, the asymmetry values support the use of the chosen fitting equation. However, A_{KT} accounts for the asymmetry of both Gaussian and exponential contributions simultaneously and cannot be used to distinguish them.

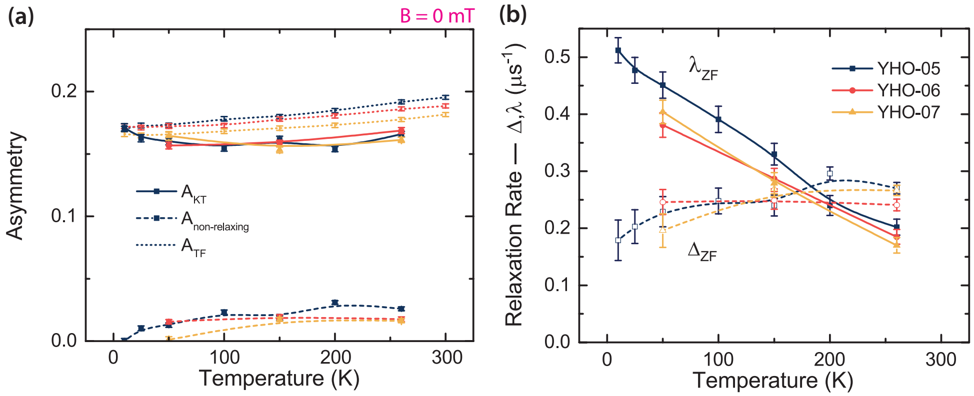

Figure 2.8: A summary of the fitting parameters obtained from the analysis of the ZF $YH_{3-2x}O_x$ data with Eq (2.11). (a) The asymmetry contributions from the ZF (A_{KT} + A_{NR}) are compared to the TF values. The sum of the two ZF components is equivalent to the TF value. (b) The two relaxation rates contributing to the total muon depolarisation, where λ_{ZF} is related to quickly fluctuating electron moments, while Δ_{ZF} is related to nuclear moments, mostly H^-. Lines are guides to the eye.

More detailed information about the muon environment can be obtained from the relaxation rates shown in Figure 2.8b. The Gaussian relaxation rate can be related to nearby nuclei (mainly H^-). The magnitude of Δ_{ZF} (~0.2 μs^{-1}) is almost equivalent to the σ_{ZF} found in $YH_{2-\delta}$ (Fig. 2.4c) for static H^-, in line with the fact that the films we measured are oxyhydrides (or oxygenated YH_x) with a significant quantity of H^- rather than the oxide (Y_2O_3). Further, the largely temperature-independent trend of Δ_{ZF} suggests that H^- is static within the muon lifetime (2.2 μs) for all three measured oxyhydrides. It is possible that H^- mobility in these compounds is hindered by the presence of O^{2-} ions, anion disorder, and other effects. Thus, the onset temperature for diffusion may be above 300 K. In general, H^- conductivity in oxyhydrides has been reported for temperatures in the range of 400-600 K [7, 63]. Further, some rare-earth metal oxyhydrides are predicted to form anion-disordered compounds, reducing the ionic mobility [8].

The exponential relaxation rate, on the other hand, can be related to electron moments and serves as further evidence in favour of the transition state model. We showed that in $YH_{2-\delta}$, relaxation rates related to nuclei with large magnetic moments (specifically H^-) are in the range of ~0.22 μs^{-1}. Thus, the magnitude of λ_{ZF} (~0.5 μs^{-1}) cannot be explained by considering nuclei in proximity to Mu^+. Rather, λ_{ZF} has to be the result of electrons near Mu^+, since only such interactions between Mu^+ and electronic moments can lead to larger depolarisation rates compared to interaction with nuclear moments [14, 32, 44]. This is relevant to the transition state model where in the final configuration, Mu^+ is sensitive to the magnetic moment of the neighbouring polaronic electron and the Mu^+-polaron distance increases with temperature, leading to a gradual reduction of the exponential relaxation rate, λ_{ZF}.

2.3.3 *in situ* Illumination

Rare-earth metal oxyhydride thin-films exhibit a photochromic effect [9], the origin of which is not yet clear. We performed *in situ* μ^+SR experiments to see if the muon behaviour is affected by optical illumination. This muon behaviour is discussed in terms of the transition state model proposed in Sec. III.B.1, where samples measured “in the dark" exhibit a gradual, thermally-driven Mu^+ recovery.

Oxyhydride samples were illuminated and their photochromic response is shown in Figure 2.9a. A transmission spectrum is collected every 15 s from which the average transmittance (λ = 450-1000 nm) is calculated with respect to time. The relative contrast is plotted to normalise for the initial transmittance of the samples which differ slightly. The samples were illuminated for 2 h by a 385 nm LED (grey area in figure), during which the samples became opaque. After illumination, the original transparent state was recovered within 2 h. The amount of colour change which occurred is called the contrast and the time with which the samples return to their transparent state is called the bleaching time, τ_B (Table 2.1). The calculations for these quantities are discussed in Ref. [3, 4, 6]. Higher p_{dep} samples had the lowest photochromic contrast but the fastest τ_B, observed also in our detailed studies of the p_{dep}-dependence of the photochromic effect in various $REH_{3-2x}O_x$ [6].

Twin samples (deposited alongside those described above) were measured by μ^+SR using *in situ* illumination from a 365 nm LED. Only TF measurements were performed and were fit by Eq (2.8), where two parameters are considered for this discussion: λ_{TF} and

$A_{TF,dia}$. While λ_{TF} was constant during the measurement (Fig. 2.D.1), $A_{TF,dia}$ showed a clear difference upon illumination (Fig. 2.9b). As well, it shows a p_{dep}-dependence, with the largest change in the asymmetry for YHO-05, which also had the greatest photochromic contrast.

After many hours of bleaching (and a heating programme described in the supplemental material), the samples returned to their initial value of $A_{TF,dia}$ (Fig. 2.9b and Fig. 2.E.1). The difference in kinetics is likely due to the lower experimental temperature, which generally results in slower bleaching rates [11, 64, 65]. Nevertheless, these observations clearly establish a relation between the optical and muon behaviour under illumination, showing both reversible and p_{dep}-dependent changes.

An increased asymmetry during illumination suggests a larger diamagnetic (Mu^+ or Mu^-) and a smaller paramagnetic (Mu^0) fraction. This can happen for several reasons (Fig. 2.10a). In general, we consider three muon populations in the oxyhydrides [17]: (1) diamagnetic Mu^+ which form the bound state promptly, (2) muons which start as Mu^0, but form the bound state (Mu^+) via a transition state (delayed by lattice relaxation), and

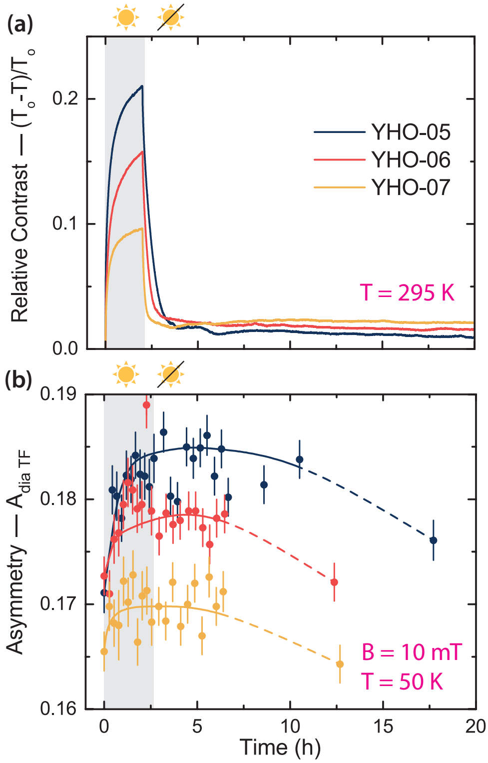

Figure 2.9: (a) The relative optical contrast with time for the $YH_{3-2x}O_x$ films under illumination of a 385 nm LED for 2 h at room temperature. The grey area indicates when the LED was on and inducing photo-darkening. (b) TF asymmetry ($A_{TF,dia}$) from *in situ* illumination by a 365 nm LED for ~2 h at 50 K. Between the last two points in every line, the temperature was increased incrementally to 300 K and then back down to 50 K to promote complete thermal bleaching (Fig. 2.E.1).

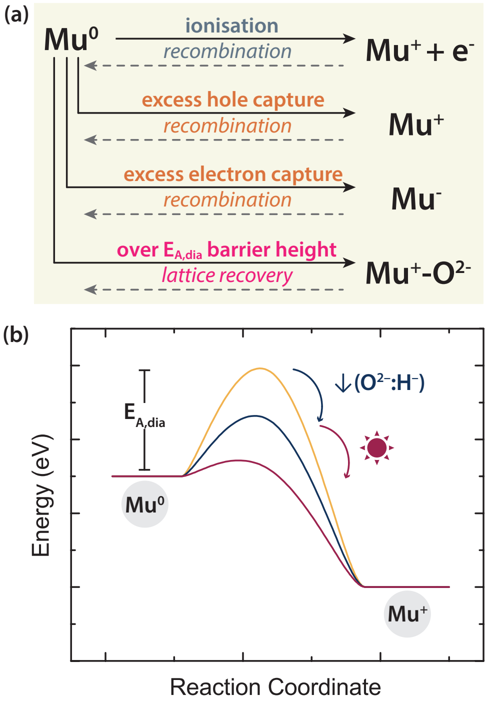

Figure 2.10: (a) Reactions showing the possible routes Mu^0 may take to form a diamagnetic species (Mu$^+$ or Mu$^-$) under illumination. Reverse arrows indicate the return to the original Mu^0 state once illumination is stopped. (b) Schematic representation of $E_{A,dia}$, an energy barrier involved in the transition state model. $E_{A,dia}$ decreased for more H-rich samples, and further decreased by *in situ* illumination. λ_{TF}, and thus $E_{A,\lambda}$, was unaffected by illumination (Fig. 2.D.1). Image inspired by Ref. [17].

(3) interstitial Mu^0 which account for the “missing fraction" of the asymmetry. The latter two may be converted to a diamagnetic state by photo-induced ionisation [66, 67]. The incident light energy was larger than the band gap, E_g, thus, sufficient to ionise in-gap states created by Mu^0 [60]. However, this is an unlikely mechanism because we expect the recovery of the Mu^0 state after light is ceased to be faster than what is shown in our results. Here the asymmetry remained elevated for several hours. So, this process cannot be treated as the main reason for the $A_{TF,dia}$ increase upon illumination.

Generally, we assume that light exposure results in charge carrier generation. Since the energy of the photo-darkening LED must be larger than E_g to induce photochromism, the first step in the mechanism is the formation of electron-hole pairs. Carrier generation can lead to a decrease of the initial Mu^0 population after thermalisation and a lower Mu^0 formation probability due to electron shielding. However, this would typically require a very high carrier density (>10^{18} cm^{-3}) [24, 68] which is likely not attained here under illumination [7–9, 53].

Photo-generated carriers can also be captured by Mu^0 to form diamagnetic Mu$^+$ or Mu$^-$ (Fig. 2.10a). However, there must again be a sufficient number of charge carriers available (>10^{17} cm^{-3}) [24, 68] such that Mu^0 formation and charge carrier capture occur very rapidly (within nanoseconds) and result in a larger diamagnetic fraction. Further, the relaxation of $A_{TF,dia}$ back to its original value is slower than expected for charge carrier recombination [69], suggesting that this is not the reason for the observed reversible increase in $A_{TF,dia}$.

In fact, the photochromic mechanism likely consists of many more reaction steps following photo-generation of carriers. For example, in Cu-doped Ag-halide glasses, electron-hole pair generation is followed by trapping, with h^+ oxidising copper ($Cu^+ \rightarrow Cu^{2+}$) and e^- reducing silver ($Ag^+ \rightarrow Ag^0$), eventually forming light-absorbing Ag^0-clusters [10, 11]. Trapping of the carriers leads to a prolonged darkened state and a bleaching process which is not instantaneous. Therefore, the aforementioned processes (shown in Fig. 2.10a) are not the main contributors to the increased $A_{TF,dia}$. Rather, the photo-generated carriers may be trapped at a defect, ion, or atom and the formation of a light-absorbing species affects the muon behaviour.

Similar to Cu-doped Ag-halide glasses, a number of papers attribute the photochromic effect in $REH_{3-2x}O_x$ thin-films to the formation of metallic clusters (discussed more in section IV.A.1) due to the increased electronic conductivity and decreased optical transparency of the darkened state [9]. If metallic ($n > 10^{21}$ cm^{-3}) clusters are formed and are large enough ($\geq$1 nm) to create sufficient static shielding of the implanted muon (Mu^+), this can prevent some Mu^0 formation, resulting in a higher diamagnetic fraction upon illumination. The increases we see in $A_{TF,dia}$ (2.9b) from the transparent (t = 0 h) to the photo-darkened state (t ~2 h) (YHO-05: ~8%, YHO-06: ~5%, YHO-07: ~3%) would imply that the volume fraction of a metallic phase decreases with increasing O^{2-} content, consistent with the observed decrease in photochromic contrast (2.9a).

However, a volume fraction of ~6% of formed metallic clusters (from Ref. [70]) is hard to reconcile with the large reduction in the Mu^0 fraction observed between the transparent and photo-darkened states. This volume fraction would only account for ~30-40% of the observed reduction in Mu^0 fraction. Further, the temperature-dependent recovery of $A_{TF,dia}$ (Fig. 2.E.1) is difficult to explain simply by metallic phase formation as we expect similar recovery temperatures for all three films, which did not happen. The most notable difference is between YHO-05 and YHO-07 which return to their original $A_{TF,dia}$ at ~260 K and ~100 K, respectively (Fig. 2.E.1a-c), showing that the light-induced changes in asymmetry are not a pure volume fraction effect. Instead, it appears that each $YH_{3-2x}O_x$ follows a different energy barrier height for bleaching to the transparent state.

Thus, although metallic cluster formation may be partially responsible for the increased $A_{TF,dia}$, we propose that the main phenomenon driving this reversible behaviour is related to the transition state model (Sec III.B.1). Within this model, $A_{TF,dia}$ depends on the energy barrier $E_{A,dia}$, which is associated with the local lattice structure and the activation energy of lattice relaxation. An increase in $A_{TF,dia}$ suggests a decrease in $E_{A,dia}$ during illumination, leading to a higher formation probability of the bound Mu^+-O^{2-} state as more muons can surmount this lower energy barrier (Fig. 2.10b). This can happen as a result of a local lattice change which facilitates the Mu^0 site change or causes the interstitial Mu^0 state to become less stable. Interestingly, the reversible increase in $A_{TF,dia}$ shows the same trend as a function of p_{dep} as the photochromic contrast and $E_{A,dia}$, supporting the connection between the transition state model, photochromism, and the importance of structural properties in the photochromic effect.

Along these lines, we conclude that a reversible change in the interstitial sublattice occurs during illumination, after which, some light-absorbing species is formed (e.g. metallic clusters). The lattice change depends on factors such as the O^{2-}:H^- ratio, amount and distribution of anion vacancies, ease of lattice distortion, and other structural properties. Eventually, oxyhydrides with lower H^- content (and lower photochromic contrast) may have smaller volume fractions of these metallic phases. Although this conclusion is possible, other theories are discussed below to suggest alternative steps after the light-induced local lattice changes (e.g. local lattice relaxations, octahedral site occupancy changes).

2.4 Discussion

2.4.1 Implications on the Photochromic Effect

When exposed to UV light, photochromic $YH_{3-2x}O_x$ thin-films exhibit a reversible and p_{dep}-dependent optical response. Remarkably, we observe a correlated (reversible) increase in the diamagnetic asymmetry of the muon during illumination. This suggests that the energy barrier for lattice relaxation, $E_{A,dia}$, is lowered by exposure to UV light, shown schematically in Figure 2.10b. To understand this change in $E_{A,dia}$ in terms of the structural properties of $YH_{3-2x}O_x$, we will discuss the various mechanisms proposed for the photochromic effect.

The first step of the photochromic mechanism in $REH_{3-2x}O_x$ is the formation of electron-hole pairs since the energy of the incident light must be larger than the E_g to induce photo-darkening. The subsequent steps and the identity of the light-absorbing species are debated. Several ideas have been proposed and are summarised below, discussed in the context of our μ^+SR results.

Formation of metallic centres by O^{2-} or H^- diffusion

In analogy to Cu-doped Ag-halide glasses [10, 11, 13, 64], several reports have suggested that the photochromic effect in $REH_{3-2x}O_x$ is due to metallic cluster formation. Ellipsometry studies on $YH_{3-2x}O_x$ thin-films, for example, suggested the formation of metallic clusters (volume fraction ~6%) in a semiconducting matrix, stating that even 2% of such clusters would result in a decrease in transparency of ~30% [70, 71]. We explained also in section III.C. that metallic cluster formation (which follows from changes in the interstitial sublattice) may explain up to ~30% of our observed changes in $A_{TF,dia}$.

However, Baba et al. [72] proposed that such metallic phases are formed due to O^{2-} diffusion, causing a reversible lattice contraction and formation of a highly oxidised thin-film surface. Such O^{2-} diffusion is hard to reconcile with the results of our study. We observed photochromism at temperatures as low as 50 K, where O^{2-} ions are usually immobile, even in O^{2-} conducting oxides [73]. Also, mobility in oxyhydrides is generally seen to involve only H^-, with O^{2-} being regarded as stationary [7, 8, 63, 74, 75]. Likewise, we find that O^{2-} behaves as a hard-shell atom, compared to the polarisable H^- ion, making O^{2-} diffusion difficult.

Alternatively, metallic centres can be formed by H^-, rather than O^{2-}, mobility. H^- has been reported as mobile in metals [76], hydrides (see above), and oxyhydrides [7, 63]. As well, an NMR study showed that a fraction of mobile H^- disappear or become stationary upon illumination [12].

We note that, prior to illumination, we did not observe H^- mobility in the oxyhydrides (Fig. 2.2b, trend of $\lambda_{TF}(T)$), contrary to this room temperature NMR study [12]. However, this apparent discrepancy may be due to the time scale of a μ^+SR experiment, since mobility should occur within the muon lifetime (2.2 μs), while NMR is sensitive to slower dynamics. So, H^- mobility in these materials may be slow with respect to the muon lifetime, making μ^+SR insensitive to this under our experimental conditions. Slow H^- dynamics could potentially explain the prolonged darkened state and bleaching kinetics [3, 4, 6], where H^- diffusion may act as the rate-limiting step for the formation/dissolution of metallic domains.

Alternatively, a DFT study predicted a mobility bottleneck for $REH_{3-2x}O_x$ containing certain cations [8], with our photochromic materials falling in the ion-insulating regime [3, 4, 6]. This implies that long-range H^- diffusion could be hampered in our photochromic materials, and may be unrelated to the underlying mechanism. Short-range mobility, though, may still play a role.

Hydroxide Formation

Another possibility is the formation of hydroxides (H^+-O^{2-}) upon illumination, as observed in mayenite ($12CaO_3{\cdot}7Al_2O_3$) [77–80]. In this oxide, UV light exposure causes a reaction where H^- ions are converted into hydroxides and release electrons, improving the conductivity and the optical absorption of the originally insulating oxide. This reaction is reversible and influenced by temperature.

As it appears to match some of our observations, the formation of a hydroxide species in our materials seems worthy of future investigation (e.g. IR spectroscopy). The proposed hydroxide may be analogous to the bound Mu^+-O^{2-} configuration, where Mu^+ mimics H^+. This suggests that hydroxide formation may be possible in our materials, assuming the muon behaves similarly to hydrogen which is not always the case [56].

However, a recent DFT study reported that, at room temperature, the hydroxide is unstable in YH_xO_y and tends to dissociate quickly, prompting the authors to exclude this mechanism [81]. More detailed studies of this reaction could be useful for determining the stability of the hydroxide species and its role in photochromism. In particular, the initial charge state of hydrogen can be important since, in our transition state model, Mu^0 is an analogue of atomic hydrogen, H^0, not H^-. It is possible that during illumination H^0 is formed at the Oc (octahedral) sites of $YH_{3-2x}O_x$ and acts as a mobile fraction, able to form a hydroxide. Such details may be investigated by NMR.

Colour Centres

The most important structural characteristics of our oxyhydrides are the vacancy concentration, vacancy type, and possibly the deformability of the lattice. In general, we expect that the presence of fewer Oc vacancies (as occurs in more H-rich $YH_{3-2x}O_x$) and a more deformable lattice lead to the lowering of $E_{A,dia}$ by either lowering the stability of the interstitial Mu^0 state or allowing for easier lattice relaxation. Since this energy barrier decreases further during illumination, some of these structural properties changed, such as the number of available Oc vacancies. This begs the question: what is occupying these vacancies during illumination?

One explanation is that colour centres have formed. These were reported in other photochromic materials [10, 82] and rare-earth compounds are known to form colour centres in some situations [65, 83]. The most basic types are known as F centres, where one electron is captured in a cation vacancy (F^+) or two electrons are trapped in an anion vacancy (F^-) [10, 83].

The presence of a paramagnetic electron (F^+) could lead to very fast depolarisation of a nearby muon due to its hyperfine coupling with the muon. This would result in a higher $\lambda_{dia,TF}$ upon illumination, contrary to our observations. Therefore, it is unlikely that an F^+-type centre is responsible for the photochromic effect here.

However, the capture of two electrons by an Oc vacancy (F^-) might not impact the muon depolarisation rate because these electrons would be paired. Also, there would be fewer Oc vacancies available, which seems to promote the Mu^+-O^{2-} configuration by lowering $E_{A,dia}$ and increasing $A_{dia,TF}$. Although this appears to agree with our *in situ* μ^+SR results, a $Y^{3+}(F^-)$ centre absorbs specific wavelengths [83], and may not necessarily lead to the broad absorption range seen in $REH_{3-2x}O_x$.

It should be noted, that many other types of colour centres are possible, and future EPR measurements may help to elucidate this.

Dihydrogen Formation

A recent computational paper suggested that the photochromic mechanism involves formation and dissolution of a “dihydrogen species", similar to a hydrogen molecule, H_2 [81]. This molecule forms between two adjacent H^- ions in an octahedral vacancy and creates a shallow donor level close to the conduction band edge. The activation energy for formation, and especially for dissolution, appears to be related to the O^{2-}:H^- ratio. The authors [81] show that dissociation of the molecule has the lowest energy barrier in O-rich compounds, which may explain the faster bleaching kinetics which they also observe. This theory is interesting because it does not require long-range structural rearrangements, with “dihydrogen" formation on a very local scale.

The formation of a “dihydrogen species" in the Oc sites of the lattice could potentially impact the muon behaviour. The stability of interstitial Mu^0 in an Oc site could change due to the formation of a new molecule in the same octahedron, although the concentration of this dihydrogen species needs to be very large to have a noticeable optical effect. We note that the formation of a hydrogen muonium molecule (as an analogue of H_2) by binding of the interstitial Mu^0 to hydrogen is not expected, in view of its large thermodynamic instability compared to the formation of a H_2 molecule [84].

However, it is important to note that Chai et al. [81] consider a defect concentration of O^{2-} in what is essentially a YH_3 lattice. In their DFT calculations, the highest O:Y ratio is 0.25. This is significantly lower than the lower boundary we expect for our photochromic thin-films (O:Y = 0.5-1.0) [5, 6, 59]. We believe that the formation of H_2 upon illumination requires a more in-depth experimental analysis (e.g. Raman spectroscopy).

2.5 Conclusion

Photochromic rare-earth metal oxyhydrides darken reversibly over a broad range of wavelengths when exposed to UV light. Based on μ^+SR data, and the electronic and structural properties of our materials, we proposed models to describe the muon behaviour in $YH_{3-2x}O_x$ thin-films with different O^{2-}:H^- ratio, compared to metallic $YH_{2-\delta}$ which serves as a reference compound.

Briefly, $YH_{2-\delta}$ shows a H-μ complex, which competes with the onset of Mu^+/H^- mobility above 150 K. The oxyhydrides, though, are better described by a transition state model, where a transition between interstitial Mu^0 and bound Mu^+-O^{2-} occurs, dependent on the activation energy for lattice relaxation, $E_{A,dia}$. This barrier decreases with reduced O^{2-}:H^- ratio, and is influenced by structural factors such as the concentration and types of available anion vacancies, and the deformability of the lattice. We also observed polaron formation at the Y-cation together with the formation of the bound state.

Upon illumination of the $YH_{3-2x}O_x$ thin-films, we observe reversible changes in the diamagnetic asymmetry of the muon related to the transition state model and correlated to the photo-darkening. Assuming the muon mimics hydrogen, one option to explain these changes is the formation of a hydroxide during photo-darkening, possibly from H^0, although a previous DFT study suggested that the hydroxide is unstable at room temperature. Another option is that changes occur in the interstitial sublattice during illumination which lower the energy barrier for muon site changes, thereby increasing the diamagnetic muon fraction. Particularly, there may be fewer available octahedral vacancies in the darkened state which could be populated by electrons (colour centres), a dihydrogen species, or H^- ions slowly moving between sites. Additional measurements are needed to understand the full reaction scheme for the photochromic effect in these materials.

References

[1] D. Chaykina, T. W. H. de Krom, G. Colombi, H. Schreuders, a. Suter, T. Prokscha, B. Dam, and S. W. H. Eijt, *Structural properties and anion dynamics of yttrium dihydride and photochromic oxyhydride thin-films examined by in situ* μ^+*SR,* Physical Review B **103**, 224106 (2021).

[2] H. Kageyama, K. Hayashi, K. Maeda, J. P. Attfield, Z. Hiroi, J. M. Rondinelli, and K. R. Poeppelmeier, *Expanding frontiers in materials chemistry and physics with multiple anions,* Nature Communications **9**, 772 (2018).

[3] F. Nafezarefi, H. Schreuders, B. Dam, and S. Cornelius, *Photochromism of rare-earth metal-oxy-hydrides,* Applied Physics Letters **111**, 103903 (2017).

[4] F. Nafezarefi, S. Cornelius, J. Nijskens, H. Schreuders, and B. Dam, *Effect of the addition of zirconium on the photochromic properties of yttrium oxy-hydride,* Solar Energy Materials and Solar Cells **200**, 109923 (2019).

[5] S. Cornelius, G. Colombi, F. Nafezarefi, H. Schreuders, R. Heller, F. Munnik, and B. Dam, *Oxyhydride nature of rare-earth-based photochromic thin films,* The Journal of Physical Chemistry Letters **10**, 1342 (2019).

[6] G. Colombi, T. De Krom, D. Chaykina, S. Cornelius, S. W. H. Eijt, and B. Dam, *Influence of cation (RE = Sc, Y, Gd) and O/H anion ratio on the photochromic properties of* REO_xH_{3-2x} *thin films,* ACS Photonics **8**, 709 (2021).

[7] K. Fukui, S. Iimura, T. Tada, S. Fujitsu, M. Sasase, H. Tamatsukuri, T. Honda, K. Ikeda, T. Otomo, and H. Hosono, *Characteristic fast* H^- *ion conduction in oxygen-substituted lanthanum hydride,* Nature Communications **10**, 2578 (2019).

[8] H. Ubukata, T. Broux, F. Takeiri, K. Shitara, H. Yamashita, A. Kuwabara, G. Kobayashi, and H. Kageyama, *Hydride conductivity in an anion-ordered fluorite structure LnHO with an enlarged bottleneck,* Chemistry of Materials **31**, 7360 (2019).

[9] T. Mongstad, C. Platzer-Björkman, J. P. Maehlen, L. P. A. Mooij, Y. Pivak, B. Dam, E. S. Marstein, B. C. Hauback, and S. Z. Karazhanov, *A new thin film photochromic material: Oxygen-containing yttrium hydride,* Solar Energy Materials and Solar Cells **95**, 3596 (2011).

[10] R. Araujo, *Inorganic photochromic systems,* Molecular Crystals and Liquid Crystals Science and Technology. Section A. Molecular Crystals and Liquid Crystals **297**, 1 (2006).

[11] D. Caurant, D. Gourier, D. Vivien, and M. Prassas, *Bleaching mechanism of silver halide photochromic glasses,* Journal of Applied Physics **73**, 1657 (1993).

[12] C. V. Chandran, H. Schreuders, B. Dam, J. W. G. Janssen, J. Bart, A. P. M. Kentgens, and P. J. M. van Bentum, *Solid-state NMR studies of the photochromic effects of thin films of oxygen-containing yttrium hydride,* The Journal of Physical Chemistry C **118**, 22935 (2014).

[13] S. K. Deb and L. J. Forrestal, *Photochromism: Chapter 7 Photochromism in Inorganic Systems*, edited by G. H. Brown, Techniques of Chemistry, Vol. 3 (Wiley-Interscience, 1971) pp. 633–665.

[14] M. Månsson and J. Sugiyama, *Muon-spin relaxation study on Li- and Na-diffusion in solids,* Physica Scripta **88**, 068509 (2013).

[15] J. Sugiyama, I. Umegaki, M. Matsumoto, K. Miwa, H. Nozaki, Y. Higuchi, T. Noritake, O. K. Forslund, M. Månsson, S. P. Cottrell, A. Koda, E. J. Ansaldo, and J. H. Brewer, *Desorption reaction in* MgH_2 *studied with* in-situ μ^+SR*,* Sustainable Energy & Fuels **3**, 956 (2019).

[16] T. U. Ito, A. Koda, K. Shimomura, W. Higemoto, T. Matsuzaki, Y. Kobayashi, and H. Kageyama, *Excited configurations of hydrogen in the* $BaTiO_{3-x}H_x$ *perovskite lattice associated with hydrogen exchange and transport,* Physical Review B **95**, 020301(R) (2017).

[17] R. C. Vilão, R. B. L. Vieira, H. V. Alberto, J. M. Gil, and A. Weidinger, *Role of the transition state in muon implantation,* Physical Review B **96**, 195205 (2017).

[18] J. N. Huiberts, R. Griessen, J. H. Rector, R. J. Wijngaarden, J. P. Dekker, D. G. de Groot, and N. J. Koeman, *Yttrium and lanthanum hydride films with switchable optical properties,* Nature **380**, 231 (1996).

[19] T. Prokscha, E. Morenzoni, K. Deiters, F. Foroughi, D. George, R. Kobler, A. Suter, and V. Vrankovic, *The new beam at PSI: A hybrid-type large acceptance channel for the generation of a high intensity surface-muon beam,* Nuclear Instruments and Methods in Physics Research Section A: Accelerators, Spectrometers, Detectors and Associated Equipment **595**, 317 (2008).

[20] E. Morenzoni, H. Gluckler, T. Prokscha, R. Khasanov, H. Luetkens, M. Birke, E. M. Forgan, C. Niedermayer, and M. Pleines, *Implantation studies of keV positive muons in thin metallic layers,* Nuclear Instruments & Methods in Physics Research Section B-Beam Interactions with Materials and Atoms **192**, 254 (2002).

[21] W. Eckstein, *Computer Simulation of Ion-Solid Interactions*, 1st ed., Springer Series in Materials Science (Springer-Verlag Berlin Heidelberg, 1991).

[22] A. Yaouanc and P. D. de Réotier, *Muon Spin Rotation, Relaxation, and Resonance: Applications to Condensed Matter*, International Series of Monographs on Physics (Oxford University Press, 2011).

[23] S. J. Blundell, *Muon-spin rotation studies of electronic properties of molecular conductors and superconductors,* Chemical Reviews **104**, 5717 (2004).

[24] B. D. Patterson, *Muonium states in semiconductors,* Reviews of Modern Physics **60**, 69 (1988).

[25] V. G. Storchak, O. E. Parfenov, J. H. Brewer, P. L. Russo, S. L. Stubbs, R. L. Lichti, D. G. Eshchenko, E. Morenzoni, V. P. Zlomanov, A. A. Vinokurov, and V. G. Bamburov, *Novel muonium centers—magnetic polarons—in magnetic semiconductors,* Physica B: Condensed Matter **404**, 899 (2009).

[26] V. Storchak, S. F. J. Cox, S. P. Cottrell, J. H. Brewer, G. D. Morris, D. J. Arseneau, and B. Hitti, *Muonium formation via electron transport in silicon,* Physical Review Letters **78**, 2835 (1997).

[27] D. C. Walker, *Muonium - a light isotope of hydrogen,* The Journal of Physical Chemistry **85**, 3960 (1981).

[28] W. J. Kossler, H. E. Schone, J. R. Kempton, B. Hitti, C. E. Stronach, G. A. Styles, and E. F. W. Seymour, *A comparative muon spin relaxation (μSR) study of titanium and yttrium dihydrides,* Journal of Less-Common Metals **129**, 327 (1987).

[29] J. Sugiyama, *Spin polarized beam for battery materials research:* $\mu^{\pm}$*SR and* β*-NMR,* Hyperfine Interactions **240**, 17 (2019).

[30] L. M. Cameron and C. A. Sholl, *Transverse field depolarization rates for muons in metals,* Journal of the Less-Common Metals **172-174**, 762 (1991).

[31] O. Hartmann, S. W. Harris, R. Wappling, and R. Hempelmann, *Challenging muon diffusion studies in f.c.c. metals,* Physica Scripta **45**, 402 (1992).

[32] H. V. Alberto, R. C. Vilão, J. M. Gil, J. P. Duarte, R. B. L. Vieira, A. Weidinger, J. P. Leitão, A. F. d. Cunha, M. G. Sousa, J. P. Teixeira, P. A. Fernandes, P. M. P. Salomé, K. Timmo, M. Loorits, A. Amato, H. Luetkens, T. Prokscha, A. Suter, and Z. Salman, *Muonium states in* Cu_2ZnSnS_4 *solar cell material,* Journal of Physics: Conference Series **551**, 012045 (2014).

[33] I. McKenzie, Z. Salman, S. R. Giblin, Y. Y. Han, G. W. Leach, E. Morenzoni, T. Prokscha, and A. Suter, *Polymer dynamics near the surface and in the bulk of poly(tetrafluoroethylene) probed by zero-field muon-spin-relaxation spectroscopy,* Physical Review E: Statistical, Nonlinear, Soft Matter Physics **89**, 022605 (2014).

[34] T. Lancaster, S. J. Blundell, P. J. Baker, M. L. Brooks, W. Hayes, F. L. Pratt, J. L. Manson, M. M. Conner, and J. A. Schlueter, *Muon-fluorine entangled states in molecular magnets,* Physical Review Letters **99**, 267601 (2007).

[35] J. H. Brewer, S. R. Kreitzman, D. R. Noakes, E. J. Ansaldo, D. R. Harshman, and R. Keitel, *Observation of muon-fluorine "hydrogen bonding" in ionic crystals,* Phys Rev B Condens Matter **33**, 7813 (1986).

[36] J. N. Huiberts, R. Griessen, R. J. Wijngaarden, M. Kremers, and C. Van Haesendonck, *Logarithmic divergence of the electrical resistivity in the metal hydride* $YH_{3-\delta}$*,* Physical Review Letters **79**, 3724 (1997).

[37] P. Ngene, T. Radeva, M. Slaman, R. J. Westerwaal, H. Schreuders, and B. Dam, *Seeing hydrogen in colors: Low-cost and highly sensitive eye readable hydrogen detectors,* Advanced Functional Materials **24**, 2374 (2014).

[38] P. Ngene, T. Radeva, R. Westerwaal, H. Schreuders, and B. Dam, *Eye readable metal hydride based hydrogen tape sensor for health applications,* Proc. of SPIE **9202**, 920203 (2014).

[39] D. Khatamian and F. D. Manchester, *The H-Y (hydrogen-yttrium) system,* Bulletin of Alloy Phase Diagrams **9**, 252 (1988).

[40] G. Majer, J. Gottwald, D. T. Peterson, and R. G. Barnes, *Model-independent measurements of hydrogen diffusivity in the yttrium dihydrides,* Journal of Alloys and Compounds **330-332**, 438 (2002).

[41] M. Di Vece and J. J. Kelly, *Electrochemical study of hydrogen diffusion in yttrium hydride switchable mirrors,* Journal of Alloys and Compounds **356-357**, 156 (2003).

[42] R. Goc, O. J. Zogal, A. H. Vuorimaki, and E. E. Ylinen, *Van Vleck second moments and hydrogen diffusion in* $YH_{2.1}$*−measurements and simulations,* Solid State Nuclear Magnetic Resonance **25**, 133 (2004).

[43] J. N. Daou and P. Vajda, *Hydrogen ordering and metal-semiconductor transitions in the system* $YH_{2\pm\delta}$*,* Physical Review B **45**, 10907 (1992).

[44] J. Sugiyama, O. K. Forslund, E. Nocerino, N. Matsubara, K. Papadopoulos, Y. Sassa, S. P. Cottrell, A. D. Hillier, K. Ishida, M. Månsson, and J. H. Brewer, *Lithium diffusion in* $LiMnPO_4$ *detected with* $\mu^{\pm}SR$*,* Physical Review Research **2**, 033161 (2020).

[45] T. R. Adams, R. L. Lichti, and T. L. Gibson, *Electric-field gradient at oxygen sites in RCBO: Effects from a positive muon,* Hyperfine Interactions **86**, 561 (1994).

[46] J. Sugiyama, K. Mukai, Y. Ikedo, H. Nozaki, M. Mansson, and I. Watanabe, *Li diffusion in* Li_xCoO_2 *probed by muon-spin spectroscopy,* Physical Review Letters **103**, 147601 (2009).

[47] M. Hiraishi, K. M. Kojima, H. Okabe, S. Takeshita, A. Koda, R. Kadono, R. Khasanov, S. Iimura, S. Matsuishi, and H. Hosono, *Magnetism driven by strong electronic correlations in the heavily carrier-doped iron oxypnictide* $LaFeAsO_{0.49}H_{0.51}$*,* Physical Review B **101**, 174414 (2020).

[48] P. Dalmas de Réotier and A. Yaouanc, *Muon spin rotation and relaxation in magnetic materials,* Journal of Physics: Condensed Matter **9**, 9113–9166 (1997).

[49] T. Prokscha, H. Luetkens, E. Morenzoni, G. J. Nieuwenhuys, A. Suter, M. Dobeli, M. Horisberger, and E. Pomjakushina, *Depth dependence of the ionization energy of shallow hydrogen states in ZnO and CdS,* Physical Review B **90**, 235303 (2014).

[50] T. U. Ito, W. Higemoto, T. D. Matsuda, A. Koda, and K. Shimomura, *Shallow donor level associated with hydrogen impurities in undoped* $BaTiO_3$*,* Applied Physics Letters **103**, 042905 (2013).

[51] R. C. Vilão, J. M. Gil, A. Weidinger, H. V. Alberto, J. Piroto Duarte, N. Ayres de Campos, R. L. Lichti, K. H. Chow, S. P. Cottrell, and S. F. J. Cox, *Acceptor level of interstitial muonium in ZnSe and ZnS,* Physical Review B **77**, 235212 (2008).

[52] V. G. Storchak, D. G. Eshchenko, J. H. Brewer, S. P. Cottrell, and R. L. Lichti, *Muonium in InSb: Shallow acceptor versus deep trap or recombination center,* Physical Review B **73**, 081203(R) (2006).

[53] A. Miniotas, B. Hjörvarsson, L. Douysset, and P. Nostell, *Gigantic resistivity and band gap changes in* GdO_yH_x *thin films,* Applied Physics Letters **76**, 2056 (2000).

[54] R. C. Vilão, R. B. L. Vieira, H. V. Alberto, J. M. Gil, A. Weidinger, R. L. Lichti, P. W. Mengyan, B. B. Baker, and J. S. Lord, *Barrier model in muon implantation and application to* Lu_2O_3*,* Physical Review B **98**, 115201 (2018).

[55] R. C. Vilão, R. B. L. Vieira, H. V. Alberto, J. M. Gil, A. Weidinger, R. L. Lichti, B. B. Baker, P. W. Mengyan, and J. S. Lord, *Muonium donor in rutile* TiO_2 *and comparison with hydrogen,* Physical Review B **92**, 081202(R) (2015).

[56] R. B. L. Vieira, R. C. Vilão, A. G. Marinopoulos, P. M. Gordo, J. A. Paixão, H. V. Alberto, J. M. Gil, A. Weidinger, R. L. Lichti, B. Baker, P. W. Mengyan, and J. S. Lord, *Isolated hydrogen configurations in zirconia as seen by muon spin spectroscopy and* ab initio *calculations,* Physical Review B **94**, 115207 (2016).

[57] A. Rabis, T. Prokscha, E. Fabbri, Z. Salman, T. Schmidt, and A. Suter, *Investigation of hydrogen-like muonium states in Nb-Doped* SnO_2 *Films,* JPS Conf. Proc. **21**, 011033 (2018).

[58] H. V. Alberto, R. C. Vilão, R. B. L. Vieira, J. M. Gil, A. Weidinger, M. G. Sousa, J. P. Teixeira, A. F. da Cunha, J. P. Leitão, P. M. P. Salomé, P. A. Fernandes, T. Törndahl, T. Prokscha, A. Suter, and Z. Salman, *Slow-muon study of quaternary solar-cell materials: Single layers and p-n junctions,* Physical Review Materials **2**, 025402 (2018).

[59] G. Colombi, S. Cornelius, A. Longo, and B. Dam, *Structure model for anion-disordered photochromic Gd oxyhydride thin films,* The Journal of Physical Chemistry C **124**, 13541 (2020).

[60] E. L. Silva, A. G. Marinopoulos, R. C. Vilao, R. B. L. Vieira, H. V. Alberto, J. Piroto Duarte, and J. M. Gil, *Hydrogen impurity in yttria:* Ab initio *and μSR perspectives,* Physical Review B **85**, 165211 (2012).

[61] E. L. da Silva, A. G. Marinopoulos, R. B. L. Vieira, R. C. Vilão, H. V. Alberto, J. M. Gil, R. L. Lichti, P. W. Mengyan, and B. B. Baker, *Electronic structure of interstitial hydrogen in lutetium oxide from DFT+U calculations and comparison study with μSR spectroscopy,* Physical Review B **94**, 014104 (2016).

[62] N. B. Mikheev and I. A. Rumer, *Stabilization of the divalent state for the lanthanides and actinides in solutions, melts and clusters,* Radiochimica Acta **85**, 49 (1999).

[63] G. Kobayashi, Y. Hinuma, S. Matsuoka, A. Watanabe, M. Iqbal, M. Hirayama, M. Yonemura, T. Kamiyama, I. Tanaka, and R. Kanno, *Pure H^- conduction in oxyhydrides,* Science **351**, 1314 (2016).

[64] S. D. Cohen and G. A. Newman, *Inorganic photochromism,* The Journal of Photographic Science **15**, 290 (1967).

[65] D. L. Staebler and S. E. Schnatterly, *Optical studies of a photochromic color center in rare-earth-doped CaF_2,* Physical Review B **3**, 516 (1971).

[66] K. Yokoyama, P. Murahari, P. Heathcote, L. Nuccio, J. S. Lord, N. A. Morley, and A. J. Drew, *Future directions of μSR—laser excitation,* Physica Scripta **88**, 068511 (2013).

[67] K. Shimomura, P. Bakule, F. L. Pratt, K. Ishida, K. Ohishi, I. Watanabe, Y. Matsuda, K. Nagamine, E. Torikai, and K. Nishiyama, *Photo detachment of negatively charged muonium in GaAs by laser irradiation,* Physics Procedia **30**, 224 (2012).

[68] T. Prokscha, K. H. Chow, Z. Salman, E. Stilp, and A. Suter, *Direct observation of hole carrier-density profiles and their light-induced manipulation at the surface of Ge,* Physical Review Applied **14**, 014098 (2020).

[69] T. Prokscha, K. H. Chow, E. Stilp, A. Suter, H. Luetkens, E. Morenzoni, G. J. Nieuwenhuys, Z. Salman, and R. Scheuermann, *Photo-induced persistent inversion of germanium in a 200-nm-deep surface region,* Scientific Reports **3**, 2569 (2013).

[70] J. Montero, F. A. Martinsen, M. García-Tecedor, S. Z. Karazhanov, D. Maestre, B. Hauback, and E. S. Marstein, *Photochromic mechanism in oxygen-containing yttrium hydride thin films: An optical perspective,* Physical Review B **95**, 201301(R) (2017).

[71] J. Montero and S. Z. Karazhanov, *Spectroscopic ellipsometry and microstructure characterization of photochromic oxygen-containing yttrium hydride thin films,* physica status solidi (a) **215**, 1701039 (2018).

[72] E. M. Baba, J. Montero, E. Strugovshchikov, E. Ö. Zayim, and S. Karazhanov, *Light-induced breathing in photochromic yttrium oxyhydrides,* Physical Review Materials **4**, 025201 (2020).

[73] B. Singh, S. Ghosh, S. Aich, and B. Roy, *Low temperature solid oxide electrolytes (LT-SOE): A review,* Journal of Power Sources **339**, 103 (2017).

[74] X. Liu, T. S. Bjørheim, and R. Haugsrud, *Formation of defects and their effects on hydride ion transport properties in a series of K_2NiF_4-type oxyhydrides,* Journal of Materials Chemistry A **6**, 1454 (2018).

[75] O. S. Fjellvåg, J. Armstrong, P. Vajeeston, and A. O. Sjåstad, *New insights into hydride bonding, dynamics, and migration in La_2LiHO_3 oxyhydride,* The Journal of Physical Chemistry Letters **9**, 353 (2018).

[76] F. J. A. den Broeder, S. J. van der Molen, M. Kremers, J. N. Huiberts, D. G. Nagengast, A. T. M. van Gogh, W. H. Huisman, N. J. Koeman, N. I. Koeman, B. Dam, J. H. Rector, S. Plota, M. Haaksma, R. M. N. Hanzen, R. M. Jungblut, P. A. Duine, and R. Griessen, *Visualization of hydrogen migration in solids using switchable mirrors,* Nature **394**, 656 (1998).

[77] K. Hayashi, S. Matsuishi, T. Kamiya, M. Hirano, and H. Hosono, *Light-induced conversion of an insulating refractory oxide into a persistent electronic conductor,* Nature **419**, 462 (2002).

[78] K. Hayashi, *Kinetics of electron decay in hydride ion-doped mayenite,* The Journal of Physical Chemistry C **115**, 11003 (2011).

[79] K. Hayashi, P. V. Sushko, Y. Hashimoto, A. L. Shluger, and H. Hosono, *Hydride ions in oxide hosts hidden by hydroxide ions,* Nature Communications **5**, 3515 (2014).

[80] K. Hayashi and H. Hosono, *Green apatites: hydride ions, electrons and their interconversion in the crystallographic channel,* Phys Chem Chem Phys **18**, 8186 (2016).

[81] J. Chai, Z. Shao, H. Wang, C. Ming, W. Oh, T. Ye, Y. Zhang, X. Cao, P. Jin, S. Zhang, and Y.-Y. Sun, *Ultrafast processes in photochromic material YH_xO_y studied by excited-state density functional theory simulation,* Science China Materials **63**, 1579 (2020).

[82] T. He and J. Yao, *Photochromism of molybdenum oxide,* Journal of Photochemistry and Photobiology C: Photochemistry Reviews **4**, 125 (2003).

[83] H. Bill and G. Calas, *Color centers, associated rare-earth ions and the origin of coloration in natural fluorites,* Phys. Chem. Minerals **3**, 117 (1978).

[84] J. Tennyson and S. Miller, *Fractionation effects in muonium–molecular hydrogen reactions,* The Journal of Chemical Physics **90**, 2524 (1989).

Appendix

2.A Optical transmission and band gap energies

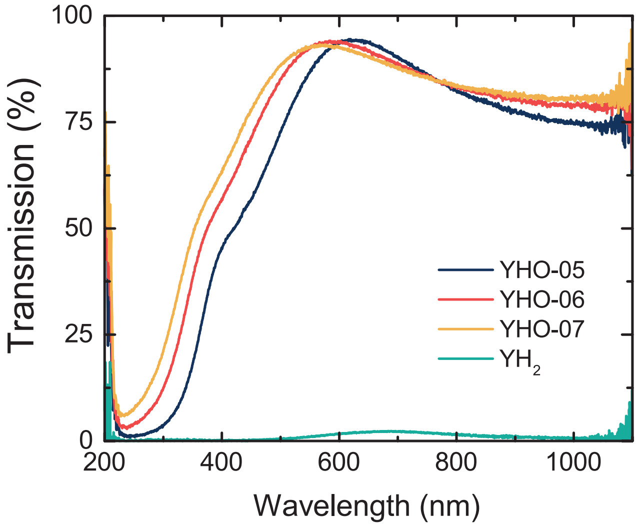

Figure 2.A.1: The final optical transmission spectra (day 10) for all of the thin-films studied here (day 10). YH_2 shows a transmission window, implying that its composition is sub-stoichiometric $YH_{1.9}$. The $YH_{3-2x}O_x$ thin-films show high optical transparency until their band edge, which shifts to higher energy values as the p_{dep} increases and the O:H ratio increases. The transmission of the $YH_{3-2x}O_x$ thin-films is not flat due to thin-film interference which results in an oscillating pattern. Because this pattern is nearly identical for all the samples, they can be assumed to be of nearly identical thickness (∼ 150 nm).

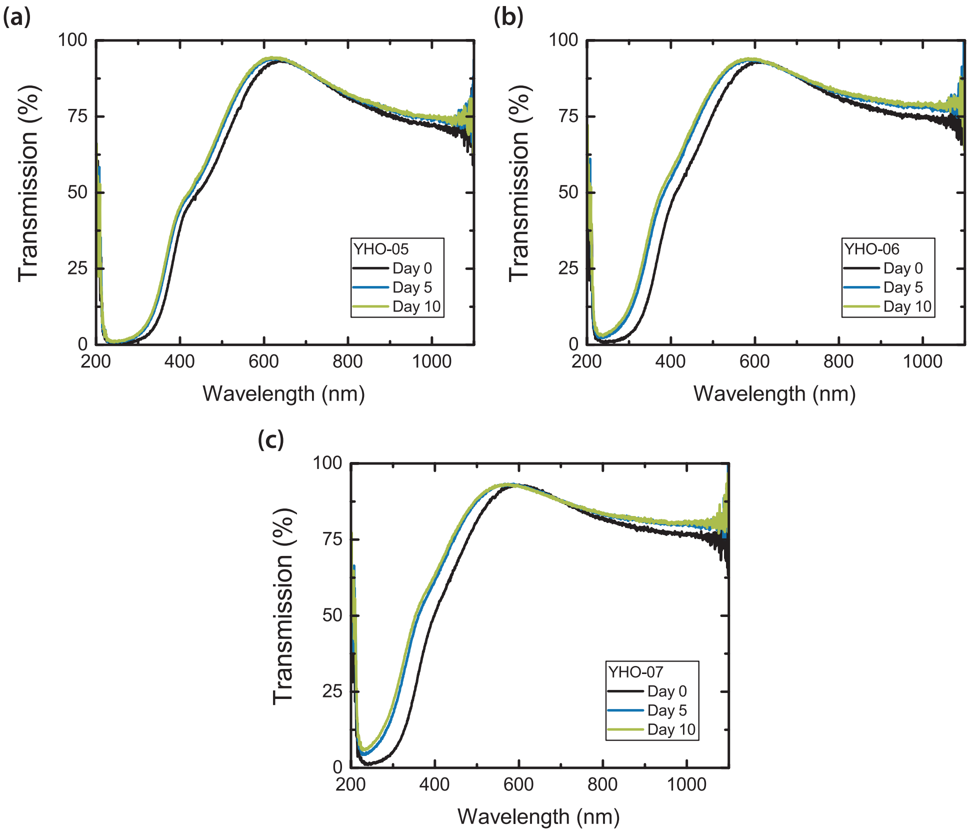

Figure 2.A.2: Optical transmission spectra of (a) YHO-05, (b) YHO-06, and (c) YHO-07 showing the progression of air-oxidation over the course of several days, where “day 0" is the day of deposition. The air-oxidation process causes the band gap energy to shift towards higher values, but is completed after less than a week. The samples were measured by μSR after the air-oxidation process stabilised.

Table 2.A.1: Calculated band gap energies for the data in Figure 2.A.2. These values are determined by fitting the data as a Tauc plot. Day 0 shows a smaller band gap energy than the others because it is from the very beginning of the air-oxidation process. By day 5, the band gap is larger due to the replacement of H^- by O^{2-}. Between day 5 and day 10, the band gap does not change significantly, meaning that the air-oxidation process has stabilised and the composition (O^{2-}:H^- ratio) is constant over time. This is consistent with our previous detailed study on the photochromic effect in $REH_{3-2x}O_x$ (RE = Sc, Y, Gd) [1].

p_{dep} (Pa)	E_g (eV) Day 0	E_g (eV) Day 5	E_g (eV) Day 10
0.5	2.38 ± 0.03	2.50 ± 0.03	2.50 ± 0.05
0.6	2.39 ± 0.03	2.53 ± 0.05	2.55 ± 0.04
0.7	2.38 ± 0.03	2.56 ± 0.03	2.58 ± 0.03

2.B Fitting zero field $YH_{2-\delta}$ data

The zero field $YH_{2-\delta}$ data (Fig. 1b) was ultimately fit by an equation describing a spin-entangled state between a hydride ion and a muon (Eq. 6). However, this equation contains several cosine functions, thus, may result in several observable oscillations. Only the first oscillation is seen in the data shown in Figure 1 because of the limitations of the LEM continuous beam for thin film studies used to acquire the data, where sufficient statistics can be obtained for a maximum of 10-12 μs.

For this reason, other equations (most notably the Kubo-Toyabe (KT) function) can be used in an attempt to fit our data as well. The KT function can be written in two forms: static and dynamic. As described in Section III.A., the TF results indicate that the muon is static until T ~ 150 K, beyond which hopping dynamics occur with an activation energy of 67 ± 13 meV. Therefore, for temperatures below 150 K, the static-KT function would be applicable, while for higher temperatures, the dynamic-KT equation may be used.

Below we show the results of fitting these three equations to our data at different temperatures. The result is that:

1. (Table SIII) the **static-KT** equation does not fit low temperature data well because it plateaus at 1/3 of the asymmetry at long t, not accounting for the damping that is present
2. (Table SII, SIV) the **dynamic-KT** and **H-μ** functions can result in similar shapes, thus, similar values for the reduced χ^2
3. (Table SIV) the reduced χ^2 is not the only important fitted parameter, so we evaluate the physical meaning behind the fitted parameters of the equation as well. For the **dynamic-KT** function, the relaxation rate ($\Delta_{ZF} \sim 0.3861$ μs^{-1}) is nearly twice as large as the value obtained from the transverse field for low temperatures ($\sigma_{TF} \sim 0.2179$ μs^{-1}). This suggests that this model is not compatible with the data.
4. (Table SV) Proper fitting of the **dynamic-KT** equation requires that the Δ_{ZF} is fixed to its low temperature value since the static width of the field distribution should not change when dynamics set in. This was attempted although the Δ_{ZF} value of 0.3861 μs^{-1} was deemed unphysical, and this did not lead to better results than the **H-μ** equation.

2.B.2 Spin-entangled H-μ complex

$$A(t) = [\ A_{H\mu}\ (\frac{1}{6} + \frac{1}{6}\cos(2\pi f_{H\mu}t) + \frac{1}{3}\cos(\pi f_{H\mu}t)\ + \frac{1}{3}\cos(3\pi f_{H\mu}t))\ \mathrm{e}^{-\frac{1}{2}\sigma_{ZF}^2 t^2}\ ] + A_{NR}$$

Table 2.B.1: Fitting results for the H-μ equation where $A_{H\mu}$ is the asymmetry related to this function, σ_{ZF} is the Gaussian relaxation rate, $f_{H\mu}$ is the frequency which can be converted to the H-μ distance, and A_{NR} is the asymmetry of the non-relaxing fraction of muons. The last column includes the reduced χ^2.

T (K)	$A_{H\mu}$	σ_{ZF} (μs^{-1})	$f_{H\mu}$ (MHz)	A_{NR}	χ^2/NDF
300	0.1845±0.0019	0.4140±0.0290	0.0040±0.0320	0.0603±0.0019	0.9638
260	0.1834±0.0026	0.4060±0.0595	0.0370±0.0160	0.0614±0.0025	0.9521
200	0.1782±0.0022	0.3150±0.0255	0.0653±0.0029	0.0660±0.0019	1.0572
150	0.1718±0.0016	0.2730±0.0190	0.0752±0.0016	0.0718±0.0013	1.0020
100	0.1717±0.0015	0.2590±0.0175	0.0775±0.0013	0.0716±0.0012	1.0045
50	0.1772±0.0016	0.2740±0.0021	0.0764±0.0016	0.0672±0.0013	1.0165
25	0.1733±0.0015	0.2590±0.0019	0.0774±0.0013	0.0679±0.0013	1.0068
10	0.1741±0.0016	0.2860±0.0021	0.0774±0.0017	0.0702±0.0013	1.0146

2.B.2 Static Gaussian Kubo-Toyabe function (static-KT)

$$A(t) = [\ A_{sKT}(\frac{1}{3}\ + \frac{2}{3}\ [1-(\Delta_{ZF}t)^2]\ \mathrm{e}^{-\frac{1}{2}(\Delta_{\mathrm{ZF}}\mathrm{t})^2})\ ] + A_{NR}$$

Table 2.B.2: Fitting results for the static Gaussian Kubo-Toyabe equation where A_{sKT} is the asymmetry related to this function, Δ_{ZF} is the Gaussian relaxation rate, and A_{NR} is the asymmetry of the non-relaxing fraction of muons. The last column includes the reduced χ^2.

T (K)	A_{sKT}	Δ_{ZF} (μs^{-1})	A_{NR}	χ^2/NDF
300	0.1918±0.0017	0.2655±0.0026	0.0390±0.0017	1.0485
150	0.1942±0.0014	0.3482±0.0026	0.0360±0.0012	1.1166
10	0.196 ±0.0014	0.3588±0.0026	0.0340±0.001	1.1696

2.B.2 Dynamic Gaussian Kubo-Toyabe function (dynamic-KT)

$$A(t) = [\ A_{dKT}(\frac{1}{2\pi i}\int_{\gamma+i\infty}^{\gamma-i\infty}\frac{f_G(\Delta_{ZF}+\Gamma)}{1-\Gamma f_G(\Delta_{ZF}+\Gamma)}\mathrm{e}^{\Delta_{ZF}t}\,d\Delta_{ZF}\ )\ ] + A_{NR}$$

$$f_G(\sigma) = \int_0^{\infty} G_{LF}\ \mathrm{e}^{-\Delta_{ZF}t}\,dt$$

$$\begin{aligned} G_{LF}(t) = 1 &- \frac{2\Delta_{ZF}^2}{(2\pi\nu)^2}\ [1-\mathrm{e}^{-0.5\Delta_{ZF}^2t^2}\cos(2\pi\nu t)] \\ &+ \frac{2\Delta_{ZF}^4}{(2\pi\nu)^3}\int_0^t \mathrm{e}^{-0.5\Delta_{ZF}^2\tau^2}\ \sin(2\pi\nu\tau)\,d\tau \end{aligned}$$

Table 2.B.3: Fitting results for the dynamic Gaussian Kubo-Toyabe equation where A_{dKT} is the asymmetry related to this function, Δ_{ZF} is the Gaussian relaxation rate, Γ is the hopping rate, A_{NR} is the asymmetry of the non-relaxing fraction of muons, and finally the reduced χ^2. The parameter ν (seen in the above equations, $\nu = \gamma_\mu \mathrm{B}/2\pi$) was fixed to 0 because this data was acquired under zero field conditions.

T (K)	A_{dKT}	Δ_{ZF} (μs^{-1})	Γ (MHz)	A_{NR}	χ^2/NDF
300	0.2047±0.0028	0.2992±0.0054	0.2190±0.0315	0.0338±0.0026	0.9619
260	0.2029±0.0021	0.3349±0.0053	0.2160±0.0260	0.0336±0.0019	0.9527
200	0.2027±0.0017	0.3652±0.0048	0.1790±0.0195	0.0345±0.0015	1.0638
150	0.1979±0.0015	0.3801±0.0046	0.1390±0.0165	0.0382±0.0013	1.0101
100	0.1983±0.0015	0.3818±0.0044	0.1190±0.0145	0.0367±0.0012	1.0098
50	0.2044±0.0015	0.3871±0.0046	0.1450±0.0165	0.0305±0.0013	1.0170
25	0.2004±0.0015	0.3850±0.0045	0.1370±0.0155	0.0345±0.0013	1.0157
10	0.2006±0.0015	0.3965±0.0047	0.1600±0.0165	0.0359±0.0013	1.0201

Table 2.B.4: Fitting results for the dynamic Gaussian Kubo-Toyabe equation with Δ_{ZF} fixed to its average low temperature value.

T (K)	A_{dKT}	Δ_{ZF} (μs^{-1})	Γ (MHz)	A_{NR}	χ^2/NDF
300	0.2197±0.0042	0.3861	0.7920±0.0465	0.0251±0.0041	1.0638
260	0.2063±0.0025	0.3861	0.4590±0.0265	0.0341±0.0023	1.0036
200	0.2027±0.0017	0.3861	0.2470±0.0155	0.0362±0.0015	1.0766

2.C Zero field Y-oxyhydride data

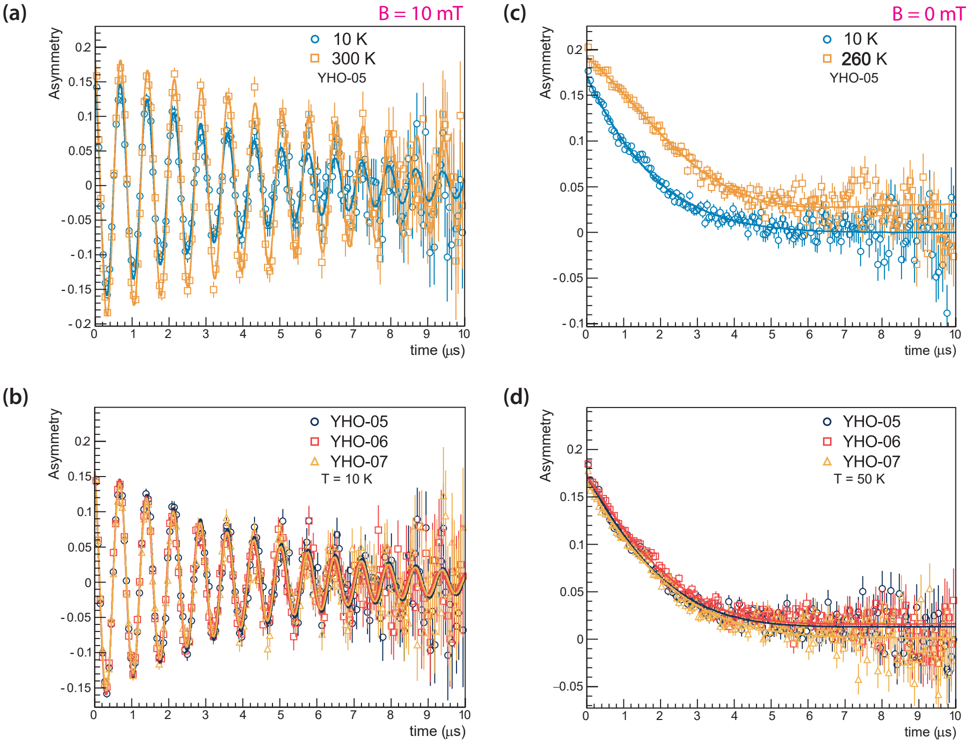

Figure 2.C.1: μ^+SR spectra for $YH_{3-2x}O_x$ thin-film samples with (a) and (b) showing the TF spectra, while (c) and (d) are from the ZF. Further, (a) and (c) show the influence of temperature on the μ^+SR spectra for YHO-05, where blue circles and orange squares correspond to 10 K and 300 K (TF) or 260 K (ZF), respectively. (b) and (d) show the influence of p_{dep} on the spectra, where navy, red, and yellow represent YHO-05, YHO-06, and YHO-07, respectively, either at 10 K (TF) or 50 K (ZF).

2.D Transverse field Y-oxyhydride: λ_{TF} under illumination

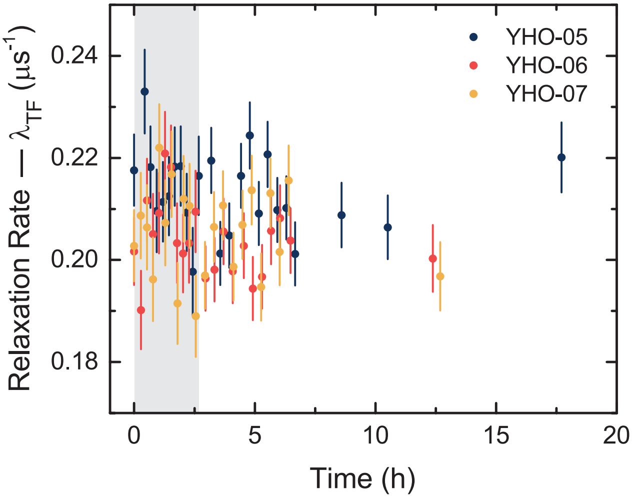

Figure 2.D.1: The three $YH_{3-2x}O_x$ thin-films were *in situ* illuminated under TF conditions where the fitting parameters are the diamagnetic asymmetry ($A_{dia,TF}$) and the Lorentzian relaxation rate (λ_{TF}). The $A_{dia,TF}$ is shown in the main text, increasing reversibly upon illumination with a UV LED. On the other hand, λ_{TF} does not change during illumination. This parameter is related to $E_{A,\lambda}$ which was calculated to be ~15 meV under “dark" conditions. This is already a very low activation energy, only slightly higher than thermal energy at 50 K (~4 meV). Therefore, if the $E_{A,\lambda}$ changed under illumination, the difference may be very small and not resolved well in our data. However, if we consider $E_{A,\lambda}$ to be unaffected by illumination, that would mean polaron formation is neither enhanced nor impeded during photochromism, and local lattice changes are more responsible for the colour changing effect.

2.E Transverse field Y-oxyhydride: Recovery of asymmetry with heating post-illumination

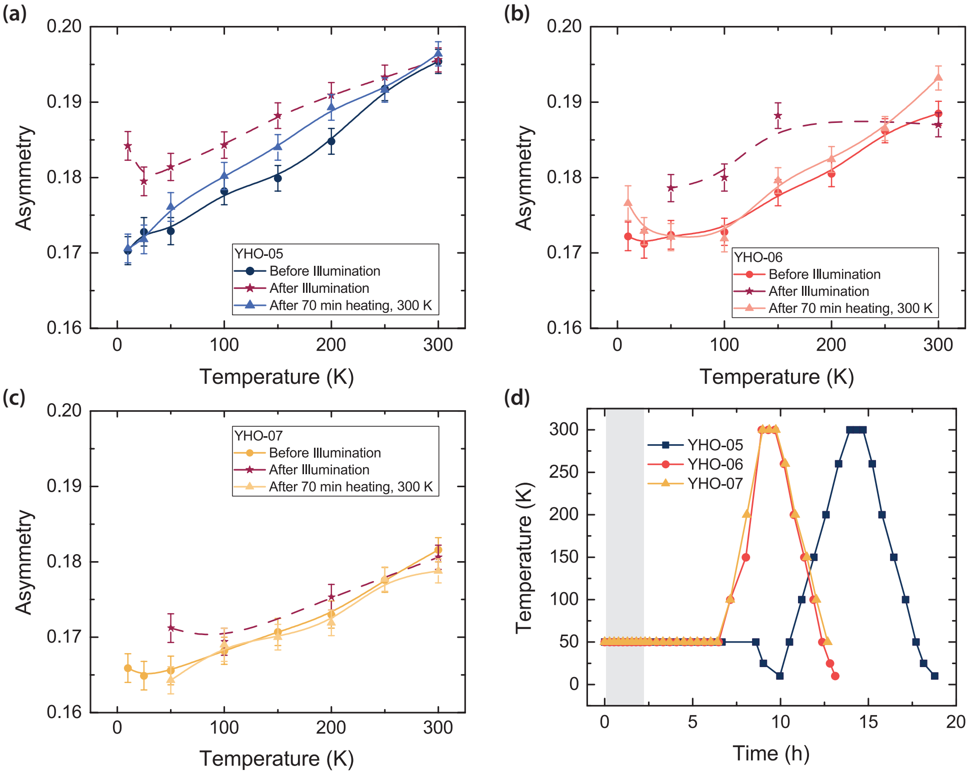

Figure 2.E.1: The TF asymmetry is plotted from *in-situ* measurements of (a) YHO-05, (b) YHO-06, and (c) YHO-07. The lines are meant to guide the eye. The asymmetries are shown for the samples (i) before any illumination was performed (circle, cooling run), (ii) after ∼2 h of illumination with the LED turned off (star, dashed line, heating run), and (iii) after heating at 300 K for 70 min (triangle, cooling run). (d) After the LED was turned off, each sample went through a different heating programme. Illumination experiments were done at 50 K and kept at this temperature for several hours. Because the $A_{dia,TF}$ did not return to its original value within that period of time, the samples were heated to see if temperature could facilitate the recovery. The asymmetry obtained during heating is indicated by the dashed line and star symbol in (a), (b), and (c). The samples were then kept at 300 K for 70 min and cooled back to low temperatures. The asymmetries obtained from cooling are indicated by the triangles in (a), (b), and (c).

References

[1] G. Colombi, T. De Krom, D. Chaykina, S. Cornelius, S. W. H. Eijt, and B. Dam, *Influence of cation (RE = Sc, Y, Gd) and O/H anion ratio on the photochromic properties of* REO_xH_{3-2x} *thin films,* ACS Photonics **8**, 709 (2021).

3

Influence of crystal structure, encapsulation, & annealing on photochromism in Nd-oxyhydrides

"Science is organized common sense where many a beautiful theory was killed by an ugly fact."
—Thomas H. Huxley

Thin films of rare-earth metal oxyhydrides show a photochromic effect, the precise mechanism of which is yet unknown. Here, we made thin films of $NdH_{3-2x}O_x$ and show that we can change the band gap, crystal structure, and photochromic contrast by tuning the composition (O^{2-}:H^-) via the sputtering deposition pressure. To protect these films from rapid oxidation, we add a thin ALD coating of Al_2O_3, which increases the lifetime of the films from 1 day to several months. Encapsulation of the films also influences photochromic bleaching, changing the time dependency from first-order kinetics. As well, the partial annealing which occurs during the ALD process results in a dramatically slower bleaching speed, revealing the importance of defects for the reversiblility (bleaching speed) of photochromism.

This chapter is partly based on *D. Chaykina, et al., "Influence of Crystal Structure, Encapsulation, and Annealing on Photochromism in Nd Oxyhydride Thin Films," The Journal of Physical Chemistry C, 126 (4), 2276-2284, 2022.* [1].

3.1 Introduction

Rare-earth metal oxyhydrides ($REH_{3-2x}O_x$) thin films receive attention due to their reversible photochromic effect [2], where the material reversibly changes colour triggered by UV light. In the presence of this incident light, the films “darken”, absorbing light over a wide range of wavelengths (visible to near-IR). Yet, when the light is removed, the original transparency is returned by “bleaching”. Such optical properties are attractive for smart window applications, especially since the bleaching speed (time required to recover the transparent state) has recently been reported as low as 9 minutes [3].

Thin films of $REH_{3-2x}O_x$ (Sc, Y, Dy, Er, Gd) are prepared by reactive magnetron sputtering of a metallic REH_2 film, which oxidises to a semiconducting photochromic oxyhydride when exposed to air [3–5]. The extent of oxidation (O^{2-}:H^- ratio) is related to the deposition pressure during sputtering, where more oxidised films are achieved by sputtering the parent REH_2 at a higher pressure which invokes a higher porosity of the as-deposited REH_2. In this way, both the type of cation (RE) and the O^{2-}:H^- ratio of these materials can be tuned, impacting their photochromic properties [3].

Although the mechanism of photochromism in these materials is not well-defined, it has been proposed that ion mobility plays a role in the process [3, 6]. This is partly because some $REH_{3-2x}O_x$ powders (RE = La, Nd) have shown pure H^- conductivity [7, 8]. In general, these large RE-cations lead to tetragonal lattices, which has sometimes been associated with anion-order [8, 9], although this last aspect is debated [10]. Smaller RE-cations, instead, result in anion-disordered cubic lattices, thus, behaving as ion-insulators [8].

Since most of the reported photochromic oxyhydrides fall in the cubic ion-insulator range (RE = Sc, Y, Dy, Er, Gd) [3–5], it may be that short-range mobility, rather than long-range, influences the photochromic effect. An NMR study of $YH_{3-2x}O_x$, for example, showed the presence of a mobile H fraction which reversibly disappeared during photochromic darkening [6]. However, it should be noted that other theories about the photochromic mechanism have been proposed, and not all involve a diffusion-related step, namely the formation of hydroxides, colour centres, and dihydrogen species [11].

Here, we investigate the structural properties of $NdH_{3-2x}O_x$ thin films and their photochromic performance. While photochromism in Nd-based oxyhydrides was reported earlier [12], a complete optical and structural analysis has been lacking so far. Rare-earth oxyhydrides based on Nd are of particular interest because they show a high H^- conductivity [8], have a large RE-cation, and have sometimes been described as anion-ordered with a tetragonal crystal structure [8, 9, 13]. These structural properties of Nd-oxyhydrides differ from the cubic oxhydrides we reported earlier[3–5], allowing for the unique opportunity to assess which structural aspects are relevant to the photochromic effect.

We find that $NdH_{3-2x}O_x$ thin films can be made by air-oxidation of $NdH_{1.9+\delta}$ films, where the O^{2-}:H^- ratio of the resultant film depends on the deposition pressure (p_{dep}). However, these films are unstable in air and require a protective coating of Al_2O_3 deposited by ALD. Remarkably, the c/a ratio of our tetragonal $NdH_{3-2x}O_x$ films depends on the p_{dep} (or O:H ratio). While all these films are photochromic, samples made at the same p_{dep} showed very different colour changing kinetics during photochromism, despite being equivalent in terms of crystal structure and optical properties. The variability in bleaching time is found to be due to: (1) the encapsulation of the film by the protective layer, and (2) the heating occurring during ALD. The former changes the order of bleaching (no longer first-order kinetics), while the latter may lead to a partial annealing of the films which eliminates some defects, slowing the bleaching time constant. This suggests that a certain "meta-stability" of an as-deposited $REH_{3-2x}O_x$ film and the associated structural defects are necessary ingredients for photochromic bleaching.

3.2 Experimental

Thin films of $NdH_{1.9+\delta}$ (~300 nm) were deposited by DC reactive magnetron sputtering of a Neodymium target (purity 99.9%, MaTecK) at 100 W in an Ar/H_2 gas mixture at a ratio of 7:1. The vacuum system was operated at a base pressure of $< 10^{-6}$ Pa. The films were grown at various deposition pressures ($p_{dep} = 0.3 - 0.9$ Pa) on 10x10 mm^2 fused silica (f-SiO_2) substrates at room temperature (~21°C). After deposition, the films were oxidized in ambient air to form the oxyhydride ($NdH_{3-2x}O_x$). For comparison, some $GdH_{3-2x}O_x$ thin films were made by the same methods and conditions ($p_{dep} = 0.7$ Pa).

The Nd-oxyhydride films are not stable in ambient air over long periods of time. Within a few days of removal from the vacuum chamber, the films fully oxidise (complete removal of H^-), which is seen as a widening of the optical band gap in the transmission spectra (Fig. 3.1, Fig. 3.A.1). To protect the films from this complete oxidation, they were coated with a conformal Al_2O_3 layer by atomic layer deposition (ALD) (Fig. 3.B.1). After taking the as-sputtered films out of vacuum, they were brought to the ALD system, limiting the ambient air-exposure during sample transport to typically a few minutes (detailed in Table 3.C.1).

The Al_2O_3 layers were deposited by ALD at 87°C using TMA (trimethylaluminum) as the precursor and O_2 as the reactant. The TMA pulse time was set to 0.06 s, followed by a waiting time of 4 s, and an O_2 plasma for 6 s at 300 W. The base pressure was ($p \sim 2$ μbar), while the process pressure varied between 0.1–0.2 mbar. After 300 cycles (1.8 h),

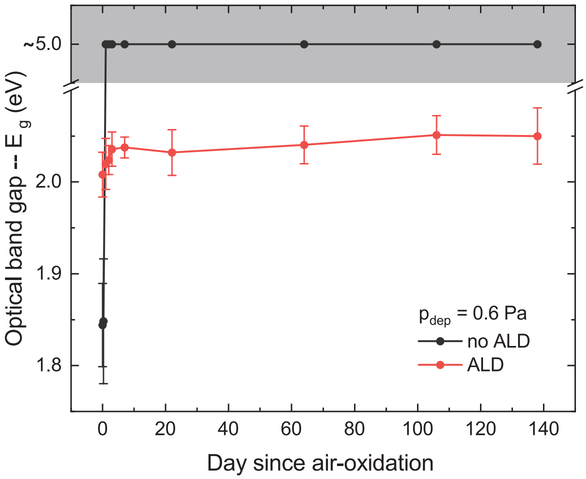

Figure 3.1: Optical band gaps for uncoated (grey) and ALD coated (red) Nd-oxyhydride thin films deposited at 0.6 Pa. Day 0 is the day of deposition and removal from the vacuum chamber. Grey filled-in area indicates that the compound is fully oxidised and no longer an oxyhydride.

the ALD layer was ~47 nm thick, determined by X-ray reflectometry (XRR) (Fig. 3.D.1). ALD coated $NdH_{3-2x}O_x$ films showed remarkably longer lifetimes, maintaining a stable composition (indicated by the reproducible optical transmission spectra) for at least 138 days, or 5 months (Fig. 3.1, Fig. 3.A.2). A band gap shift is noticeable in the ALD coated films compared to the as-deposited uncoated films (day 0) (Fig. 3.A.3), which may be due to slight oxidation from the combination of O_2 plasma and heating during ALD, an effect that likely disappears as more monolayers are deposited.

Optical transmission spectra were acquired by a custom-built optical fibre spectrometer containing a deuterium and a quartz tungsten halogen lamp (DH2000-BAL, Ocean Optics B.V.), and a Si array wavelength-dispersive spectrometer (HR4000, Ocean Optics B.V.). The transmission spectra of Nd-based thin films were measured for several days to monitor the extent of oxidation for both ALD coated and uncoated films. The optical band gap energies of the films were calculated via the Tauc method (Fig. 3.A.3, Fig. 3.F.1).

The photochromic properties of ALD coated $NdH_{3-2x}O_x$ were measured by illuminating the films with a narrow wavelength LED ($\lambda = 385$ nm) for 1 h and measuring the average transmittance ($\lambda = 450 - 1000$ nm) with respect to time. After 1 h, the LED was turned off and the bleaching process was measured for several hours until the original transparency was recovered. All optical measurements were taken at room temperature (~21°C). The photochromic effect was only measured for ALD coated films because uncoated $NdH_{3-2x}O_x$ films oxidise constantly over time, preventing any reliable time-dependent measurements.

The structural properties of the thin films were analysed by X-ray diffraction (XRD, Bruker D8 Discover) with a Cu source in grazing-incident (GI-XRD) geometry (incident angle = 3.2°, primary = 40 mm Goebel mirror with 0.6 mm slit, secondary = 8 mm motorised slit with LynxEye XE detector). Lattice constants were derived based on Pseudo-Voigt fitting of each diffraction peak considering both $k_{\alpha 1}$ and $k_{\alpha 2}$. The evaluation of the unit cell symmetry can be misinterpreted due to the influence of thin film stress and texture on the observed XRD pattern. To investigate their presence, these properties were measured in Bragg-Brentano ($\theta - 2\theta$) geometry with varying ψ angles ($\psi = 0 - 80°$) to probe crystallites of different orientation. The angle ψ describes the tilt of the sample perpendicular to the X-ray beam. Only ALD coated $NdH_{3-2x}O_x$ films were analysed by XRD since such measurements take several hours during which the uncoated samples oxidise.

3.3 Results

3.3.1 Optical properties of Nd-based thin films

Thin films of $NdH_{3-2x}O_x$ deposited between $p_{dep} = 0.3 - 0.9$ Pa result in various optical properties upon air oxidation, similar to our previous work using other rare-earth cations (RE = Sc, Y, Gd, Er, Dy) [3–5]. Films deposited at low pressures ($p_{dep} = 0.3 - 0.5$ Pa) are opaque (Fig. 3.2a), meaning low average transmittance (Fig. 3.2b), and have no optical band gap, suggesting that they largely maintain the as-deposited $NdH_{1.9+\delta}$ composition [14–18].

The dihydride phase of the films deposited at $p_{dep} < 0.6$ Pa is further confirmed by the small transparency window observable in the transmission spectrum (Fig. 3.E.1), typical of RE-dihydrides [3–5, 19, 20]. The transmission spectrum for the 0.5 Pa sample, however, shows a larger transparency window, extending towards longer wavelengths. This film could be very minimally oxidised, yet still maintaining the metallic properties of as-deposited $NdH_{1.9+\delta}$ [14, 15, 17, 18].

However, films deposited at and above a critical deposition pressure[4] ($p^{*}_{dep} \sim 0.6$ Pa) are more transparent (Fig. 3.2a, Fig. 3.2b) and have an optical band gap (Fig. 3.2c). This is expected since, as the deposition pressure increases, thin films produced by sputtering are progressively more porous. Eventually, this porosity is sufficient to allow for the oxidation of the as-deposited $NdH_{1.9+\delta}$ film in air, and the appearance of semiconducting properties that are characteristic of oxyhydrides ($NdH_{3-2x}O_x$) [3, 4].

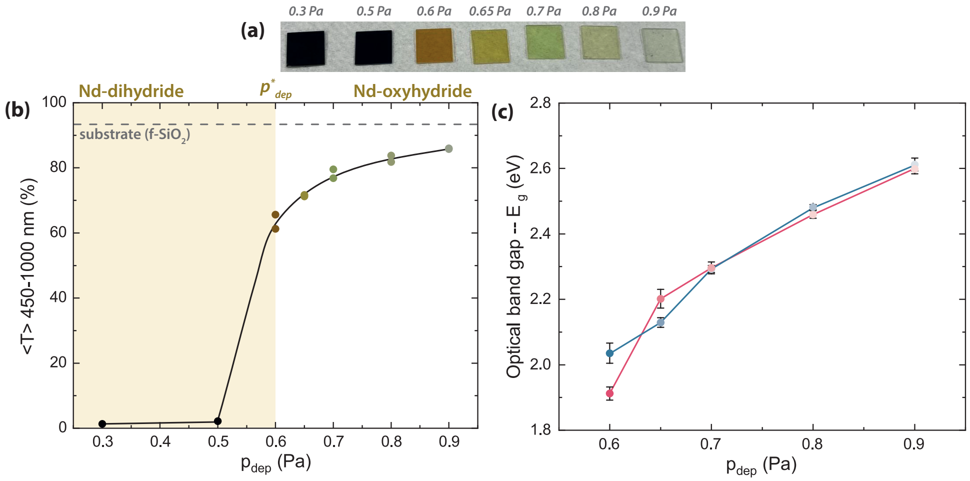

Figure 3.2: (a) Image of a set of Nd-based thin films considered for this work. They are arranged by deposition pressure (p_{dep}) from 0.3 Pa (left) to 0.9 Pa (right). (b) Average transmittance ($\lambda = 450 - 1000$ nm) of $NdH_{3-2x}O_x$ thin films sputtered at different p_{dep}. (c) Optical band gaps (E_g) of films deposited at and above the critical deposition pressure ($p^{*}_{dep} \sim 0.6$ Pa). Pink and blue lines indicate films which showed "slow" or "fast" photochromic bleaching, respectively.

The optical band gap increases with the deposition pressure (Fig. 3.2c) for $p_{dep} \geq 0.6$ Pa. The relationship between the anion composition and the band gap is a phenomenon seen often in multi-anion compounds such as oxyhydrides [3, 5], oxyhalides [21], and oxynitrides [22]. Since the oxyhydride valence band is comprised of the oxide and hydride states, and O^{2-} is more electronegative than H^{-}, a replacement of H^{-} by O^{2-} shifts the valence band down [23]. This was further investigated experimentally using a combination of RBS and ERDA to confirm that $REH_{3-2x}O_x$ (RE = Sc, Y, Gd) thin films deposited at higher pressures contain more O^{2-} and have a larger band gap [3, 5]. Since the $NdH_{3-2x}O_x$ films described here are produced by the same methods, we expect the same trends to appear here, namely that $NdH_{3-2x}O_x$ films deposited at 0.9 Pa have a larger optical band gap and O^{2-}-content than those deposited at 0.6 Pa.

Notably, the band gap energies observed here for $NdH_{3-2x}O_x$ films ($E_g = 1.91 - 2.61$ eV) span over a wider range than what was found for other rare-earth metal oxyhydrides ($REH_{3-2x}O_x$, RE = Sc, Y, Gd: $E_g = 2.2 - 2.5$ eV) [3, 5] for a similar set of p_{dep} (Fig. 3.F.1). Since the optical band gap and the O^{2-}:H^{-} ratio are related, this may indicate that stable Nd-based oxyhydride thin films can be made in a larger composition range than for the other RE-cations. A similar trend has been observed, for example, by Fukui, K., *et al.* [10], where a larger stable composition range was found for La-oxyhydride powders compared to Y-oxyhydrides. Another possibility is that a larger spread in E_g can be generated for a similar O^{2-}:H^- range due to the higher polarisability of Nd compared to the smaller Sc, Y, and Gd cations. Cation-based band gap engineering was shown, for example, in oxysulfides, where the conduction band was shifted by changing the RE-cation gradually from Gd to Ce [24].

3.3.2 Structural properties

The cation size is an important determining factor for the structure of $REH_{3-2x}O_x$, where large cations (La-Nd) often lead to tetragonal ($P4/nmm$) lattices [13, 25] with anion-ordering [9] and long-range anion mobility [8]. Smaller RE-cations (Sm-Er) should then result in cubic ($Fm\bar{3}m$), anion-disordered, and anion insulating materials [8, 9, 26]. However, alternative structures were reported for RE = Y, La, Dy, Er, and Lu (orthorhombic *Pnma*, monoclinic $P2_1/m$, cubic $F\bar{4}3m$) [10, 27, 28]. Eventually, though, the crystal structure of the best H^- conductor thus far ($LaH_{3-2x}O_x$) [7] was identified as tetragonal, but anion-disordered [10], challenging the view that anion-order is a necessity for long-range diffusion and a direct consequence of a tetragonal lattice.

Importantly, all of the aforementioned studies dealt with powder $REH_{3-2x}O_x$, and often only in stoichiometric compositions (REHO). For thin films, only $Fm\bar{3}m$ has been reported for RE = Sc, Y, Gd, Dy, and Er [3–5, 29]. The situation is less obvious for thin films of $NdH_{3-2x}O_x$, where some authors obtained a cubic crystal structure by epitaxy [30], and others were not able to assign a crystal structure from XRD. Specifically, many authors use the low intensity (101) reflection to distinguish between $Fm\bar{3}m$ and $P4/nmm$ since it only appears for the latter space group [8, 9, 26]. However, Aðalsteinsson *et al.* [12] did not find this reflection for their $NdH_{3-2x}O_x$ films and assigned no space group. Therefore, it is unclear whether Nd-oxyhydride thin films exhibit a tetragonal crystal structure as their powdered counterparts do [8, 13].

Also for our ALD coated $NdH_{3-2x}O_x$ thin films, we did not observe any (101) reflection, even with careful measurement at low θ (Fig. 3.G.3). This could be due to: (1) the presence of a cubic lattice, (2) the inherent low intensity of this reflection (at least 10x lower intensity than (220), (002) [8, 9]), (3) an absence of anion-order [7], (4) thin film texture (Fig. 3.H.2). To exclude the latter possibility, we performed XRD measurements tilting the film in the direction perpendicular to the X-ray beam by ψ = 0 - 80°. Since none of these measurements show a (101) peak, its absence is not caused by thin film texture. Because it is not immediately apparent if our $NdH_{3-2x}O_x$ thin films are tetragonal or cubic, we assign the reflections observed from XRD by their expected notation for a face-centred cubic lattice. Here, the (200) reflection is used to calculate "*a*" (or the (220) in the case of 0.3 Pa), while (111) is used to calculate "*c*". In case the unit cell is truly cubic, the two values should be equal ($c/a = 1$). Otherwise, if $c/a \neq 1$, there is a degree of tetragonal distortion.[1]

XRD patterns for films deposited below p^*_{dep} are shown in Fig. 3.G.1. The result for 0.3 Pa is in agreement with the fcc $NdH_{1.9+\delta}$ structure. The average lattice constant ($a = 5.52 \pm 0.01$ Å, Fig. 3.3a) is only slightly larger than the literature value ($a \sim 5.46$ Å) [15, 16]. For 0.5

---

[1] When the unit cell is indeed tetragonal, the (200) from cubic notation is indexed instead as a doublet of the (220) and (002) planes. Conversion from a_{200} to a_{220} can be done by $a_{220} = a_{200}/\sin(45^\circ)$. After performing this conversion, our values for *a* and *c* remain consistent with the literature.

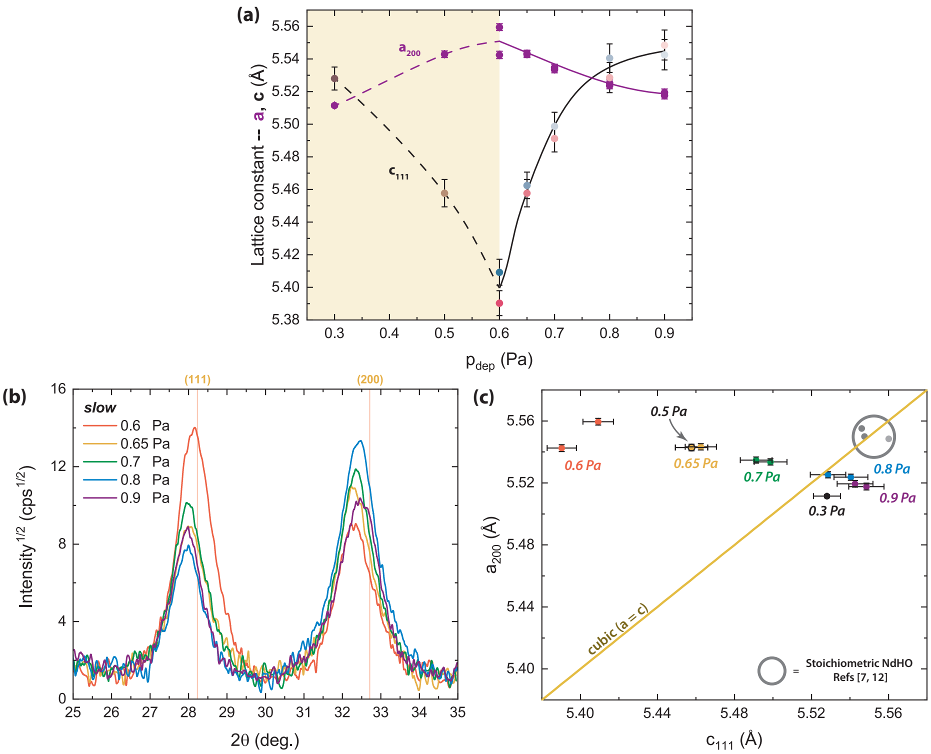

Figure 3.3: (a) Zoomed-in GI-XRD patterns of the (111) and (200) reflections for ALD coated $NdH_{3-2x}O_x$ films sputtered at different pressures showing the change with O^{2-}:H^- ratio (full patterns in Fig. 3.G.2). Red reference lines are for the fcc (cubic) $NdH_{1.9+\delta}$ pattern from ICDD-PDF database # 00-89-4199. Data shown is with 2-pt smoothing. (b) The calculated lattice constants based on the (111) and (200) reflections. (c) To show the extent of tetragonal distortion, the two lattice constants are plotted against each other with a reference line for perfect cubic unit cell ($a = c$).

Pa, on the other hand, Figure 3.3a shows an expansion of a_{200} and a compression of c_{111}, meaning that this film is tetragonal ($c/a = 0.985$). Apparently, even a minimal addition of O^{2-} is sufficient to induce a tetragonal structure.

Figure 3.3b shows the XRD patterns for five ALD coated $NdH_{3-2x}O_x$ thin films produced at and above the critical p_{dep} (full patterns in Fig. 3.G.2). In general, as p_{dep} increases, the (200) reflection shifts to larger 2θ, while the (111) peaks largely remain at the same position. Based on the calculated a_{200} and c_{111} lattice constants (Fig. 3.3a), samples made close to the critical pressure (0.6 Pa) show a tetragonal lattice with a c/a ratio of ~0.973, while those made at 0.9 Pa have a ratio of ~1.005. Since the p_{dep} and O:H composition are related [3, 5], we find that as more O^{2-} is incorporated into the $NdH_{3-2x}O_x$ lattice, the difference between a_{200} and c_{111} decreases, and the oxyhydride appears less tetragonal.

This difference in c/a and the tetragonal distortion is further highlighted in Figure 3.3c where the two lattice constants are plotted together with a reference line for a perfect cubic lattice ($a = c$). The 0.3 Pa sample is close to the cubic line, in accordance with the notion that it is $NdH_{1.9+\delta}$. Nd-oxyhydride samples made at 0.8-0.9 Pa also tend towards the cubic line, while all the others are clearly tetragonal ($a > c$). Therefore, by changing the deposition pressure, we can produce $NdH_{3-2x}O_x$ films of slightly different crystal structures.

In Figure 3.3c, we also compare our samples to the stoichiometric NdHO powders reported in Refs. [8, 13]. Our values for a_{200} are in agreement with those of stoichiometric NdHO, but our c_{111} is consistently smaller. Although substrate clamping of the thin film can prevent complete expansion during air-oxidation, we found no residual stress in our films (Fig. 3.H.3, Table 3.H.1) and no significant peak shifts during heating of the films for ~30 h at 87°C (Fig. 3.J.1), suggesting that the tetragonal distortion $c/a \neq 1$ we observe is an intrinsic material property.

We further note that some of our films are more tetragonally distorted than the literature reports, with a minimum c/a of 0.973 for 0.6 Pa, while Widerøe, M., *et al.* [13] and Ubukata, H., *et al.* [8] report 1.000 and 0.998-1.000, respectively. This could be due to the composition, where films produced at $p_{dep} > 0.8$ Pa tend towards a stoichiometric NdHO composition, while all the others are H-rich. This aligns with our previous work [3, 5] where we show that our photochromic $REH_{3-2x}O_x$ thin films produced by air-oxidation of a sputtered dihydride generally encompass the H-rich regime of the REH_3-RE_2O_3 composition line [23]. We, therefore, consider that the c/a ratio is a function of the O^{2-}:H^- ratio, where less tetragonal distortion is present for a composition close to the stoichiometric NdHO, perhaps due to the decreased occupation of octahedral interstitial sites [3, 5, 11, 31].

At this point, it is not possible to determine if these films differ in terms of anion-ordering due to the lack of neutron diffraction data. However, we assume for now that these films, similar to our previous studies [5, 23], are anion-disordered, especially since we did not find any super-structure reflections in the XRD indicative of anion-ordering. The disordered nature of the films may be due to the methods by which we produce these materials, and the apparent greater stability of anion-disordered RE-oxyhydrides away from the stoichiometric REHO composition [10, 23].

3.3.3 Photochromic properties of $NdH_{3-2x}O_x$

$REH_{3-2x}O_x$ thin films (RE = Sc, Y, Gd, Dy, Er) have photochromic properties, where the films darken during UV-light exposure, and bleach back to their original transparency when the light is removed. The relative photochromic contrast ($|T - T_0|/T_0$) over time for our $NdH_{3-2x}O_x$ films is shown in Figures 3.4a and 3.4b. Darkening occurs for 1 h using light with energy greater than the band gap (λ = 385 nm), which increases the relative contrast as the film becomes optically darker. The maximum colour change after 1 h is called the photochromic contrast (ΔT).

All of the $NdH_{3-2x}O_x$ films measured and presented in Figures 3.4a and 3.4b were coated by a protective ALD layer. The addition of this ALD coating appears to change the nature of the bleaching kinetics such that our typical expression for the rate of change during bleaching based on first-order kinetics (τ_B) [3, 4, 29] is no longer valid. This is visible for ALD coated $NdH_{3-2x}O_x$ (Fig. 3.4c) and ALD coated $GdH_{3-2x}O_x$ films (Fig. 3.I.1) when compared to a Gd-based film without the coating. If the assumption of first-order kinetics is correct, a linear time dependency should be visible in Figure 3.4c; this is only true for the *uncoated* $GdH_{3-2x}O_x$ film. Therefore, for this work, we define a new value, $\tau_{B,50\%}$, which is the time required to lose 50% of the darkened contrast (grey line in Fig.

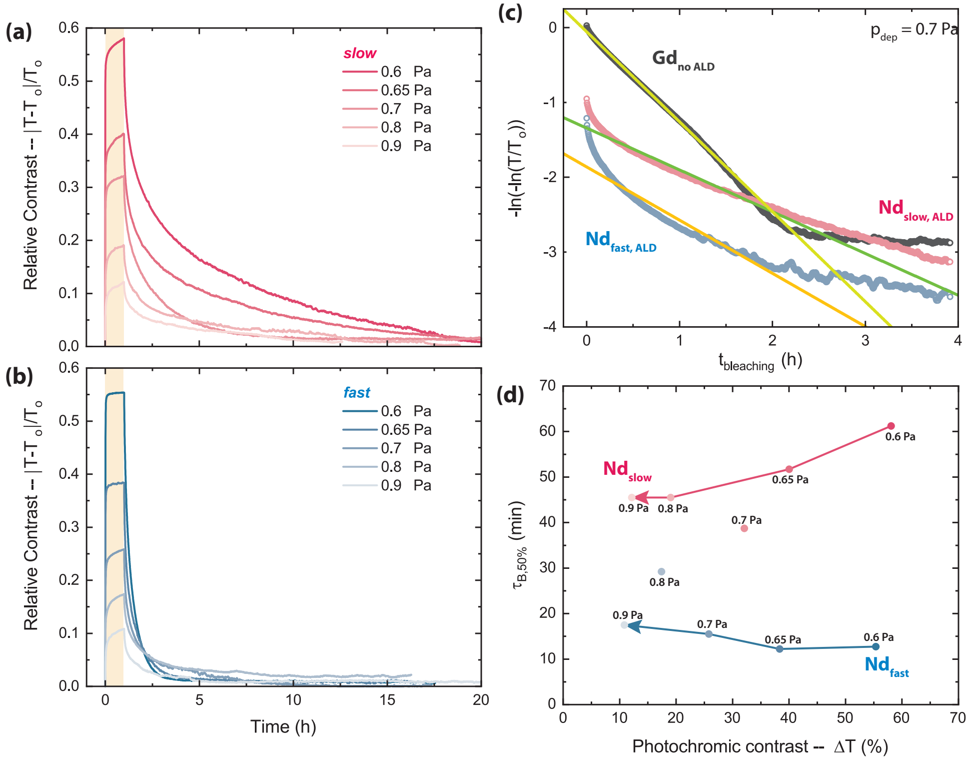

Figure 3.4: The change in relative photochromic contrast ($|T-T_0|/T_0$) over time during the photochromic effect for a set of $NdH_{3-2x}O_x$ thin films with (a) slow (pink) or (b) fast (blue) kinetics. The yellow box represents the time during which the samples were illuminated (1 h). (c) Double logarithm plot normally used to derive the first-order bleaching rate constant from the linear time dependency. Only the uncoated $GdH_{3-2x}O_x$ film (black) shows the expected linear trend, while the coated $NdH_{3-2x}O_x$ films (pink, blue) cannot be described by this kinetic model. (d) Photochromic contrast (after 1 h of illumination) and bleaching time for all the samples shown in (a,b). Labels indicate the deposition pressure.

3.5a).

We have shown earlier that the photochromic efficiency of a $REH_{3-2x}O_x$ thin film depends not only on the RE-cation, but on the p_{dep} (O^{2-}:H^- ratio) of the film [3]. Briefly, films made at higher p_{dep} resulted in a higher O-content, lower ΔT, and faster τ_B. Comparing to the photochromic contrast of ALD coated Nd-based films, this expected p_{dep}-dependent trend is reproduced, since the largest contrast appears for $p_{dep} = 0.6$ Pa and the lowest for 0.9 Pa.

On the other hand, the bleaching speed ($\tau_{B,50\%}$) does not follow any specific trend and we find a wide array of values (Fig. 3.4d). While we can distinguish between “slow” and “fast” samples (Fig. 3.4a, Fig. 3.4b), the bleaching times do not show a dependence on p_{dep}. The irreproducibility of the bleaching time can also be observed in $GdH_{3-2x}O_x$, used here as a reference to compare photochromism in ALD coated and uncoated films (Fig. 3.I.1). Without the ALD coating, the bleaching speed of $GdH_{3-2x}O_x$ films made at the same p_{dep}

is fairly reproducible, which changes dramatically with the addition of the coating.

We can eliminate some reasons for why $\tau_{B,50\%}$ varies in such a wide range. In principle, two films deposited at the same p_{dep} should be identical, and in many ways they are. We compared the following properties, finding, for example, two 0.6 Pa samples of $NdH_{3-2x}O_x$ to be identical in terms of their: (1) band gaps (O^{2-}:H^- ratios) (Fig. 3.2c), (2) crystal structure and lattice constants (Fig. 3.3c), and (3) thin film stress and texture (Fig. 3.H.2-3.H.3).

Instead, we studied the procedure used to deposit the ALD coating which requires heating of the films to 87°C for a minimum of 1 h 48 min, along with a few minutes of transfer time between vacuum and air (Fig. 3.5a). Since our samples are normally deposited, oxidised, handled, and measured entirely at room temperature, this heating can cause an annealing effect that has not been observed in previous experiments. This is especially important considering that the air-oxidation used for the preparation of our films is rapid, leading to a potentially "meta-stable" state of the film. As well, our sputtered films tend to be polycrystalline and can contain many microstructural defects. To test the effect of annealing under vacuum ($p \sim 2$ μbar), we made several $NdH_{3-2x}O_x$ films at 0.6 Pa and deposited the ALD coating onto them. Some films were removed directly after the ALD procedure was completed ($t_{heating} = 1.9$ h), while the others were left in the vacuum chamber at 87°C for additional time.

The bleaching speed ($\tau_{B,50\%}$) is strongly dependent on $t_{heating}$ (Fig. 3.5b), with longer annealing times leading to progressively slower bleaching. Since annealing can affect the structure of a material, XRD patterns were obtained for these films (Fig. 3.J.1). However, we find that the lattice constants (peak positions), texture (peak intensity ratios), microstrain (FWHM), and crystal structure (c/a) do not change significantly during heating, suggesting that long-range ordering that is probed by XRD is not affected by ~ 30 h of heating at 87°C, but local/short-range order may be altered. These latter aspects are then relevant to the photochromic effect. These can include, for example, reorganisation of occupied and vacant interstitial sites (i.e., changes in the compositional and structural homogeneity of the films, anion ordering), partial removal and/or line defects, growth of grains/removal of

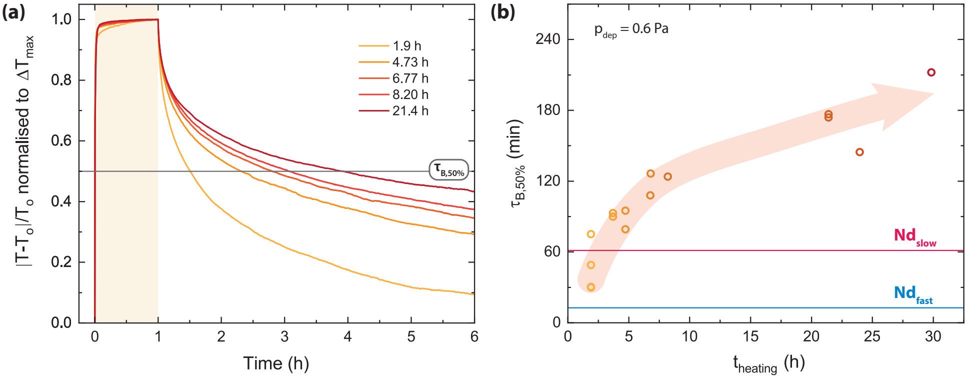

Figure 3.5: (a) Relative photochromic contrast normalised to the maximum contrast for annealed $NdH_{3-2x}O_x$ films made at $p_{dep} = 0.6$ Pa. Normalisation was done to better visualise the bleaching speeds of films made at progressively longer $t_{heating}$. (b) Bleaching time constants ($\tau_{B,50\%}$) for several $NdH_{3-2x}O_x$ films made at $p_{dep} = 0.6$ Pa with controlled heating times. Pink and blue lines indicate the "slow" and "fast" samples discussed in Fig. 3.4.

grain boundaries, and others. From Doppler-broadening positron annihilation spectroscopy (DB-PAS), the formation of point defects upon heating is also regarded as a possible process that occurs during progressive heating (Fig. 3.J.3, Table 3.J.1). For example, H_2 liberation during heating could give rise to an increase in neutral divacancies [3, 32].

3.4 Discussion

We found that our $NdH_{3-2x}O_x$ films are photochromic despite having a different crystal structure compared to our previous reports on other RE-cations [3–5]. RE-oxyhydrides based on Sc, Y, Gd, Dy, and Er exhibit a cubic $Fm\bar{3}m$ crystal structure, while the Nd-oxyhydrides we present here are tetragonal to varying degrees dependent on p_{dep}. This shows that the photochromic effect is robust and not influenced by any particular symmetry aspects.

The protective ALD coating changes the kinetics of bleaching from the first-order behaviour we normally find. [4, 29] We observe this effect also when comparing coated and uncoated $GdH_{3-2x}O_x$ films (Fig. 3.I.1). Whether or not encapsulation of $REH_{3-2x}O_x$ thin films influences the photochromic effect is being debated [33–35], but is outside the scope of this work. We suppose that the ALD coated films are better described by a series of processes with no single rate-constant, or by kinetics of a different order. Precise conclusions require more insight about the underlying mechanism of the photochromic effect, which is still missing.

Therefore, we focus primarily on the heating in the ALD chamber, and the effect of this on the photochromic properties of $NdH_{3-2x}O_x$ films. During this heating, local/short-range changes such as reorganisation of the anion-sublattice, removal of line defects, and a slight growth of grains are possible. Although these changes are difficult to quantify, they can play an important role during photochromism. Several theories have been put forth to explain this effect in $REH_{3-2x}O_x$ thin films [11] without unanimous consensus. However, important phenomena can be identified and assessed within the context of this work.

We note that while the bleaching speed was dramatically influenced by heating (becoming ~6 times slower after 30 h of heating), the photochromic contrast did not show the same trend, barely changing with heating (Fig. 3.J.2). Thus, although the contrast and bleaching speed have often been considered related, this does not appear to be true for ALD coated $NdH_{3-2x}O_x$ films. We suggest that darkening and bleaching do not depend on the same factors. Darkening likely depends on the presence and concentration of H^- and O^{2-} ions in the material since neither RE-hydrides nor RE-oxides are photochromic, and the photochromic contrast here only depends on the p_{dep} (O:H ratio) (Fig. 3.K.1). Bleaching, on the other hand, is more difficult in an annealed material, perhaps due to a greater stability of the optically absorbing species in an annealed material.

For example, some proposed theories describe the separation of a metallic phase during darkening, and re-mixing back into a single phase upon bleaching. The driving force for phase de-segregation/bleaching can be impacted by annealing. Our as-deposited $REH_{3-2x}O_x$ thin films may have an inherent anion-disorder, inhomogeneity, and/or overall “meta-stability” which may make the dissolution of the metallic phase more favourable, a property annealed away with heating. Therefore, an annealed film would retain the darkened state for a longer period of time.

Other ideas about the mechanism of photochromism involve the trapping of charge carriers by formation of H^0 *via* the excitation of an electron from H^-. For bleaching to occur, this neutral species would have to recombine with a released electron, but this may be more difficult in an annealed material if the H^0 can diffuse very far. Another option is that H^0 can form a "dihydrogen" molecule [36], where again the energetic stability of the species in the post-annealed material is important.

3.5 Conclusion

We prepared $NdH_{3-2x}O_x$ thin films by air-oxidation of as-deposited $NdH_{1.9+\delta}$ thin films sputtered at different deposition pressures. As the deposition pressure increases, so does the O^{2-}:H^- ratio and optical band gap, while the photochromic contrast decreases. The films appear to be tetragonal, with the c/a ratio approaching 1 as the deposition pressure, thus the O^{2-}:H^- ratio, increases. Although this does not influence the photochromic effect, the tunability of the crystal structure could be important for other applications such as ion mobility.

Importantly, these films are unstable in air without a protective coating of Al_2O_3 deposited by ALD. Although this coating increases the stability of these films from 1 up to at least 138 days, it changes the observed bleaching kinetics. The time evolution of bleaching can no longer be described by the first-order kinetics observed for uncoated films. In addition, we find that the values for the bleaching time constant become dependent on the time spent heating in the ALD chamber (temp. = 87°C, $p \sim 2\ \mu$bar).

We assume that the heating which occurs during the deposition of the protective coating results in a reduced defect concentration. As the samples were left in the ALD chamber for longer periods of time, the bleaching rate became slower, suggesting that the presence of defects in the material (e.g., grain boundaries, vacancies) and the overall imperfections of the as-deposited material are important to the reversibility of the photochromic effect. The stability of the dark species in the oxyhydride matrix may determine the bleaching speed, and annealing the oxyhydride acts to stabilise the darkened state, increasing the time needed for bleaching.

References

[1] D. Chaykina, F. Nafezarefi, G. Colombi, S. Cornelius, L. J. Bannenberg, H. Schreuders, and B. Dam, *Influence of crystal structure, encapsulation, and annealing on photochromism in Nd oxyhydride thin films,* The Journal of Physical Chemistry C **126**, 2276 (2022).

[2] T. Mongstad, C. Platzer-Björkman, J. P. Maehlen, L. P. A. Mooij, Y. Pivak, B. Dam, E. S. Marstein, B. C. Hauback, and S. Z. Karazhanov, *A new thin film photochromic material: Oxygen-containing yttrium hydride,* Solar Energy Materials and Solar Cells **95**, 3596 (2011).

[3] G. Colombi, T. De Krom, D. Chaykina, S. Cornelius, S. W. H. Eijt, and B. Dam, *Influence of cation (RE = Sc, Y, Gd) and O/H anion ratio on the photochromic properties of* REO_xH_{3-2x} *thin films,* ACS Photonics **8**, 709 (2021).

[4] F. Nafezarefi, H. Schreuders, B. Dam, and S. Cornelius, *Photochromism of rare-earth metal-oxy-hydrides,* Applied Physics Letters **111**, 103903 (2017).

[5] S. Cornelius, G. Colombi, F. Nafezarefi, H. Schreuders, R. Heller, F. Munnik, and B. Dam, *Oxyhydride nature of rare-earth-based photochromic thin films,* The Journal of Physical Chemistry Letters **10**, 1342 (2019).

[6] C. V. Chandran, H. Schreuders, B. Dam, J. W. G. Janssen, J. Bart, A. P. M. Kentgens, and P. J. M. van Bentum, *Solid-state NMR studies of the photochromic effects of thin films of oxygen-containing yttrium hydride,* The Journal of Physical Chemistry C **118**, 22935 (2014).

[7] K. Fukui, S. Iimura, T. Tada, S. Fujitsu, M. Sasase, H. Tamatsukuri, T. Honda, K. Ikeda, T. Otomo, and H. Hosono, *Characteristic fast* H^- *ion conduction in oxygen-substituted lanthanum hydride,* Nature Communications **10**, 2578 (2019).

[8] H. Ubukata, T. Broux, F. Takeiri, K. Shitara, H. Yamashita, A. Kuwabara, G. Kobayashi, and H. Kageyama, *Hydride conductivity in an anion-ordered fluorite structure LnHO with an enlarged bottleneck,* Chemistry of Materials **31**, 7360 (2019).

[9] H. Yamashita, T. Broux, Y. Kobayashi, F. Takeiri, H. Ubukata, T. Zhu, M. A. Hayward, K. Fujii, M. Yashima, K. Shitara, *et al.*, *Chemical pressure-induced anion order-disorder transition in LnHO enabled by hydride size flexibility,* Journal of the American Chemical Society **140**, 11170 (2018).

[10] K. Fukui, S. Iimura, J. Wang, T. Tada, T. Honda, K. Ikeda, T. Otomo, and H. Hosono, *Stabilization factor of anion-excess fluorite phase for fast anion conduction,* Chemistry of Materials **33**, 1867 (2021).

[11] D. Chaykina, T. W. H. de Krom, G. Colombi, H. Schreuders, a. Suter, T. Prokscha, B. Dam, and S. W. H. Eijt, *Structural properties and anion dynamics of yttrium dihydride and photochromic oxyhydride thin-films examined by in situ* μ^+*SR,* Physical Review B **103**, 224106 (2021).

[12] S. M. Aðalsteinsson, M. V. Moro, D. Moldarev, S. Droulias, M. Wolff, and D. Primetzhofer, *Correlating chemical composition and optical properties of photochromic rare-earth oxyhydrides using ion beam analysis,* Nuclear Instruments and Methods in Physics Research Section B: Beam Interactions with Materials and Atoms **485**, 36 (2020).

[13] M. Widerøe, H. Fjellvåg, T. Norby, F. Willy Poulsen, and R. Willestofte Berg, *NdHO, a novel oxyhydride,* Journal of Solid State Chemistry **184**, 1890 (2011).

[14] P. Vajda and J. N. Daou, *Rare Earths-Hydrogen,* Solid State Phenomena **49-50**, 71 (1996).

[15] G. G. Libowitz and A. J. Maeland, *Hydrides,* in *Handbook on the Physics and Chemistry of Rare Earths*, edited by K. A. Gschneidner, Yr. and L. Eyring (North-Holland Publishing Company, 1979) Book section 26, pp. 299–336.

[16] W. L. Korst and J. C. Warf, *Rare earth-hydrogen systems. i. structural and thermodynamic properties,* Inorganic Chemistry **5**, 1719 (1966).

[17] R. C. Heckman, *Hall effect and conductivity in the neodymium-hydrogen system,* J. Chem. Phys. **48**, 196 (1968).

[18] R. S. Gupta and S. Chatterjee, *Electronic energy bands and optical properties of* NdH_3, J. Phys. F: Met. Phys. **14**, 2549 (1984).

[19] P. Ngene, T. Radeva, M. Slaman, R. J. Westerwaal, H. Schreuders, and B. Dam, *Seeing hydrogen in colors: Low-cost and highly sensitive eye readable hydrogen detectors,* Advanced Functional Materials **24**, 2374 (2014).

[20] A. T. M. van Gogh, D. G. Nagengast, E. S. Kooij, N. J. Koeman, J. H. Rector, R. Griessen, C. F. J. Flipse, and R. J. J. G. A. M. Smeets, *Structural, electrical, and optical properties of* $La_{1-z}Y_zH_x$ *switchable mirrors,* Physical Review B **63** (2001), 10.1103/PhysRevB.63.195105.

[21] D. Kato, K. Hongo, R. Maezono, M. Higashi, H. Kunioku, M. Yabuuchi, H. Suzuki, H. Okajima, C. Zhong, K. Nakano, *et al.*, *Valence band engineering of layered bismuth oxyhalides toward stable visible-light water splitting: Madelung site potential analysis,* Journal of the American Chemical Society **139**, 18725 (2017).

[22] D. Oka, Y. Hirose, M. Kaneko, S. Nakao, T. Fukumura, K. Yamashita, and T. Hasegawa, *Anion-substitution-induced nonrigid variation of band structure in* $SrNbO_{3x}N_x$ $(0 \leq x \leq 1)$ *epitaxial thin films,* ACS Applied Materials & Interfaces **10**, 35008 (2018).

[23] G. Colombi, R. Stigter, D. Chaykina, S. Banerjee, A. P. M. Kentgens, S. W. H. Eijt, B. Dam, and G. de Wijs, *Energy, metastability, and optical properties of anion-disordered* REO_xH_{3-2x} *RE = (Y, La) oxyhydrides: a computational study,* Physical Review B **105**, 054208 (2022).

[24] C. Larquet, A.-M. Nguyen, E. Glais, L. Paulatto, C. Sassoye, M. Selmane, P. Lecante, C. Maheu, C. Geantet, L. Cardenas, *et al.*, *Band gap engineering from cation balance: The case of lanthanide oxysulfide nanoparticles,* Chemistry of Materials **31**, 5014 (2019).

[25] B. Malaman and J. F. Brice, *Etude structurale de l-hydruro-oxyde LaHO par diffraction des rayons X et par diffraction des neutrons,* Journal of Solid State Chemistry **53**, 44 (1984).

[26] J. Ueda, S. Matsuishi, T. Tokunaga, and S. Tanabe, *Preparation, electronic structure of gadolinium oxyhydride and low-energy 5d excitation band for green luminescence of doped* Tb^{3+} *ions,* Journal of Materials Chemistry C **6**, 7541 (2018).

[27] N. Zapp, H. Auer, and H. Kohlmann, *YHO, an air-stable ionic hydride,* Inorganic Chemistry **58**, 14635 (2019).

[28] N. Zapp, D. Sheptyakov, and H. Kohlmann, *Computational chemistry-guided syntheses and crystal structures of the heavier lanthanide hydride oxides DyHO, ErHO, and LuHO,* Crystals **11**, 750 (2021).

[29] F. Nafezarefi, S. Cornelius, J. Nijskens, H. Schreuders, and B. Dam, *Effect of the addition of zirconium on the photochromic properties of yttrium oxy-hydride,* Solar Energy Materials and Solar Cells **200**, 109923 (2019).

[30] D. Kutsuzawa, Y. Hirose, Y. Sugisawa, J. Kikuda, D. Sekiba, and T. Hasegawa, *Enhanced ferromagnetic transition temperature in* NdO_xD_y *epitaxial thin films,* Physical Review Materials **3**, 044408 (2019).

[31] G. Colombi, S. Cornelius, A. Longo, and B. Dam, *Structure model for anion-disordered photochromic Gd oxyhydride thin films,* The Journal of Physical Chemistry C **124**, 13541 (2020).

[32] M. P. Plokker, S. W. H. Eijt, F. Naziris, H. Schut, F. Nafezarefi, H. Schreuders, S. Cornelius, and B. Dam, *Electronic structure and vacancy formation in photochromic yttrium oxy-hydride thin films studied by positron annihilation,* Solar Energy Materials and Solar Cells **177**, 97 (2018).

[33] D. Moldarev, L. Stolz, M. V. Moro, S. M. Aðalsteinsson, I.-A. Chioar, S. Z. Karazhanov, D. Primetzhofer, and M. Wolff, *Environmental dependence of the photochromic effect of oxygen-containing rare-earth metal hydrides,* Journal of Applied Physics **129**, 153101 (2021).

[34] M. V. Moro, S. M. Aðalsteinsson, T. T. Tran, D. Moldarev, A. Samanta, M. Wolff, and D. Primetzhofer, *Photochromic response of encapsulated oxygen-containing yttrium hydride thin films,* physica status solidi (RRL) - Rapid Research Letters **15**, 2000608 (2021).

[35] E. M. Baba, J. Montero, E. Strugovshchikov, E. Ö. Zayim, and S. Karazhanov, *Light-induced breathing in photochromic yttrium oxyhydrides,* Physical Review Materials **4**, 025201 (2020).

[36] J. Chai, Z. Shao, H. Wang, C. Ming, W. Oh, T. Ye, Y. Zhang, X. Cao, P. Jin, S. Zhang, and Y.-Y. Sun, *Ultrafast processes in photochromic material* YH_xO_y *studied by excited-state density functional theory simulation,* Science China Materials **63**, 1579 (2020).

Appendix

3.A Optical transmission of uncoated & ALD coated $NdH_{3-2x}O_x$ films

Oxidation in ambient air is a necessary step for the formation of our $NdH_{3-2x}O_x$ films. However, likely due to the reactivity of neodymium, these films are not stable in air. This is visible by optical transmission measurements, where the transmission of a semiconductor has a characteristic shape. At low energy (long wavelength), the transparency should be high (limited only by the substrate) since this energy is not sufficient to excite carriers across the band gap. Once this threshold (band gap) is reached, however, the transparency decreases to zero and the light is absorbed.

It has been shown in previous work that the optical band gap of RE-oxyhydrides is related to the O^{2-}:H^- ratio, where more oxidised samples lead to larger band gaps [1]. Eventually, a fully oxidised sample (e.g., Nd_2O_3 or $Nd(OH)_3$) have band gaps so large that they are outside the measurement range of the equipment used here.

The evolution of the optical band gaps of uncoated Nd-oxyhydride films, thus, shows that the band gap expands rapidly, and a fully oxidised film is formed within 2 days of air-exposure. Nd-oxyhydride films coated by ALD maintain a more stable optical band gap (therefore, composition) for at least 5 months. We can compare a freshly ALD coated film to the change in transmission for an uncoated film. Although it appears that the band gap of the material expands during the ALD process, this new composition is maintained for at least 5 months.

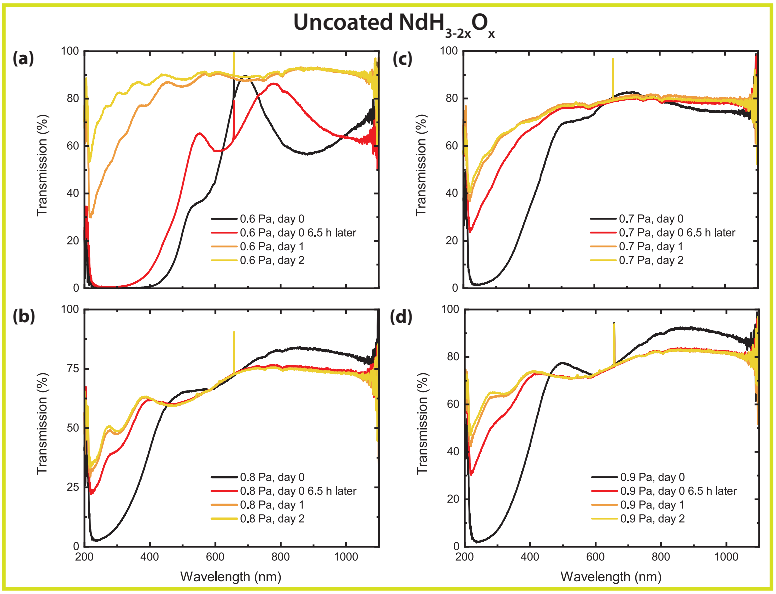

Figure 3.A.1: Optical transmission spectra for some Nd-oxyhydride thin films produced at different deposition pressures ($p_{dep} = 0.6 - 0.9$ Pa *without* a protective coating. Day 0 is the day of deposition and onset of air oxidation. The low transmission at short wavelengths is related to the band gap of the material. This absorption edge quickly shifts to the left (larger band gap), resulting in a completely oxidised (no H^-) compound by day 2 for all deposition pressures.

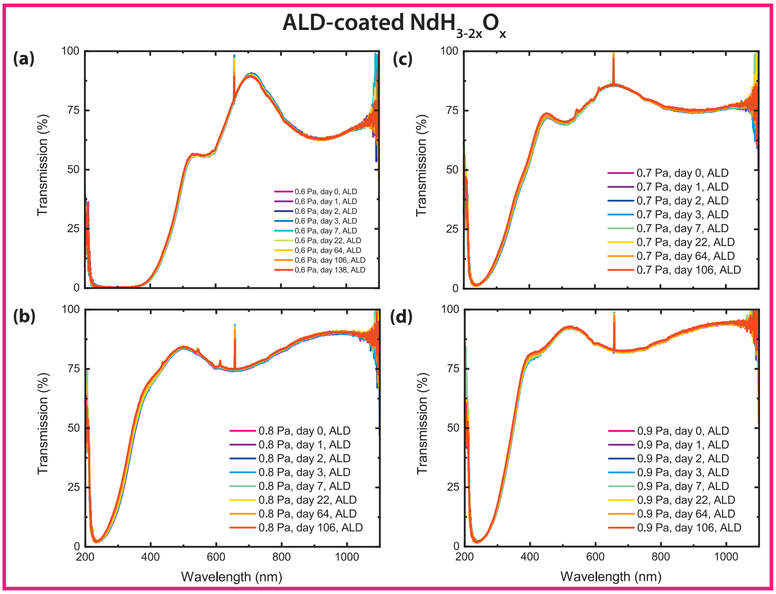

Figure 3.A.2: Optical transmission spectra for some Nd-oxyhydride thin films produced at different deposition pressures ($p_{dep} = 0.6 - 0.9$ Pa *with* a protective coating of Al_2O_3 deposited onto the films by ALD. Unlike the uncoated films, these Nd-oxyhydrides are stable in ambient air for at least 138 days since the absorption edge shows little-to-no shift over time. This implies that no signficant oxidation occurs for these films, substantially extending their lifetime.

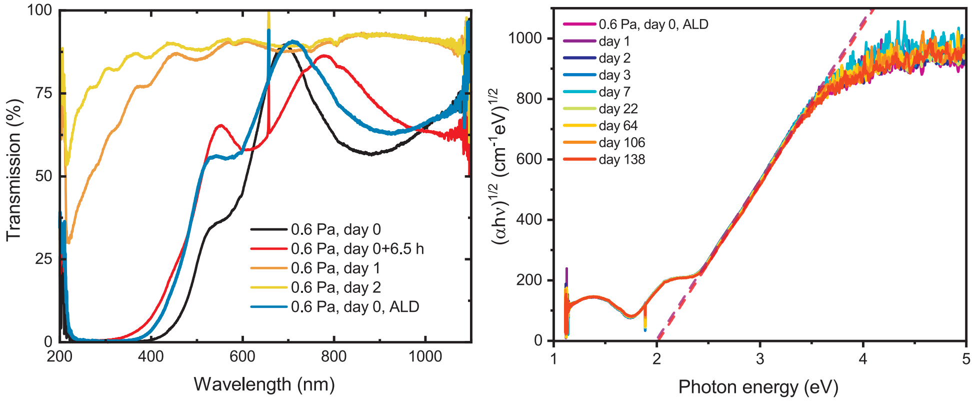

Figure 3.A.3: (left) A comparison of uncoated and coated Nd-oxyhydride films deposited at 0.6 Pa. The black line is the transmission spectrum of a film before ALD, and the blue line is after ALD. The band gap opens slightly during this process. Despite this oxidation, an ALD coated sample will maintain this composition for at least 138 days, unlike the uncoated film. (right) Tauc plots for the transmission data of ALD-coated Nd-oxyhydride films deposited at 0.6 Pa. Fitting lines for day 0 and day 138 are shown, where the x-intercepts (indicating the optical band gap) are similar. Shifts towards the right are related to an expansion of the optical band gap.

3.B Microscopy & imaging of ALD coating

Our $NdH_{3-2x}O_x$ films were coated by an ALD layer of Al_2O_3 to protect them from rapid oxidation. Below, we show the characterisation of this layer by atomic force microscopy (AFM) where we show that it is conformal (Fig. 3.B.1).

However, although this coating indeed protects our films from complete oxidation for at least 5 months, we noticed that imperfections can occur sometimes, for example, in the presence of dust (Fig. 3.B.2). The coating will deposit on the dust particle, which can fall off later and reveal either the substrate or a part of unprotected $NdH_{3-2x}O_x$. This results in pinholes in the coating which act as centres of oxidation. If there are enough pinholes, complete oxidation can take place. This is also a further testament to the positive function of the coating, without which, the samples cannot retain their composition.

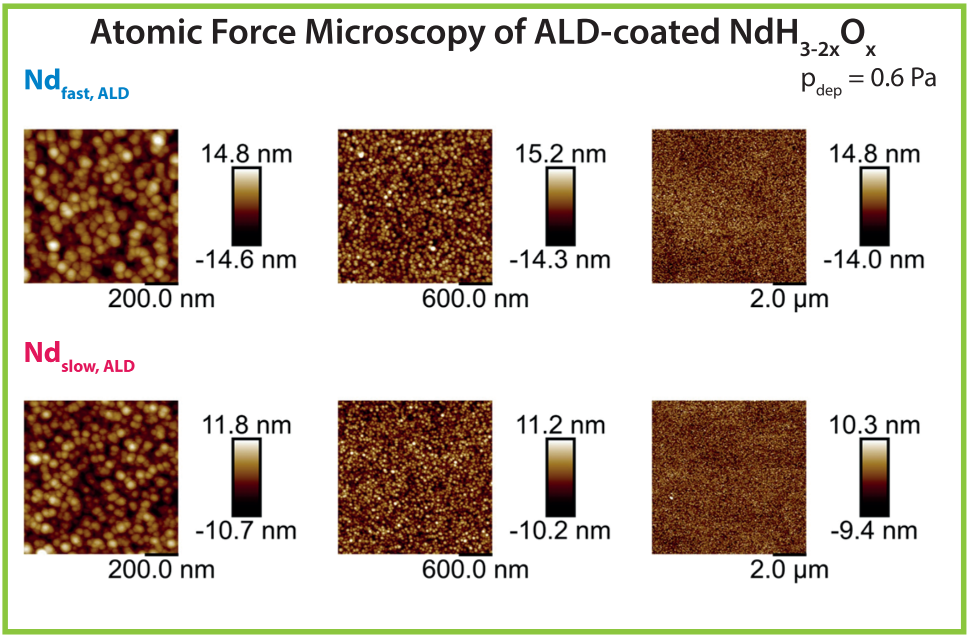

Figure 3.B.1: Topographic images of two $NdH_{3-2x}O_x$ films (p_{dep}) taken by atomic force microscopy (AFM) at different magnifications. The layer appears conformal over an area of several microns.

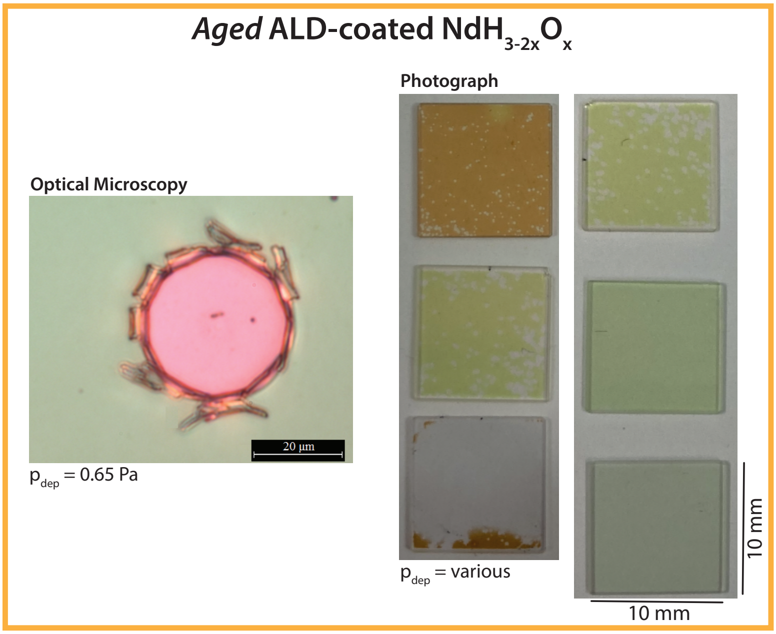

Figure 3.B.2: (left) Image of a pinhole in an ALD coated $NdH_{3-2x}O_x$ film (p_{dep} = 0.65 Pa) taken by differential interference contrast microscopy for optimal image contrast. (right) Photographs of 10x10 mm^2 ALD coated samples which are several months old showing various degrees of defects in their coating and extent of oxidation.

3.C Air-oxidation conditions for measured films

Table 3.C.1: List of all the oxyhydride samples considered in this work. p_{dep} is the deposition pressure used to sputter the sample, while “s" and “f" are used to denote which samples exhibited slow or fast bleaching kinetics, respectively. “Heat" refers to the set of samples which were treated for controlled amounts of time on the heated ALD deposition stage. The temperature is the average temperature during air-oxidation, and the transfer time is the time spent transferring the samples from the sputtering vacuum chamber to the ALD vacuum chamber (where a protective layer was deposited).

p_{dep} (Pa)	T (°C)	Transfer time (min)
0.6-**s**	21.4	2
0.6-**f**	21.5	36.5
0.65-**s**	21.6	3.5
0.65-**f**	20.3	2.5
0.7-**s**	20.3	2.5
0.7-**f**	21.6	1.5
0.8-**s**	22.1	2
0.8-**f**	20.8	3
0.9-**s**	20.8	3
0.9-**f**	20.3	2.5
0.6-**heat**	21.6	2.7

3.D ALD coating thickness determination

X-ray reflectometry (XRR) was performed to determine the layer thickness of the ALD deposited Al_2O_3 coating. For this purpose, an Al_2O_3 layer was deposited under exactly the same conditions on a fused quartz substrate. The XRR measurements were performed with a Bruker D8 Discover equipped with a Cu X-ray tube (Cu-kα, λ = 0.154 nm) and a LYNXEYE XE detector operating in 0D mode. The data, displayed in Figure 3.D.1 and fitted with GenX3 [2], reveal a layer thickness of 47 nm, a roughness of 0.9 nm, and a scattering length density of 1.0 r_eÅ^{-1} the Al_2O_3 layer, corresponding to a density of approximately 3.4 g/cm^3.

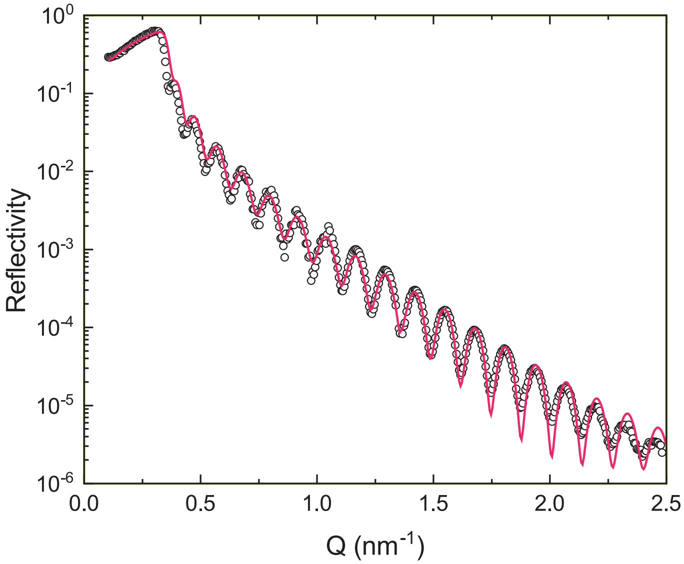

Figure 3.D.1: X-ray reflectometry measurement of the Al_2O_3 sample deposited on a fused quartz substrate under the same conditions as the Al_2O_3 deposited on the $NdH_{3-2x}O_x$ samples. The dots indicate the measurement points, while the continuous line indicates the fit to the data.

3.E Optical transmission of $NdH_{3-2x}O_x$ films below p^*

In our previous work on $REH_{3-2x}O_x$ thin films made by air-oxidation of REH_2, we have shown that there is a critical deposition pressure (p^*), above which, the oxyhydride phase is formed [1, 3]. Below we show the transmission spectra for two films made below this critical deposition pressure. Films made below p^* should largely maintain their RE-dihydride composition and oxidise very minimally. This is visible especially for the ALD coated films, whose transmission spectra do not show any changes for at least 21 days. For the uncoated films, however, the transmission spectra in the initial days after removal from the vacuum chamber show very low transmission (characteristic of a RE-dihydride), but later oxidise a bit. This is true primarily for the sample deposited at 0.5 Pa which, by day 41, resembles the transmission spectrum expected for an oxyhydride.

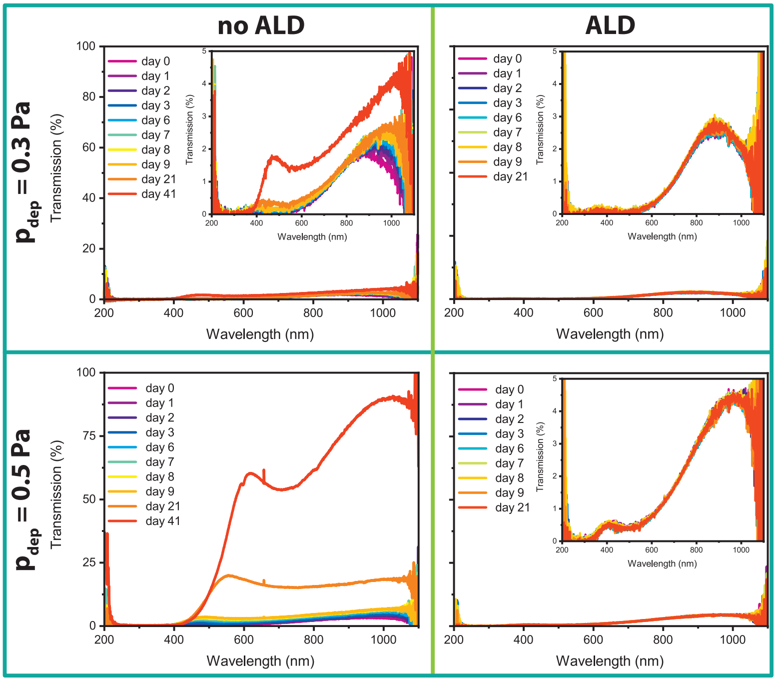

Figure 3.E.1: Nd-based films deposited at 0.3 (top) and 0.5 (bottom) Pa. The transmission spectra of these samples with (right) and without(left) an ALD coating were taken for several weeks after removal from the sputtering vacuum chamber. insets are provided to show the data at very low transmission. Samples coated with a protective layer retain their composition for at least 21 days, while samples without the coating progressively oxidise. This effect is more pronounced for the 0.5 Pa sample which resembles an oxyhydride by day 41.

3.F Optical band gap comparison to other RE-oxyhydrides

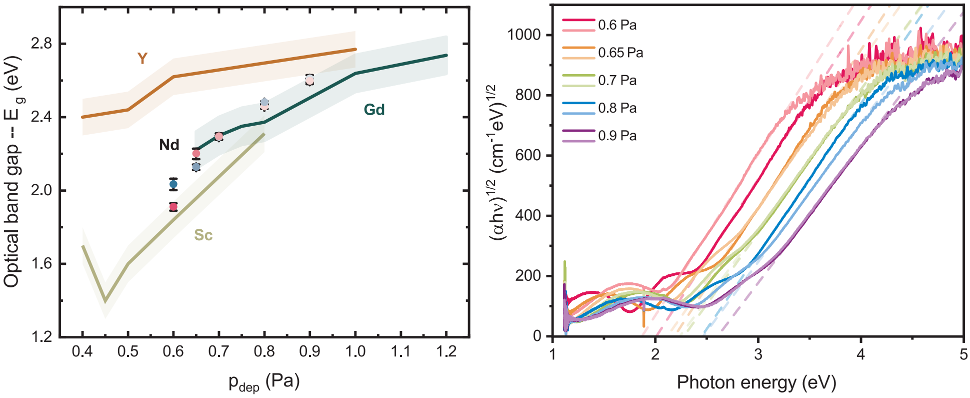

Figure 3.F.1: (left) The optical band gaps of Nd-based samples are shown with respect to deposition pressure, and compared to the results of Sc-, Y-, and Gd-base films from Ref. [1]. (right) Tauc plots for two samples at each sputtering deposition pressure used for this work. Fits of the linear region are shown as dotted lines and the x-intercepts are used to determine the optical band gaps.

3.G X-ray diffraction

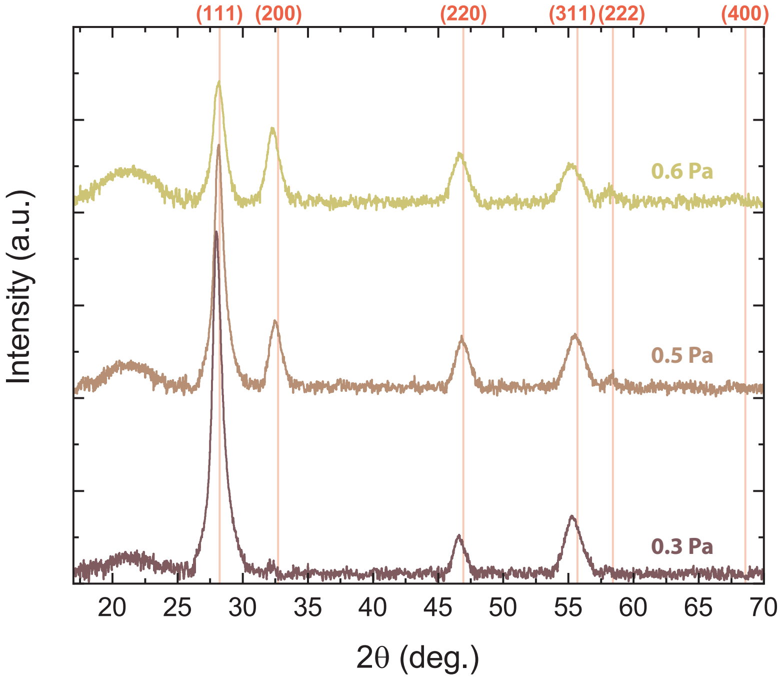

Figure 3.G.1: GI-XRD patterns for $NdH_{3-2x}O_x$ films made at and below the critical deposition pressure ($p^* \sim 0.6$ Pa). Samples made at 0.3 Pa resemble $NdH_{1.9+\delta}$, while an oxyhydride is obtained at 0.6 Pa. Red reference lines are for the fcc (cubic) $NdH_{1.9+\delta}$ pattern from ICDD-PDF database # 00-89-4199. The lattice of the 0.3 Pa is slightly larger than the reference pattern, and peaks are missing due to texture. The 0.5 and 0.6 Pa samples are tetragonal, thus, each peak shows a slightly different deviation from the cubic $NdH_{1.9+\delta}$ reference lines.

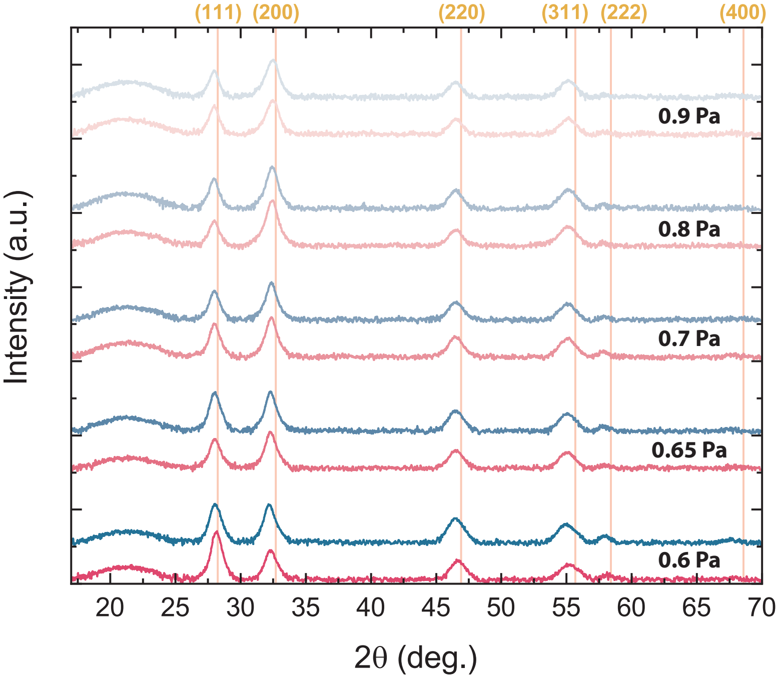

Figure 3.G.2: GI-XRD patterns for “slow” (pink) and “fast” (blue) bleaching $NdH_{3-2x}O_x$ films sputtered at various deposition pressures. The broad peak centred at around $2\theta = 21.5^{\circ}$ originates from the underlying fused silica substrate. Red reference lines are for the fcc (cubic) $NdH_{1.9+\delta}$ pattern from ICDD-PDF database # 00-89-4199. The (111) and (200) peaks, for example, deviate from the cubic NdH_2 reference lines to different extents due to the tetragonality of these samples.

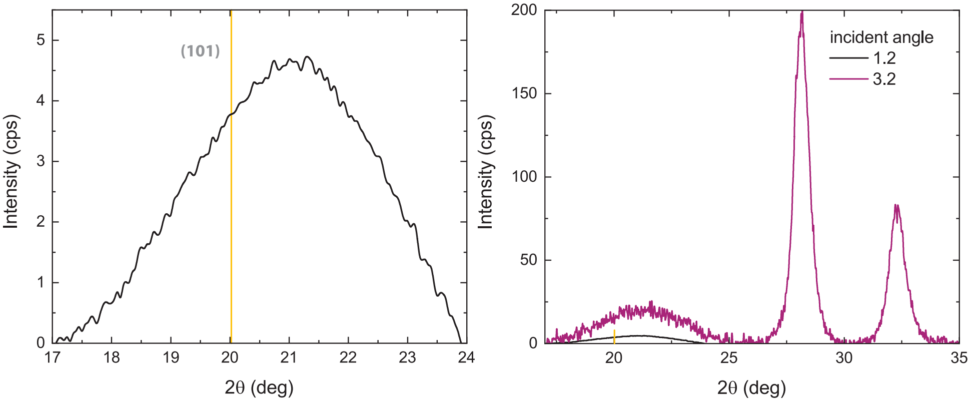

Figure 3.G.3: (left) GI-XRD signal obtained at low θ for a $NdH_{3-2x}O_x$ sample deposited at 0.6 Pa. The expected position of the (101) reflection is indicated by a yellow vertical line. This reflection is useful for discriminating between the most reported space groups for RE-oxyhydrides, $P4/nmm$ and $Fm\bar{3}m$, because it is only present for the former. However, even with careful scanning with a low incident angle (1.2°), only the signal of the underlying fused silica substrate is observable for one of the most tetragonal samples. (right) This low θ scan is compared to the data shown in Figure 3.G.2 for the same sample. According to the literature [4], the intensity of the (101) peak should be approximately 10 times lower than that of the (200) reflection. Based on that, we would expect the (101) reflection here to have an intensity of around 8 cps, which may be hidden under the substrate signal for incident angle 3.2°, but visible for 1.2°. However, others report an even lower intensity of the (101) [5, 6].

3.H Thin film texture & strain

Thin films can be analysed for their texture and macro-stress by measuring diffraction patterns at different values of ψ. The angle ψ defines the tilt of the sample perpendicular to the X-ray beam, allowing for the measurement of crystallites of different orientations. We measured four $NdH_{3-2x}O_x$ films with Bragg-Brentano (θ-2θ) geometry and a ψ angle varying between 0-80°. The full XRD patterns for this are shown in Figure 3.H.1. These four films can be compared to assess the influence of not only p_{dep}, but also $\tau_{B,50\%}$ since two of the films showed "slow" kinetics, and two showed "fast" kinetics (specified in Table 3.H.1).

Growing thin films can develop a "texture", meaning that, although the film is polycrystalline, these crystals have a preferred out-of-plane orientation. This increases the intensity of some reflections, while decreasing the intensity of others. In extreme cases, some reflections may even disappear, as we see for our $NdH_{1.9+\delta}$ film (Fig. 3.G.1).

To examine if our ALD coated $NdH_{3-2x}O_x$ films are indeed **textured**, we compared the intensity ratios of the (200) and (111) reflections as a function of ψ. We define the intensity ratio, δ, as:

$$\delta = \frac{I_{111}}{(I_{111} + I_{200})} \tag{3.1}$$

where I_{111} and I_{200} are the intensities of the (111) and (200) reflections, respectively. The results are shown in Figure 3.H.2. In case of random orientation, we expect a value of 0.55-0.67 for δ based on the structure factor and depending on composition. We find that δ changes slightly with p_{dep} which is a consequence of the differing compositions (structure factors) of these samples. As well, δ changes with ψ as different planes satisfy diffraction conditions with the change in tilt. Thus, we conclude that our films are only slightly textured.

Macro-strain is quantified by assessing the peak shifts for various ψ angles. This is done in Figure 3.H.3, where the peak shifts are displayed as $(d - d_o)/d_o$, and d_o is the value at $\psi = 0°$. This can be calculated for all the reflections which appear in the XRD pattern, however, the (220) and (222) reflection intensities were too low and reliable results could not be obtained. The slopes of the lines in Figure 3.H.3 give an indication of the macro-strain that is present in our films. Notably, the determination of macro-strain by this method relies on the assumption that the stress is uniform, isotropic, and biaxial. These assumptions are not true for weakly textured films, even so, they provide some valuable insights into the microstructural properties of our films.

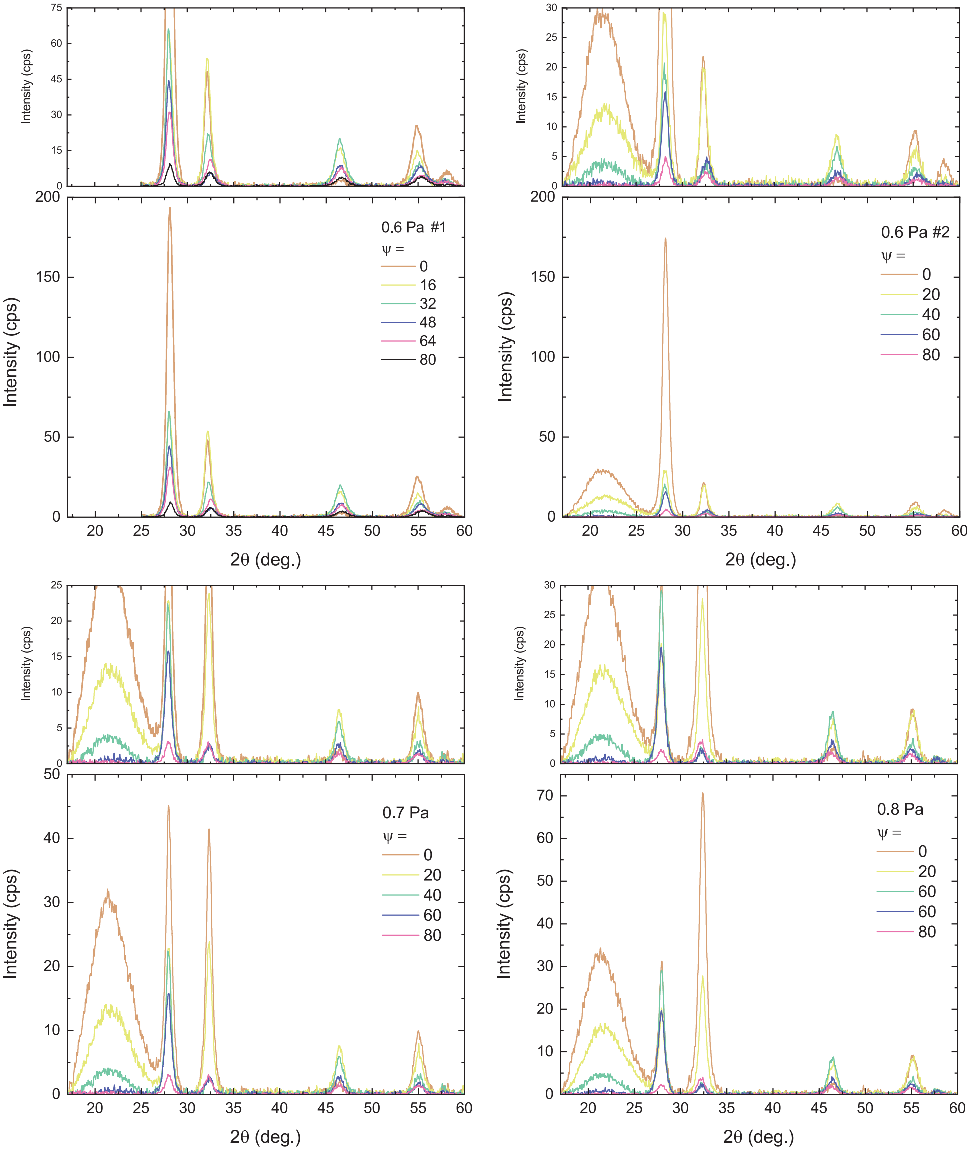

Figure 3.H.1: XRD patterns for the 4 $NdH_{3-2x}O_x$ films measured at different ψ angles. Above each graph showing the patterns is a zoom-in version showing the low intensity peaks obtained for high ψ values.

Table 3.H.1: Table comparing the extent of tetragonality of $NdH_{3-2x}O_x$ films to the amount of macrostrain they possess. The crystal structure of a thin film material can sometimes be misinterpreted due to the underlying stresses in the film. This can cause, for example, the assignment of a tetragonal lattice to a film which is actually cubic. However, we show here that the extent of tetragonality is always larger than the effect of macro-strain, confirming that our films are tetragonal. The macro-strain is obtained from the average of the three slopes fitted from Fig. 3.H.3, and converted to a percentage.

p_{dep} (Pa)	c/a	% tetragonality	% macro-strain
0.6-**f**	0.987	1.28	-0.15
0.6-**s**	0.988	1.23	-0.64
0.7-**f**	0.995	0.49	0.10
0.8-**s**	0.996	0.36	0.30

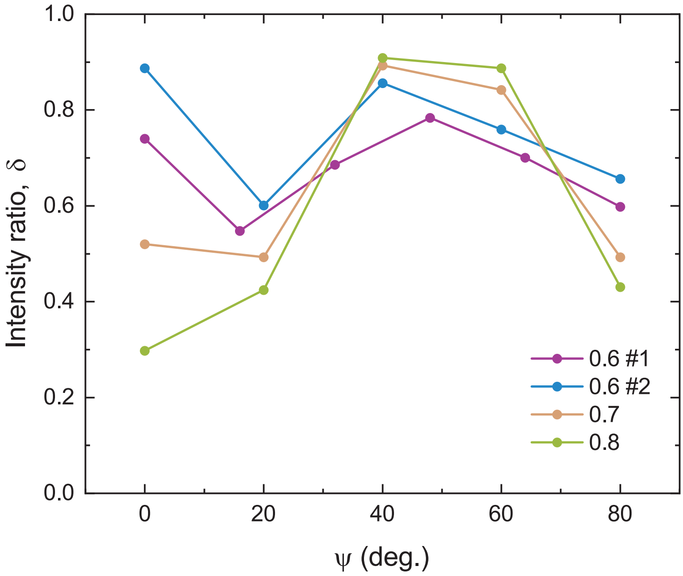

Figure 3.H.2: Intensity ratios (δ) of four $NdH_{3-2x}O_x$ films showing a slight preferential orientation towards the (200) reflection.

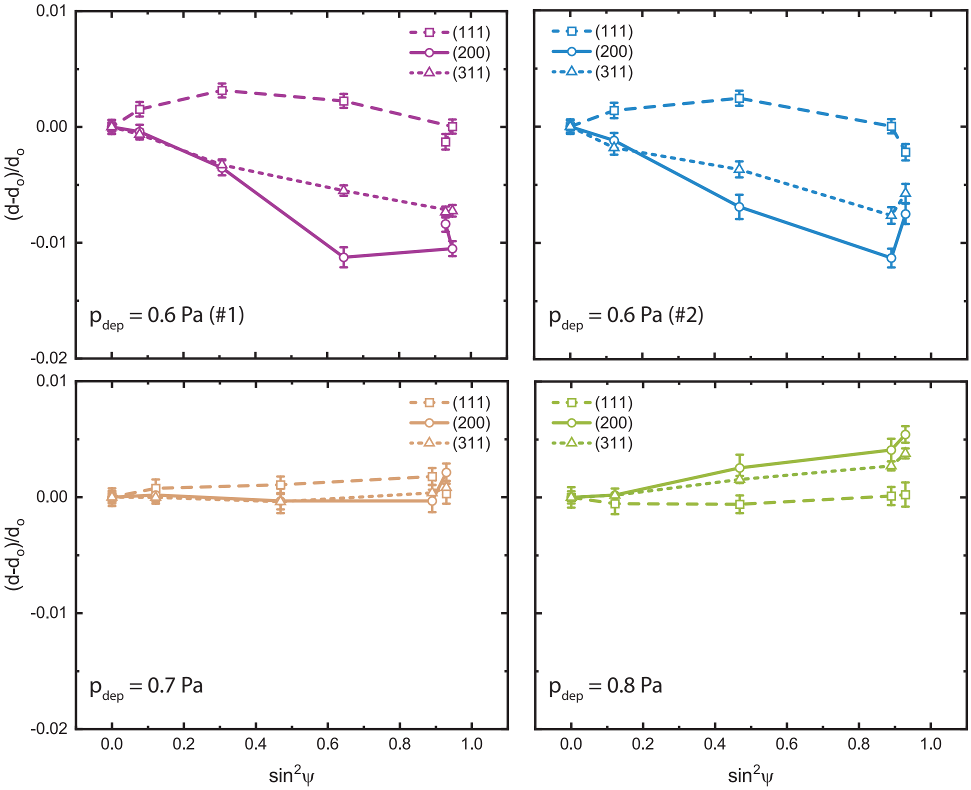

Figure 3.H.3: Analysis of macrostrain for 4 $NdH_{3-2x}O_x$ films. Dashed lines are derived from the (111) peak positions, solid lines from (200), and dotted lines from (311). The slopes of these lines are related to the macrostrain.

3.I Reference behaviour of uncoated & coated $GdH_{3-2x}O_x$ films

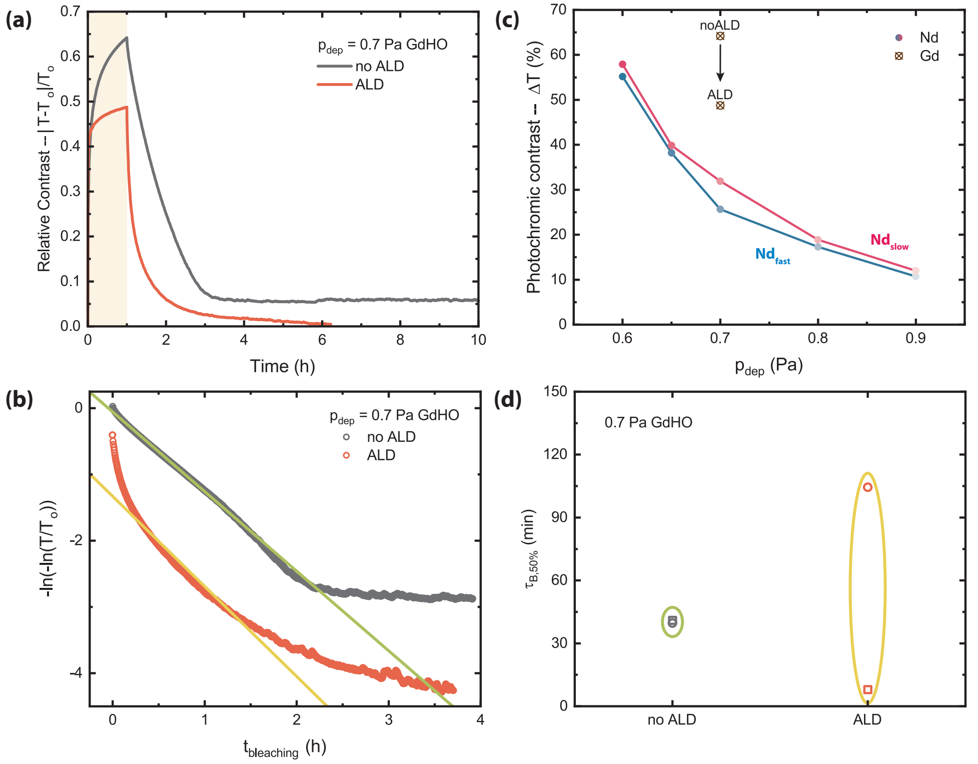

Figure 3.I.1: Since the photochromic effect in uncoated $NdH_{3-2x}O_x$ films cannot be reliably measured, we compare coated and uncoated $GdH_{3-2x}O_x$ films as a reference case for the effect of the protective layer: (a) Relative photochromic contrast for Gd-based films with (red) and without (grey) an ALD coating. (b) The bleaching of the coated (red) and uncoated (grey) Gd-based films shown in a double logarithm plot. Previous reports have used the slope of such a graph to obtain the negative reciprocal of the first-order bleaching rate constant [1, 3, 7]. This is in agreement with the bleaching of the uncoated sample, but does not describe the coated film. (c) Comparison of the photochromic contrast of Nd- and Gd-based films, along with the change in contrast for a Gd-based film when the ALD layer is applied. (d) The reproducibility of the bleaching time constant ($\tau_{B,50\%}$) is shown for uncoated and coated Gd-based films. The spread in values for uncoated films is very small, while for coated films, the variability is much larger.

3.J Heating of 0.6 Pa films

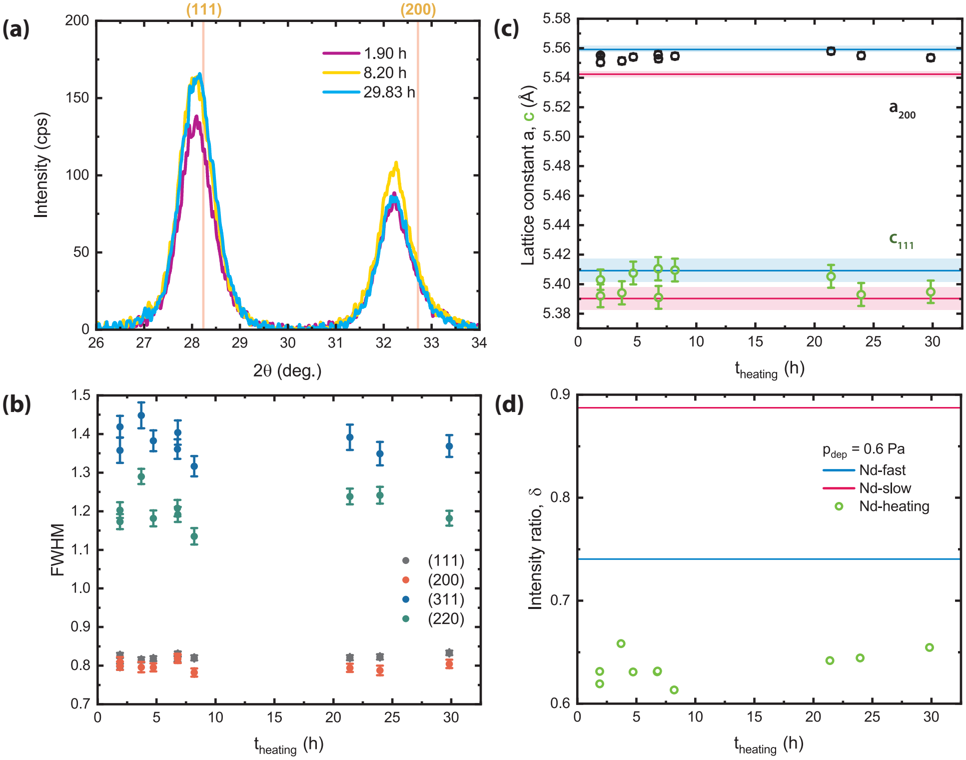

Figure 3.J.1: (a) GI-XRD patterns for three NdH$_{3-2x}$O$_x$ films (p_{dep} = 0.6 Pa) heated for various times at 87°C in the ALD chamber ($p \sim 2$ μbar). Only the (111) and (200) reflections are shown. Red reference lines are for the fcc (cubic) NdH$_{1.9+\delta}$ pattern from ICDD-PDF database # 00-89-4199. Several quantities can be derived from those XRD patterns such as (b) the full-width half-maxima of all the visible reflections, (c) the lattice constants a_{200} and c_{111}, and (d) the intensity ratio ($\delta = \frac{I_{111}}{(I_{111}+I_{200})}$). None of these quantities change significantly during ~30 h of heating at 87°C. The shaded pink and blue areas in (c) indicate the error associated with the lattice constant for slow and fast bleaching NdH$_{3-2x}$O$_x$ films (0.6 Pa), respectively. As well, in (d), the pink and blue lines show the intensity ratios for the slow and fast bleaching samples, respectively.

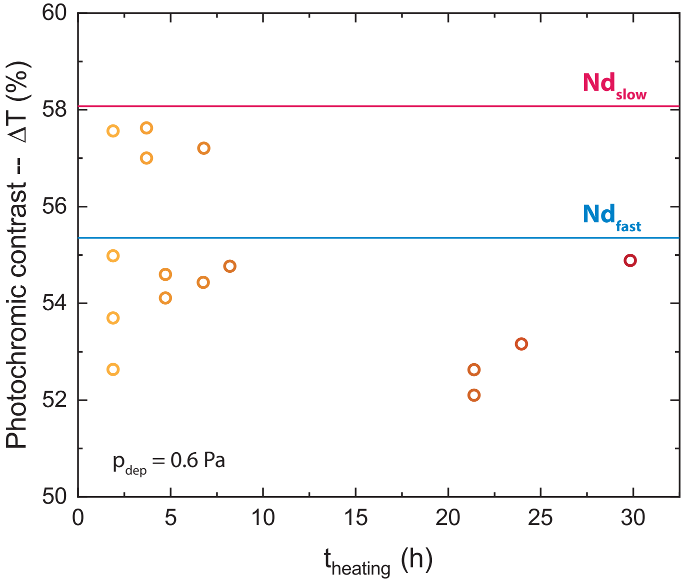

Figure 3.J.2: The photochromic contrast obtained for films heated for different durations in the ALD vacuum chamber. Pink and blue lines refer to the “slow” and “fast” bleaching samples presented in the main text Figure 3. No significant differences can be observed for the photochromic contrast with heating.

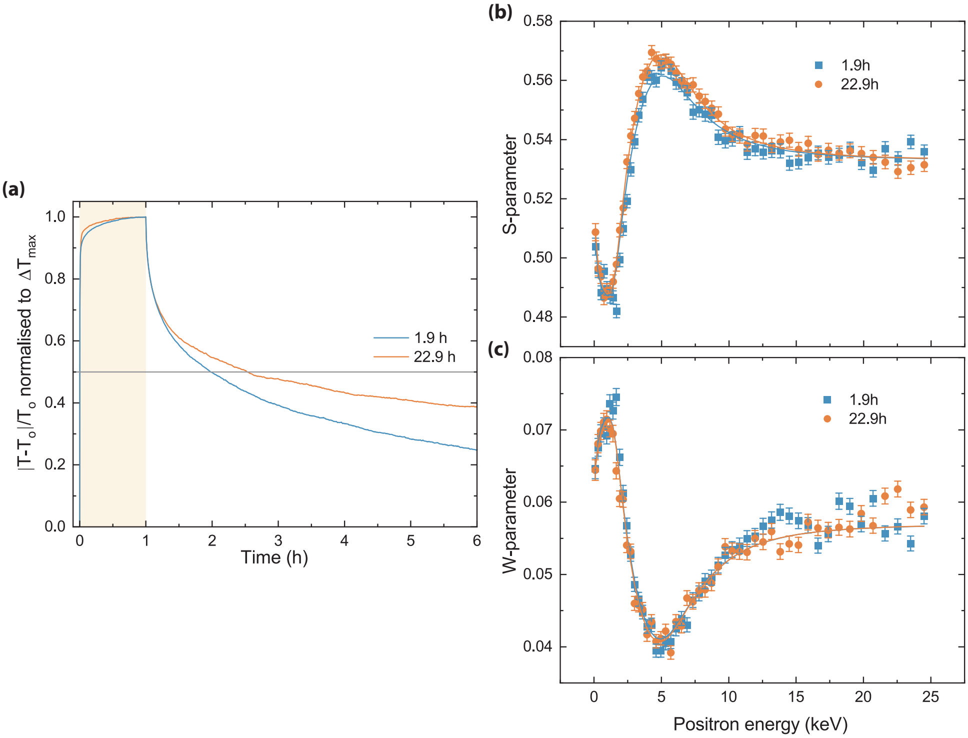

Figure 3.J.3: (a) Relative photochromic contrast normalised to the maximum contrast for $NdH_{3-2x}O_x$ films (p_{dep} = 0.6 Pa) heated for 1.9 h and 22.9 h. The bleaching speed becomes slower with progressively longer heating. To understand this effect, doppler broadening positron annihilation spectroscopy (DB-PAS) depth profiles were taken from which the (a) S- and (b) W-parameters can be derived. The results are shown in Table 3.J.1. The increase in S and decrease in W have been observed in $YH_{3-2x}O_x$ as permanent changes due to either heating [8] or illumination [1], potentially explained by the formation of neutral divacancies as anion vacancies are created (e.g., H_2 liberation). This is an example of one explanation for the changes that may occur during progressive heating.

Table 3.J.1: The S- and W-parameters derived from DB-PAS depth profiles for ALD-coated $NdH_{3-2x}O_x$ films (p_{dep} = 0.6 Pa) heated for 1.9 h and 22.9 h. The change in the two parameters is shown as a percentage. The bleaching speeds ($\tau_{B,50\%}$) are also shown based on Figure 3.J.3a with their percent difference.

heating time (h)	S-parameter	W-parameter	$\tau_{B,50\%}$ (min)
1.9	0.573 ± 0.001	0.036 ± 0.0003	58.5
22.9	0.581 ± 0.001	0.0356 ± 0.0003	91.8
	+1.4 %	-1.1%	+57%

3.K Photochromism & lattice constant comparison to other RE-oxyhydrides

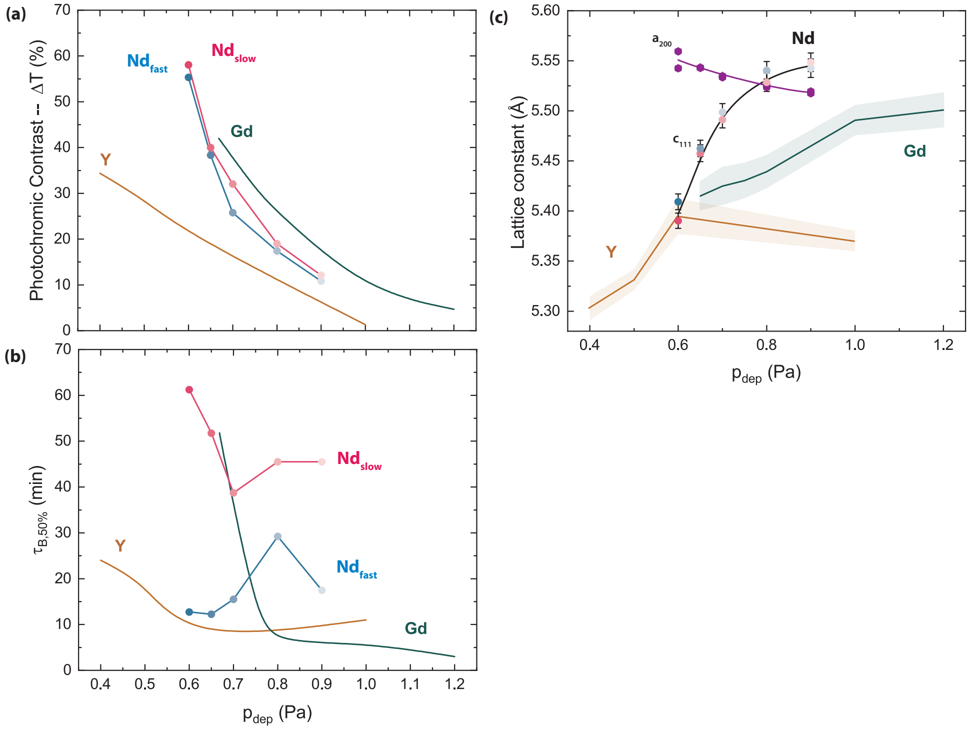

Figure 3.K.1: A comparison of our coated $NdH_{3-2x}O_x$ films to the uncoated Y- and Gd-based films from Ref. [1] with respect to (a) photochromic contrast, (b) bleaching speed, and (c) lattice constant. In terms of photochromism, the Y- and Gd-films were half the thickness of our $NdH_{3-2x}O_x$ films, and the illumination time was also half of what we use in this work. Additionally, the Y- and Gd-films exhibit a cubic crystal structure, so only one lattice constant (a) is given for them.

References

[1] G. Colombi, T. De Krom, D. Chaykina, S. Cornelius, S. W. H. Eijt, and B. Dam, *Influence of cation (RE = Sc, Y, Gd) and O/H anion ratio on the photochromic properties of* REO_xH_{3-2x} *thin films,* ACS Photonics **8**, 709 (2021).

[2] M. Björck and G. Andersson, *GenX: an extensible X-ray reflectivity refinement program utilizing differential evolution,* Journal of Applied Crystallography **40**, 1174 (2007).

[3] F. Nafezarefi, H. Schreuders, B. Dam, and S. Cornelius, *Photochromism of rare-earth metal-oxy-hydrides,* Applied Physics Letters **111**, 103903 (2017).

[4] H. Ubukata, T. Broux, F. Takeiri, K. Shitara, H. Yamashita, A. Kuwabara, G. Kobayashi, and H. Kageyama, *Hydride conductivity in an anion-ordered fluorite structure LnHO with an enlarged bottleneck,* Chemistry of Materials **31**, 7360 (2019).

[5] M. Widerøe, H. Fjellvåg, T. Norby, F. Willy Poulsen, and R. Willestofte Berg, *NdHO, a novel oxyhydride,* Journal of Solid State Chemistry **184**, 1890 (2011).

[6] H. Yamashita, T. Broux, Y. Kobayashi, F. Takeiri, H. Ubukata, T. Zhu, M. A. Hayward, K. Fujii, M. Yashima, K. Shitara, *et al.*, *Chemical pressure-induced anion order-disorder transition in LnHO enabled by hydride size flexibility,* Journal of the American Chemical Society **140**, 11170 (2018).

[7] F. Nafezarefi, S. Cornelius, J. Nijskens, H. Schreuders, and B. Dam, *Effect of the addition of zirconium on the photochromic properties of yttrium oxy-hydride,* Solar Energy Materials and Solar Cells **200**, 109923 (2019).

[8] M. P. Plokker, S. W. H. Eijt, F. Naziris, H. Schut, F. Nafezarefi, H. Schreuders, S. Cornelius, and B. Dam, *Electronic structure and vacancy formation in photochromic yttrium oxy-hydride thin films studied by positron annihilation,* Solar Energy Materials and Solar Cells **177**, 97 (2018).

4

Aliovalent Ca-doping of yttrium oxyhydride thin films & implications for photochromism

> *"I'm not the smartest fellow in the world, but I can sure pick smart colleagues."*
> *— Franklin D. Roosevelt*

To develop an understanding of the photochromic effect in rare-earth metal oxyhydride thin films ($REH_{3-2x}O_x$, here RE = Y), we explore the aliovalent doping of the RE-cation. We prepared Ca-doped yttrium oxyhydride thin films ($(Ca_zY_{1-z})H_xO_y$) by reactive magnetron co-sputtering with Ca-doping concentrations between 0-36% (atomic %). All of the films are semiconductors with a constant optical band gap for Ca-content below 15%, while the band gap expands for compositions above 15%. Ca-doping affects the photochromic properties, resulting in: (1) a lower photochromic contrast, likely due to a lower H^- concentration, and (2) a faster bleaching speed, caused by a higher pre-exponential factor. Overall, these results point to the importance of the H^- concentration for the formation of a "darkened" phase, and the local rearrangement of these H^- for the kinetics of the process.

This chapter is partly based on *D. Chaykina, et al., "Aliovalent Ca-doping of Yttrium Oxyhydride Thin Films and Implications for Photochromism," The Journal of Physical Chemistry C, 126 (34), 14742–14749, 2022.* [1].

4.1 Introduction

Rare-earth metal oxyhydrides ($REH_{3-2x}O_x$) are multi-anion compounds which have gained attention in recent years because they exhibit a photochromic effect [2]. Thin films of $REH_{3-2x}O_x$ (RE = Sc, Y, Nd, Gd, Dy, Er) [3–7] are transparent semiconductors which "darken", or become opaque, when exposed to light with photon energy greater than their band gap ($E_{incident} > E_g$). When this light is removed, the materials return to their transparent state. Although this so-called photochromic effect is promising for applications such as smart windows, the precise mechanism involved in this effect is yet unknown.

Many properties have been evaluated for their influence on photochromism such as the anion and cation compositions [3, 5], and the defects or inhomogeneities present in the film [6, 8]. One explanation for photochromism has emerged involving a structural rearrangement [9, 10], perhaps by local diffusion [11], to segregate a metallic phase [2, 12, 13] of high H^- content [8, 12, 13]. On the other hand, some suggest the formation of in-gap states by H_2 [14] or OH^- [15] generation, as well as H^- exchange between phases [16].

What all these ideas have in common is the displacement of H^- by some mechanism for the creation of a meta-stable "darkened" phase. The mobility of this ion may be enhanced by the creation of anion vacancies throughout the structure, which can be achieved by aliovalent doping. This method involves substituting a cation in the material by one of a lower oxidation state, and creating anion vacancies to maintain charge neutrality. Using this method for (perovskite) oxyhydrides [17] and (rare-earth metal) oxychlorides [18, 19] resulted in improved anion mobility. Here, we dope yttrium oxyhydrides with calcium (Ca^{2+} vs. Y^{3+}) in order to assess the effect of this on especially the kinetics of the photochromic effect. Until now, it has been shown that a larger O:H ratio results in a faster bleaching speed, but it is not clear if this is due to the increase in O^{2-}-content or the associated anion vacancies [5].

We show that we can successfully dope yttrium oxyhydride thin films with calcium in the range of 0-36% Ca. To compensate for this substitution, the concentration of H^- ions appears to be reduced, while the concentration of O^{2-} increases slightly. Above a Ca-content of ~15%, the lattice is strained anisotropically, and the optical band gap expands, which may be related processes. All of the films are photochromic, and show a reduction of the photochromic contrast with the substitution of Y for Ca. We propose that the Ca substitution reduces the fraction of octahedral H^- and that these entities are important for formation of a "darkened" phase. The bleaching speed is faster as Ca is substituted into the structure due to an increased pre-exponential factor which we attribute to the greater fraction of octahedral vacancies.

4.2 Experimental Methods

Ca-doped yttrium oxyhydride thin films ($(Ca_zY_{1-z})H_xO_y$, ~300 nm) were prepared by reactive magnetron co-sputtering of Ca (MaTecK, 99.9%) and Y (Stanford, 99.99%) metal targets onto 10×10 mm quartz plates (MaTecK) at room temperature (~21°C) and an Ar/H_2 (7:1 flow) atmosphere. Following from our previous work on $REH_{3-2x}O_x$ thin films (RE = Sc, Y, Nd, Gd, Dy, Er) [3–6], the combined Ar/H_2 deposition pressure (p_{dep}) affects the as-deposited RE-dihydride; we found that if p_{dep} is below a critical pressure ($p^* \sim 0.4$ Pa for Y) [3, 5], the film remains a metallic RE-dihydride, but above p^*, it forms a semiconducting oxyhydride upon ambient air-exposure (Fig. 4.1). Similarly, we find that upon air exposure, the as-deposited CaY-hydride films become semiconducting, although some of the films already seem to incorporate oxygen when measured in the glovebox before air-exposure (glovebox: [H_2O] and [O_2] < 0.1 ppm), perhaps due to oxidation from residual gasses [20]. For this work, we used only one p_{dep} of 0.5 Pa in order to survey the effect of Ca-doping on the photochromic properties, using a range of Ca-concentrations (atomic %). Co-sputtering was achieved by altering the input DC power to the two targets while keeping a constant total metal flux (Fig. 4.A.1, Table 4.A.1) of YH_2 and Ca (Fig. 4.A.2). Before deposition, the chamber was kept at a base pressure below 10^{-6} Pa.

The composition of the $(Ca_zY_{1-z})H_xO_y$ films was measured by ion beam analysis using Rutherford backscattering (RBS) and elastic recoil detection (ERD). RBS (ERD) was performed at the DIFFER Ion Beam Facility using a 2.5 MeV ^{4}He ion beam at a 0° (75°) incident angle and 170° (23°) scattering angle. The former is used to analyse heavy elements (Ca, Y, O), while the latter is sensitive to light elements (H). For ion beam analysis, the $(Ca_zY_{1-z})H_xO_y$ thin films were deposited onto glassy carbon substrates (8×8 mm) and Si wafers with a native oxide (SiO_2/Si, 10×10 mm). The thickness of these films was ~150 nm. RBS/ERD data was fitted using SIMNRA [21, 22].

Dopper broadening positron annihilation spectroscopy (DB-PAS) was used to probe the phase nature of the Ca-doped yttrium oxyhydride thin films. Depth profiles were collected at room temperature by varying the positron (e^+) implantation energy between 0.1 and 25 keV with the variable energy positron beam (VEP) facility at the Reactor Institute Delft. The energy distribution of the annihilation γ-rays was measured with a high purity Ge detector (cooled by liquid nitrogen) which has an energy resolution of 1.2 keV. The resulting S- and W-parameters were fitted using the VEPFIT programme.

X-ray diffraction (XRD, Bruker D8 Discover) was used to study the effect of Ca-doping on the crystal structure of Y-oxyhydride thin films in grazing incident geometry (GI-XRD, incident angle = 2°, primary = 40 mm Goebel mirror with 0.6 mm equatorial slit and 2.5°

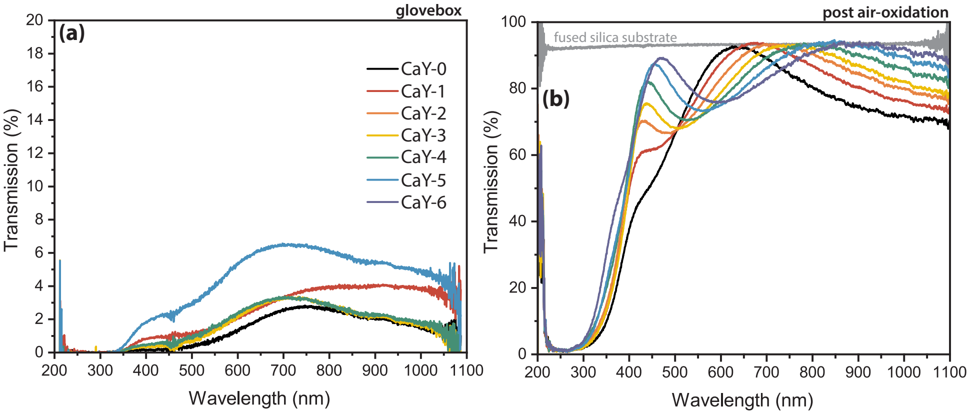

Figure 4.1: Optical transmission spectra for Ca-doped Y-based thin films (a) in the glovebox before oxidation, and (b) post air-exposure, showing the dihydride and oxyhydride phases, respectively. Samples CaY-0 to CaY-6 correspond to the Ca-contents which vary from 0% to 36% (see Fig. 2(c)).

axial Soller slit, secondary = 0.2° equatorial Soller slit, LynxEye XE detector in 0D mode) and a Cu source. To find the d-spacing for each peak, they were fit by a double pseudo-Voigt function considering both $K_{\alpha 1}$ and $K_{\alpha 2}$.

First-principle density functional theory (DFT) calculations were conducted with the Vienna *Ab-initio* Simulation Package (VASP) [23, 24] on model structures of $(Ca_zY_{1-z})H_{3-2x-z}O_x$ (x = 0.75, z ~ 3% to 20%) based on the special quasi random structures (sQS) of our previous work [25]. Within the scheme of the projector augmented wave (PAW) method [26, 27], a plane-wave basis set is used and periodic boundary conditions are applied. Standard frozen core PAW potentials are used, and the H 1s, O 2s2p, Y 4s4p4d5s, and Ca 3s3p4s are treated as valence shells. For each structure, all cell parameters and atomic positions are simultaneously optimized employing the PBE generalized gradient approximation for the exchange-correlation functional [28, 29]. After that, the modified Becke-Johnson (mBJ) exchange potentials in combination with L(S)DA-correlation have been used to compute the electronic properties [30, 31]. In all cases, integrations over the Brillouin zone are performed on a $3 \times 3 \times 3$ Γ-centred K-mesh using a Gaussian smearing of 0.05 eV, and convergence (δE <0.1 meV) is reached with a kinetic energy cut-off of 850 eV.

4

Optical transmission spectra were measured by a custom-built set-up consisting of an optical-fibre spectrometer, a deuterium/quartz tungsten halogen lamp (DH2000-BAL, Ocean Optics B.V.), and a Si array wavelength-dispersive spectrometer (HR4000, Ocean Optics B.V.). Optical band gap energies were determined using the Tauc method [32] (Fig. 4.B.1). Photochromism was measured by illuminating the thin films for 1 h with a narrow wavelength LED ($\lambda = 385$ nm, $I \sim 75$ mW/cm^2). The average transmission ($\lambda = 450 - 1000$ nm) was plotted with respect to time at room temperature (~21.5°C). After illumination, the film was left to "bleach" until its original transparency was recovered. Temperature sweeps were done with the addition of heating at the sample stage (25-55°C).

4.3 Results & Discussion

4.3.1 Composition & Phase Nature

The compositions of rare-earth metal oxyhydride thin films (made by post-oxidation of the as-deposited RE-dihydride) have been assessed in our previous work using RBS and ERD, finding that the empirical formula $REH_{3-2x}O_x$ (RE = Sc, Y, Gd) describes these materials well [4]. Starting from the $REH_{1.9}$, upon exposure to air, tetrahedral H^- is partly replaced by O^{2-}, displacing part of the hydride ions to the octahedral positions [33]. In the case of aliovalent doping of $YH_{3-2x}O_x$ with Ca, we expect that one anionic charge should be removed for every Ca cation substituted. Therefore, we evaluated the compositions of our films in terms of: (1) the Ca:Y ratios, and (2) the relative change in the anion (O^{2-}, H^-) content.

Figure 4.2 shows the results of this composition analysis (full spectra in Fig. 4.C.1) for $YH_{1.9+\delta}$ (reference without Ca or O, grey), $YH_{3-2x}O_x$ (reference without Ca, black), and a series of doped Y-oxyhydrides with progressively higher Ca-content. The samples are referred to as CaY-#, with CaY-0 having 0% Ca doping and CaY-6 having the highest Ca-content. Comparing first the cations, Figures 4.2a and b show the tandem decrease of the Y peak and increase of the Ca peak intensities, suggesting that the cationic ratio was successfully changed by adjusting the DC power to the metal targets during sputtering.

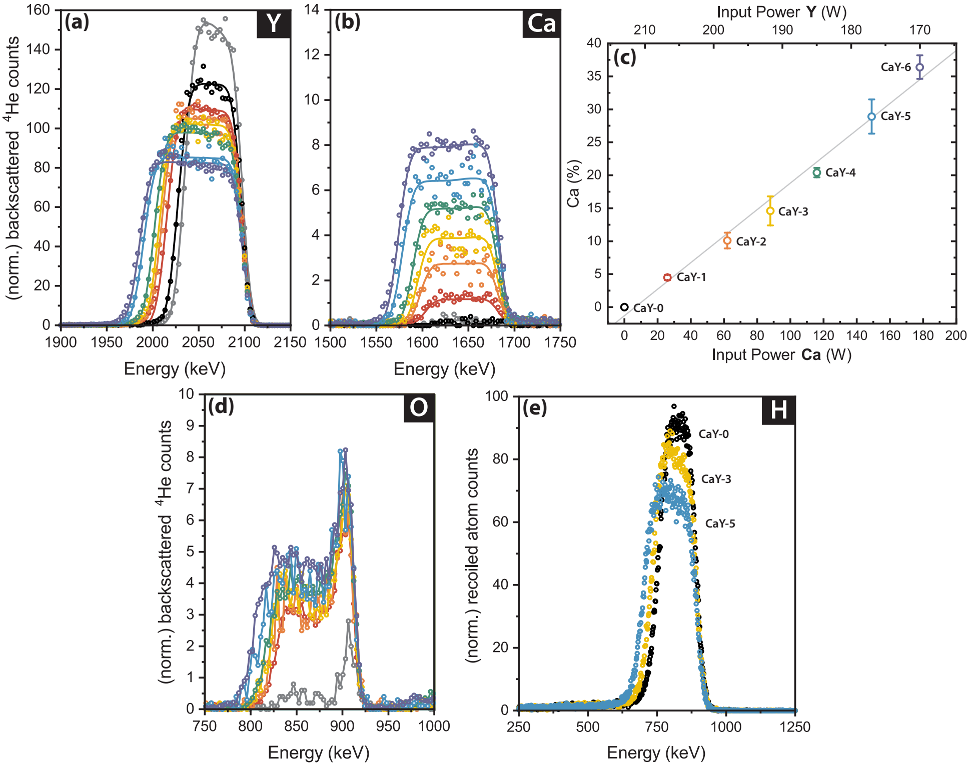

Figure 4.2: Overview of the compositions of Ca-doped oxyhydride thin films $(Ca_zY_{1-z})H_xO_y$. For (a) and (b), the lines are from simulations of the composition using SIMNRA. RBS data for (a) yttrium, (b) calcium, and (d) oxygen are shown for $YH_{1.9+\delta}$ and a series of oxyhydrides with gradually higher Ca-content, where the black points are for CaY-0 (0% Ca) and purple points are for CaY-6 with the most Ca. (c) The Ca-content calculated from RBS along with the input power to the Ca and Y targets during co-sputtering showing the linear relationship. (e) ERD results for hydrogen as more calcium is added to yttrium oxyhydride. All RBS and ERD data are normalised to account for differences in accumulated charge.

Plotting this ratio against the input power during sputtering (Fig. 4.2c) reveals a roughly linear relationship.

For the anions, we qualitatively conclude that the concentration of O does not strongly depend on the Ca/Y ratio (Fig. 4.2d), while the H content decreases more significantly with the addition of Ca (Fig. 4.2e). Apparently, in the given oxidation conditions, this substitution results primarily in the formation of hydride vacancies (instead of oxide vacancies) to maintain charge neutrality.

The phase nature of these films is important to assess, since Ca is a highly reactive element with a strong tendency towards oxidation, and one can imagine that phase segregation may occur where Ca creates a secondary phase within the Y-oxyhydride matrix instead of participating in aliovalent doping of the oxyhydride. First, we address the presence of a metallic Ca phase within the oxyhydride. From optical transmission measurements of the $Ca_zY_{1-z}H_x$ films in the glovebox before air-exposure (Fig. 4.1a), the addition of Ca did not lower the transmission of the material compared to the undoped $YH_{\sim 1.9}$. While the sub-stoichiometric $YH_{\sim 1.9}$ has a transparency window in the visible region [34], Ca metal is completely opaque, and the presence of a separate Ca phase would, thus, lower the overall transmission of the material [35]. After air-exposure, the maxima of transmission (caused by thin film interference) touch the transmission of the substrate, meaning that the films have the maximum transparency possible. Had there been a metallic phase, this value would also be lowered. As well, positron annihilation spectroscopy (Fig. 4.D.1) can be used to rule out the presence of small metallic secondary phases since the positron may annihilate preferentially in metallic centres [8, 36, 37]. When a significant amount of Ca metallic domains would have been formed, a larger increase in the positron Doppler broadening S-parameter is expected than what is observed here [8, 38]. Two samples with either 0% or 20% Ca have nearly the same S-parameter (Fig. 4.D.1, Table 4.D.1), suggesting that no metallic phases are present in either case, and that their cation vacancy structure is similar.

Next, it is also possible that CaH_2 forms a secondary phase within the Y-oxyhydride matrix. However, from the optical transmission measurements shown in Fig. 4.1a, the optical band gap which emerges before air-exposure resembles that of the oxyhydride phase (~2.5 eV), rather than the CaH_2 phase (~4.4-5.2 eV) [39, 40]. This is likely due to the partial pressure of H_2 used during sputtering, which may be too low to achieve the CaH_2 state (Fig. 4.A.2). The appearance of an optical band gap before air-exposure could instead be due to small amounts of O_2 contamination in the glovebox introduced during sample transfer. As well, the reduction of the H peak from ERD with the addition of Ca suggests that there is no CaH_2 formation (Fig. 4.2e), because the presence of this phase would not require H to leave the sample to maintain charge neutrality.

Last, we address the possibility of oxidised Ca phases (CaO, $Ca(OH)_2$) within the Y-oxyhydride matrix. Based on the optical transmission spectra of the films after air-exposure (Fig. 4.1b), the transmission and band gap appear to be similar to the oxyhydride phase. Ca-oxides and -hydroxides have larger band gap energies than the oxyhydride, so they are not visible in the transmission spectra. However, we do not see evidence of any secondary phases in the XRD patterns (Fig. 4.3a). Thus, we conclude that no crystalline oxide nor hydroxide phases of calcium form in the film.

Therefore, we propose that the thin films discussed here are single phase Ca-doped Y-oxyhydrides ($(Ca_zY_{1-z})H_xO_y$), where Ca substitutes for Y in the lattice (0-36% Ca, atomic %), and the H^- fraction decreases for charge neutrality. There are many examples of single phase compounds containing both yttrium and calcium such as hydrides [39, 41], fluorides [42], and others [43, 44]. The success of this substitution involving Ca and Y may be attributed to the similar ionic radii of these two elements (Ca^{2+} = 1-1.12 Å, Y^{3+} = 0.9-1.02 Å) [45]. To this long list of single phase Ca/Y compounds, we suggest to add Ca-doped Y-oxyhydrides for which we find that a stable thin film can be synthesised for a Ca-content of at least 0-36%.

4.3.2 Structure

We investigate the crystal structures of our films using grazing incident X-ray diffraction (GI-XRD), as shown in Figure 4.3a and Figure 4.E.1. Thin films of $YH_{3-2x}O_x$ made by the same methods as used here are face-centred cubic (fcc, $Fm\bar{3}m$) [3–5, 46]. The GI-XRD patterns in Figure 4.3a show the expected reflections for a fcc lattice for all samples regardless of Ca-doping. However, we could not identify a unique lattice constant for all of these films. We use the vertical grey lines to denote the 2θ reflections of CaY-0 (or $YH_{3-2x}O_x$ with 0% Ca) and illustrate how Ca-doping influences these peak positions. With increasing Ca-content, the (111) reflections remain at the same position as the 0% sample, while the other reflections shift to different 2θ for Ca concentrations >5%.

To better visualise this effect, the relative d-spacing (with respect to the undoped film) for each reflection is shown in Figure 4.3b. The d_{111} plane is constant for all Ca-doping concentrations, while the other planes expand upon increasing Ca-doping. Importantly, they do not expand to the same extent, with the d_{200} plane expanding by 0.4%, while the d_{220} and d_{311} planes by ~0.6-0.7% when comparing 0% and 36% Ca. This suggests that the lattice is strained in specific directions by the addition of Ca. This strain deforms the lattice by <1%, such that it is no longer cubic, but rather an orthorhombic lattice where $a \neq b \neq c$. This lattice strain may be caused by the slight difference in the ionic radii of Ca^{2+} and Y^{3+},

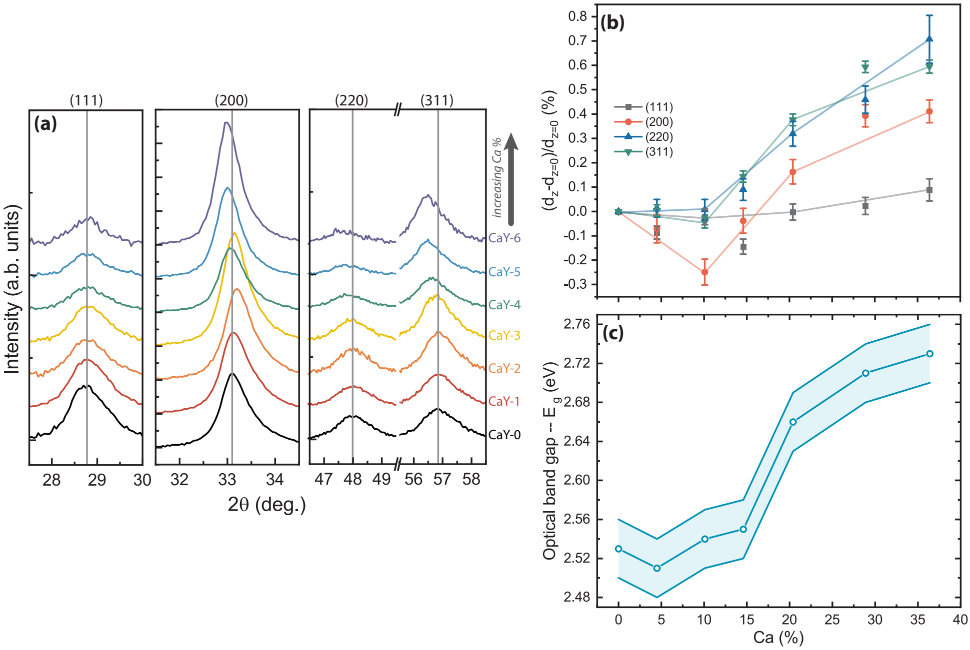

Figure 4.3: (a) GI-XRD patterns for $(Ca_zY_{1-z})H_xO_y$ with different Ca-content. Vertical grey lines are references for the reflections of the 0% Ca sample. (b) Relative change in d-spacing for different reflections as a function of Ca-content showing the increase in strain for Ca-contents >15%, and that the strain is not isotropic. Lines are guides for the eye. (c) Change in the optical band gap energy as a function of Ca-content, showing an increase above 15% Ca.

or the accumulation of vacancy defects.

4.3.3 Optical Properties

The optical band gap energies for the films studied here are presented in Figure 4.3c with respect to their Ca-doping concentration. The band gap is quite constant at a value of ~2.52 eV until a Ca-doping level of ~15%, at which point the band gap expands. This expansion could be explained either by the composition of the thin film, the lattice strain, or a combination of both.

In previous studies, changes in the band gap were attributed to the composition. For example, a higher O:H ratio generally results in a wider band gap [4, 5]. Here, we do not see a sudden change in the O^{2-} content for CaY-4 from RBS (Fig. 4.2d), but it may be that the content of H^- decreases enough at this composition to widen the optical band gap. From DFT simulations of 0% and 23% Ca compositions (Fig. S7), there is an indication that the H valence band maximum recedes slightly, widening the band gap by about 6%, which is of similar magnitude as observed experimentally. It should be noted that the cationic substitution itself does not seem to affect the band gap, since the Ca states are outside the gap. Only changes in the H^- composition appear important here.

In addition, lattice strain, as observed in Figure 4.3b, may cause the band gap to expand. Both the lattice and band gap expansions become significant around the same Ca-content of ~15%. The concept of strain-engineering the band gap has been used in many semiconductors [47], and may play a role here.

4.3.4 Photochromism

The photochromic properties of the films are measured by illuminating them with a 385 nm LED for 1 h and measuring the average transmission ($\lambda = 450 - 1000$ nm) as a function of time. The two main figures of merit for photochromic materials are the contrast (maximum amount of change in transparency), and the bleaching speed (time required to return to the original transparent state). The data presented in Figure 4.4a shows the relative contrast ($\Delta T(\%) = |T - T_0|/T_0$) instead of the average optical transmission in order to normalise for slight differences in absolute transmission, and show the change in photochromic contrast more clearly. Before illumination, samples are transparent ($\Delta T = 0$). This increases as the samples “darken” under illumination (yellow shaded area), and decreases back to the transparent state after illumination.

The photochromic contrast linearly decreases with the substitution of Y for Ca (Fig. 4.4b), suggesting a direct relationship between the two quantities. Interestingly, the extrapolation of this linear relationship leads to a prediction that no photochromic contrast should be measured for a doping level of ~54% Ca. We suspect that this linear relationship is actually an indication of the importance of hydride ions in the sample, specifically octahedral hydride ions (Fig. 4.5). While it is true that Y also decreases with the addition of Ca, that alone cannot justify the disappearance of the contrast as there would still be a significant fraction of Y in the film. On the other hand, there can be a large difference in the properties of octahedral vs. tetrahedral H^-, making the decrease in the population of certain H^- potentially significant for the observed properties of the material. Not only are the octahedral H^- likely the first to leave the structure upon oxidation [4, 33], but they are often cited as more mobile than tetrahedral H^- either due to the lower formation energy

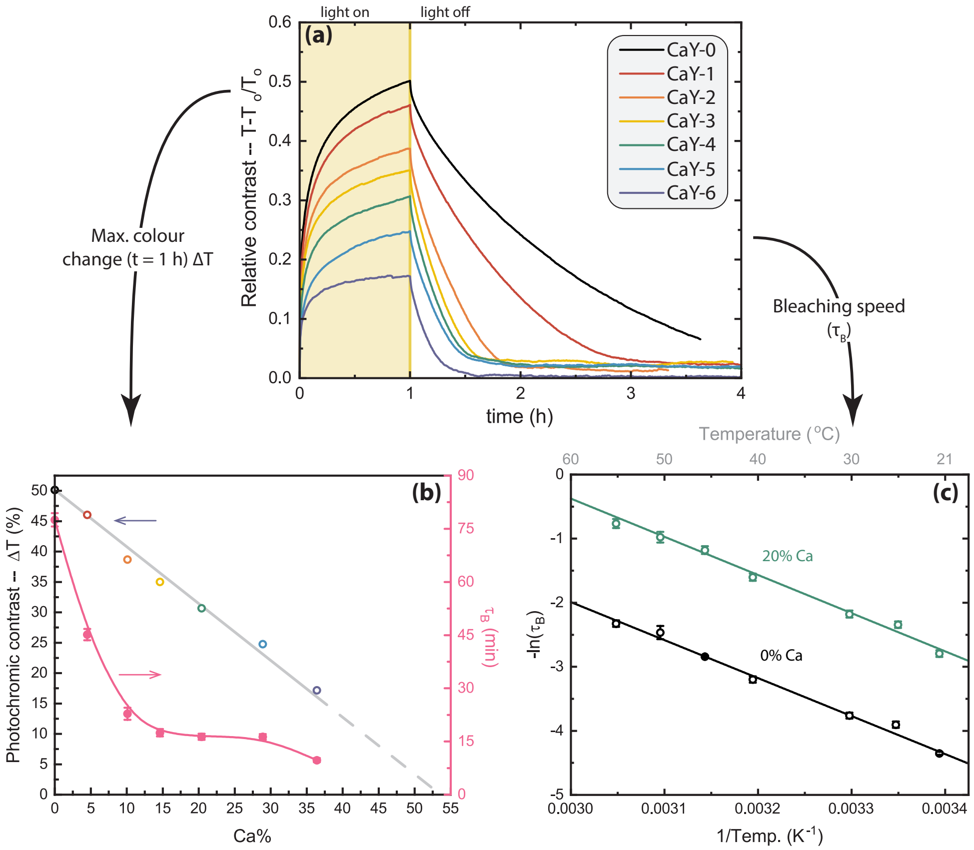

Figure 4.4: (a) Relative contrast for (Ca$_z$Y$_{1-z}$)H$_x$O$_y$ thin films with varying Ca-content. When the sample is transparent, the relative contrast is 0. During 1 h of illumination, the contrast increases, and later decreases back to 0 when the illumination is stopped. (b) (left y-axis) The maximum relative contrast as a function of Ca-content. Extrapolation of the linear relationship leads to a prediction of 0% contrast when the Ca-doping concentration is ~54%. (right y-axis) The bleaching speed (τ_B) becomes faster with the addition of Ca, although following a non-linear relationship. (c) Arrhenius plot of the bleaching speed for (Ca$_z$Y$_{1-z}$)H$_x$O$_y$ thin films containing 0% and 20% Ca, showing that differences in bleaching speed are not due to an altered activation energy of the process, but are dependent on the pre-exponential factor.

for an octahedral H vacancy [15], or their weaker electrostatic interactions with O^{2-} (more distance) [48]. Having these mobile H^- could be an essential ingredient to the formation and dissolution of a “darkened” phase.

The bleaching speed, on the other hand, does not show a linear relationship to the amount of Ca in the samples, although a monotonous decrease can be recognised (Fig. 4.4b). To understand this trend, we studied the temperature dependence of the bleaching speed for a set of 0% Ca and a 20% Ca samples (21-55°C), which follows an Arrhenius relation (Fig. 4.4c). The bleaching time constant (τ_B) is derived from first-order kinetics, and is related to

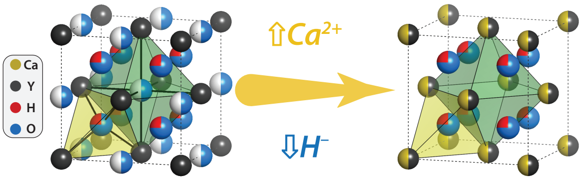

Figure 4.5: Schematic image of the anion disordered $(Ca_zY_{1-z})H_xO_y$ unit cell where Ca is a yellow circle, Y is black, H is blue, O is red, and unoccupied sites are white. The disordered nature of the anions is indicated by partial occupation of the interstitial sites, explained in Ref. [4]. When Ca is added, it replaces Y in the lattice, but since the precise position is unknown, this is also represented as partial occupation on all fcc lattice positions. We propose that addition of Ca is compensated by the removal of H^- ions from the octahedral sites, such that at a composition of ~54% Ca (or 50% in this idealised model), all octahedral sites are vacant and the photochromic contrast is 0% (see text).

the concentration of the "dark" species ($c(t)$):

$$c(t) = c_0 e^{-kt} = c_0 e^{-\left(\frac{1}{\tau_B}\right)t}. \tag{4.1}$$

Combining this with the Lambert-Beer law and the absorption coefficient results in the following [46]:

$$\ln\left(-\ln\left(\frac{T}{T_0}\right)\right) = -\left(\frac{1}{\tau_B}\right)t + \ln(c_0\sigma d), \tag{4.2}$$

showing that τ_B can be extracted from the slope of the linear fit of a $\ln(-\ln(T/T_0))$ vs. t plot (Fig. 4.G.1, 4.H.1). When the temperature is constant, it is clear from Figure 4.4a (21.5°C) that the bleaching speed of the samples becomes faster with increasing Ca-content. Considering a range of temperatures, an Arrhenius relationship can be written as:

$$\ln\left(\frac{1}{\tau_B}\right) = \ln\left(\frac{1}{\tau_0}\right) + \left(\frac{-E_A}{k_B}\right)\left(\frac{1}{Temp.}\right), \tag{4.3}$$

such that the slope of a $\ln(1/\tau_B)$ vs. $(1/Temp.)$ plot is related to the activation energy (E_A), and the y-intercept is related to the pre-exponential factor ($\ln(1/\tau_0) = ln(k_0)$). This is displayed in Figure 4.4c and Table 4.1; the E_A for the two samples are equivalent, while the pre-exponential factors are different. Specifically, the 20% Ca sample, whose τ_B at room temperature is ~79% lower than the 0% Ca sample, shows a pre-exponential factor that is higher by a factor of five. Therefore, we conclude that the determining factor here for the bleaching speed is the attempt frequency.

The rationalisation of the attempt frequency in this context is not straight-forward, since this parameter can be interpreted in many ways. If τ_B is related to the conventional diffusion of H^- from the "darkened" phase to its original position, the attempt frequency could be explained by the amount of vacant sites, hopping distance, and other factors. Given our previous reasoning on the relation between the Ca doping and the amount of octahedral hydrogen, an explanation involving the increasing amount of octahedral vacancies is the most consistent one, and points to a *short-range* diffusion mechanism related to bleaching. On the other hand, for RE-oxyhydrides with proven *long-range* H^- conductivity (RE = La) [49], changes in this conductivity were also attributed to the pre-exponential factor rather than the E_A, but citing complex interactions of many H^- ions as the source.

Table 4.1: Activation energies (E_A) and pre-exponential factors ($\tau_0 = 1/k_0$) for two samples with either 0% Ca or 20% Ca doping in yttrium oxyhydride thin films. These parameters are derived from the bleaching time constant measured at temperatures between 21-55°C, showing that the effect of Ca-doping is to increase the pre-exponential factor.

Ca (%)	E_A (eV)	τ_0 (s)	k_0 (s^{-1})
0	0.51 ± 0.02	2.3×10^{-9}	4.4×10^{8}
20	0.51 ± 0.03	4.2×10^{-10}	2.4×10^{9}

4.4 Conclusion

In conclusion, we have prepared single phase aliovalently doped yttrium oxyhydride thin films with Ca (0-36%, atomic %). These films were made by reactive magnetron co-sputtering and air-oxidation to achieve the oxyhydride phase. The composition of the cations was verified by RBS, and qualitative analysis of the anions (by RBS and ERD) showed that the O-content was largely unaffected by Ca-doping, while the H-content decreased. As well, the addition of >15% Ca resulted in the appearance of anisotropic lattice strain and a moderate expansion of the optical band gap, two effects which may be related. Importantly, all of these films are photochromic, showing that the photochromic contrast decreases with the addition of Ca, possibly due to the removal of octahedral H^- that may be essential for the creation of a "darkened" phase. The bleaching speed became faster due to Ca-doping, indicating a potential relation between the bleaching speed, the attempt frequency, and the number of octahedral vacancies. These results point to the importance of local H^- diffusion for the understanding of the photochromic mechanism, although a full explanation of this effect should account for other aspects of these materials such as anion disorder and other inhomogeneities.

References

[1] D. Chaykina, I. Usman, G. Colombi, H. Schreuders, B. Tyburska-Pueschel, Z. Wu, S. Eijt, L. J. Bannenberg, G. A. de Wijs, and B. Dam, *Aliovalent calcium doping of yttrium oxyhydride thin films and implications for photochromism,* The Journal of Physical Chemistry C **126**, 14742–14749 (2022).

[2] T. Mongstad, C. Platzer-Björkman, J. P. Maehlen, L. P. A. Mooij, Y. Pivak, B. Dam, E. S. Marstein, B. C. Hauback, and S. Z. Karazhanov, *A new thin film photochromic material: Oxygen-containing yttrium hydride,* Solar Energy Materials and Solar Cells **95**, 3596 (2011).

[3] F. Nafezarefi, H. Schreuders, B. Dam, and S. Cornelius, *Photochromism of rare-earth metal-oxy-hydrides,* Applied Physics Letters **111**, 103903 (2017).

[4] S. Cornelius, G. Colombi, F. Nafezarefi, H. Schreuders, R. Heller, F. Munnik, and B. Dam, *Oxyhydride nature of rare-earth-based photochromic thin films,* The Journal of Physical Chemistry Letters **10**, 1342 (2019).

[5] G. Colombi, T. De Krom, D. Chaykina, S. Cornelius, S. W. H. Eijt, and B. Dam, *Influence of cation (RE = Sc, Y, Gd) and O/H anion ratio on the photochromic properties of* REO_xH_{3-2x} *thin films,* ACS Photonics **8**, 709 (2021).

[6] D. Chaykina, F. Nafezarefi, G. Colombi, S. Cornelius, L. J. Bannenberg, H. Schreuders, and B. Dam, *Influence of crystal structure, encapsulation, and annealing on photochromism in Nd oxyhydride thin films,* The Journal of Physical Chemistry C **126**, 2276 (2022).

[7] S. M. Aðalsteinsson, M. V. Moro, D. Moldarev, S. Droulias, M. Wolff, and D. Primetzhofer, *Correlating chemical composition and optical properties of photochromic rare-earth oxyhydrides using ion beam analysis,* Nuclear Instruments and Methods in Physics Research Section B: Beam Interactions with Materials and Atoms **485**, 36 (2020).

[8] Z. Wu, T. de Krom, G. Colombi, D. Chaykina, G. van Hattem, H. Schut, M. Dickmann, W. Egger, C. Hugenschmidt, E. Brück, B. Dam, and S. W. H. Eijt, *Formation of vacancies and metallic-like domains in photochromic rare-earth oxyhydride thin films studied by in-situ illumination positron annihilation spectroscopy,* Physical Review Materials **6**, 065201 (2022).

[9] D. Chaykina, T. W. H. de Krom, G. Colombi, H. Schreuders, a. Suter, T. Prokscha, B. Dam, and S. W. H. Eijt, *Structural properties and anion dynamics of yttrium dihydride and photochromic oxyhydride thin-films examined by in situ* μ^+*SR,* Physical Review B **103**, 224106 (2021).

[10] E. M. Baba, J. Montero, E. Strugovshchikov, E. Ö. Zayim, and S. Karazhanov, *Light-induced breathing in photochromic yttrium oxyhydrides,* Physical Review Materials **4**, 025201 (2020).

[11] C. V. Chandran, H. Schreuders, B. Dam, J. W. G. Janssen, J. Bart, A. P. M. Kentgens, and P. J. M. van Bentum, *Solid-state NMR studies of the photochromic effects of thin films of oxygen-containing yttrium hydride,* The Journal of Physical Chemistry C **118**, 22935 (2014).

[12] J. Montero, F. A. Martinsen, M. García-Tecedor, S. Z. Karazhanov, D. Maestre, B. Hauback, and E. S. Marstein, *Photochromic mechanism in oxygen-containing yttrium hydride thin films: An optical perspective,* Physical Review B **95**, 201301(R) (2017).

[13] J. Montero and S. Z. Karazhanov, *Spectroscopic ellipsometry and microstructure characterization of photochromic oxygen-containing yttrium hydride thin films,* physica status solidi (a) **215**, 1701039 (2018).

[14] J. Chai, Z. Shao, H. Wang, C. Ming, W. Oh, T. Ye, Y. Zhang, X. Cao, P. Jin, S. Zhang, and Y.-Y. Sun, *Ultrafast processes in photochromic material YH_xO_y studied by excited-state density functional theory simulation,* Science China Materials **63**, 1579 (2020).

[15] Y. Komatsu, R. Shimizu, R. Sato, M. Wilde, K. Nishio, T. Katase, D. Matsumura, H. Saitoh, M. Miyauchi, J. R. Adelman, R. M. L. McFadden, D. Fujimoto, J. O. Ticknor, M. Stachura, I. McKenzie, G. D. Morris, W. A. MacFarlane, J. Sugiyama, K. Fukutani, S. Tsuneyuki, and T. Hitosugi, *Repeatable photoinduced insulator-to-metal transition in yttrium oxyhydride epitaxial thin films,* Chemistry of Materials **34**, 3616 (2022).

[16] M. Hans, T. T. Tran, S. M. Aðalsteinsson, D. Moldarev, M. V. Moro, M. Wolff, and D. Primetzhofer, *Photochromic mechanism and dual-phase formation in oxygen-containing rare-earth hydride thin films,* Advanced Optical Materials **8**, 2000822 (2020).

[17] F. Takeiri, K. Aidzu, T. Yajima, T. Matsui, T. Yamamoto, Y. Kobayashi, J. Hester, and H. Kageyama, *Promoted hydride/oxide exchange in $SrTiO_3$ by introduction of anion vacancy via aliovalent cation substitution,* Inorganic Chemistry **56**, 13035 (2017).

[18] N. Imanaka, K. Okamoto, and G. Y. Adachi, *Water-insoluble lanthanum oxychloride-based solid electrolytes with ultra-high chloride ion conductivity,* Angew Chem Int Ed Engl **41**, 3890 (2002).

[19] K. Shitara, A. Kuwabara, K. Hibino, K. Fujii, M. Yashima, J. R. Hester, M. Umeda, N. Nunotani, and N. Imanaka, *Ionic conduction mechanism in Ca-doped lanthanum oxychloride,* Dalton Transactions **50**, 151 (2021).

[20] M. Zubkins, I. Aulika, E. Strods, V. Vibornijs, L. Bikse, A. Sarakovskis, G. Chikvaidze, J. Gabrusenoks, H. Arslan, and J. Purans, *Optical properties of oxygen-containing yttrium hydride thin films during and after the deposition,* Vacuum **203**, 111218 (2022).

[21] M. Mayer, *SIMNRA User's Guide , Report IPP 9/113*, Report (Max-Planck-Institut für Plasmaphysik, 1997).

[22] M. Mayer, *Simnra, a simulation program for the analysis of nra, rbs and erda,* in *Proceedings of the 15th International Conference on the Application of Accelerators in Research and Industry*, American Institute of Physics Conference Proceedings, Vol. 475, edited by J. Duggan and I. Morgan (1999) p. 541.

[23] G. Kresse and J. Furthmüller, *Efficient iterative schemes for ab initio total-energy calculations using a plane-wave basis set,* Physical Review B **54**, 11169 (1996).

[24] G. Kresse and J. Furthmüller, *Efficiency of ab-initio total energy calculations for metals and semiconductors using a plane-wave basis set,* Computational Materials Science **6**, 15 (1996).

[25] G. Colombi, R. Stigter, D. Chaykina, S. Banerjee, A. P. M. Kentgens, S. W. H. Eijt, B. Dam, and G. de Wijs, *Energy, metastability, and optical properties of anion-disordered* REO_xH_{3-2x} *RE = (Y, La) oxyhydrides: a computational study,* Physical Review B **105**, 054208 (2022).

[26] P. E. Blöchl, *Projector augmented-wave method,* Physical Review B **50**, 17953 (1994).

[27] G. Kresse and D. Joubert, *From ultrasoft pseudopotentials to the projector augmented-wave method,* Physical Review B **59**, 1758 (1999).

[28] J. P. Perdew, K. Burke, and M. Ernzerhof, *Generalized gradient approximation made simple,* Physical Review Letters **77**, 3865 (1996).

[29] J. P. Perdew, K. Burke, and M. Ernzerhof, *Generalized gradient approximation made simple,* Physical Review Letters **78**, 1396 (1997).

[30] F. Tran and P. Blaha, *Accurate band gaps of semiconductors and insulators with a semilocal exchange-correlation potential,* Physical Review Letters **102**, 226401 (2009).

[31] A. D. Becke and E. R. Johnson, *A simple effective potential for exchange,* The Journal of Chemical Physics **124**, 221101 (2006).

[32] J. Tauc, *Optical properties and electronic structure of amorphous Ge and Si,* Mat. Res. Bull. **3**, 37 (1968).

[33] G. Colombi, S. Cornelius, A. Longo, and B. Dam, *Structure model for anion-disordered photochromic Gd oxyhydride thin films,* The Journal of Physical Chemistry C **124**, 13541 (2020).

[34] P. Ngene, T. Radeva, M. Slaman, R. J. Westerwaal, H. Schreuders, and B. Dam, *Seeing hydrogen in colors: Low-cost and highly sensitive eye readable hydrogen detectors,* Advanced Functional Materials **24**, 2374 (2014).

[35] D. G. Nagengast, A. T. M. v. Gogh, E. S. Kooij, B. Dam, and R. Griessen, *Contrast enhancement of rare-earth switchable mirrors through microscopic shutter effect,* Applied Physics Letters **75**, 2050 (1999).

[36] C. V. Falub, P. E. Mijnarends, S. W. H. Eijt, M. A. van Huis, A. van Veen, and H. Schut, *Electronic structure and orientation relationship of li nanoclusters embedded in mgo studied by depth-selective positron annihilation two-dimensional angular correlation,* Physical Review B **66**, 075426 (2002).

[37] M. A. van Huis, A. van Veen, H. Schut, C. V. Falub, S. W. H. Eijt, P. E. Mijnarends, and J. Kuriplach, *Positron confinement in embedded lithium nanoclusters,* Physical Review B **65**, 085416 (2002).

[38] K. Asano, R. Westerwaal, A. Anastasopol, L. Mooij, C. Boelsma, P. Ngene, H. Schreuders, S. W. H. Eijt, and B. Dam, *Destabilization of Mg hydride by the formation of nanometer-sized clusters in the immiscible Mg-Ti system,* The Journal of Physical Chemistry C **119**, 12157 (2015).

[39] H. Mizoguchi, S. Park, T. Honda, K. Ikeda, T. Otomo, and H. Hosono, *Cubic fluorite-type* CaH_2 *with a small bandgap,* Journal of American Chemical Society **139**, 11317 (2017).

[40] M. Gonzalez-Silveira, R. Gremaud, H. Schreuders, M. J. van Setten, E. Batyrev, A. Rougier, L. Dupont, E. G. Bardaji, W. Lohstroh, and B. Dam, *In-situ deposition of alkali and alkaline earth hydride thin films to investigate the formation of reactive hydride composites,* The Journal of Physical Chemistry C **114**, 13895 (2010).

[41] S. Villa-Cortes and O. De la Pena-Seaman, *Electron- and hole-doping on* ScH_2 *and* YH_2*: effects on superconductivity without applied pressure,* J Phys Condens Matter **33**, 425401 (2021).

[42] S. Bergstøl, B. B. Jensen, and H. Neumann, *Tveitite, a new calcium yttrium fluoride,* Lithos **10**, 81 (1977).

[43] S. Attaf, M. F. Mosbah, A. Vecchione, and R. Fittipaldi, *The influence of doping with Ca and Mg in* $YBa_2Cu_3O_{7-\delta}$ *ceramic,* EPJ Web of Conferences **29**, 00003 (2012).

[44] A. Augieri, T. Petrisor, G. Celentano, L. Ciontea, V. Galluzzi, U. Gambardella, A. Mancini, and A. Rufoloni, *Effect of Ca doping in YBCO superconducting thin films,* Physica C: Superconductivity **401**, 320 (2004).

[45] R. D. Shannon, *Revised effective ionic radii and systematic studies of interatomic distances in halides and chalcogenides,* Acta Crystallographica **A32**, 751 (1976).

[46] F. Nafezarefi, S. Cornelius, J. Nijskens, H. Schreuders, and B. Dam, *Effect of the addition of zirconium on the photochromic properties of yttrium oxy-hydride,* Solar Energy Materials and Solar Cells **200**, 109923 (2019).

[47] K.-H. Kao, A. S. Verhulst, R. Rooyackers, B. Douhard, J. Delmotte, H. Bender, O. Richard, W. Vandervorst, E. Simoen, A. Hikavyy, R. Loo, K. Arstila, N. Collaert, A. Thean, M. M. Heyns, and K. D. Meyer, *Compressively strained SiGe band-to-band tunneling model calibration based on p-i-n diodes and prospect of strained SiGe tunneling field-effect transistors,* Journal of Applied Physics **116**, 214506 (2014).

[48] K. Fukui, S. Iimura, A. Iskandarov, T. Tada, and H. Hosono, *Room-temperature fast* H^- *conduction in oxygen-substituted lanthanum hydride,* Journal of American Chemical Society **144**, 1523 (2022).

[49] K. Fukui, S. Iimura, T. Tada, S. Fujitsu, M. Sasase, H. Tamatsukuri, T. Honda, K. Ikeda, T. Otomo, and H. Hosono, *Characteristic fast H^{-} ion conduction in oxygen-substituted lanthanum hydride,* Nature Communications **10**, 2578 (2019).

Appendix

4.A Co-sputtering of Ca and Y

To deposit Ca-doped yttrium oxyhydride thin films, Ca and Y metal targets were co-sputtered with a reactive gas mixture (Ar/H_2 = 7:1, p_{dep} = 0.5 Pa). The amount of Ca-doping in the sample was controlled by altering the input power to the two metal targets.

To do this, we first established an atomic flux (ϕ_M) vs. input DC power relationship for the two targets, which is expected to be linear (Fig. S4.4). We sputtered Y and Ca individually (Ar/H_2 = 7:1, p_{dep} = 0.5 Pa), at different input power, and measured the thickness of the films by profilometry. Using the film thickness deposited for a known period of time, we can determine the sputtering rate for a particular input power (r, cm/s), and then the flux by:

$$\phi_M = \frac{N_A r d}{m} \tag{4.4}$$

where ϕ_M is the flux of material M, N_A is Avogadro's number, d is the density of material M, and m is the molar mass of the material M.

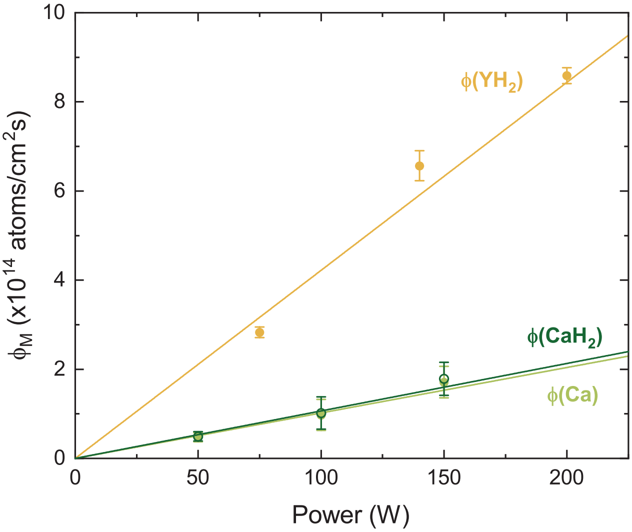

Figure 4.A.1: The relationship between the flux (ϕ_M) and input DC power for Y- and Ca-based targets during sputtering with a deposition pressure of 0.5 Pa (7:1 Ar/H_2). For Ca-based films, the data was calculated considering both Ca (light green) and CaH_2 (dark green) as the sputtered species, but this did not influence the slope significantly.

To use Eq. 4.4, it is necessary to know the identity of the sputtered species since that determines the density and molar mass. For Y-based films, it is known that before air-exposure, the as-deposited film is $YH_{1.9+\delta}$ [1–3]. However, the film oxidises to the oxyhydride phase before its thickness is measured. Therefore, the flux obtained in Figure S4.4 is slightly underestimated since the oxidation of the as-deposited dihydride will lead to a slight expansion [1, 2]. However, this is still a valid *estimation* for the necessary sputtering conditions to achieve Ca-doped films.

In terms of the Ca-based films, whether Ca or CaH_2 is being deposited does not influence the flux/power estimation significantly (Fig. 4.4). Despite that, we show evidence in favour

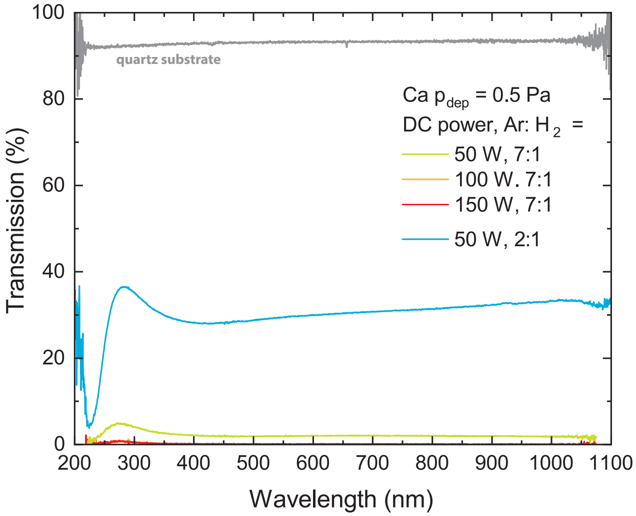

Figure 4.A.2: Transmission spectra for four Ca-based films with a reference for the maximum transmission possible given by the quartz substrate. The green (50 W), orange (100 W), and red (150 W) curves are for samples made by sputtering a Ca target at 0.5 Pa (Ar/H_2 = 7:1). The low transmission is indicative of Ca metal. The blue curve (50 W) is for a sample sputtered at a higher H_2 partial pressure (0.5 Pa, Ar/H_2 = 2:1), and may represent CaH_2.

of the idea that Ca is deposited, perhaps with a small amount of H incorporation. Ca-based films were sputtered at 50, 100, and 150 W and a pressure of 0.5 Pa (Ar/H_2 = 7:1). The transmission spectra of these films were measured in the glovebox and are shown in Figure 4.A.2. All three films show very low transmission, which does not resemble CaH_2. In general, Ca is expected to be an opaque metal, while CaH_2 is a semiconductor with a band gap around either 2.5 eV for the cubic phase or, more commonly, 4.4-5.2 eV for the orthorhombic phase [4, 5]. It may be that the sputtering rate of Ca is too fast, and the partial pressure of H_2 is too low to create the dihydride phase under the conditions we use for sputtering the Ca-doped yttrium oxyhydride thin films.

A previous work on *in situ* deposition of (orthorhombic) CaH_2 by sputtering used a much higher H_2 partial pressure than our methods ($Ar:H_2$ = 1:2), and an RF power source [5]. In Figure 4.A.2 we sputtered one film with a much higher H_2 partial pressure and achieved a film with a band gap of $\sim$ 4.0 eV, likely CaH_2. Thus, it may be possible to sputter CaH_2, if a sufficiently high H_2 partial pressure is used. However, we suppose that the Ca deposited under our standard conditions is mostly Ca, although the exact composition does not affect the flux estimation significantly. We note that the Ca films had to be covered by a thin layer of metal with a known thickness to protect the Ca films from oxidation while profilometry measured were performed.

Producing films with different Ca-doping concentrations requires balancing the input power given to the Y and Ca targets, while keeping the total flux at the same value. The total flux (ϕ_{total}) is the summation of the YH_2 and Ca fluxes ($\phi_{YH_2} + \phi_{Ca}$), and we set this value to 9×10^{14} atoms/cm^2-s. This value for the total flux is chosen for practical reasons, i.e., so that the resultant necessary input power to the targets is not too high or too low.

The calculated input power to the targets is shown in Table 4.A.1.

Table 4.A.1: Calcium and yttrium were co-sputtered by reactive magnetron sputtering to produce Ca-doped $YH_{3-2x}O_x$ thin-films. The total flux (ϕ_{total}) was kept constant at a value of 9×10^{14} atoms-cm/s by adjusting the input power to each target (based on the desired Ca:Y ratio).

Sample ID	Power Y (W)	Power Ca (W)
CaY-0	213	0
CaY-1	207	26
CaY-2	198	62
CaY-3	192	88
CaY-4	185	116
CaY-5	177	149
CaY-6	170	178

4.B Tauc plots

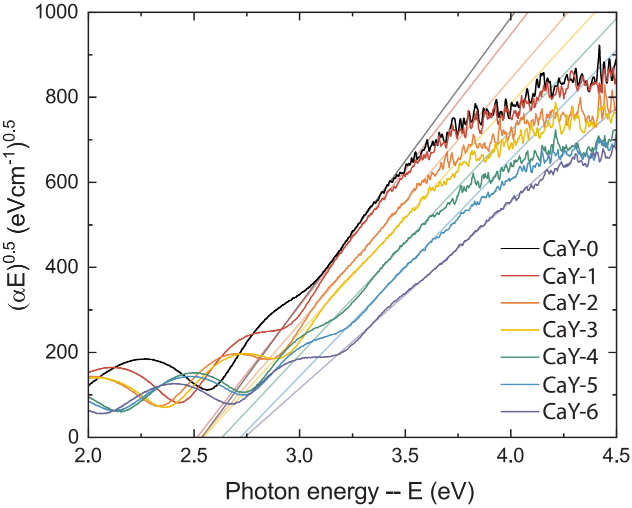

Figure 4.B.1: Optical transmission spectra for Ca-doped Y-oxyhydride thin films were converted to Tauc plots and fitted with a linear regression extrapolated to the x-axis. The x-intercept indicates the optical band gap of the material. It is clear that the band gap expands slightly starting with sample CaY-4, which has a Ca-content of ∼15%.

4.C RBS

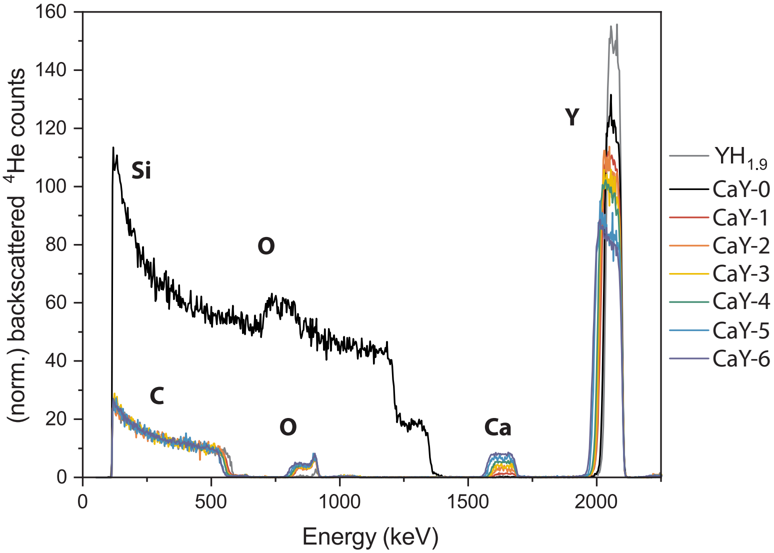

Figure 4.C.1: Rutherford backscattering (RBS) spectra for a series of samples with increasing Ca-content. All samples containing Ca (CaY-1 to CaY-6) were measured on glassy carbon substrates, while the undoped Y-oxyhydride (CaY-0) was on a substrate of SiO_2/Si which not only obscured the O peak, but has a different background offset due to the underlying silicon.

4.D DB-PAS

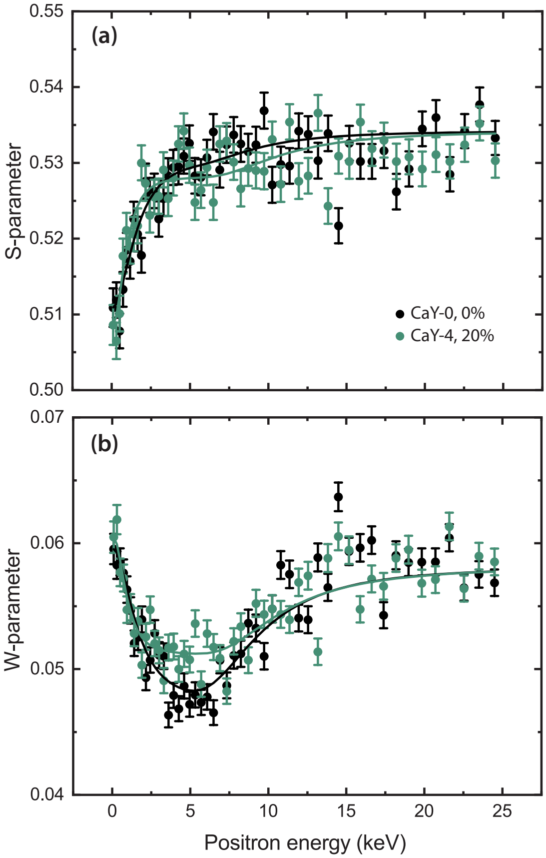

Figure 4.D.1: The (a) S-parameter and (b) W-parameter from positron annihilation depth profiles of CaY-0 (black) and CaY-4 (green). The data were fitted by VEPFIT, represented by the solid lines. The S-parameter is generally related to point defect structure and electronic structure, while the W-parameter is influenced by changes in the local chemical environment of the positron annihilation site.

Table 4.D.1: The S- and W-parameters derived from DB-PAS depth profiles for 0% and 20% Ca in $(Ca_zY_{1-z})H_xO_y$ thin films. The change in the two parameters is shown as a percentage. From this, we conclude that: (1) the cation vacancy structure in these two materials is similar, (2) there are no metallic centres in the Y-oxyhydride matrix, and (3) the local chemical environments of the positron annihilation sites of the two materials are slightly different. The last point is explained by the wider optical band gap of the 20% Ca film, and the slightly higher O:H ratio as some of the H^- is removed.

Ca (%)	S-parameter	W-parameter
0	0.5302 ± 0.0003	0.0476 ± 0.0002
20	0.5282 ± 0.0003	0.0512 ± 0.0002
	-0.4 %	+7.6%

4.E XRD

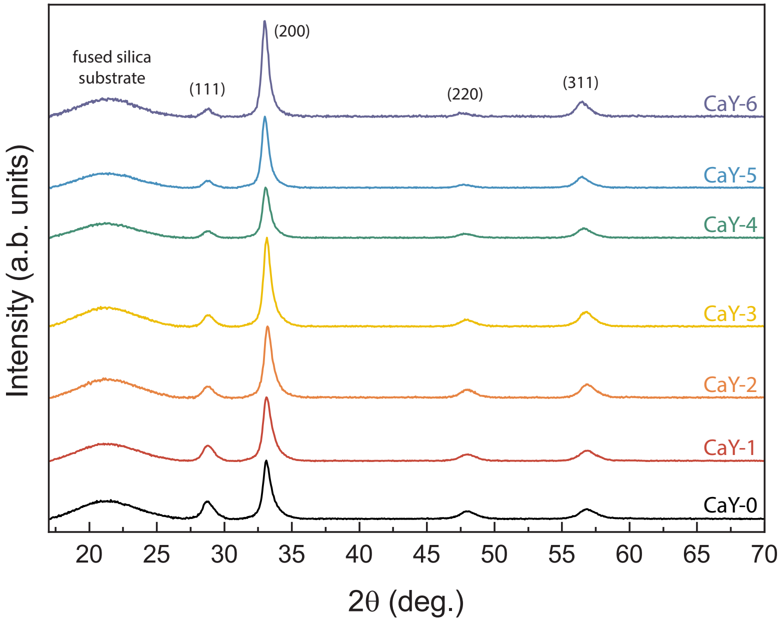

Figure 4.E.1: Full grazing incident X-ray diffraction patterns for samples with increasing Ca content from CaY-0 (0%) to CaY-6 (36%).

4.F DFT

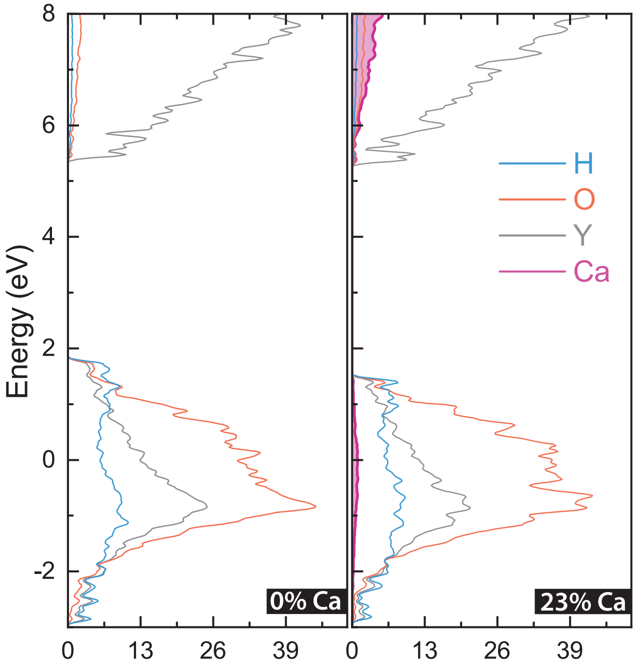

Figure 4.F.1: Simulated density of states for two compositions of Ca: (left) 0% and (right) 23%. The contributions of H (blue), O (red), Y (grey), and Ca (pink) to the band structure are shown.

4.G Bleaching curves

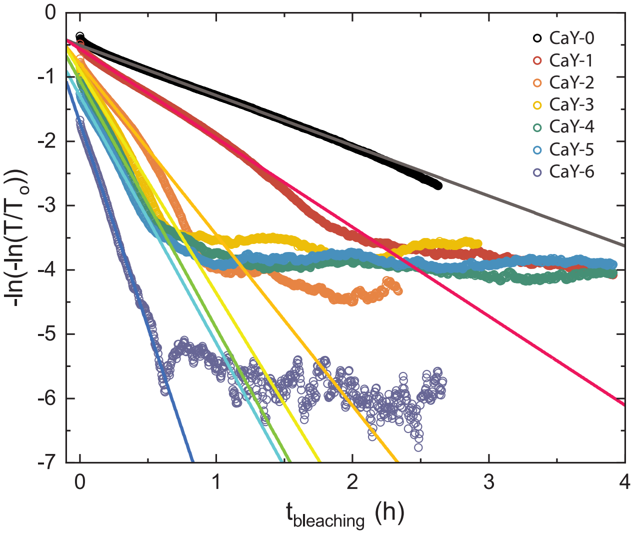

Figure 4.G.1: The bleaching speed (τ_B) for samples with increasing Ca-content are derived from the slope of this plot based on first-order kinetics. It is clear that when the Ca-content increases, the bleaching speed becomes faster.

4.H PCE for Arrhenius

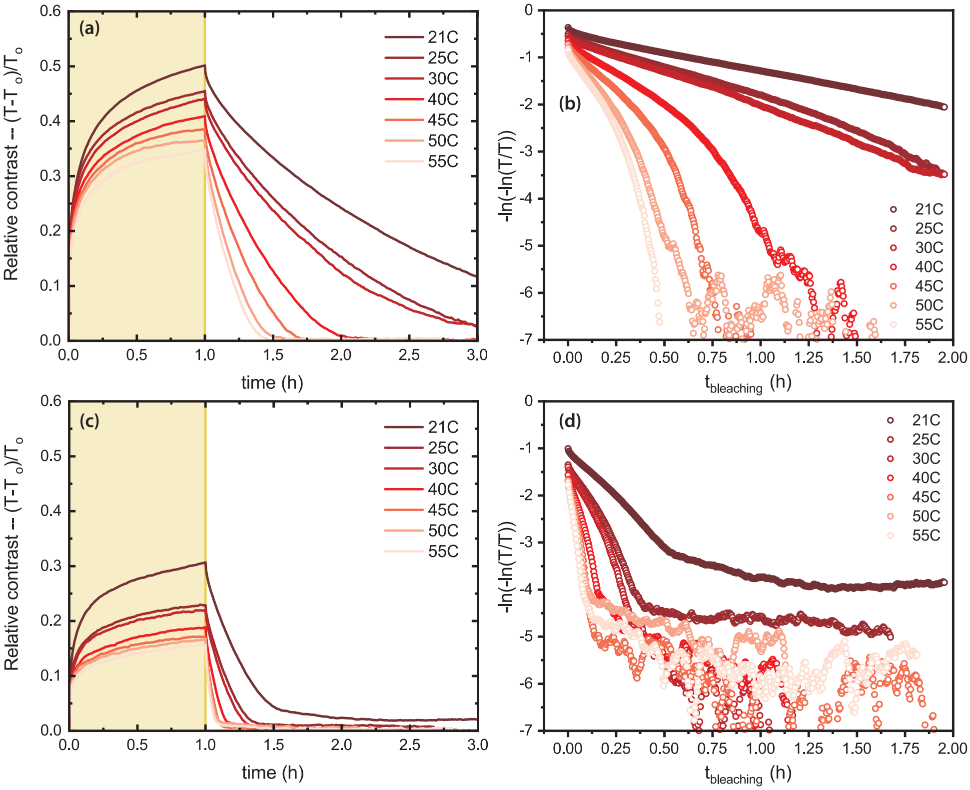

Figure 4.H.1: The photochromic effect was measured for a set of (a) 0% Ca and (c) 20% Ca films at different temperatures between 21.5 and 55°C. The bleaching time constants (τ_B) for each temperature were derived from the linear fits for (b) 0% Ca and (d) 20% Ca.

References

[1] G. Colombi, T. De Krom, D. Chaykina, S. Cornelius, S. W. H. Eijt, and B. Dam, *Influence of cation (RE = Sc, Y, Gd) and O/H anion ratio on the photochromic properties of* REO_xH_{3-2x} *thin films,* ACS Photonics **8**, 709 (2021).

[2] S. Cornelius, G. Colombi, F. Nafezarefi, H. Schreuders, R. Heller, F. Munnik, and B. Dam, *Oxyhydride nature of rare-earth-based photochromic thin films,* The Journal of Physical Chemistry Letters **10**, 1342 (2019).

[3] D. Chaykina, T. W. H. de Krom, G. Colombi, H. Schreuders, a. Suter, T. Prokscha, B. Dam, and S. W. H. Eijt, *Structural properties and anion dynamics of yttrium dihydride and photochromic oxyhydride thin-films examined by in situ* μ^+SR*,* Physical Review B **103**, 224106 (2021).

[4] H. Mizoguchi, S. Park, T. Honda, K. Ikeda, T. Otomo, and H. Hosono, *Cubic fluorite-type* CaH_2 *with a small bandgap,* Journal of American Chemical Society **139**, 11317 (2017).

[5] M. Gonzalez-Silveira, R. Gremaud, H. Schreuders, M. J. van Setten, E. Batyrev, A. Rougier, L. Dupont, E. G. Bardaji, W. Lohstroh, and B. Dam, *In-situ deposition of alkali and alkaline earth hydride thin films to investigate the formation of reactive hydride composites,* The Journal of Physical Chemistry C **114**, 13895 (2010).

5

Analysing charge transport in Gd-oxyhydride thin films by EIS

> *"Results! Why, man, I have gotten a lot of results.*
> *I know several thousand things that won't work."*
> *—Thomas Alva Edison*

This chapter concerns the use of electrochemical impedance spectroscopy (EIS) to understand charge transport in rare-earth metal oxyhydride thin films. At present, it is not clear if the thin films studied throughout this thesis exhibit long-range ion mobility, mixed conduction, or are simply semiconductors. This chapter begins with an overview of H^- conductivity in (bulk) oxyhydrides, showing that pure H^- conductivity has been shown in some oxyhydrides, although there is a debate about whether this property extends to Gd-oxyhydrides. Next, some theoretical background to EIS is given because this technique is complex, and the analysis of the output signal should be done carefully. This is especially true when trying to discriminate between semiconductors and ion conductors, which can show similar response in a Nyquist plot. Last, very initial results for Gd-oxyhydride thin films are presented, showing that the conductivity in Gd-oxyhydride thin films is dominated by electrons/holes, and that the temperature stability of as-deposited films is poor above 70°C. Annealing of the samples results in an improved temperature stability in this range. A prospective for the measurement of other oxyhydride materials is given.

5.1 Introduction to H^- conductors

Solid-state materials capable of pure ionic conductivity (negligible electronic conductivity) are of interest for a number of devices such as batteries and fuel cells, where these materials act as an electrolyte. Particularly, solid-state hydride (H^-) conductors could be useful in this context, especially given the high standard redox potential (H^-/H_2, -2.3 V) and low electronegativity of hydrides [1]. High conductivity of H^- has been shown in metal hydrides such as BaH_2, SrH_2, and CaH_2 (σ_{H^-} ~10^{-1}-10^{-2} S/cm), although only at high temperatures (~557-727°C) [2, 3]. Thus, there is a motivation to develop materials with H^- conductivity at low/moderate temperatures.

The first reports of H^- conductivity in oxyhydride materials were focussed on compounds with a Ruddlesden-Popper (K_2NiF_4-type) crystal structure (Fig. 5.1a). Over time, and with more such materials reported in the literature, the factors influencing H^- conductivity in these types of materials was understood so that recently, a high H^- conductivity of 10^{-2} S/cm was found for $Ba_{1.75}LiH_{2.7}O_{0.9}$ following a high temperature phase transition [10]. However, this maximum conductivity is observed at temperatures lower than metal hydrides, but still relatively high (315°C) (Fig. 5.1b).

At the same time, cubic rare-earth (RE) metal oxyhydrides were investigated for H^- mobility, showing the highest conductivity observed for any oxyhydride thus far for $LaH_{3-2x}O_x$ ($2.6{\times}10^{-2}$ S/cm) [11]. The authors showed that the O:H ratio of La-oxyhydride greatly impacts H^- mobility because the presence of O^{2-} ions suppresses electronic conductivity, but too much O^{2-} also impedes H^- motion [13]. Therefore, in the first instance of room temperature H^- conductivity in an oxyhydride, the sample prepared was a $LaH_{3-2x}O_x$ with a high H-content (x = 0.1) [13].

In this work, however, we use neither La-oxyhydrides, nor bulk powder materials. Instead, we produce and measure thin films of Gd-oxyhydrides. The thin film nature of the sample can result in several differences compared to bulk powder analysis: (1) other pro-

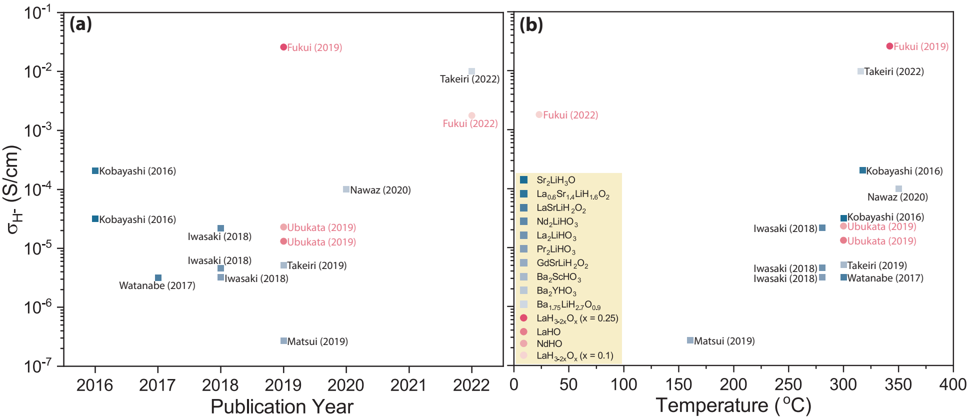

Figure 5.1: Overview of the H^- conductivities reported in oxyhydrides based on EIS measurements with respect to (a) publication year and (b) measurement temperature. In both cases, the best conductivity reported for the material is included in the plot here. Oxyhydrides with a Ruddlesden-Popper (K_2NiF_4-type) crystal structure are indicated in blue [4–10], while the fluorite (cubic) rare-earth metal oxyhydrides are indicated in pink [11–13].

cesses such a surface diffusion become relevant for thin films, (2) the measured conductivity can take a different value due to a shorter diffusion distance between electrodes, (3) different defect structure, and many others. As well, thin film energy storage is technologically relevant, especially for small devices.

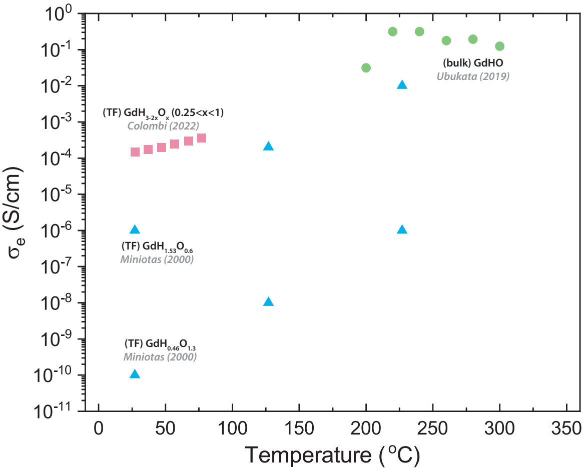

Figure 5.2: The electronic conductivity reported for Gd-oxyhydrides. The green circles are based on Ref. [12] for bulk stoichiometric GdHO measured by EIS. Pink squares are for thin film Gd-oxyhydrides from Ref. [14] measured using the Van der Pauw method and blocking electrodes. The blue triangles are for Gd-oxyhydride thin films with different O:H ratios from Ref. [15] measured using unknown electrodes and a DC input.

From the point-of-view of chemistry, predictions have been made about the ionic mobility in Gd-oxyhydrides. Ubukata et al. [12] showed that their stoichiometric GdHO *powders* show no ionic conductivity due to a bottleneck radius created by the cations which is too small to allow indirect H^- hopping between tetrahedral and octahedral interstitial sites. This reasoning was extended to all RE-oxyhydrides where RE = Sm-Er. The authors derived a very high temperature-independent electronic conductivity for GdHO ($\sim 10^{-1}$ S/cm) based on EIS (Fig. 5.2).

The electronic conductivity of Gd-oxyhydride *thin films* has been characterised either with unknown [15] or blocking [14] electrodes, showing a DC conductivity in the range of $10^{-4} - 10^{-10}$ S/cm depending on the O:H ratio, and for a temperature range of 300-600 K or 300-350 K, respectively (Fig. 5.2). These results are on a different order of magnitude compared to the bulk GdHO and show a clear temperature-dependence. In particular, the activation energies reported by Miniotas et al. [15] were ~0.79-0.99 eV, close to the activation energies for H^- mobility in bulk La- (1.0-1.3 eV) [11, 12] and Nd-oxyhydrides (1.1 eV) [12].

The goal of this chapter is to use Gd-oxyhydride as a case study for how to employ both AC and DC methods to understand the transport properties of the material. Since there are many dynamic processes that can occur in a thin film, careful analysis should be performed to understand these phenomena. Using AC and DC methods, below we explain how to analyse such a material, with theoretical and experimental examples. The methods used here can be used for other oxyhydride thin films.

5.2 AC & DC responses of materials

This section will first explain: (1) some basic aspects of electrochemical impedance spectroscopy, (2) the expected results when measuring metals, semiconductors, and ion conductors by EIS and DC methods, and (3) a brief comment on mixed conductors.

5.2.1 Electrochemical impedance spectroscopy (EIS) basics

This chapter makes use of a technique called electrochemical impedance spectroscopy (EIS) where a small AC signal is applied to a material in order to understand its charge transport properties. At the EIS2022 summer school at the University of Bath, Prof. Frank Marken described EIS like when you shake a gift box to figure out what is inside without opening it. This technique is important because it is perhaps the easiest and most direct way to characterise long-range ionic transport through the material, and to get detailed transport information in general. However, it is also a very complicated technique with many important considerations, thus, many reasons for a reader to invalidate the presented data. In fact, papers are published regularly trying to teach different subfields of electrochemistry and materials science how to use EIS properly for their purposes [16–19], and to find consensus on basic details such as how to obtain reliable data [20]. There are also questions about how to use and interpret certain very popular elements for EIS analysis [21]. This is all to say that a complicated technique deserves a proper introduction, such as the one given by Lasia in Ref. [22]. Below, I briefly review many key aspects of the technique.

In EIS, an alternating voltage is applied to the sample in a range of frequencies to characterise the numerous processes which can occur at different time-scales. Since the input voltage and output current in an EIS experiment are alternating, they are represented by sinusoidal functions that can be expressed also as an exponential (via Euler's relationship):

$$V(t) = V_o \mathrm{e}^{i\omega t} \tag{5.1}$$

$$I(t) = I_o \mathrm{e}^{i(\omega t)+\phi} \tag{5.2}$$

Here, ω is the frequency ($\omega = 2\pi f$), while V_o and I_o are the amplitudes of the sine waves. The term ϕ is a phase angle between the voltage and current. If the measured material consists of frequency-dependent elements such as capacitors, the current will be out of phase with the voltage and ϕ will be non-zero.

Using the alternating voltage and current does not lead to a simple resistance, but rather an impedance (Z):

$$Z = \frac{V_o \mathrm{e}^{i\omega t}}{I_o \mathrm{e}^{i(\omega t)} \mathrm{e}^{i\phi}} = |Z| \mathrm{e}^{-i\phi} \tag{5.3}$$

The impedance consists of real (Z') and imaginary (Z'') components:

$$Z = Z' + iZ'' \tag{5.4}$$

which, when plotted against each other, result in a Nyquist plot or Cole-Cole plot (Fig. 5.3). This is a useful plot for quickly determining which equivalent circuit elements are present in the equivalent circuit model of the sample. This is because the impedances of the most used circuit elements (resistors, capacitors, and inductors) are written as follows:

$$Z_R = R \tag{5.5}$$

$$Z_C = \frac{1}{i\omega C} \tag{5.6}$$

$$Z_L = i\omega L, \tag{5.7}$$

where R is resistance, C is capacitance, and L is inductance. According to these equations, a resistor has no frequency dependence so that voltage and current are always in phase (ϕ=0) and the impedance has only a real component. Capacitance, on the other hand, has a ϕ of -90° (or 270°) and a negative sign for the imaginary impedance ($-Z''$). The opposite is true for inductance. In a Nyquist plot, a resistor would only appear on the x-axis (Z'=Z''=0), capacitive components appear in the upper quadrant ($-Z''$), and inductive components in the lower quadrant ($+Z''$).

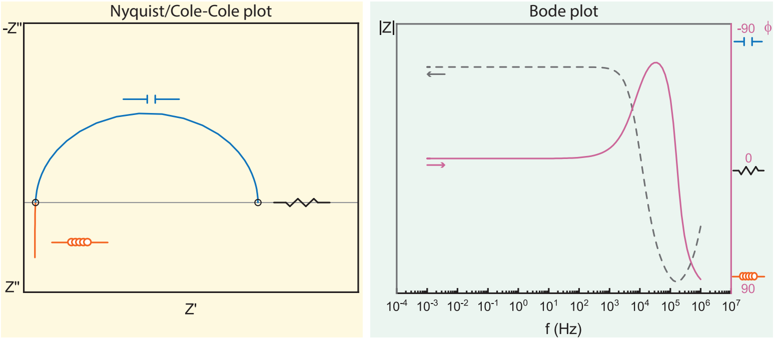

Figure 5.3: Examples of Nyquist/Cole-Cole and Bode plot representations of EIS data using an LR(RC) circuit. In a Nyquist plot, one can quickly identify if C, R, or L components are needed in the equivalent circuit model based on which quadrant the data is in. In a Bode plot, this is done based on the trends of ϕ (solid pink line) and $|Z|$ (dashed grey line) with frequency. While the L results in a +90° value for ϕ, C results in the opposite, -90°. At lower frequencies, when the signal is dominated by R, ϕ is 0.

The disadvantage of a Nyquist plot is that the frequency is not visible in the graph and has to be added manually. Bode plots solve this, displaying the ϕ angle and the magnitude of the impedance ($|Z|$) as a function of frequency (Fig. 5.3). The magnitude of impedance is defined as:

$$|Z| = \sqrt{Z'^2 + Z''^2}. \tag{5.8}$$

Once EIS data is displayed visually in one of these plots, it should be modelled with an equivalent circuit which represents the processes occurring in the sample. In general, resistors are interpreted as electronic/ionic conductivity, contact resistance, and charge-transfer. Capacitors indicate adsorption of charges, formation of a double layer, or dielectric capacitance. The interpretation of an inductor depends on the frequency range in which it appears. At high frequencies, it is due to practical aspects of the measurement, such as inductive contributions from the measurement cables, which can be minimised in a variety of ways. At low frequencies, the “inductor” can several different interpretations, discussed later. It is important to keep these concepts in mind when building an equivalent circuit model so that the model does not stray far away from physical meaning.

Figure 5.4 shows some possible steps one can take in measuring a sample, assessing the data quality, and fitting it. After taking a measurement, the first step should be data validation using a Kramers-Kronig (KK) transform which states that the real part of the impedance can be obtained from its imaginary part (and vice versa) if either of them is available for all frequencies. A proper EIS measurement requires that certain criteria are met, namely linearity, causality, stability, and finiteness, defined in many sources such as Refs. [16, 22]. Briefly, the small signal applied to the sample should perturb it without changing it (voltage does not cause any reactions), and the output current should be a direct consequence of the voltage applied. As well, the sample should be stable during the measurement because an EIS measurement is already time-dependent. These criteria can be validated by doing a KK transform of the data to ensure that the real and imaginary components are consistent. Data that does not comply with this KK transform should not be analysed by equivalent circuit modelling. It is possible, sometimes, that only a certain frequency range of the data is non-compliant, in which case, the fitted frequency range can be limited to avoid the non-compliant.

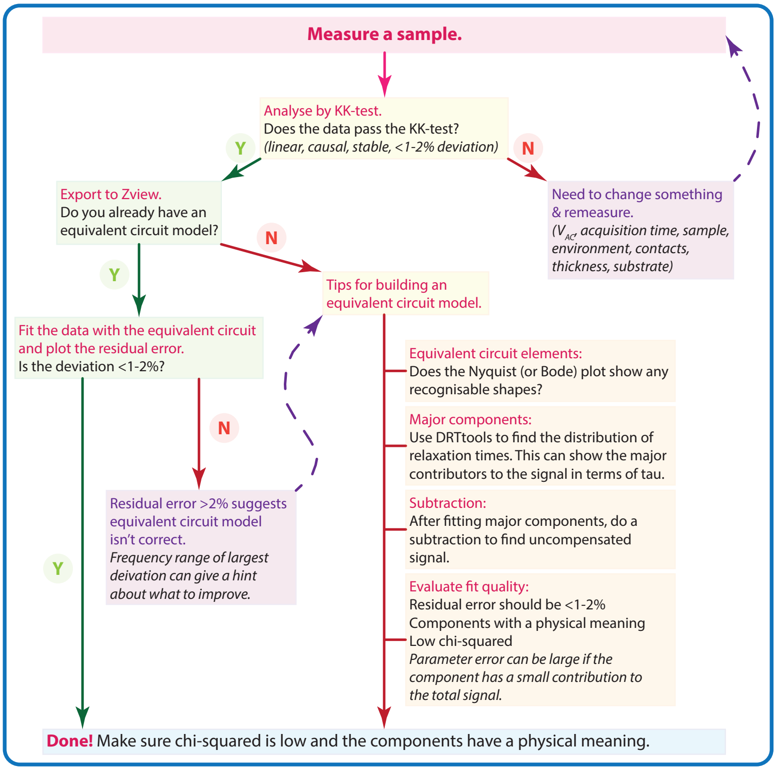

Figure 5.4: Scheme that one can follow when doing EIS experiments in order to obtain valid data and fit it with an appropriate equivalent circuit model. The residual error is the difference between the data and the fit resulting from the chosen equivalent circuit model.

Next, equivalent circuit modelling begins. If there is already some knowledge in the literature about similar systems, those reported circuits should be used to model the data. However, if that does not fit the data well (meaning that it is not a good representation of the processes occurring in this sample), or if there is no pre-existing circuit to use, it is possible to build one from scratch. Hints about which circuit elements to use are hidden in several places. As mentioned previously, the shape of the Nyquist plot already gives some suggestions, but sometimes it is not clear, for example, how many time constants (RCs in parallel) are present in the data. For that, software such as DRTtools can, in principle, be used [23]. As well, one can do a subtraction of the data to see what is not yet compensated by the equivalent circuit used.

Eventually, though, there is a limit to how far the interpretation can go. It is not always justified to add more components to improve the fit of the data. For this, there are tests such as the F-test and the t-test which are used to essentially make sure that adding more degrees of freedom to the fit (adding more circuit elements) actually improves the fit. As well, the addition of more components should be correspond to some (electro-)chemical process in the material to maintain the physical meaning of the equivalent circuit model.

At the end of all these steps, one should have reliable data with a good fit, but there is still the question of interpretation. Something that should be kept in mind with this issue is that there is no unique equivalent circuit model to fit a data set. There will always be several different circuits that fit the data equally well. However, with some understanding of the sample, one circuit can appear more correct than the others. As well, the precise placement of circuit elements in the model can be debated. Generally speaking, elements placed in parallel are considered to be occurring simultaneously, while elements in series are occurring separately or on different time-scales [24]. An example of mistaken placement is shown in Figure 5.5, where the Warburg element (representing diffusion) is put in two different places. Figure 5.5a is the Randles circuit and considers the double-layer capacitance (C_{dl}), charge-transfer at the electrode surface (R_{ct}), and the diffusion of ions (Z_w) to be related processes in the same parallel circuit. The other circuit in Fig. 5.5b will likely give the same fit quality, but there is no physical reason to separate the Warburg element from the other related Faradaic processes.

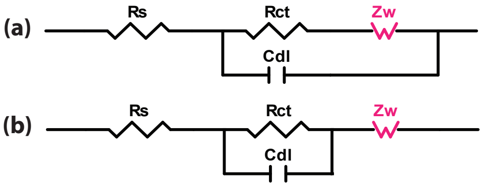

Figure 5.5: Equivalent circuits that would probably gave the same fit result, but different in their placement of the Warburg diffusion element (in pink). The equivalent circuit in (a) is the classic Randles circuit, while (b) is an example of a less-correct placement of the Warburg element.

The information gathered from EIS, in combination with results from DC measurements, is used to understand the total transport of the charge carriers in the material. Specific situations are explained below. Important to note is that the total conductivity of a material (σ_{total}) can be written as:

$$\sigma_{total} = \sigma_{H^-} + \sigma_{e^-}, \tag{5.9}$$

where σ_{H^-} is the ionic conductivity of H^- ions and σ_{e^-} is the electronic conductivity. Limit cases include semiconductor ($\sigma_{e^-} >> \sigma_{H^-}$) and pure ion conductors ($\sigma_{e^-} << \sigma_{H^-}$).

5.2.2 Metal (high σ_{e^-})

A metal, from the point-of-view of EIS, behaves as a resistor which simply conducts charge carriers with some energy dissipation:

$$Z_{metal} = R. \tag{5.10}$$

Since there is no dependence on frequency, there is no imaginary component to the impedance. On a Nyquist plot this would result in a point on the Z' axis. On a Bode plot the $|Z|$ would be a straight line at the value of R and ϕ would be 0. These expectations are based on theoretical considerations, and experimental measurements of real systems differ slightly, namely that at very high frequencies, an inductive response ($\phi > 0^\circ$) can be observed which is usually due to noise from the cables.

DC measurements of a metal should follow Ohms law:

$$V = IR, \tag{5.11}$$

where an input of a DC voltage (V) gives an output of current (I). The linear slope of an I-V curve should be $1/R$. The same R should be obtained from both AC and DC measurements. As well, both conductivities can decrease with increasing temperature due to scattering of conduction electrons.

5.2.3 Pure semiconductor (only σ_{e^-} or σ_{h^+})

When an AC signal is applied to a sample, all the constituents of the sample respond such as the electrons, ions, and dipoles. In a pure semiconductor (no ionic contribution), only electron polarisation is considered, but many dynamics processes involving electrons are outside the time/frequency range of EIS (Fig. 5.6) [16, 19]. Nevertheless, the EIS response of semiconductors is rarely represented by a simple resistor indicating its DC conductivity. In fact, Nyquist plots for semiconductors often show a semicircle, indicative of a resistor and capacitor in parallel. This can happen for a number of reasons.

First, which dynamic processes are visible in the EIS frequency range depends on the material being studied. In the case of perovskite solar cells reviewed in Ref. [19], some recombination mechanisms fall in the EIS time-scale. As well, applying a voltage to the material can also influence which processes are visible, given that the carrier mobility, for example, is low. These fast electronic dynamics, however, are not seen in the experiments described below.

Instead, interfacial capacitance is more important in the context of rare-earth metal oxyhydrides. As the name suggests, the source of the capacitive element is the interface, for example between the oxyhydride and the metal contact [17, 19]. When a metal and a semiconductor are in contact, band bending occurs, forming either Ohmic or non-Ohmic (rectifying) contact. Even in the case of Ohmic contacts, an interfacial capacitance, along with a charge-transfer resistance, can be seen in the EIS response.

Lastly, geometric capacitance is seen for some bulk materials and is based on the dielectric constant of the material, along with its geometry (size) [19]. For thin film

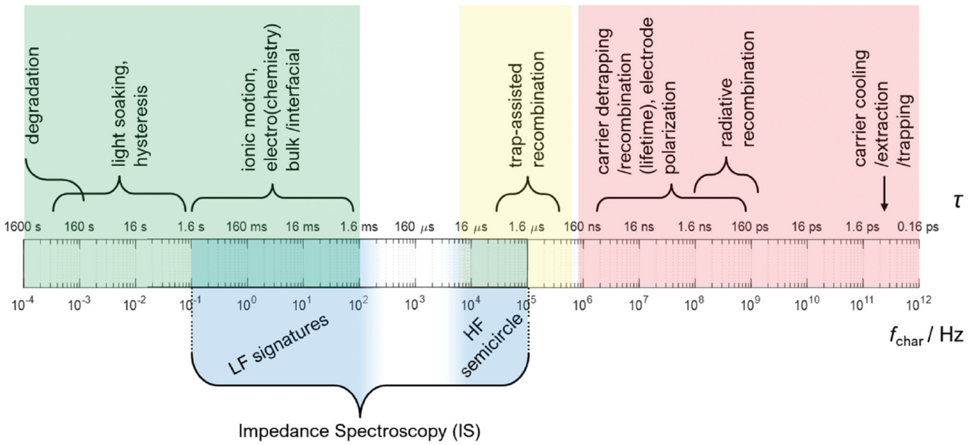

Figure 5.6: Image showing the timescales of several electronic, ionic, and electrochemical processes that can happen in a perovskite solar cell material (τ), compared to the frequency range (f, blue) of EIS (or IS, in this figure). Adapted from Ref. [19].

semiconductor materials such as perovskites or oxyhydrides, the expected geometric capacitance is in the range of 10^{-8} F/cm^2 (if the dielectric constant is 10-20 and the thickness is 500 nm).

DC measurements of the conductivity should, in general, show an Ohmic response, assuming the contacts to the semiconductor are appropriate (no Schottky barrier). With temperature, unlike a metal, the conductivity should increase with increasing temperature as more charge carriers have the energy to hop to the conduction band.

5.2.4 Pure ion conductor (only σ_{H^-})

A perfect ion conductor is typically modelled using several circuit elements, but the main ones are the R and C components in parallel (or Q, discussed later). While the resistance, in this case, is straightforward and related to the resistance (eventually conductivity) of the charge carrier (ion), the capacitance is not usually reported in the literature or discussed at all. One explanation are presented below. At high frequency (ω), a semicircle emerges where C dominates in the RC parallel circuit based on the following equation for the circuit:

$$Z_{RC} = \frac{R}{1 + i\omega RC} \tag{5.12}$$

Capacitance in a real capacitor is defined by charge accumulation at a surface, but this description is not applicable here. Instead, in a highly simplified model that considers only the polarisation of charges, the capacitance related to ion mobility can be interpreted as the time-scale on which the ion can actually respond to the applied signal. Imagine an ion sitting in a potential well with an energy barrier to hop from one site to the next (Fig. 5.7). When an oscillating voltage is applied, if the frequency is too fast (high), the ion is too big and does not have time to respond to fast signals. Eventually, when the frequency is low enough, the ion can respond by jumping over its barrier. The “time” it takes for the ion to move (or “charge”) and begin contributing to ionic conduction is the RC-time constant of the semicircle. When the frequency of the applied voltage signal matches the hopping time constant, the highest point of the semicircle should be reached. Beyond this point, at lower frequencies, the R takes over in Eq. 5.12 which can be converted to the ionic conductivity, since all of the ions can now respond to the applied oscillating signal.

Figure 5.7: Ion hopping between sites when the thermal energy and applied AC frequency conditions are met. This process is represented by the C in the (RC) circuit. Image adapted from Ref. [25]

The aforementioned explanation is, again, highly simplified and may stray too far from real phenomena since ions are constantly moving in a real material, and are doing so in all directions. In that way, the applied oscillating voltage simply disturbs a phenomena that is already happening by, for example, generating an electric field in a particular direction such that more ions move in that direction than had done so without the external field.

The RC circuit does not often end with the semicircle stopping on the real axis. Instead, at low frequencies, several things can happen, partly dependent on the electrodes used to study the solid-state electrolyte (Fig. 5.8) [16, 26]. "Blocking" electrodes (which do not accept charge from ions) can result in a capacitive low frequency response due to the build-up of ionic charges at the interface of the electrode|electrolyte (Fig. 5.8 grey). "Reversible" electrodes (which can undergo a charge-transfer reaction with the ion) can show a number of different responses. One, already mentioned above, is the Warburg diffusion tail. If a 45° tail extends from the semicircle, it is a sign of mass-transport limited diffusion (Fig. 5.8 red). Other versions of the Warburg exist, but are not discussed here. Another possible response is a frequency dependent resistor, as observed in Ref. [5, 8] (Fig. 5.8 blue). This is not possible to fit with any circuit elements, and likely does not meet KK-validation criteria. The physical meaning is also vague, and may indicate a slow

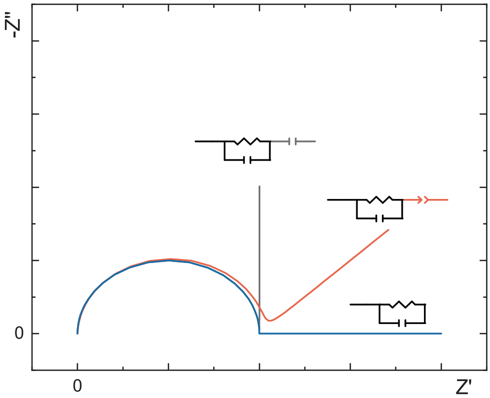

Figure 5.8: Nyquist plot of an RC circuit with different low frequency responses, represented by different equivalent circuit elements.

evolution towards equilibrium. Authors who have reported such low frequency features ignored them while fitting with an equivalent circuit model. However, regardless of all these aspects, in theory, a pure ion conductor should show the same response for ionic conductivity when using blocking and reversible electrodes, except for the response at low-frequency. This was shown, for example, by Takeiri et al. [8] where the same ionic conductivity and activation energy were derived for Ba_2ScHO_3 using either Pd (reversible) or Au (blocking) electrodes.

Next, several different semicircles can be seen if several processes happen at different time-scales (RC = τ) [25, 27]. For bulk powder analysis, authors often report the bulk and grain boundary components of the total ionic mobility which can have different time constants, but are not always discernable from each other. As well, in practice, the capacitance is often simulated as a constant phase element (Q), which allows for some "non-ideality" of the capacitor:

$$Z_Q = \frac{1}{Q(i\omega)^n}, \tag{5.13}$$

where Q is the "capacitance" of the constant phase element and n is the non-ideality factor. When n is 1, an ideal capacitor (C) is obtained, and when n is 0.5, it simulates a Warburg diffusion element. The source of the "non-ideality" is still a point of discussion [21]. Some interpret $n < 1$ as essentially anything that will result in a distribution of time constants such as physical properties (porosity, roughness, or otherwise inhomogeneous interfaces/surfaces) under the so-called fractal model [22]. However, this interpretation has been challenged widely [21]. Another way of understanding the constant phase element, is to consider, again, that all ions are moving constantly and in all directions. Inhomogeneities throughout the lattice can give rise to a distribution in activation energies, which would result in $n < 1$ [28]. In general, to avoid over-fitting, the acceptable range of n is normally 1-0.8 or 0.7 [17], although this is not strict and can be case-dependent.

From DC measurements, a perfect ion conductor should show zero current output for all voltages *if the electrodes are blocking*. In this case, the charge carrier (e.g., H^-) cannot undergo any reaction with the electrode, so it cannot give up an electron to the contacts that can move through the circuit. Only contacts that are reversible (for H^- that would be e.g., Pd) can accept the electron from a mobile H^-, resulting in a current output.

5.2.5 Mixed conductors

Hebb-Wagner polarisation

For materials where ionic conductivity is dominant (or for mixed conductors), one can still extract the electronic contribution to the total conductivity using the Hebb-Wagner method which is an asymmetric DC polarisation method [29, 30]. Different constant voltages are applied to the sample and the current decay is observed. The current decay is fit using the following equation [11, 13]:

$$I(t) = I_0 \mathrm{e}^{-t/\tau} + I_\infty \tag{5.14}$$

where I_0 is the initial current, I_∞ is the steady-state current, and τ is the time constant for current decay. The current (I_∞) at each voltage (V) is plotted in an I-V curve, where the slope is 1/R which can be converted to the electronic conductivity.

The important aspect of this type of measurement is the choice of contact metals; one should be blocking, and the other reversible. Next, as described by Huggins in Ref. [30], the polarisation of the material should be such that the ions are pushed away from the blocking electrode. This results in an ion depletion region in the material, stopping ionic transport. In the case of negative ions (H^-), the blocking electrode should be negatively polarised.

Although this method is followed by some authors [4], the need to choose appropriate metals and polarise the material correctly make the measurement hard to execute correctly. Many authors simply use two blocking electrodes to characterise the electronic conductivity [13]. In this case, it should only be clarified that the electrodes are truly blocking. The expectation is that the ionic current is blocked at the blocking electrodes because the ions cannot transfer charge to the electrode, thus, cannot contribute to the current going through the circuit.

5.3 Transport in Gd-oxyhydride thin films

5.3.1 Experimental methods

Contact arrangement

During this project, we went through several generations of contact arrangements. Thin films can be measured in-plane and out-of-plane, which can make a difference for the observed conductivity [31, 32]. Here, we first attempted out-of-plane measurements with the contacts described in Ref. [14] (used in that publication for Van der Pauw and Hall effect). This resulted in very large resistances in the EIS data and, more importantly, inductive loops at low frequencies (Fig. 5.9a). Such loops or hooks have been reported by many people, sometimes referred to as an inductance, and other times as a differential negative capacitance [33]. Although the interpretation of the differential negative capacitance depends on the system and material being measured, this feature has been ascribed to

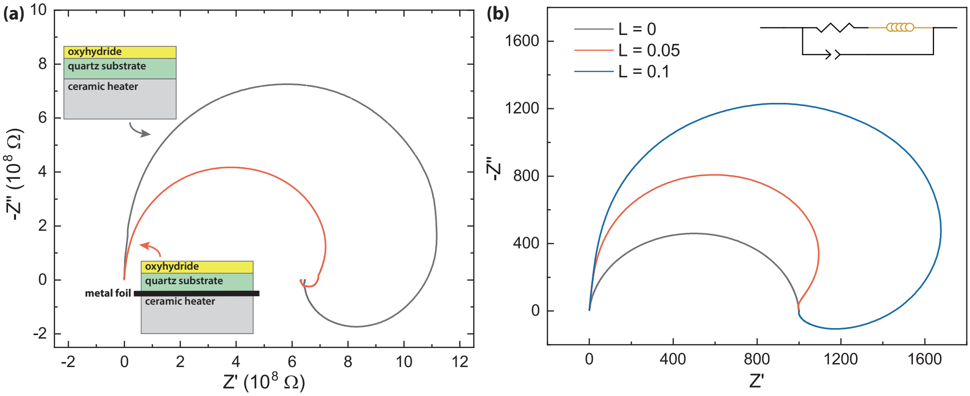

Figure 5.9: (a) An example of measurements done using Gd-oxyhydride thin film on a quartz substrate and sitting on a ceramic heater. The sample had contacts for in-plane measurements. In the grey line, a large low frequency inductive loop is visible. When a metal foil is placed between the quartz substrate and ceramic heater and the sample is measured again, the inductive loop is still present, although significantly smaller. (b) Simulations of what happens to an (RQ) circuit when the “inductive loop” element is included. For all three simulations, R is 1000 Ω, Q is 0.01 nF, and n is 0.95. The strength of the inductive element is varied from 0 (grey), to 0.05 H (red), and finally to 0.1 H (blue), showing the impact of this element on the appearance of the data.

adsorption of reaction intermediates related to electrochemical reactions [24] and chemical reactions that cause changes in the electrode as a result of corrosion [34] or catalysis [35–37], among other examples. However, none of these can be used to explain the inductive loops observed here.

The inductive loops shown in Figure 5.9a are explained in Ref. [38] where this behaviour is attributed to the electric field that goes through the sample leaking to other materials, such as the metallic shielding around the sample. This happens if the measured material is highly resistive. In our case, the current likely leaked to the underlying quartz substrate, or even the ceramic heater under that. The proof of this is shown in Figure 5.9a, where a large inductive loop is visible for a measured sample, which decreases (although not entirely) when a piece of metal is placed between the ceramic heater and quartz substrate. Figure 5.9b also shows simulations of the impact of these loops on the data, which is to somewhat obscure the RC or RQ circuit of interest. Therefore, it is best to prevent the appearance of these loops, for example by using a conductive substrate.

However, not all conductive substrates are equally useful. Silicon wafer substrates resulted in inductive loops as well, perhaps due to the native oxide on Si. The idea of in-plane measurements was, therefore, discarded.

From this point forward, we pursued out-of-plane measurements. The first design involved a metal substrate, the oxyhydride, and a pattern of circular top contacts. The problems with this were two-fold: (1) the adhesion of the oxyhydride layer to some metals like Ti is really poor and the oxyhydride would flake off within minutes after air-exposure, and (2) the probes from the micro-probe station used to contact the films would slowly pierce through the multi-layered stack until it reached the bottom metal. This is shown in (Fig. 5.A.1) and was also observed in, for example, Ref. [39].

The final and most successful design is shown in Figure 5.10a which has the “contact pads” removed from the sample itself. Figure 5.10b also shows a schematic of the cross-section of the measured area, showing that out-of-plane measurements may be even be better than in-plane because of the columnar structure obtained during sputtering (seen by e.g., SEM in Ref. [40]). This is the design used for the data discussed below.

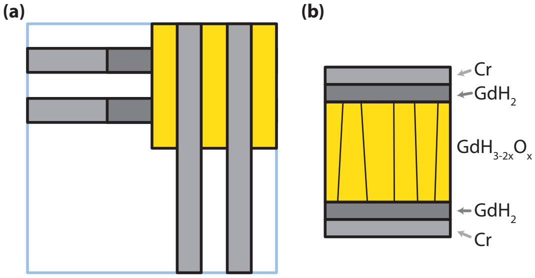

Figure 5.10: (a) Schematic image of the contact arrangement used here to perform out-of-plane measurements of conductivity. The bottom contact strips are Cr|GdH_2, the yellow layer is Gd-oxyhydride, and the top contact strips are GdH_2|Cr. (b) Simplistic image of the sample cross-section showing that this arrangement is ideal for studying conductivity along the columnar structure made by sputtering.

Oxyhydride

Thin films of Gd-oxyhydride ($GdH_{3-2x}O_x$) were deposited by reactive magnetron sputtering a Gd metal target (99.9%, MaTecK) in a mixture of Ar/H_2 (7:1 based on flow), and using a DC power supply to the target at 160 W. While the base pressure of the vacuum chamber was kept below 10^{-6} Pa, the deposition pressure during sputtering was 0.7 Pa, resulting in porous $GdH_{1.9+\delta}$ film [41]. The thickness of the oxyhydride film (~25-700 nm) is controlled by the deposition time. The deposition was performed at room temperature (~21°C) and the sample was oxidised in air.

The bottom and top contacts consisted of Cr and GdH_2 layers. The Cr layer was deposited by sputtering a Cr target at a deposition pressure of 0.3 Pa (Ar only) and an input power of 200 W. The GdH_2 was deposited by sputtering a Gd metal target (99.9%, MaTecK) at a deposition pressure of 0.3 Pa (Ar/H_2 7:1) and an input power of 200 W. The deposition times 10 minutes in both cases. To deposit the bottom contact, Cr was deposited first, followed by GdH_2. The opposite is true for the top contact.

Transport measurements

The electrical response of the sample was measured in AC and DC modes using a Solartron Modulab XM with the femtoammeter and reference cell to measure low currents and to eliminate inductance from the cables, respectively. The sample was kept inside the measurement cell (micro-probe station, Nextron MPS-CHH) in a 2-electrode mode. The cell was evacuated to 10^{-6} mbar, and then a constant flow of 5% H_2 (95% Ar) gas (pressure = 10^{-3} mbar) was introduced for measurement.

For AC measurements, the voltage amplitude was 500 mV, measured between 100 kHz-100 mHz (although the low frequency limit sometimes differs between measurements to avoid low frequency artefacts). Before fitting, impedance data were validated using the Kramers-Kronig (KK) transform with the software developed from Ref. [42, 43]. Then, equivalent circuit models were built and fit to the impedance data using Zview and considering both Nyquist and Bode plots.

For DC measurements, the open circuit voltage was measured and the current decay at constant voltage was measured for several minutes (0.1-0.3 V). The decay was fitted by Eq. (5.14) and plotted in an I-V curve, taking the slope as 1/R. For all measurements, the temperature was controlled between room temperature (~21°C) and 300°C.

5.3.2 Results & Discussion

To understand the transport properties of Gd-oxyhydride thin films, both AC and DC conductivities (σ_{AC} and σ_{DC}) were measured for 25, 300, and 700 nm Gd-oxyhydride thin films. First, σ_{AC} for Gd-oxyhydride is obtained from equivalent circuit modelling of the EIS response, as shown in Figures 5.B.1, 5.C.1, and 5.D.1. KK-transforms of some data sets show that the data is valid for the frequency ranges used for fitting (Fig. 5.E.1), although improvements can be made. For example, more recent measurements (not shown here) using a lower AC voltage amplitude (10 mV) have shown significantly better KK-compliance (<1%), suggesting that using an AC voltage amplitude of 500 mV may push the sample out of equilibrium. After the data was fit, a relative residuals plot was made to compare the measured data and the output from the equivalent circuit model, suggesting that the model used here is sufficient, although more detailed models may be found in the future (Fig. 5.F.1).

For now, accepting the data and fit quality, several important observations can be made based on the Nyquist and half-Bode plots presented in the appendix and in Figure 5.11 for the 300 nm Gd-oxyhydride film, namely that: (1) the AC response of the measured material

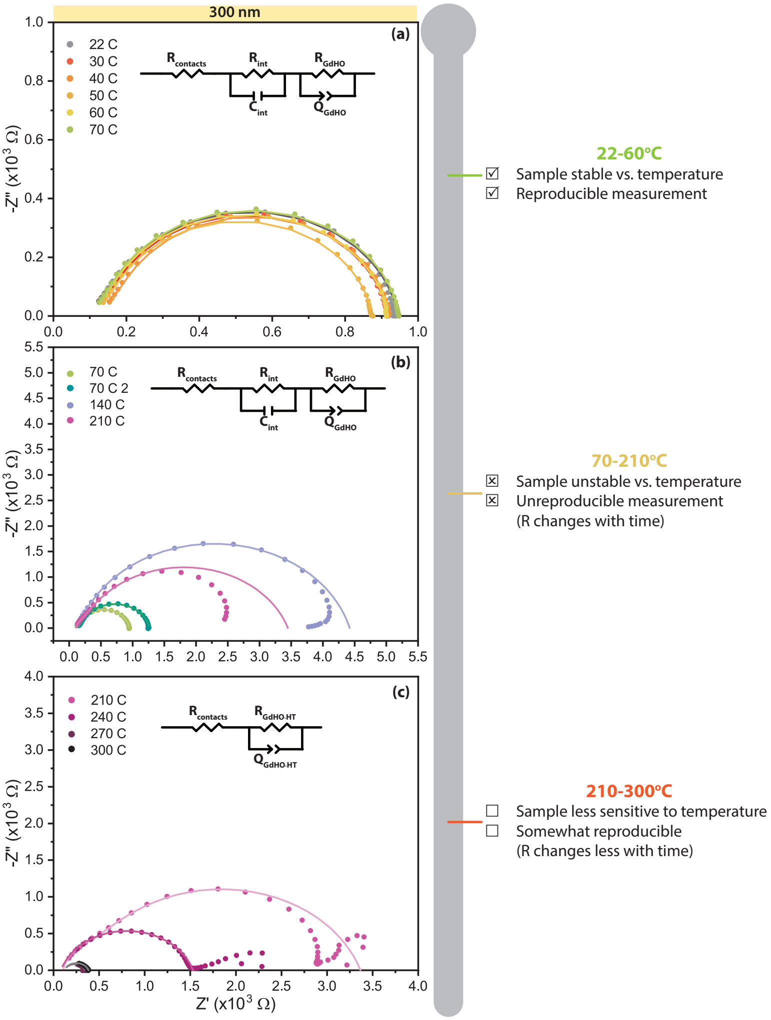

Figure 5.11: Nyquist plots for 300 nm Gd-oxyhydride in three regimes of temperature: (a) regime I 22-60°C, (b) regime II 70-210°C, and (c) regime III 210-300°C. All solid lines represent the fit of the equivalent circuit model included as an inset to the figures. On the side are details about the behaviour of the sample in the three temperatures regimes, mainly that the sample changes significantly between 70-210°C during the first heating programme, making those results and any conductivity derived from them unreliable. At higher temperatures (210-300°C), the changes in the sample are less severe and the data is more reproducible. More details are available in the Appendix.

consists of more than one RC component, (2) there is a temperature-dependence, and (3) there is a dependence on the film thickness.

The equivalent circuit model used to fit the EIS response was either an R(RC)(RC) or R(RC)(RQ) model for all the films as measured between room temperature (21°C) and ~210°C (Figs. 5.11, 5.12a). Due to the fast time constants of these two components (10^{-6} s for the first, and 10^{-5} s for the second) considering the 25 and 300 nm films, it was determined that these are likely due to electronic, rather than ionic, conductivity based on the general guidelines given by, for example, Figure 5.6. Specifically, the first RC component is likely due to the interface between the metal GdH_2 and semiconducting Gd-oxyhydride, where the resistance is due to charge-transfer (R_{int}), the capacitance is related to the interface and build up of charges (C_{int}), and the conductivity is called σ_{int}. Details about this conductivity can be found in Figure 5.G.1, but it is not discussed here. Instead, the more important component from the equivalent circuit model is the second RC or RQ which represents the Gd-oxyhydride layer itself, the conductivity will be called σ_{GdHO}.

The temperature dependence of σ_{GdHO} is shown in Figures 5.12b and c for the 25 and 300 nm Gd-oxyhydride films, respectively, and the Nyquist plots from which this is derived are shown for the 300 nm sample in Figure 5.11. We identify three different temperature regimes based on changes in σ_{GdHO}. Regime I is the low temperature regime (22-60°C), where the films show a conductivity of 10^{-4}-10^{-5} S/cm, although this differs slightly depending on the film thickness. The conductivity is only weakly dependent on temperature, with an activation energy of 0.04 eV (25nm) or 0.01 eV (300 nm) (Fig. 5.13), lower than the value from Ref. [14] for Gd-oxyhydride thin films (~0.1 eV), potentially explained by differences in sputtering deposition conditions (160 vs 175 W, 0.7 Pa vs 0.75 Pa). Additionally, while an RC fits well for the 25 nm film in this temperature range, the 300 nm film is best fit by an RQ with a non-ideality factor of ~0.92-0.94, suggesting some minor inhomogeneity in the thicker film, which may be a result of, for example, a compositional gradient after air-oxidation.

Between 70-210°C (regime II), σ_{GdHO} decreases with increasing temperature, which is unexpected for a semiconductor, but was observed also in Ref. [14]. As well, around 90°C, the RC component related to σ_{GdHO} for the 25 nm film does not fit the data any longer, and the data is better represented by an RQ. For both the 25 and 300 nm films, as the temperature increases, the non-ideality factor for Q becomes smaller. More detailed information can be seen from the half-Bode plots for the 300 nm Gd-oxyhydride thin film which was measured at 140 and 210°C several times (Fig. 5.H.1). The peak in phase angle widens as the film is kept at 140°C, indicating that time constant associated with this dynamic process is becoming more dispersed. This is likely the result of annealing, as seen in Chapters 3 and 6, where no changes could be observed from XRD between 70-100°C, but an annealing effect is visible from 100°C and above, evidenced by the decrease in spread of the lattice constant values calculated from the three main reflections. It is not clear, however, why this annealing effect should have a negative impact on the observed conductivity. Others have suggested that oxidation occurs above 100°C [44] which could potentially explain these changes in σ_{GdHO}. However, we tried to prevent oxidiation here by keeping the sample under vacuum (10^{-6} mbar) and introducing a constant flow of H_2 gas (10^{-3} mbar).

Around 210-300°C (regime III), there is only one RQ component present at these temperatures in the equivalent circuit model, which will be referred to as $\sigma_{GdHO-HT}$. This

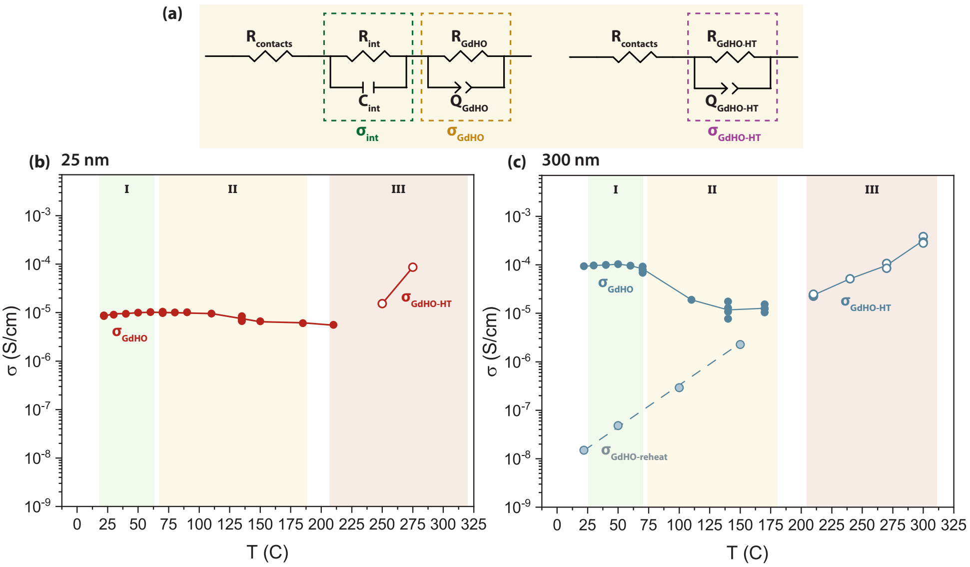

Figure 5.12: (a) Equivalent circuit models used to fit the EIS data for 25 and 300 nm Gd-oxyhydride thin films. The R(RC)(RQ) was used for regimes I and II for both films, although for the 25 nm film in regime I, the data was best represented by R(RC)(RC). In regime III, the (RC) component disappeared, and the data was best fit by the R(RQ) circuit. (b) and (c) show the temperature dependent electronic conductivity for 25 and 300 nm Gd-oxyhydride thin films, respectively. Only σ_{GdHO} and $\sigma_{GdHO-HT}$ are shown since these are expected to represent the conductivity of the Gd-oxyhydride film at low and high temperatures, respectively. The 300 nm was reheated to 150°C, and fitted by the R(RC)(RQ) circuit, where the conductivity based on (RQ) represents the Gd-oxyhydride ($\sigma_{GdHO-reheat}$).

conductivity increases with temperature, although following an entirely different temperature dependence compared to σ_{GdHO} in regime I. Here, the activation energy is 1.7 eV (25 nm) or 0.69 eV (300 nm) (Fig. 5.13), resembling the results from Ref. [15] instead of Ref. [14]. This could be due to the formation of a more temperature-stable annealed phase of the Gd-oxyhydride, compared to the as-deposited air-oxidised meta-stable film before heat treatment.

Interestingly, at 210°C for the 300 nm Gd-oxyhydride film, another peak is observed in the phase angle at low frequencies (Fig. 5.H.1). However, this part of the data is not KK-compliant (Fig. 5.I.1), so no attempts were made to fit it. Several conclusions can be made about this peak, the most sceptical of which would call this peak a measurement artefact. It is not clear, at this moment, if that is true. The peak reappears again at 240 and 270°C, shifting towards higher frequencies with increasing temperature. A somewhat ambitious interpretation of the data could call this an indication of ionic mobility. The time-scale of this dynamic process is in the range of 10-0.1 s, which is the general range expected for ionic motion (Fig. 5.6). The reality is likely that, as the sample changes at higher temperatures, some H_2 escapes the sample [45], which can involve some ionic mobility. This was seen best for the 700 nm sample which started to colour around 250°C, and was dark by 315°C (Fig. 5.D.1d), similar to what was described in Chapter 6. This low frequency peak was not found for the 700 nm film, however, because the AC response in EIS was non-stationary, thus, the measurement was stopped before low frequencies could

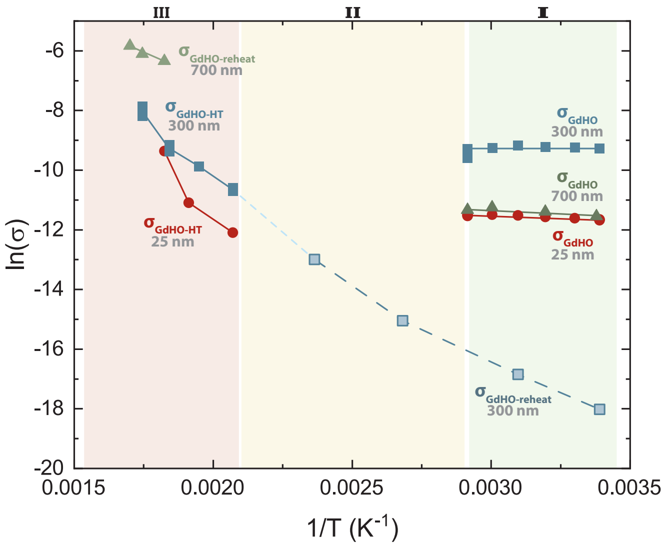

Figure 5.13: Arrhenius plot of the electronic conductivity (S/cm) for 25 nm (red), 300 nm (blue), and 700 nm (green) Gd-oxyhydride thin films based on their σ_{GdHO} and $\sigma_{GdHO-HT}$ values from EIS. For the 25 nm sample, stable conductivity was obtained between 22-70°C and 210-275°C, although with different activation energies. For the 300 nm sample, the same is true, however, this film was cooled down and then reheated to 150 °C (light blue, $\sigma_{GdHO-reheat}$). Upon reheating, the larger activation energy found between 210-300°C. For the 700 nm sample, both AC and DC data were difficult to fit either due to artefacts or non-Ohmic responses. The data at low temperatures (22-70°C) is an estimate of the conductivity, producing a similar result to the other two samples. The sample was heated to 140°C, cooled down, and reheated to 315°C. Only the AC data at very high temperatures could be evaluated, leading again to the higher activation energy. Coloured boxes indicate the different temperature regimes mentioned in Figure 5.G.1.

be reached. For this reason, quantitative data about the conductivity in the 700 nm film is limited to what is seen in Figure 5.13.

After heating to 300°C, the 300 nm film was cooled back to room temperature, and heated again while measuring the AC response from 22-150°C (Fig. 5.J.1). The conductivity of the film after heating is significantly lower ($\sigma_{GdHO-reheat} \sim 10^{-8}$ S/cm) than its original state ($\sigma_{GdHO} \sim 10^{-4}$ S/cm), but it is more stable with respect to temperature (Fig. 5.12). As well, the conductivity continues to follow the large activation energy of at least 0.5 eV that was observed for $\sigma_{GdHO-HT}$ (Fig. 5.13). This all suggests that the post-annealed sample reflects a more temperature-stable phase of the material, with temperature trends similar to those reported in Ref. [15].

For DC measurements, the current decay over time and for different DC voltages was fitted by equation 5.14, and then used in an I-V plot to obtain σ_{DC}. This was also done for the 300 nm sample that was reheated from 22-150°C. The comparison of σ_{DC} and the different components to σ_{AC} can be found in Figure 5.G.1. Briefly, σ_{DC} is always comparable to the sum of the various components associated with the Gd-oxyhydride thin film (σ_{GdHO}, $\sigma_{GdHO-HT}$, and $\sigma_{GdHO-reheat}$). Given that blocking contacts are used here, it is clear that the Gd-oxyhydride thin films measured here are dominated by electronic conductivity, since a pure ion conductor would show a significantly larger σ_{AC} than σ_{DC}.

5.4 Conclusions

The transport properties of Gd-oxyhydride thin films were assessed by AC and DC methods at different temperatures and film thickness. The conductivity appears to be dominated by electrons/holes, although the activation energy of this process differs depending on the state of the film. After deposition and air-oxidation, the activation energy is very low (0.01-0.04 eV for 22-60°C). However, between 70-210°C, the samples undergo irreversible changes, likely in both structure and composition. Above these temperatures, the sample conductivity increases again, but at a larger activation energy (0.69-1.7 eV). This new state of the film proves to be stable since this high activation energy is retrieved when the sample is cooled and then reheated again while measuring the conductivity. Therefore, two conclusions are notable from these results: (1) Gd-oxyhydride is a primarily electron/hole conductor rather than an ion-dominated conductor, and (2) the films produced by sputtering and rapid air-oxidation do not represent the most thermally stable phase of the oxyhydride. To make reliable measurements at high temperatures, the films should be heat treated during preparation of the sample. We suggest that the high temperature changes in the sample include local redistribution of ions at low temperatures (70-100°C), annealing at moderate temperatures (100-210°C), and the release of some H_2 at high temperatures (210-315°C).

In terms of the bigger picture of RE-oxyhydrides as solid-state H^- conductors, the methods described here could be extended to other RE-oxyhydrides. Nd-oxyhydride, for example, showed pure H^- in its bulk stoichiometric form [12]. Y-oxyhydride was also reported to show H^- redistribution initiated by 0.5-1 V [46]. Aliovalent doping of this film, as described in Chapter 4, could offer a way to increase the H^- conductivity of the oxyhydride, although such doping can sometimes improve electron/hole conductivity as well. Thus, there is room to evaluate other materials to build a larger picture of which materials lead to H^- conductivity (or not), and what materials properties are necessary for this.

In addition, there is some room to improve the oxyhydride thin films to better isolate ionic mobility, if it is at all contributing to the total conductivity of the sample. One simple way is to limit the film thickness or decrease the amplitude of the input AC signal. The data for the 700 nm sample was difficult to analyse due to the presence of low frequency artefacts, which become more and more problematic as the sample conductivity decreases. Next, the samples can be pre-annealed before measurement so that the temperature-stable phase of the material is measured. Last, higher pressure H_2 can be added to the measurement cell to see if the conductivity and thermal stability of the sample differ under these conditions.

References

[1] H. Kageyama, K. Hayashi, K. Maeda, J. P. Attfield, Z. Hiroi, J. M. Rondinelli, and K. R. Poeppelmeier, *Expanding frontiers in materials chemistry and physics with multiple anions,* Nature Communications **9**, 772 (2018).

[2] M. C. Verbraeken, E. Suard, and J. T. S. Irvine, *Structural and electrical properties of calcium and strontium hydrides,* Journal of Materials Chemistry **19**, 2766 (2009).

[3] M. C. Verbraeken, C. Cheung, E. Suard, and J. T. Irvine, *High* H^- *ionic conductivity in barium hydride,* Nature Materials **14**, 95 (2015).

[4] G. Kobayashi, Y. Hinuma, S. Matsuoka, A. Watanabe, M. Iqbal, M. Hirayama, M. Yonemura, T. Kamiyama, I. Tanaka, and R. Kanno, *Pure* H^- *conduction in oxyhydrides,* Science **351**, 1314 (2016).

[5] A. Watanabe, G. Kobayashi, N. Matsui, M. Yonemura, A. Kubota, K. Suzuki, M. Hirayama, and R. Kanno, *Ambient pressure synthesis and* H^- *conductivity of* $LaSrLiH_2O_2$*,* Electrochemistry **85**, 88 (2017).

[6] Y. Iwasaki, N. Matsui, K. Suzuki, Y. Hinuma, M. Yonemura, G. Kobayashi, M. Hirayama, I. Tanaka, and R. Kanno, *Synthesis, crystal structure, and ionic conductivity of hydride ion-conducting* Ln_2LiHO_3 *(Ln = La, Pr, Nd) oxyhydrides,* Journal of Materials Chemistry A **6**, 23457 (2018).

[7] N. Matsui, G. Kobayashi, K. Suzuki, A. Watanabe, A. Kubota, Y. Iwasaki, M. Yonemura, M. Hirayama, and R. Kanno, *Ambient pressure synthesis of* La_2LiHO_3 *as a solid electrolyte for a hydrogen electrochemical cell,* Journal of the American Ceramic Society **102**, 3228 (2019).

[8] F. Takeiri, A. Watanabe, A. Kuwabara, H. Nawaz, N. I. P. Ayu, M. Yonemura, R. Kanno, and G. Kobayashi, Ba_2ScHO_3*:* H^- *conductive layered oxyhydride with* H^- *site selectivity,* Inorganic Chemistry **58**, 4431 (2019).

[9] H. Nawaz, F. Takeiri, A. Kuwabara, M. Yonemura, and G. Kobayashi, *Synthesis and* H^- *conductivity of a new oxyhydride* Ba_2YHO_3 *with anion-ordered rock-salt layers,* Chemical Communications **56**, 10373 (2020).

[10] F. Takeiri, A. Watanabe, K. Okamoto, D. Bresser, S. Lyonnard, B. Frick, A. Ali, Y. Imai, M. Nishikawa, M. Yonemura, T. Saito, K. Ikeda, T. Otomo, T. Kamiyama, R. Kanno, and G. Kobayashi, *Hydride-ion-conducting* K_2NiF_4*-type Ba-Li oxyhydride solid electrolyte,* Nature Materials **21**, 325 (2022).

[11] K. Fukui, S. Iimura, T. Tada, S. Fujitsu, M. Sasase, H. Tamatsukuri, T. Honda, K. Ikeda, T. Otomo, and H. Hosono, *Characteristic fast* H^- *ion conduction in oxygen-substituted lanthanum hydride,* Nature Communications **10**, 2578 (2019).

[12] H. Ubukata, T. Broux, F. Takeiri, K. Shitara, H. Yamashita, A. Kuwabara, G. Kobayashi, and H. Kageyama, *Hydride conductivity in an anion-ordered fluorite structure LnHO with an enlarged bottleneck,* Chemistry of Materials **31**, 7360 (2019).

[13] K. Fukui, S. Iimura, A. Iskandarov, T. Tada, and H. Hosono, *Room-temperature fast H^- conduction in oxygen-substituted lanthanum hydride,* Journal of American Chemical Society **144**, 1523 (2022).

[14] G. Colombi, B. Boshuizen, D. Chaykina, L. Hsu, H. Schreuders, T. J. Savenije, and B. Dam, *Relation between photochromism and photoconductivity in REO_xH_{3-2x} thin films,* in preparation (2022).

[15] A. Miniotas, B. Hjörvarsson, L. Douysset, and P. Nostell, *Gigantic resistivity and band gap changes in GdO_yH_x thin films,* Applied Physics Letters **76**, 2056 (2000).

[16] E. von Hauff, *Impedance spectroscopy for emerging photovoltaics,* The Journal of Physical Chemistry C **123**, 11329 (2019).

[17] A. R. C. Bredar, A. L. Chown, A. R. Burton, and B. H. Farnum, *Electrochemical impedance spectroscopy of metal oxide electrodes for energy applications,* ACS Applied Energy Materials **3**, 66 (2020).

[18] V. Vivier and M. E. Orazem, *Impedance analysis of electrochemical systems,* Chemical Reviews **122**, 11131 (2022).

[19] E. von Hauff and D. Klotz, *Impedance spectroscopy for perovskite solar cells: characterisation, analysis, and diagnosis,* Journal of Materials Chemistry C **10**, 742 (2022).

[20] I. V. Krasnikova, M. A. Pogosova, A. O. Sanin, and K. J. Stevenson, *Toward standardization of electrochemical impedance spectroscopy studies of li-ion conductive ceramics,* Chemistry of Materials **32**, 2232 (2020).

[21] A. Lasia, *The origin of the constant phase element,* The Journal of Physical Chemistry Letters **13**, 580 (2022).

[22] A. Lasia, *Electrochemical Impedance Spectroscopy and its Applications* (Springer, New York, USA, 2014).

[23] T. H. Wan, M. Saccoccio, C. Chen, and F. Ciucci, *Influence of the discretization methods on the distribution of relaxation times deconvolution: Implementing radial basis functions with DRTtools,* Electrochimica Acta **184**, 483 (2015).

[24] H. Cesiulis, N. Tsyntsaru, A. Ramanavicius, and G. Ragoisha, *The study of thin films by electrochemical impedance spectroscopy,* in *Nanostructures and Thin Films for Multifunctional Applications*, NanoScience and Technology (Springer International Publishing Switzerland, 2016) Book section Chapter 1, pp. 3–42.

[25] A. Delgado, M. F. García-Sánchez, J.-C. M'Peko, A. R. Ruiz-Salvador, G. Rodríguez-Gattorno, Y. Echevarría, and F. Fernández-Gutierrez, *An elementary picture of dielectric spectroscopy in solids: Physical basis,* Journal of Chemical Education **80**, 1062 (2003).

[26] A. D. Franklin, *Electrode effects in the measurement of ionic conductivity,* Journal of the American Ceramic Society **58**, 465 (1975).

[27] M. A. Danzer, *Generalized distribution of relaxation times analysis for the characterization of impedance spectra,* Batteries **5**, 53 (2019).

[28] B. A. Boukamp, *Personal communication,* (2022).

[29] I. Riess, *Measurement of ionic-conductivity in semiconductors and metals,* Solid State Ionics **44**, 199 (1991).

[30] R. A. Huggins, *Simple method to determine electronic and ionic components of the conductivity in mixed conductors a review,* Ionics **8**, 300 (2002).

[31] E. Navickas, M. Gerstl, F. Kubel, and J. Fleig, *Simultaneous measurement of the in- and across-plane ionic conductivity of ysz thin films,* Journal of The Electrochemical Society **159**, B411 (2012).

[32] H. Duan, C. C. Yuan, N. Becerra, L. J. Small, A. Chang, J. M. Gregoire, and R. B. van Dover, *High-throughput measurement of ionic conductivity in composition-spread thin films,* ACS Combinatorial Science **15**, 273 (2013).

[33] D. Klotz, *Negative capacitance or inductive loop? - a general assessment of a common low frequency impedance feature,* Electrochemistry Communications **98**, 58 (2019).

[34] L.-n. Xu, J.-y. Zhu, M.-x. Lu, L. Zhang, and W. Chang, *Electrochemical impedance spectroscopy study on the corrosion of the weld zone of 3Cr steel welded joints in* CO_2 *environments,* International Journal of Minerals, Metallurgy, and Materials **22**, 500 (2015).

[35] R. Jiang, H. R. Kunz, and J. M. Fenton, *Electrochemical oxidation of* H_2 *and* H_2/CO *mixtures in higher temperature* ($T_{sub} > 100^\circ C$) *proton exchange membrane fuel cells: Electrochemical impedance spectroscopy,* Journal of The Electrochemical Society **152**, A1329 (2005).

[36] U. Krewer, M. Christov, T. Vidaković, and K. Sundmacher, *Impedance spectroscopic analysis of the electrochemical methanol oxidation kinetics,* Journal of Electroanalytical Chemistry **589**, 148 (2006).

[37] T. V. Reshetenko, K. Bethune, M. A. Rubio, and R. Rocheleau, *Study of low concentration CO poisoning of Pt anode in a proton exchange membrane fuel cell using spatial electrochemical impedance spectroscopy,* Journal of Power Sources **269**, 344 (2014).

[38] J. Fleig, J. Jamnik, J. Maier, and J. Ludvig, *Inductive loops in impedance spectroscopy caused by electrical shielding,* J. Electrochem. Soc. **143**, 3636 (1996).

[39] A. K. Opitz and J. Fleig, *Investigation of* O_2 *reduction on Pt/YSZ by means of thin film microelectrodes: The geometry dependence of the electrode impedance,* Solid State Ionics **181**, 684 (2010).

[40] S. Cornelius, G. Colombi, F. Nafezarefi, H. Schreuders, R. Heller, F. Munnik, and B. Dam, *Oxyhydride nature of rare-earth-based photochromic thin films,* The Journal of Physical Chemistry Letters **10**, 1342 (2019).

[41] G. Colombi, T. De Krom, D. Chaykina, S. Cornelius, S. W. H. Eijt, and B. Dam, *Influence of cation (RE = Sc, Y, Gd) and O/H anion ratio on the photochromic properties of* REO_xH_{3-2x} *thin films,* ACS Photonics **8**, 709 (2021).

[42] B. A. Boukamp, *A linear Kronig-Kramers transform test for immittance data validation,* Journal of The Electrochemical Society **142**, 1885 (1995).

[43] B. A. Boukamp, *Electrochemical impedance spectroscopy in solid state ionics: recent advances,* Solid State Ionics **169**, 65 (2004).

[44] C. C. You and S. Z. Karazhanov, *Effect of temperature and illumination conditions on the photochromic performance of yttrium oxyhydride thin films,* Journal of Applied Physics **128**, 013106 (2020).

[45] D. Moldarev, L. Stolz, M. V. Moro, S. M. Aðalsteinsson, I.-A. Chioar, S. Z. Karazhanov, D. Primetzhofer, and M. Wolff, *Environmental dependence of the photochromic effect of oxygen-containing rare-earth metal hydrides,* Journal of Applied Physics **129**, 153101 (2021).

[46] T. Yamasaki, R. Takaoka, S. Iimura, J. Kim, H. Hiramatsu, and H. Hosono, *Characteristic resistive switching of rare-earth oxyhydrides by hydride ion insertion and extraction,* ACS Applied Materials & Interfaces **14**, 19766 (2022).

Appendix

5.A Sample tearing from probes

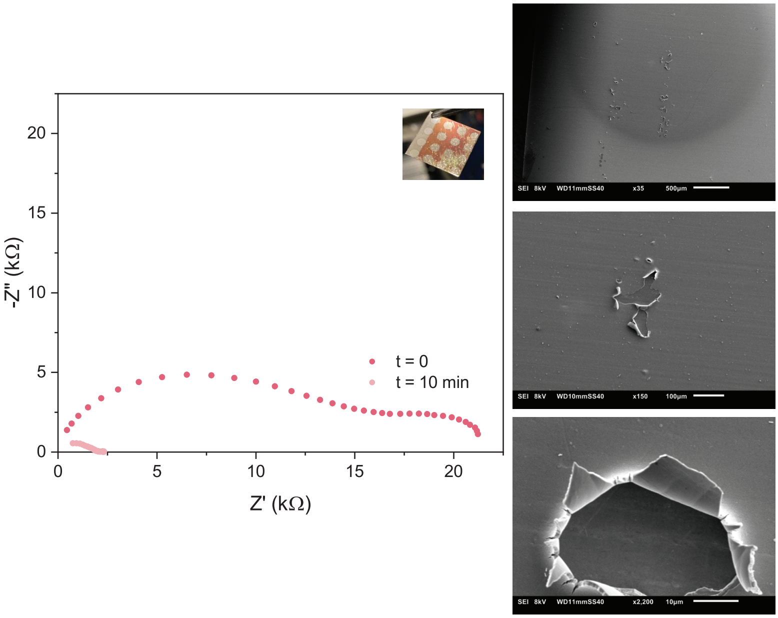

Figure 5.A.1: (left) Nyquist plot for Gd-oxyhydride with a Mo metal foil as the bottom contact and circular sputtered Mo top contacts, as shown in the photo inset of the graph. When the sample is measured twice 10 minutes apart, the response is very different due to the probes piercing through the Mo top contact and Gd-oxyhydride. (right) SEM images at different magnifications showing how the probes from the micro-probe station pierce through the sample.

5.B AC analysis of 25 nm Gd-oxyhydride film with respect to temperature

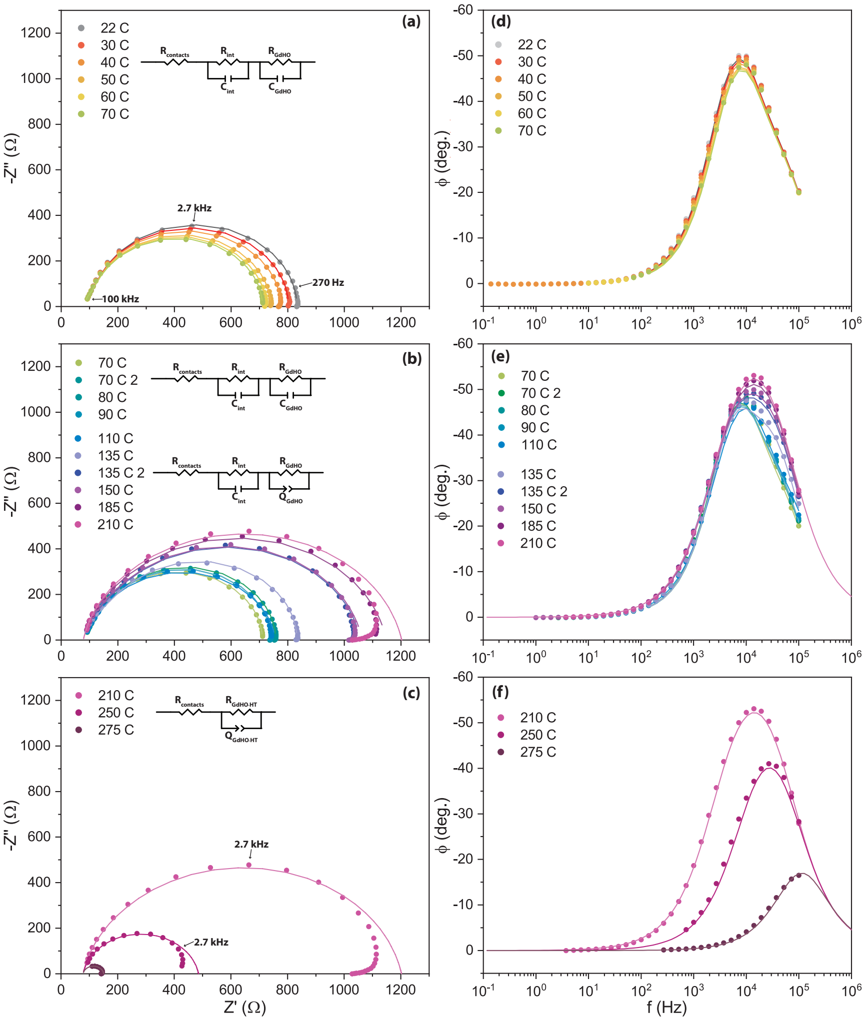

Figure 5.B.1: Nyquist plots for 25 nm Gd-oxyhydride (0.7 Pa) are shown for different temperature ranges: (a) 22-70°C, (b) 70-210°C, and (c) 210-275°C. The equivalent circuits used to fit the data are shown next to the legends. (d), (e), and (f) show the corresponding ϕ angle change with frequency (half of the Bode plot). All the lines in these plots are the equivalent circuit fit. At low temperatures (22-70°C), there are two RC components related to the interface between Gd-oxyhydride and GdH_2, and to Gd-oxyhydride thin film itself. When the temperature increases, the resistance (width of semicircle) becomes unreproducible. Another change occurs at 135°C, where the RC related to the Gd-oxyhydride film becomes better represented by an RQ. It is likely that the sample is changing slowly with temperature such that one distinct time constant cannot describe the data, leading to the use of Q. At very high temperatures (210-275°C), the interface component disappears, and the resistance decreases with temperature. In the legend, when a “2” follows the temperature label, it indicates that two measurements were performed at this temperature this is the second one.

5.C AC analysis of 300 nm Gd-oxyhydride film with respect to temperature

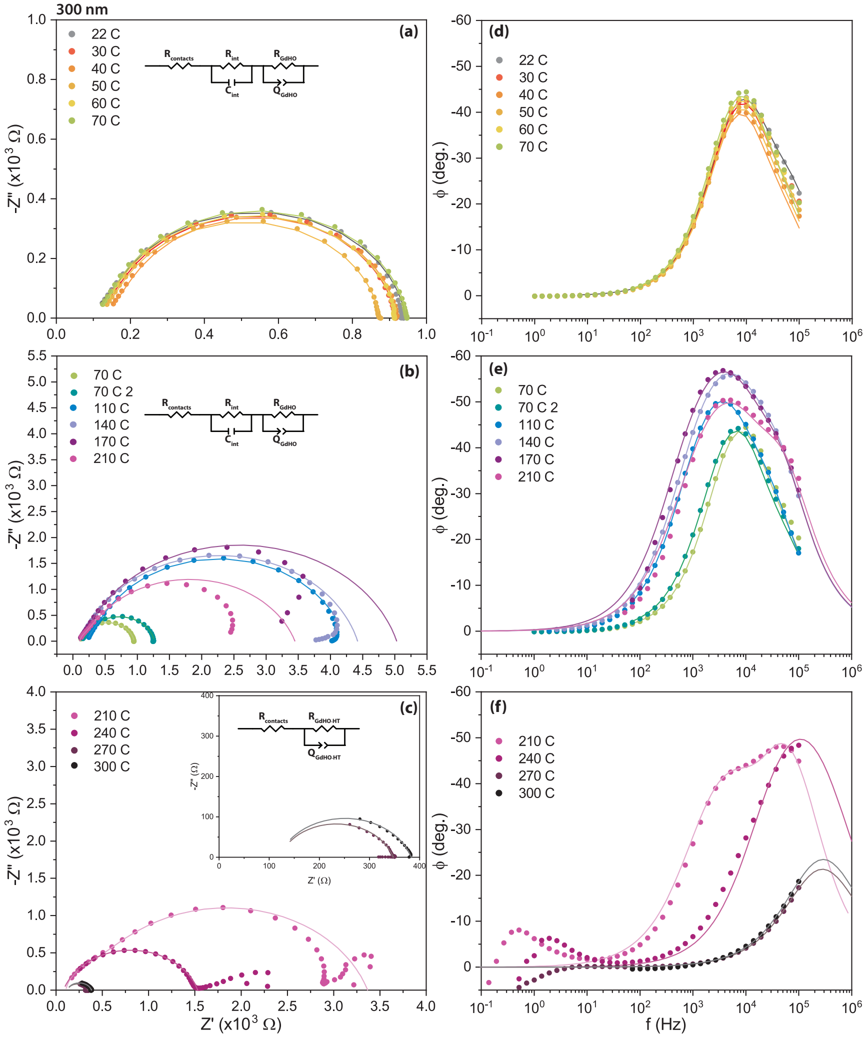

Figure 5.C.1: Nyquist plots for 300 nm Gd-oxyhydride (0.7 Pa) are shown for different temperature ranges: (a) 22-70°C, (b) 70-210°C, and (c) 210-300°C. The equivalent circuits used to fit the data are shown next to the legends. (d), (e), and (f) show the corresponding ϕ angle change with frequency (half of the Bode plot). All the lines in these plots are the equivalent circuit fit. The same two components of the equivalent circuit model are used here as for the 25 nm thin film. As well, unreproducible behaviour is shown in the second temperature regime. At high temperatures, only the R(RQ) related to the contacts and the Gd-oxyhydride are visible. In the legend, when a “2” follows the temperature label, it indicates that two measurements were performed at this temperature this is the second one.

5.D AC analysis of 700 nm Gd-oxyhydride film with respect to temperature

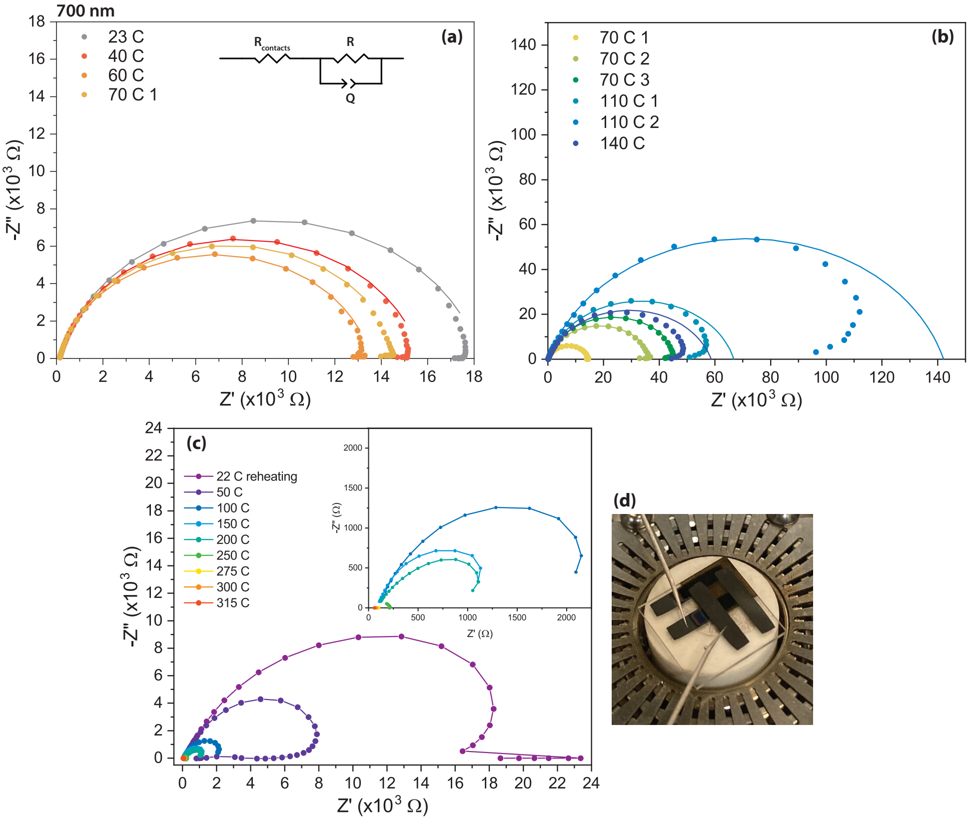

Figure 5.D.1: The 700 nm Gd-oxyhydride thin film was heated from 22-140°C, shown in the Nyquist plots in (a) and (b). The lines in these graphs are the fit result for an R(RQ) equivalent circle. The data becomes irreproducible above 70°C, and the low frequency hook becomes more severe as the overall resistance of the film increases, leading to problems with reliable fitting of the data. This is especially true in (c) where the film was reheated from 22-315°C. The semicircle in the Nyquist plot turns inward, making reliable fitting difficult. Only data for 250-315°C could be assessed because the respond from the Nyquist plot was essentially a simple R. In this temperature range, the sample also changed colour visibly, as shown in (d) for 315°C.

5.E KK-validation of data obtained from measurements for 25 and 300 nm Gd-oxyhydride

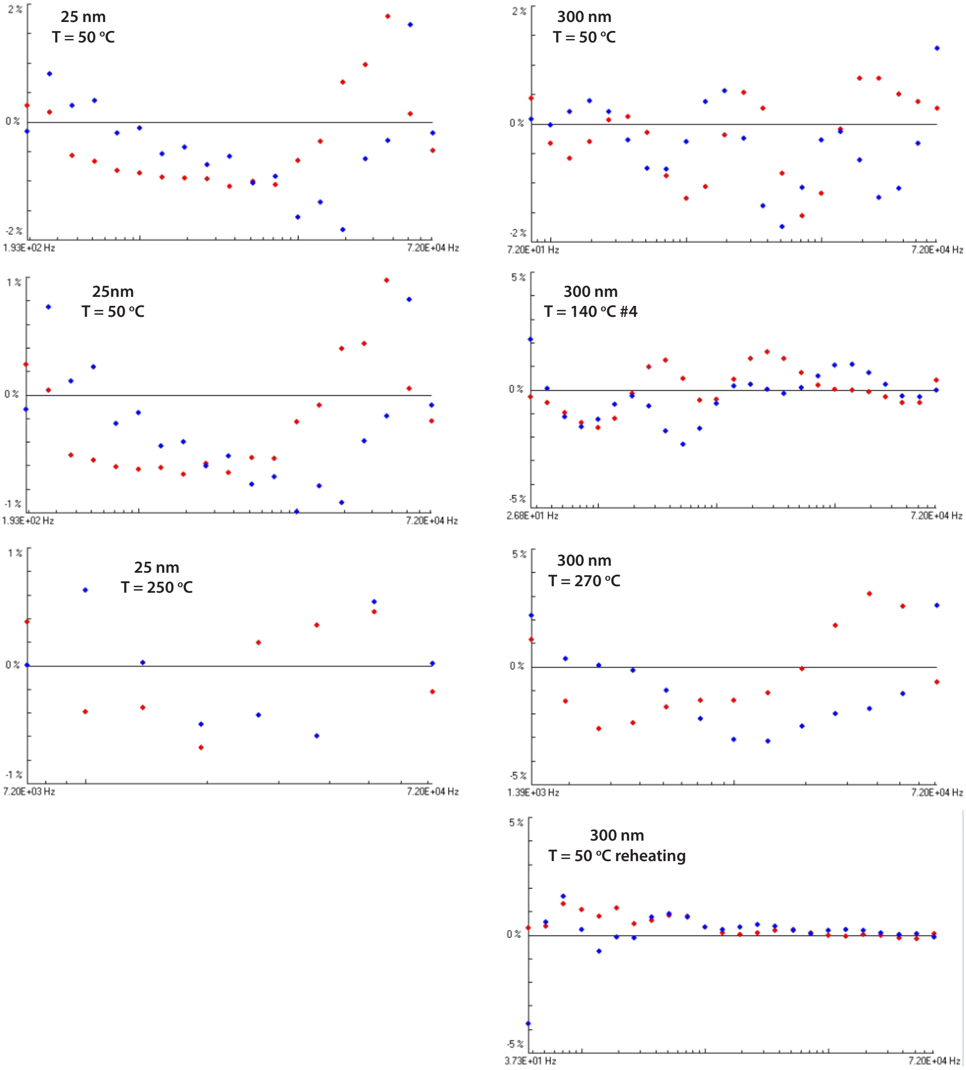

Figure 5.E.1: The KK-validation test of the data was performed based on Ref. [1, 2] for 3 data sets for the 25 nm and the 300 nm samples of Gd-oxyhydride. One data set from each of the three temperatures regimes is taken. The KK-test is only done for the frequency range that was used for fitting. Deviations below 2% are considered reasonable, although oscillating patterns in these graphs may be cause for concern. For the 300 nm sample, another plot is shown for the sample at 50°C during the second heating (reheating).

5.F Fit quality assessment for 25 nm sample measured at 50°C

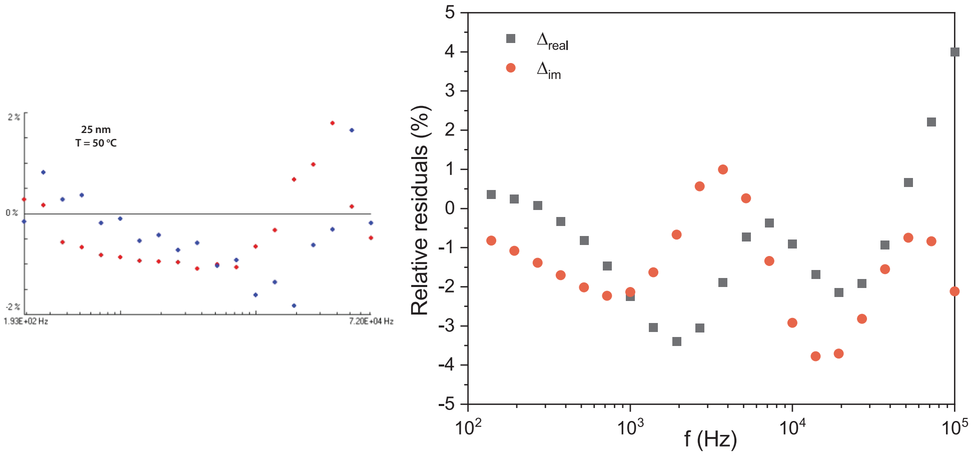

Figure 5.F.1: For the 25 nm Gd-oxyhydride sample measured at 50°C, two procedures were followed to validate the methods used. (right) The measured data itself was validated by the KK-transform. Since the deviations of the real and imaginary components to the impedance were below 2%, the data was assumed to be valid in this frequency range and a fit was performed with an R(RC)(RC) circuit. (left) The fit quality can be assessed using a relative residuals plot which compares the measured data with the output from the fit. Similar deviations in both plots indicate an acceptable fit. Here, this is mostly true, although future work should involve both improving the measurement and the equivalent circuit model. In particular, oscillations in the residuals plot (right) indicate that there may be a missing component from the equivalent circuit model.

5.G Comparison of AC and DC conductivity

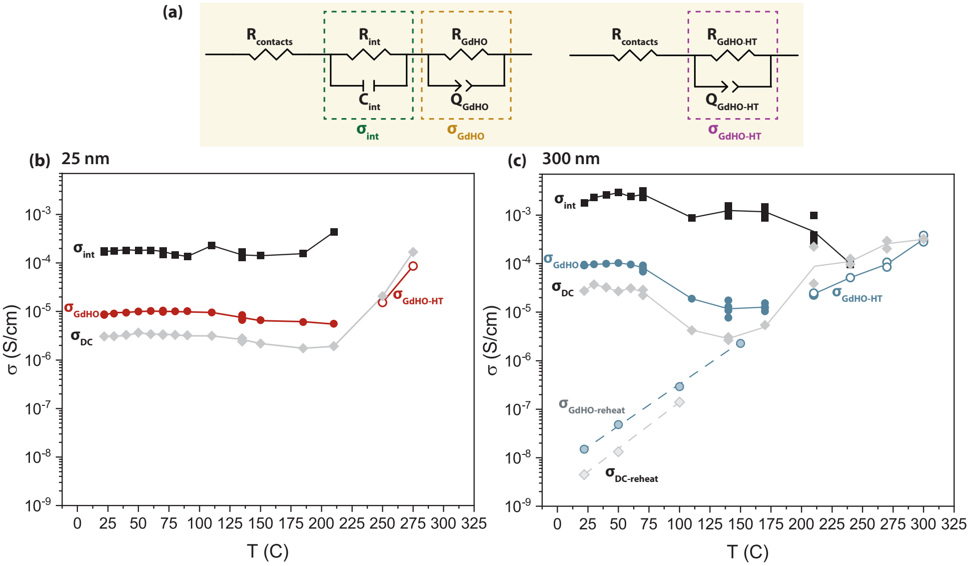

Figure 5.G.1: (a) The equivalent circuit models used to fit the data, and indications of which RC or RQ components were used to calculated the three different conductivities. Until ~210°C (regimes I and II), data for both 25 and 300 nm can be fitted by an R(RC)(RQ) or R(RC)(RC) circuit, where the RC (σ_{int}) may be related to the GdH_2|Gd-oxyhydride interface, while the second component (σ_{GdHO}) is related to the Gd-oxyhydride. At higher temperatures (regime III), the interfacial component disappears and only the conductivity of the oxyhydride is visible ($\sigma_{GdHO-HT}$). The DC conductivity (σ_{DC}) was measured by fitting the current decay for different DC voltages. The 300 nm sample was cooled down to 22°C and heated again until 150°C. During this, the conductivities were measured again ($\sigma_{GdHO-reheat}$ and $\sigma_{DC-reheat}$). The $\sigma_{int-reheat}$ is not shown, but it was temperature independent and slightly lower than its original value.

5.H Detailed look at heating of 300 nm film in regimes II & III

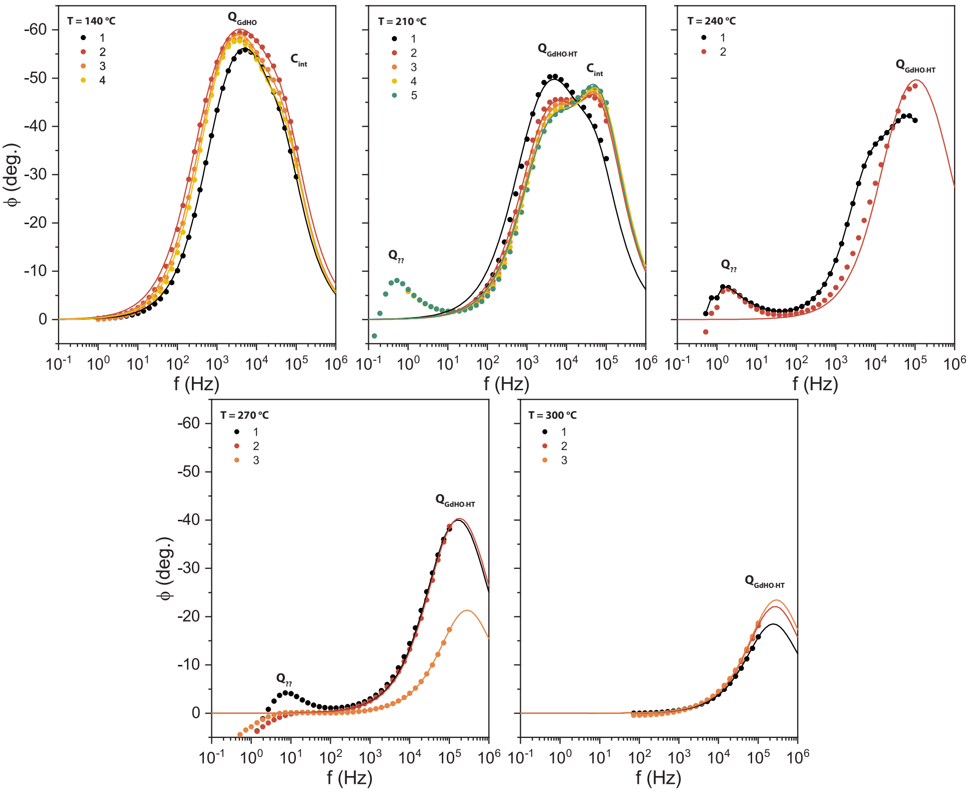

Figure 5.H.1: Half-Bode plots for the first heating of the 300 nm film. Measurements were taken multiple times at 140, 210, 240, 270, and 300°C. The peaks in -ϕ are indicators of the capacitive components present. At 140°C, heating causes the peak to broaden as the sample is better represented by a Q with a decreasing non-ideality factor. At higher temperatures, the interfacial capacitance disappears and a third low frequency component appears. This low frequency element has to be related to some slow processes such as ionic motion, but can also be a measurement artefact.

5.I Low frequency component in regime III for 300 nm film

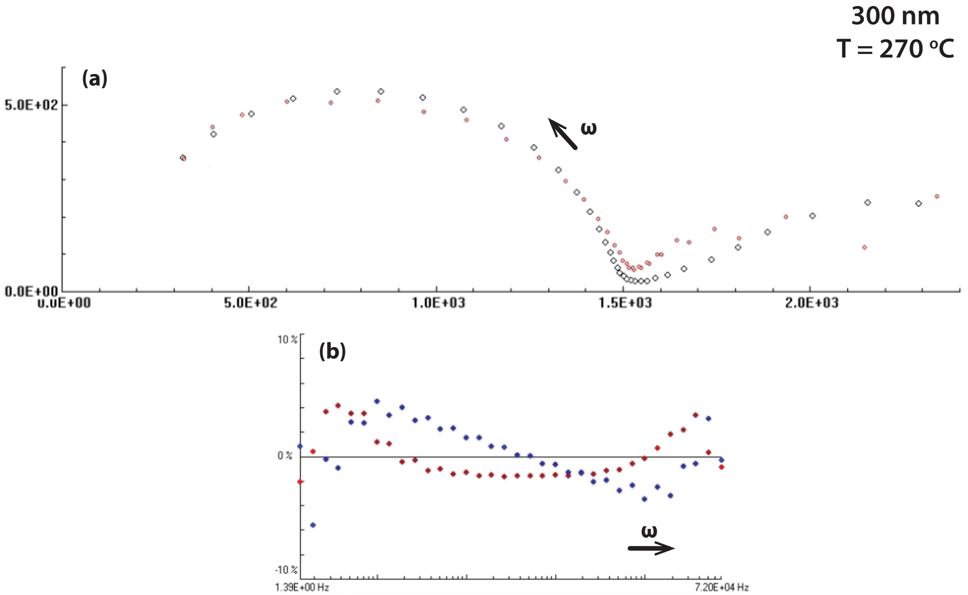

Figure 5.I.1: One of the curves from the measurement of the 300 nm Gd-oxyhydride thin film at 270°C was evaluated for its KK-compliance using the programme described in Ref. [1, 2]. Graph (a) shows the Nyquist plot of the data (black) and the KK-compliant plots (red), while (b) shows the extend of deivation between the real and imaginary components. While the main arc is reasonably compliant (deviation <2%), the low frequency component is clearly non-compliant and should not be analysed by equivalent circuit modelling.

5.J Reheating 300 nm Gd-oxyhydride

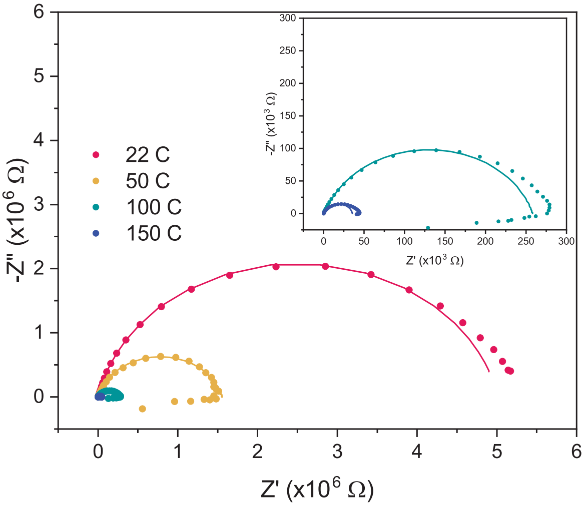

Figure 5.J.1: Nyquist plots for the 300 nm Gd-oxyhydride film after a second round of heating until 150°C. The inset shows the Nyquist plots for 100 and 150°C.

References

[1] B. A. Boukamp, *A linear Kronig-Kramers transform test for immittance data validation,* Journal of The Electrochemical Society **142**, 1885 (1995).

[2] B. A. Boukamp, *Electrochemical impedance spectroscopy in solid state ionics: recent advances,* Solid State Ionics **169**, 65 (2004).

6

Destroying photochromism

"If we knew what it was we were doing, it would not be called research, would it?"
— Albert Einstein

Sometimes during the PhD, or maybe as a result of a Friday afternoon experiment, you find something strange that cannot be turned into a paper. And yet! you still want people to know about it. This chapter includes the details of things which were intriguing, but not fully developed. Specifically, discussed here are instances where either the photochromic contrast was reduced to nearly 0%, or the bleaching speed was extended to "infinitely" slow speeds. Some ideas are given for why these events occurred.

6.1 Reducing photochromic contrast

This thesis and several others have been plagued by the question, “What is the nature of this photochromic effect in rare-earth metal oxyhydrides?” Several studies (including some in this thesis) have even tried to enhance the effect, sometimes in an effort to understand it better, and other times to gain performance in view of applications. However, no one is talking about how to get rid of this effect, so I will start this conversation here. For now, I will define **“eliminating photochromism” as the decrease of the photochromic contrast to ∼0%**.

6.1.1 Case 1

The first time I nearly destroyed the photochromic effect in a material was in the summer of 2020. I was preparing a yttrium oxyhydride thin film (0.6 Pa) for a student project where we were interested in the temperature-dependence of photochromism. Importantly, the temperature here is the one set at the measurement stage during photochromism.

As sometimes happens with sputtering, the Y target arc’d during the deposition. Curious about what would happen, I simply turned the power supply back on, and sputtered for another several minutes until the target arc’d again. I turned on the power supply one more time until the last arc, ending the deposition here. Figure 6.1 shows the results of the photochromic measurements (5 cycles of 1 h illumination, 1 h bleaching) for three twins made under these conditions, and performed at 40, 60, and 80°C. The photochromic contrast for all three samples is well below the expected >30%, but the highest temperature measurements in particular showed almost no contrast at all. It is not clear what was so detrimental to photochromism here. It is possible that the films had an **overall different grain size** compared to our normal films or that the film is not really continuous and acts more like a **“multi-layered” film** with distinct interfaces or compositions throughout. Microscopy (SEM, AFM, TEM) can be used to characterise these properties.

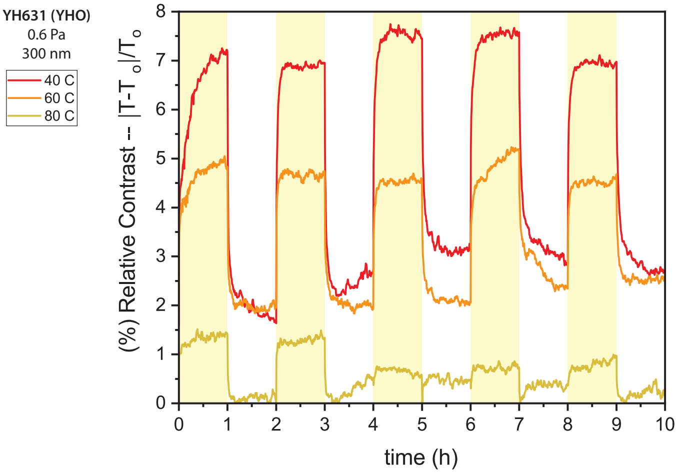

Figure 6.1: Relative photochromic contrast monitored over time for five illumination cycles measured for three twin films of Y-oxyhydride prepared at 0.6 Pa, but with the Y sputtering target arcing twice during the deposition. The yellow regions indicate when the LED was on during illumination.

6.1.2 Case 2

The next time that I almost destroyed photochromism was in the summer of 2021. With my mind on electrochemical impedance, I sputtered a thick film of gadolinium oxyhydride (0.7 Pa as-deposited GdH_2 oxidised in air) on a substrate with Au contacts. This sample was measured under vacuum ($> 10^{-6}$ mbar) and at temperatures ranging between 21 and 350°C. From the transport measurements, it was clear that the film was changing because the conductivity improved by several orders of magnitude. Visually, the film became very dark (Fig. 6.2), but recovered some of its transparency upon exposure to air.

Using *in situ* XRD (vacuum $>10^{-4}$ mbar) (Fig. 6.3), we could see that heating up to 350°C resulted in an annealing effect, where the lattice constant “a” derived individually from the three visible reflections had a smaller spread in values and the reflections appeared more intense and narrow. As well, the (222) reflection started to appear from ~300°C. However, other changes occurred as well. Upon cooling, the lattice compressed by approximately 0.02 Å. Upon exposure to air, the lattice constant started to expand, perhaps due to oxidation. Despite any possible oxidation, the sample appeared dark as in the image in Figure 6.3.

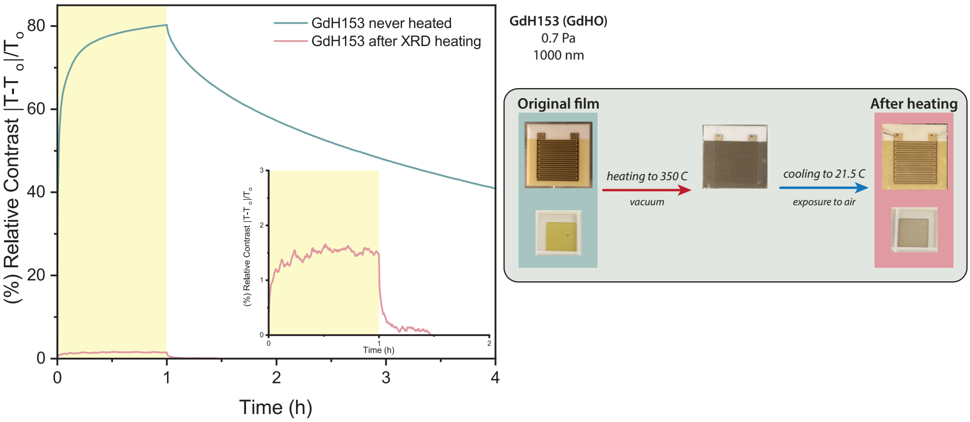

Figure 6.2: (left) Relative contrast of a standard Gd-oxyhydride thin film (blue) compared to a twin sample that was heated treated under vacuum (pink). (inset) A zoom in of the heat treated measurement, showing the nearly 0% photochromic contrast. (right) Photographs of the visual appearance of the samples before treatment, after heating under vacuum, and release to air.

Moving to photochromism, the samples shown in Figure 6.2 were measured at the same temperature (~21°C), but one was heat-treated before the measurement. This is not the same as Case 1. Comparing the photochromic properties of an untreated film and a film which went through the *in situ* XRD heating programme ((1) heated to 350°C under vacuum, (2) cooled to 25°C under vacuum, and (3) exposed to air again), the heat-treated film had a contrast of ~1.5%. Here, the conclusion was that **structural changes certainly occur as a result of heating, but also chemical changes may have happened**, for example, the release of some hydrogen during heating and further oxidation when exposed to air again. Furthermore, these results made me think about the potential for these materials to be considered **“thermochromic”**, given their propensity for “darkening” (phase segregating?) in response to, not only UV light, but also heat. Similar to Case 1, the contrast is very low, but the bleaching speed is very fast. At present, it is not clear why pre-heating to

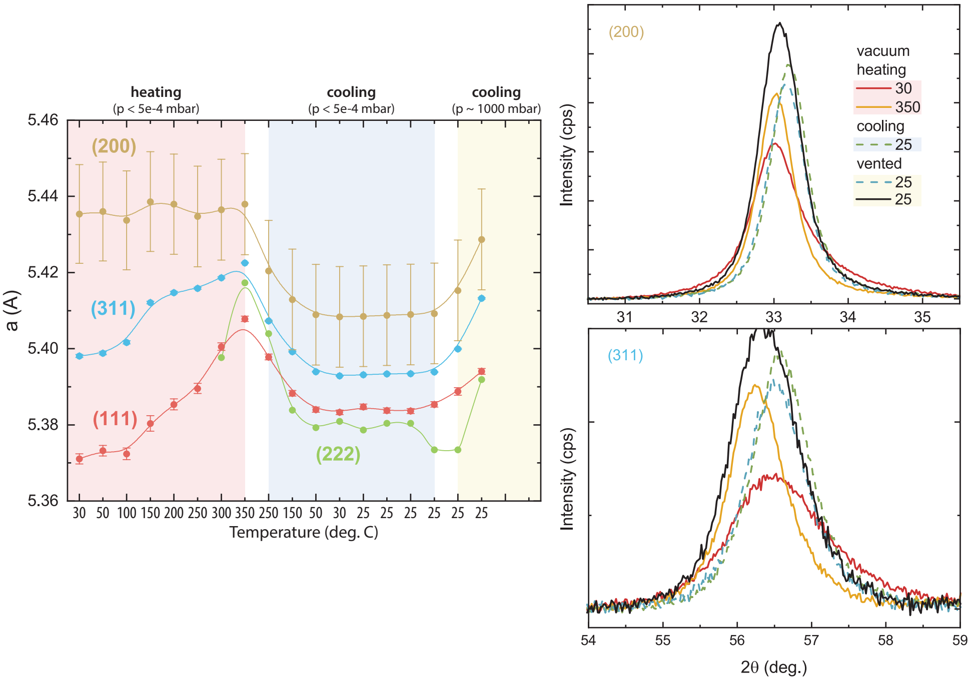

Figure 6.3: (left) *In situ* XRD was performed for the sample (on fused silica) described in Fig. 6.2. First, the sample was heated under vacuum (<5e-4 mbar) from 30 to 350°C. Then it was cooled to 25°C under the same vacuum and measured four times at 25°C. Last, the cell was vented and the sample was measured twice in air at 25°C. This figure shows the lattice constant "a" derived from each visible reflection in the XRD patterns. (right) Changes in the (200) (top) and (311) (bottom) reflections from XRD at different points in the programme. Red and orange lines are during heating at 30 and 350°C, respectively. After cooling, the fourth measurement at 25°C is shown as a green dashed line. Then the cell was vented and the sample was measured twice, showed as a blue dashed line and a black solid line. The peak positions clearly change, indicated also by the changes in "a" in the left graph.

350°C and measuring at room temperature (Case 2) and no pre-heating but measuring a "multi-layered" film at 80°C would result in similar results for photochromism. This can be, again, related to structural or compositional changes which should be measured to gain more insight.

6.2 Infinite bleaching time

6.2.1 Case 3

We can also define the **"elimination of photochromism" as a situation where the bleaching speed is infinitely long**, such that the "darkened" state persists for unusually long periods of time. I have also produced this case, ironically when I thought I made the most careful material possible. In hindsight, **my guess is that this "carefulness" is precisely the issue**. Here, the sample in question is a gadolinium oxyhydride (0.75 Pa), oxidised in an atmosphere of dry O_2, and coated with an ALD coating of Al_2O_3 without exposure to air. To achieve this, the sample was packed in the glovebox in a sealed tube and transferred to the glovebox of the ALD system. Then the sample was moved into the ALD chamber via the glovebox, preventing contact with air.

After coating the sample by ALD, the photochromic properties were measured, revealing a bleaching speed on the order of several days. Such slow bleaching speeds have only been shown by our group for Sc-oxyhydrides until this point [1], although some evidence was also shown in Chapter 3 that the heating during ALD causes the slowing of the bleaching speed. As well, epitaxial Y-oxyhydride films showed a persistent “darkened” state which could only be bleached by heating the film to 125°C under Ar gas [2].

Comparing this result to an air-oxidised gadolinium oxyhydride thin film reveals the extent of difference. Again, it is possible that the defects and inhomogeneities in our films allow for the reversibility of the photochromic effect, giving some driving force for the de-segregation or re-mixing of the ““darkened”” phase into the oxyhydride matrix.

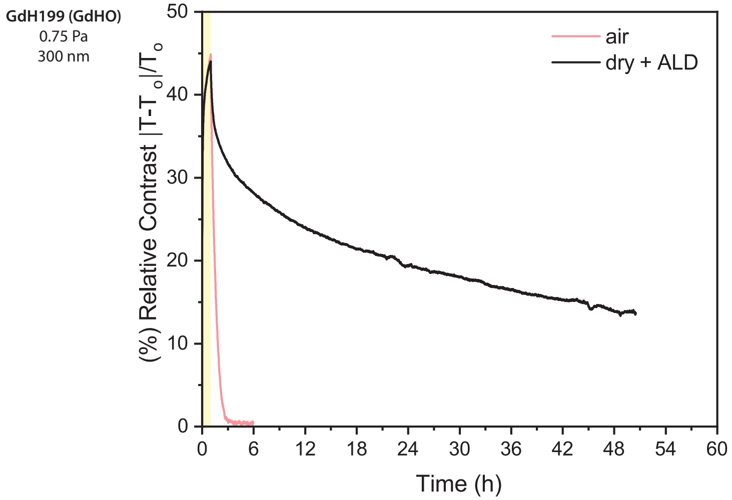

Figure 6.4: Relative contrast for two Gd-oxyhydride samples: (pink) standard air-oxidised film, (black) film oxidised with dry O_2 and coated with Al_2O_3 by ALD which involves heating for 2 h.

References

[1] G. Colombi, S. Cornelius, A. Longo, and B. Dam, *Structure model for anion-disordered photochromic Gd oxyhydride thin films,* The Journal of Physical Chemistry C **124**, 13541 (2020).

[2] Y. Komatsu, R. Shimizu, R. Sato, M. Wilde, K. Nishio, T. Katase, D. Matsumura, H. Saitoh, M. Miyauchi, J. R. Adelman, R. M. L. McFadden, D. Fujimoto, J. O. Ticknor, M. Stachura, I. McKenzie, G. D. Morris, W. A. MacFarlane, J. Sugiyama, K. Fukutani, S. Tsuneyuki, and T. Hitosugi, *Repeatable photoinduced insulator-to-metal transition in yttrium oxyhydride epitaxial thin films,* Chemistry of Materials **34**, 3616 (2022).

7

Outlook on further research

Using the insights gathered throughout the PhD, below I describe my outlook on photochromism and H^- mobility in rare-earth oxyhydride thin films. In particular, I give an idea for the mechanism behind photochromism that involves the formation of H-deficient (instead of H-rich) phases locally in the oxyhydride matrix. In terms of H^- mobility, I comment on the relationship between mobility and photochromism to the extent that is possible based on Chapters 2 and 5. As well, I mention the possibility of using rare-earth metal oxyhydrides for energy storage and the aspects that should be taken into account for further development.

7.1 Photochromism

7.1.1 The darkened phase is H-deficient

Starting with photochromism, after all the experiments performed here and discussed at length in the chapters above, I have a scheme in mind for the mechanism behind the photochromic effect in rare-earth metal oxyhydrides. Being a chemist, I think in terms of reactions. The initial steps of the photochromic effect are likely a redox reaction initiated by the light-induced oxidation of H^- to H^0 and subsequent reduction of the rare-earth cation:

$$\begin{aligned} H^- &\rightarrow H^0 + e^- && (7.1)\\ RE^{3+} + e^- &\rightarrow RE^{2+}. && (7.2) \end{aligned}$$

A different set of reactions leading to the same products can be written as follows considering photo-generated electron/hole pairs:

$$\begin{aligned} H^- + h^+ &\rightarrow H^0 && (7.3)\\ RE^{3+} + e^- &\rightarrow RE^{2+}. && (7.4) \end{aligned}$$

Since the products (H^0 and RE^{2+}) are always the same, the difference between Equations 7.1 and 7.3 is the perspective; either H^- is an electron generator or a hole trap. Given that the energy of the incident light during photochromism has to be greater than the band gap, the formation of electron/hole pairs is considered a necessary first step in the photochromic mechanism, leading to the process in Equations 7.3 and 7.4.

These reactions (Equations 7.3 and 7.4) are very general. When considering the actual composition of an oxyhydride material, the following reactions can be written for a stoichiometric RE-oxyhydride:

$$REHO \rightarrow REO + H^0, \tag{7.5}$$

or for the most H-rich composition expected to be a stable oxyhydride [1]:

$$REH_2O_{0.5} \rightarrow REHO_{0.5} + H^0. \tag{7.6}$$

Importantly, I propose here that these reactions take place on a very **local** scale, and not throughout the entirety of the material. This suggestion follows from one of the proposed mechanisms for photochromism where metallic clusters form upon illumination. The key difference, however, between this scheme and what has been presented in the literature so far is the **composition of the darkened phase**, which has often been referred to as H-rich [2–6]. Here, I argue that, from a chemical point-of-view, the formation of H-deficient phases in the oxyhydride matrix are more likely and that these **H-deficient phases are the light absorbers (conductive species) responsible for photochromism (photo-conductivity)**. In the extreme case, that would be a rare-earth monoxide (REO), but any H-deficient phase between $REHO_{0.5}$ and REO should be sufficient, depending on the initial composition of the oxyhydride.

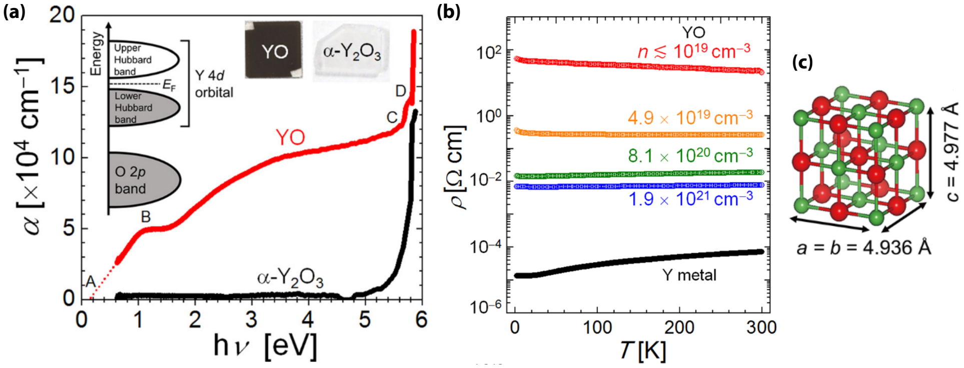

Figure 7.1: Details about yttrium monoxide (YO) from Kaminaga, et al. [7]: (a) crystal structure of YO, (b) optical absorption of YO compared to Y_2O_3 and a possible explanation of the small band gap of YO, and (c) electrical resistivity of YO as a function of temperature, where the resistivity depends on the partial pressure of O_2 during thin film growth (PLD). Explanations for the various features marked in (b) can be found in Ref. [7].

There are several reasons why a H-deficient, or in the extreme case a RE-monoxide, could be responsible for the photochromic/photoconductive effect we observe. A work from Kaminaga, et al. [7] on yttrium monoxide (YO) showed that the monoxide has a high conductivity (10^{-1}-10^3 S/cm), small band gap, high carrier density (10^{19}-10^{21} cm^{-3}), and a large absorption coefficient for a wide wavelength range (0.6-4 eV or 2066-310 nm) (Fig. 7.1a,b). This is important because along with the optical colour change, the conductivity of RE-oxyhydrides increases by several orders of magnitude in the darkened state [8, 9]. The absorption of a large wavelength range is also very unique and is important for explaining the fact that RE-oxyhydrides, even in the dark state, absorb light between visible and IR light [10].

The same work mentioned that other RE-monoxides based on La, Ce, Pr, Nd, Sm, and Gd also show high conductivity and metastability just like YO [7, 11–15]. Two points are important from this: (1) the ability to form a monoxide is common to most RE-cations, similar to the ability to form oxyhydrides and show photochromism, and (2) the metastability of the monoxide may play a role in the reverse process of photochromism. Expanding on the second point, one of the interesting parts about photochromism is that it is reversible, so that the phase formed during darkening needs a driving force to return back to the oxyhydride composition. That seems to be true when considering the darkened phase as a monoxide. As well, RE-monoxides with different cations could have different energetics, perhaps explaining the different bleaching rates observed for Gd and Nd (fast) compared to Dy and Er (slower) or some differences in contrast [10, 16, 17].

Lastly, the crystal structures of RE-monoxides are cubic, although with a smaller lattice constant (Fig. 7.1c). This also matches the observations of lattice contraction during the photochromic effect [4] and what may be a thermochromic effect (Chapter 6).

Several experiments can be done with our thin film materials to test this hypothesis, although it should be kept in mind that if the experiment is *ex situ*, the measurement has to be fast or at low temperatures since the darkened state gradually disappears without the incident light. Kaminaga, et al. [7] used XPS to identify the oxidation state of Y compared to the standard Y_2O_3. Previous XPS measurements of illuminated Y-oxyhydride thin films showed an increase in the peak intensity corresponding to the Y^{2+} state compared to Y^{3+} for the darkened state [18]. Further work can involve *in situ* measurements, films made by dry oxidation to limit the presence of unwanted hydroxyl features in the XPS, and the use of more references to characterise Y_2O_3, YH_2, and YO. As well, NMR can be useful for determining the identity of the darkened phase, for example, using the presence or absence of a Knight shift and how that relates to the charge carrier density of the material. Although a Knight shift was observed in Ref. [19], we have since made a lot of progress in understanding these materials and how to prepare thin films with more homogeneous composition. Therefore, it remains to be seen if the Knight shift appears again in more recent data [20].

7.1.2 The role of hydrogen

The role of H^- in this scheme of photochromism is as a side character. While some works propose the formation of H-rich oxyhydride or even *dihydride* domains as the ones responsible for changes in optical transmission and conductivity [2–6], here the **H^- is simply a charge carrier trap** according to Eq. 7.3. During darkening, the photoexcitation triggers H^- to trap a hole, forming the neutral H^0. Later, during bleaching, the H^0 must recombine with an electron to return the oxyhydride composition with H^- and the RE-cation 3+ oxidation state.

We have seen that composition (O:H ratio, Ref. [16]) and aliovalent doping (Chapter 4, Ref. [21]) influence the photochromic contrast and bleaching speed. In the scheme I have presented, the contrast is a function of the H^- composition of the sample, where more H^- are available to trap h^+ and balance the charge of the newly reduced RE^{2+} cation. For the bleaching speed, if it is only dependent on the recombination of H^0 and RE^{2+}, then the speed may be related directly to the quantity of H^0, which would result in equivalent trends of contrast and bleaching speed. However, this is not the case as seen from Chapters 3 and 4 (Refs. [17],[21]).

Instead, I think that a second phenomena can occur to further prolong the darkened state in H-richer oxyhydrides. If several octahedral sites contain H^0, a “dihydrogen” complex can form between H^0-H^0, reminiscent of the proposal from Chai, et al. [22]. This could explain the slower bleaching in H-richer films and the faster bleaching for aliovalently doped films. It is still not clear, on the other hand, why heat treatment of our films should influence the photochromic effect as seen in Chapters 3 and 6.

In theory, H^0 could be a mobile species, but in this framework, mobility is not necessary. In fact, mobility was not observed by μ^+SR (muon was sensitive to other phenomena), NMR, nor EIS (electron-dominated signal, signs of mobility only at high temperatures).

Another point here is about side reactions. It is known that although the photochromic effect is reversible, the transmission after 1 cycle is not returned 100%. After many cycles, there is even a memory effect where repeated illumination a slower bleaching speed [8]. It is possible that some H^0 react to form hydroxyl groups [23] or H_2 molecules [24], two examples of irreversible reactions. That would result in not all electrons recombining with an H^0.

Lastly, comparing this model to the popular ideas in the literature reveals some key points of attention. First, if all H^- ions in the material retain their negative charge state during illumination while the cation is reduced (RE-dihydride cluster formation), two problems arise: (1) lack of charge balance in the material, and (2) excess holes which are at odds with the observed electron-dominant conductivity of the darkened state [9]. Next, the segregation of a H-rich, or even dihydride phase, requires the mobility of ions to a specific location at an unknown distance. This is difficult to imagine given the lack of evidence to show that H^- mobility is possible in our materials at room temperature. As well, it is not clear where these metallic clusters would form, thus, how far H^- ions should travel.

7.2 H^- mobility

Chapters 2 and 5 describe attempts to probe H^- mobility on different time- and length-scales. From μ^+SR, no H^- mobility was observed in the oxyhydride thin films either because it is not possible under those conditions (temperature, time-scale, length-scale), or because the muon was distracted by other interactions with O^{2-}. With EIS, we investigated Gd-oxyhydride thin films on the complete opposite temperature, time-scale, and length-scale, finding that the material is dominated by electronic conductivity, rather than ionic. However, at very high temperatures, there was a signal which could either be an artefact or related to some H^- mobility as a result of sample decomposition (H_2 released from the sample). Therefore, Gd-oxyhydride in its current state may not be a good candidate for solid-state H^- conductors. However, from all these results we learn that our films are meta-stable, and when given enough energy (be it by UV-light or 250°C of thermal energy), they will darken. It is still a question, though, if this darkening requires an element of ionic mobility/redistribution and at what length-scale.

In terms of applications, I think there is room for RE-oxyhydrides in the energy storage landscape given the rapid development of technologically relevant materials. However, it is unclear how stable these materials are, how they survive with repeated charge/discharge cycles, or if they are meant more for primary batteries. It may be that the unstable temperature behaviour shown for thin films in Chapter 5 is not observed for bulk powders. Returning to a point raised in the introduction of this thesis, however, the implementation of rare earth metals in another new application is not completely justified, in my view, unless recycling of the elements or very long term device usage is expected.

References

[1] G. Colombi, R. Stigter, D. Chaykina, S. Banerjee, A. P. M. Kentgens, S. W. H. Eijt, B. Dam, and G. de Wijs, *Energy, metastability, and optical properties of anion-disordered* REO_xH_{3-2x} *RE = (Y, La) oxyhydrides: a computational study,* Physical Review B **105**, 054208 (2022).

[2] J. Montero, F. A. Martinsen, M. García-Tecedor, S. Z. Karazhanov, D. Maestre, B. Hauback, and E. S. Marstein, *Photochromic mechanism in oxygen-containing yttrium hydride thin films: An optical perspective,* Physical Review B **95**, 201301(R) (2017).

[3] J. Montero and S. Z. Karazhanov, *Spectroscopic ellipsometry and microstructure characterization of photochromic oxygen-containing yttrium hydride thin films,* physica status solidi (a) **215**, 1701039 (2018).

[4] E. M. Baba, J. Montero, E. Strugovshchikov, E. Ö. Zayim, and S. Karazhanov, *Light-induced breathing in photochromic yttrium oxyhydrides,* Physical Review Materials **4**, 025201 (2020).

[5] M. Hans, T. T. Tran, S. M. Aðalsteinsson, D. Moldarev, M. V. Moro, M. Wolff, and D. Primetzhofer, *Photochromic mechanism and dual-phase formation in oxygen-containing rare-earth hydride thin films,* Advanced Optical Materials **8**, 2000822 (2020).

[6] Z. Wu, T. de Krom, G. Colombi, D. Chaykina, G. van Hattem, H. Schut, M. Dickmann, W. Egger, C. Hugenschmidt, E. Brück, B. Dam, and S. W. H. Eijt, *Formation of vacancies and metallic-like domains in photochromic rare-earth oxyhydride thin films studied by in-situ illumination positron annihilation spectroscopy,* Physical Review Materials **6**, 065201 (2022).

[7] K. Kaminaga, R. Sei, K. Hayashi, N. Happo, H. Tajiri, D. Oka, T. Fukumura, and T. Hasegawa, *A divalent rare earth oxide semiconductor: Yttrium monoxide,* Applied Physics Letters **108**, 122102 (2016).

[8] T. Mongstad, C. Platzer-Björkman, J. P. Maehlen, L. P. A. Mooij, Y. Pivak, B. Dam, E. S. Marstein, B. C. Hauback, and S. Z. Karazhanov, *A new thin film photochromic material: Oxygen-containing yttrium hydride,* Solar Energy Materials and Solar Cells **95**, 3596 (2011).

[9] G. Colombi, B. Boshuizen, D. Chaykina, L. Hsu, H. Schreuders, T. J. Savenije, and B. Dam, *Relation between photochromism and photoconductivity in* REO_xH_{3-2x} *thin films,* in preparation (2022).

[10] F. Nafezarefi, H. Schreuders, B. Dam, and S. Cornelius, *Photochromism of rare-earth metal-oxy-hydrides,* Applied Physics Letters **111**, 103903 (2017).

[11] T. Yamamoto, K. Kaminaga, D. Saito, D. Oka, and T. Fukumura, *Rock salt structure GdO epitaxial thin film with a high ferromagnetic curie temperature,* Applied Physics Letters **117**, 052402 (2020).

[12] J. M. Leger, N. Yacoubi, and J. Loriers, *Synthesis of neodymium and samarium monoxides under high pressure,* Inorganic Chemistry **19**, 2252 (1980).

[13] J. M. Leger, P. Aimonino, J. Loriers, P. Dordor, and B. Coqblin, *Transport properties of SmO,* Physics Letters A **80**, 325 (1980).

[14] J. M. Leger, N. Yacoubi, and J. Loriers, *Synthesis of rare earth monoxides,* Journal of Solid State Chemistry **36**, 261 (1981).

[15] H. Shimizu, D. Oka, K. Kaminaga, D. Saito, T. Yamamoto, N. Abe, N. Kimura, D. Shiga, H. Kumigashira, and T. Fukumura, *Rocksalt-type PrO epitaxial thin film as a weak ferromagnetic Kondo lattice,* Physical Review B **105**, 014442 (2022).

[16] G. Colombi, T. De Krom, D. Chaykina, S. Cornelius, S. W. H. Eijt, and B. Dam, *Influence of cation (RE = Sc, Y, Gd) and O/H anion ratio on the photochromic properties of* REO_xH_{3-2x} *thin films,* ACS Photonics **8**, 709 (2021).

[17] D. Chaykina, F. Nafezarefi, G. Colombi, S. Cornelius, L. J. Bannenberg, H. Schreuders, and B. Dam, *Influence of crystal structure, encapsulation, and annealing on photochromism in Nd oxyhydride thin films,* The Journal of Physical Chemistry C **126**, 2276 (2022).

[18] F. Nafezarefi, *Photochromic Properties of Rare-Earth Oxyhydrides*, Ph.D. thesis, Delft University of Technology (2020).

[19] C. V. Chandran, H. Schreuders, B. Dam, J. W. G. Janssen, J. Bart, A. P. M. Kentgens, and P. J. M. van Bentum, *Solid-state NMR studies of the photochromic effects of thin films of oxygen-containing yttrium hydride,* The Journal of Physical Chemistry C **118**, 22935 (2014).

[20] S. Banerjee, D. Chaykina, B. Dam, G. de Wijs, and A. Kentgens, *Investigating photochromism in rare-earth metal oxyhydrides (Y, Sc) by solid-state NMR,* in preparation (2023).

[21] D. Chaykina, I. Usman, G. Colombi, H. Schreuders, B. Tyburska-Pueschel, Z. Wu, S. Eijt, L. J. Bannenberg, G. A. de Wijs, and B. Dam, *Aliovalent calcium doping of yttrium oxyhydride thin films and implications for photochromism,* The Journal of Physical Chemistry C **126**, 14742–14749 (2022).

[22] J. Chai, Z. Shao, H. Wang, C. Ming, W. Oh, T. Ye, Y. Zhang, X. Cao, P. Jin, S. Zhang, and Y.-Y. Sun, *Ultrafast processes in photochromic material* YH_xO_y *studied by excited-state density functional theory simulation,* Science China Materials **63**, 1579 (2020).

[23] D. Chaykina, T. W. H. de Krom, G. Colombi, H. Schreuders, a. Suter, T. Prokscha, B. Dam, and S. W. H. Eijt, *Structural properties and anion dynamics of yttrium dihydride and photochromic oxyhydride thin-films examined by in situ* μ^+SR*,* Physical Review B **103**, 224106 (2021).

[24] D. Moldarev, L. Stolz, M. V. Moro, S. M. Aðalsteinsson, I.-A. Chioar, S. Z. Karazhanov, D. Primetzhofer, and M. Wolff, *Environmental dependence of the photochromic effect of oxygen-containing rare-earth metal hydrides,* Journal of Applied Physics **129**, 153101 (2021).

Summary

The intention of this PhD was to: (1) test the extent to which photochromism and H^- mobility were related, and (2) learn more about the fundamental aspects of both phenomena. The proposed relationship between photochromism and H^- mobility was inspired by the analogy to other photochromic materials (Cu-doped Ag-halide glasses) and some results showing changes in the oxyhydride material that could be explained by the rearrangement of atoms.

The first method by which these questions were addressed was muon spin rotation (μ^+SR), where muons (μ^+) are implanted into the sample and interact with the sample environment. In the case of oxyhydrides, this interaction was primarily electrostatic (Mu^+-O^{2-}). No mobility was observed on the length/time-scale of this experiment, either because there is no mobility of H^- under these conditions, or because the muon was distracted by interactions with O^{2-}. Instead, we learned that the muon forms muonium (Mu^0) in our films, but recovers Mu^+ as the temperature increases. The activation energy associated with this change was dependent on the deposition pressure (O:H ratio) of the Y-oxyhydride thin film. During photochromism, this energy barrier changed, suggesting that the environment around the muon in the darkened state was different, primarily that the octahedral sites are likely filled by some species, making the Mu^0 state unstable.

Next, we tested to see if the photochromic effect would be significantly different if the rare-earth cation was Nd, the reasons being that (1) bulk Nd-oxyhydrides are proven H^- conductors and (2) they exhibit a different crystal structure from our other oxyhydrides. However, we did not find any significant differences between Nd- and Gd-oxyhydride thin films and their photochromic properties, meaning that the crystal structure does not impact the photochromic effect. Instead, we accidentally found that heating the films at 87°C before measuring the photochromic effect (at room temperature) makes the most significant difference. Oddly, no differences were observed in the XRD patterns of films heated for different lengths of time. Therefore, the changes that occur during this “annealing” may be related to, for example, rearrangement of the anions to create a more homogeneous composition throughout the film.

Then, we doped Y-oxyhydride thin films aliovalently using Ca. This is a common technique used to create anion vacancies throughout the crystal structure of the material. As a result, certain properties of the material change such as ionic mobility, which tends to improve with more anion vacancies. Here, we showed that Ca-doped Y-oxyhydrides can be made by co-sputtering, and characterised the compositional, structural, and optical properties. Most importantly, this aliovalent substitution caused large changes in the photochromic effect, namely that the contrast was predicted to disappear for a Ca-content of ~50% and the bleaching speed became faster. For the former, we suggested that at this composition, all the octahedral H^- could be vacated to compensate for the addition of Ca, thus, eliminating

the photochromic contrast. For the latter, we measured the photochromic effect at different temperatures to observe the Arrhenius behaviour of the bleaching time constant. The activation energy for bleaching was the same regardless of Ca-content, but the pre-exponential factor increased when Ca was added, explaining the faster bleaching. In this regard, we suggested that octahedral H^- are necessary to induce the photochromic effect, and some local hopping is likely needed for bleaching.

Lastly, EIS showed that Gd-oxyhydride is predominantly an electronic conductor and that as-deposited films are metastable. Changes in the conductivity (Chapter 5), the structure (Chapter 6), and potentially the composition occur at temperatures above 70°C. At 210-300°C, a weak signal is observed which may be an indication of ionic mobility, although this is unconfirmed at this moment. In the same temperature range, some films have shown a thermochromic effect, darkening in colour. We establish methods for analysis charge transport in the materials, list some of the considerations one should keep in mind, and suggest how to improve the measurements for the further analysis of other oxyhydride materials.

With these aspects in mind, the photochromic effect could be due to the trapping of photo-generated electron/hole pairs, where H^0 and RE^{2+} are formed. One option to describe the darkened phase is a H^-deficient phase and the observed mobility is due to local motion of H^0. During bleaching, this H^0 has to hop throughout the material to find RE^{2+} and recombine with an electron to regain the oxyhydride composition.

Samenvatting

Het doel van dit doctoraat was om: (1) te testen in hoeverre fotochromisme en H^- mobiliteit gerelateerd zijn, en (2) meer te weten te komen over de fundamentele aspecten van beide fenomenen. De voorgestelde relatie tussen fotochromisme en H^- mobiliteit is geïnspireerd door de analogie met andere fotochromische materialen (zoals Cu-gedoteerd Ag-halide glas) en door sommige resultaten die veranderingen tonen in de oxyhydride materiaal wat verklaard kan worden door de herordening van de atomen.

De eerste methode waarmee deze vragen zijn geadresseerd was muon spin rotatie (μ^+SR), waarbij muonen (μ^+) worden geïmplanteerd in het sample en reageren met de omgeving van het sample. In de context van oxyhydriden is deze interactie voornamelijk elektrostatisch (Mu^+-O^{2-}). Er was geen mobiliteit geobserveerd voor de lengte/tijd-schaal van dit experiment, ofwel omdat er geen mobiliteit van H^- is onder deze voorwaarden, of omdat de interactie tussen de muon en O^{2-} sterker was. In plaats daarvan hebben we gevonden dat het muon in onze films muonium (Mu^0) vormt, maar terugkeert naar Mu^+ bij hogere temperatuur. De activeringsenergie geassocieerd met deze verandering van de Mu^0/Mu^+ ratio hangt af van de depositie druk (O:H ratio) van de Y-oxyhydride dunne film. Tijdens fotochromisme veranderd deze energie barrière, waarschijnlijk omdat de omgeving rond het muon in de verdonkerd staat anders is. Dit betekend dat voornamelijk de octaëdrische posities gevuld zijn met atomen, waardoor de Mu^0 staat onstabiel wordt.

Daarna hebben we getest of fotochromisme anders is wanneer het zeldzame aardmetaal kation Nd is in plaats van Sc, Y, of Gd. Nd heeft namelijk verschillende eigenschappen vergeleken met Sc, Y, en Gd-oxyhydriden: (1) bulk Nd-oyhydriden zijn bewezen H^- conductors, en (2) Nd-oxyhydriden hebben een andere kristalstructuur. We hebben echter geen significante verschillen tussen het fotochromisme van Nd- en Gd-oxyhydride dunne films gevonden. Dit betekent dat de kristal structuur niet belangrijk is voor fotochromisme. In plaats van de kristal structuur hebben we wel een effect gevonden bij het verwarmen van fotochromische materialen bij 87°C. Er waren geen veranderingen in de XRD patronen van de films geobserveerd, ongeacht de duratie van verhitting. Daarom denken wij dat de veranderingen tijdens de verhittingsstap het resultaat zijn daarvan, bijvoorbeeld, de herschikking van anionen tot een film met een meer homogene compositie.

Vervolgens hebben we Y met Ca vervangen, ook wel bekend als “aliovalente doping”. Dit is een vaak gebruikte techniek om anionische openingen in het materiaalrooster te creëren. Deze anionische openingen zijn belangrijk voor onder andere de mobiliteit van ionen; als er meer anionische openingen in het materiaal zijn, dan zal de mobiliteit hoger zijn. Hier hebben we laten zien dat Ca-gedoteerde Y-oxyhydriden gemaakt kunnen worden door middel van co-sputteren, en dat zo de compositionele, structurele en optische eigenschappen gekarakteriseerd kunnen worden. De meest belangrijke conclusie was dat de “aliovalente doping” grote veranderingen maakt in het fotochromisch effect, namelijk dat de fotochromisch contrast verdwijnt bij 50% Ca terwijl de verblekingssnelheid sneller werd. Voor het voorgenoemde suggereren wij dat bij deze compositie alle octaëdrische H^- atomen zijn verwijderd om te compenseren voor de toevoeging van Ca^{2+} en daarmee het fotochromisch contrast elimineren. Ook hebben we bij verschillende temperaturen het fotochromisch effect gemeten, om zo het Arrhenius gedrag van de verblekingstijdconstante te observeren. De activeringsenergie voor verbleking was hetzelfde ongeacht de Ca-concentratie, maar de pre-exponentiële factor schaalde mee met de Ca-concentratie. Daarom suggereerden wij dat de octaëdrische posities nodig zijn om het fotochromische effect te initiëren, en dat ionen lokaal in het raster moeten kunnen springen om voor verbleking te zorgen.

Als laatste hebben wij met EIS aangetoond dat Gd-oxyhydride zich voornamelijk als elektron geleider gedraagt en dat het materiaal meta-stabiel was. Veranderingen in de geleidbaarheid (Hoofdstuk 5), de structuur (Hoofdstuk 6), en mogelijk de compositie gebeuren bij temperaturen hoger dan 70°C. Bij 210-300°C, was er een zwak signaal geobserveerd waarvoor we op dit moment geen verklaring hebben, maar mogelijk duidt op de mobiliteit van ionen. In dit temperatuurbereik hebben sommige films een thermochroom effect laten zien, waarbij de film donkerder wordt bijeen hogere temperatuur. We hebben analysemethodes vastgesteld waarmee lading transport kan worden geanalyseerd en sommige belangrijke consideraties voor de analyse van EIS resultaten opgesomd. We stellen ook verbetergingen aan de meting voor om de analyse van andere oxyhydride materialen te versoepelen.

In conclusie, het fotochroom effect is mogelijk het gevolg van het vangen van fotogegenereerde elektron/gat paren, waarbij H^0 en RE^{2+} worden gevormd. Een optie om de verdonkerde staat te beschrijven is met een H-arme fase waar de geobserveerde mobiliteit verklaard wordt door de verplaatsing van H^0 ionen. Tijdens verbleking moet H^0 door het materiaal springen om een RE^{2+} te vinden. Na een geschikte positie te vinden recombineert H^0 met een elektron om te oxyhydride compositie opnieuw te verkrijgen.

Vertaald door Diana Chaykina en geverifieerd door Mark Sassenberg.

Acknowledgments

Four years of coffees, late night trains home, snickers bars, bloodsweatandtears, have led to the document you're reading now. The most important ingredients in this formula, though, were the people who were along for the ride with me.

First, to my promotor **Bernard**, thank you for all your support during the last few years. Your patience was invaluable as I tried to navigate different obstacles throughout the PhD. You encouraged me to experiment, not just in the lab, but with my soft skills. You have always listened and given your honest perspective. And my co-promotor **Stephan**, thank you for supporting my work and always having a positive perspective. You contain a wealth of physics knowledge and are a great teacher.

To my friends and co-workers at MECS...

Herman, my daily supervisor, therapist, career coach, problem fixer, etc. I am convinced you already solved the "mysteries" of the photochromic effect a long time ago, but won't tell anyone. Without your help, this thesis wouldn't exist at all, and I thank you a lot for being a great coworker and friend. I also want to extend my gratitude to the other technicians who supported my work: **Joost** with ALD, **Bart** with XPS and the PHOCS, **Marcel** with AFM, **Xiaohui** with XRD, and **Duco** with SEM/EDX. You've all contributed not only to my work, but also my understanding and knowledge about these techniques.

Steffen, I really enjoyed getting to know you. You're super nice, caring, and brilliant. You helped me find my footing at the beginning of the PhD and supported me throughout.

Lars, sarcastic, funny, knowledgable, and always had my back. I appreciated your wisdom when I was stressed, your advice on life and science, and the camaraderie we shared.

Shrestha, starting our PhD's at the same time on this very complex topic, I think we have both come a long way from where we began. It's been fun growing and persevering together for 4 years, and updating each other about our lives every time you come pick up samples. I am really proud of you for all that you've been able to achieve, both in science and in your personal life. You're a super sweet person!

Sanjana, I think you said it in your thesis too, but it's really funny to think about how some friendships start - all it took was one 3 h video call during a global pandemic to bring us together! You've contributed so much to my joy and mental/emotional health, and I can't thank you enough for your company, for the positive vibes, and for trying to fight my imposter syndrome.

Mark, what started as just two nerds taking the bus to Rotterdam together, turned into office mates who recite rap lyrics together as if it's a joint concert in the office, to friends make non-verbal noises towards each other with complete mutual understanding. You've made me laugh and kept me company a lot.

Dylan, one of the first times we met, you had just started your PhD and you saw me having a several-weeks-long existential crisis, so I was surprised when you (1) didn't quit academia after seeing this display and (2) were comfortable being my friend. It's been fun to hang with you at the department and at our weekly DnD nights. You're a super creative and compassionate person!

Peter, underneath the neutral evil surface ... is just more neutral evil. No, no, kidding!! Inside there is actually a very nice person. Thanks for all your efforts with our DnD campaign, but also thanks for being a good friend. You have the unique ability of calling me out with just a glare, but you also make sure my character doesn't perish after making the least advisable choice.

Robin, you are one of the funniest people I know, gifted with good comedic timing. The emotional debriefs in the office meant a lot to me, and I loved your navy stories.

Martin, intelligent and unique person, I enjoyed your company and depth of thinking you apply to everything. I admire your ability to ask good, challenging, thought-provoking questions that can stop me in my tracks.

Fahimeh, so lovely and kind, thank you for being so supportive during the beginning of my PhD. You pushed me to feel more confident and comfortable with taking the lead.

Nate, I really appreciated your spontaneous energy and the evening walks around Rotterdam. You helped me feel welcomed when I first moved to the Netherlands.

Audrey, **Mark W**, and **Divya**, thanks for making the office a place where we can all laugh, discuss, complain, and just generally support one another.

To the people who make my life easier by helping with everything from figuring out my contract to sending infinite express packages to Nijmegen, **Wil**, **Rajshree**, **Adinda**, and **Roos**, thank you all for your help.

and to the rest of MECS and ChemE, **Wilson** (thanks for being so welcoming and for bringing that NYC energy), **Tom** (thanks for your help and advice along the way), **Fokko**, **Hans**, **Georgy**, **Davide**, **Sid** (see you at Kilimanjaro), **Aaron**, **Anirudh**, **Dowon**, **Recep**, **Bernhard** (thanks for always being so kind and supportive to me), **Hugo**, **Nienke**, **Pranav**, **Maryam**, **Marijn**, **Kai**, **Erdem**, and **Ziying**, thank you all for creating a friendly environment!

As well, to all the students who have been a part of my PhD journey...

Tom, you are a really gifted person. I don't think I could have done that project with anyone else but you. Besides your contribution to the science aspects of this PhD, on a personal level, you are great, funny, and you survived an intense, sleepless, muon week with me in Switzerland. You're really a gem!

Ismene, being able to excel at both academics and athletics is truly exceptional. I wish you luck in everything you want to pursue. It was really fun working with you.

Florianne, super driven with a lot of energy. Keep pursuing your goals.

Florine, a sensitive soul, I am glad you are following your dreams and I'm excited to see what you do next.

Lotte, you are really brilliant and have a positive outlook on things. I'm still impressed by how beautiful your lab notes are, the way you handled such a complex topic, and how quickly you developed both theoretical knowledge and hands-on lab skills. I'm sure you will thrive in anything you choose to do.

Sophie, in some ways, the yin to my yang, yet somehow it works. You had a difficult project in your hands and I'm super proud of you for taking it on with so much independence. You're super sweet, open, and intelligent. It's been fun working with you!

To some of the people I've met doing random things in the Netherlands...

Thomas, I love your vibe so much because you are so unapologetically you. I'm really glad that we could connect during Dutch class because you've been an awesome friend to me. You are a super cozy, reliable, honest person and I adore that.

Safia, hanging out with you in Rotterdam was one of the highlights of living there. Whenever you'd text me to go out, I knew I was about to find myself in an excellent restaurant and chatting the whole evening. You're a super down-to-earth person and we just bonded on so many levels. I hope we find ourselves in the same country again soon.

and a quick thanks to the people I met at language classes, ballet, rollerskating, roller derby, volunteering with Democrats Abroad & Rotaract, etc. for giving me a way to express myself outside the university!

To all my people over in New York City! Even if I am abroad for long periods of time, coming back to you all feels homey.

Polina, we've been there through so many of the crazy ups and downs of life together and

I'm so glad that we've both landed where we are today - happy and shining. You're like family to me and I look forward to seeing what we come up with next.

Sophia & Vivian, even though we are in 3 different time zones, I've appreciated so much that we could keep in touch and support each other as we develop ourselves, our careers, and our personal lives. One of the only nice things covid did was allow me to attend some of your important life events virtually, and for you to attend mine. Hugs to you both!

Sarah & Bobby, every time we see each other, it's like nothings changed and we can go back to the same nonsense that brought us together. We've all come a long way since Adelphi and I love seeing you grow together!

Andrew & Vivian, you've known me since the moment I realised I wanted to pursue a career in chemistry and physics, and you've been with me through this journey all the way to the PhD. I hope we can continue to hype each other up and navigate adulthood together.

Mashrur, life is a series of coincidences and both of us moving to the Netherlands at the exact same time, without planning or discussing it amongst each other is one of those happy ones. I love having your energy around. You're super creative and unstoppable, and I'm glad I can be in your orbit.

And to my family...

Giorgio, throughout these 4 years you have been everything from my closest colleague, to one of my closest friends, to my confidant, support system, and source of comfort. You not only understand and encourage me, but you go on adventures with me and add to much light and happiness to my life. I'm excited to see where life takes us next!

Mom, thank you for your support through all the twists and turns of my life trajectory. You keep me grounded and practical, listen to my life dramas, and give me advice. You are the purest example of a perseverance and resilience - no one can do what you do. You're a really incredible person.

Dad, thank you for cheering me on and reminding me that it's important to relax from time to time, and focus on hobbies to maintain good well-being.

To **Danik**, you are my rock and I adore you so much. It truly means a lot to me that we can support each other and keep each other laughing at all times. Even when you're exhibiting extreme little brother behaviour, you're still my buddy and I appreciate you.

Diana Chaykina
Scheveningen, October 2022

List of Publications

14. **D. Chaykina**, L. Kortstee, G. Colombi, H. Schreuders, B. Dam, B. A. Boukamp, "Electronic and ionic transport in rare-earth metal oxyhydride thin films (RE = Y, Y:Ca, Gd, Nd) characterised by EIS," *in preparation.*

13. S. Banerjee, **D. Chaykina**, B. Dam, G. de Wijs, A. Kentgens, "Investigating photochromism in rare-earth metal oxyhydrides (Y, Sc) by solid-state NMR," *in preparation.*

12. S. Banerjee, **D. Chaykina**, B. Dam, G. de Wijs, A. Kentgens, "Understanding the ScHO structure by solid-state NMR," *in preparation.*

11. S. Banerjee, **D. Chaykina**, R. Stigter, G. Colombi, B. Dam, G. de Wijs, A. Kentgens, "Solid state NMR studies on yttrium oxyhydrides: exploring multi-anion chemistry," *in preparation.*

10. G. Colombi, **D. Chaykina**[1], H. Schreuders, B. Dam, "Photochromic samarium oxyhydride thin films," *in preparation.*

9. G. Colombi, B. Boshuizen, **D. Chaykina**, L. Hsu, H. Schreuders, T. J. Savenije, B. Dam, "Relation between photochromism and photoconductivity in REO_xH_{3-2x} thin films," *in preparation.*

8. **D. Chaykina**, I. Usman, G. Colombi, H. Schreuders, B. Tyburska-Pueschel, Z. Wu, S. W. H. Eijt, L. J. Bannenberg, G. A. de Wijs, B. Dam, "Aliovalent Ca-doping of Yttrium Oxyhydride Thin Films and Implications for Photochromism," *The Journal of Physical Chemistry C*, 126 (34), 14742–14749, **2022**.

7. Z, Wu, T. W. H. de Krom, G. Colombi, **D. Chaykina**, G. van Hatten, H. Schut, M. Dickmann, W. Egger, C. Hugenschmidt, E. Brück, B. Dam, S. W. H. Eijt, "Formation of vacancies and metallic-like domains in photochromic rare-earth oxyhydride thin films studied by *in-situ* illumination positron annihilation spectroscopy," *Physical Review Materials*, 6, 065201, **2022**.

6. G. Colombi, R. Stigter, **D. Chaykina**, S. Banerjee, A. P. M. Kentgens, S. W. H. Eijt, B. Dam, G. A. de Wijs, "Energy, metastability, and optical properties of anion-disordered RO_xH_{3-2x} (R = Y, La) oxyhydrides: A computational study," *Physical Review B*, 105, 054208, **2022**.

5. **D. Chaykina**, F. Nafezarefi, G. Colombi, S. Cornelius, L. J. Bannenberg, H. Schreuders, B. Dam, "Influence of Crystal Structure, Encapsulation, and Annealing on Photochromism in Nd Oxyhydride Thin Films," *The Journal of Physical Chemistry C*, 126 (4), 2276-2284, **2022**.

4. **D. Chaykina**, T. W. H. de Krom, G. Colombi, H. Schreuders, A. Suter, T. Prokscha, B. Dam, S. W. H. Eijt, "Structural properties and anion dynamics of yttrium dihydride and photochromic oxyhydride thin films examined by *in situ* μ^+SR," *Physical Review B*, 103, 224106, **2021**.

3. G. Colombi, T. W. H. de Krom, **D. Chaykina**, S. Cornelius, S. W. H. Eijt, B. Dam, "Influence of Cation (RE = Sc, Y, Gd) and O/H Anion Ratio on the Photochromic Properties of REO_xH_{3-2x} Thin Films," *ACS Photonics*, 8(3), 709-715, **2021**.

---

[1] co-first author

2. S. Zankowski, **D. Chaykina**, P. Vereecken, “Interconnected Ni nanowires integrated with Li_xMnO_2 as fast charging and high volumetric capacity cathodes for Li-ion batteries,” *The Journal of Materials Chemistry A*, 8, 14178-14189, **2020**.

1. S. W. H. Eijt, T. W. H. de Krom, **D. Chaykina**, H. Schut, G. Colombi, S. Cornelius, W. Egger, M. Dickmann, C. Hugenschmidt, B. Dam, “Photochromic YO_xH_y Thin Films Examined by *in situ* Positron Annihilation Spectroscopy,” *Acta Physica Polonica Series A*, 137(2), 205-208, **2020**.

Curriculum Vitæ

Diana Chaykina

Diana Chaykina was born in Gomel, Belarus on the 6th of August, 1994. At the end of 1998, she moved to New York City in the United States of America with her parents. She graduated from Brooklyn Technical High School in 2012 with a major in chemistry. She then finished her bachelor's degree in 2016 as a chemistry major and physics minor at the Honors College of Adelphi University in Garden City, New York, USA. During this time, she went to the University of Warsaw in Warsaw, Poland for two summers (2014, 2015) to do research projects in photoelectrochemistry involving Cd-based thin films, and a photo-active biosensor.

Having this experience in Europe, Diana decided to do her master's degree in Leuven, Belgium at the Catholic University of Leuven, studying nanoscience, nanotechnology, and nanoengineering (focus on nanochemistry and nanomaterials). With this degree, she earned the title *burgerlijk ingenieur* in 2018. Her master's thesis topic was focussed on the conversion of precursor materials to lithium manganese oxide on a nanostructured current collector for a flexible thin film battery.

Finally, Diana landed in the Materials for Energy Conversion and Storage (MECS) group at Delft University of Technology in Delft, The Netherlands, under the supervision of prof. dr. Bernard Dam. She studied rare-earth metal oxyhydride thin films, with a focus on how to manipulate these materials to achieve different properties (for example, photochromic or transport properties). The results of this work are detailed in this thesis.